MONOGRAFIE, STUDIA, ROZPRAWY

M29

# SELECTED PROBLEMS OF MECHANICAL ENGINEERING AND MAINTENANCE

edited by Norbert Radek

Kielce 2012

**MONOGRAFIE, STUDIA, ROZPRAWY NR M29**

**Redaktor Naukowy serii**
**NAUKI TECHNICZNE – BUDOWA I EKSPLOATACJA MASZYN**
prof. dr hab. inż. Stanisław ADAMCZAK, dr h.c.

**Reviewers:**
Bogdan Antoszewski – Kielce University of Technology
Konrad Bartkowiak – Friedrich-Alexander University Erlangen-Nuremberg, Germany
Vyacheslav Bilousov – Donetsk National University, Ukraine
Tadeusz Burakowski – Institute of Precision Mechanics
Otakar Bokůvka – University of Žilina, Slovakia
Roman Domański – Warsaw University of Technology
Avraham Harnoy – New Jersey Institute of Technology, USA
Janusz Konstanty – AGH University of Science and Technology
Czesław Kundera – Kielce University of Technology
Evgeny Levashov – Moscow Institute of Steel and Alloys, Russia
Tomasz Otmianowski – Bolesław Markowski Higher School of Commerce in Kielce
Leszek Radziszewski – Kielce University of Technology
Yuriy Shalapko – Khmielnytskyi National University, Ukraine
Oleg Shinkaruk – Khmielnytskyi National University, Ukraine
Vladimir Sidorov – Moscow State University of Civil Engineering, Russia
Sławomir Spadło – Kielce University of Technology
Jan Szybka – AGH University of Science and Technology
Ken Watkins – University of Liverpool, United Kingdom
Włodzimierz Zowczak – Kielce University of Technology

**Redakcja techniczna**
Aneta DYNKOWSKA

**Projekt okładki**
Tadeusz UBERMAN



PL ISSN 1897-2691

Samodzielna Sekcja „Wydawnictwo Politechniki Świętokrzyskiej”
25-314 Kielce, al. Tysiąclecia Państwa Polskiego 7
tel./fax 41 34 24 581
e-mail: wydawca@tu.kielce.pl
www.tu.kielce.pl/organizacja/wydawnictwo

# CONTENTS

## Foreword

For developing technologies and production techniques it is important to provide for product quality and effectiveness. The properties of a product that ensure appropriate quality and effectiveness pose new technical challenges for both experts in various fields of technology and also economists, for whom those properties are related to the needs of the economy.

Advancements in different areas of the theory of exploitation of technical objects make it possible to apply modern solutions to design procedure planning and optimisation, construction, machine building and operation. Here, the main criteria are quality and the effective use.

The new field of machine and technical instrument exploitation has been developing dynamically. It relies on the fundamentals of exploitation sciences, which primarily include exploitation systems, technical diagnostics and surface engineering.

The term ***diagnostics*** originates from the Greek language, in which *diagnosis* means recognition, differentiation and assessment, and *diagnostike techne* refers to the art of finding differences and making diagnosis. ***Technical diagnostics***, a knowledge field formed already within exploitation sciences, deals with the assessment of the technical condition of machines by means of investigating the working processes and those that accompany the machine operation, and also by testing the properties of the items manufactured using a given machine.

Essentially, technical diagnostics involves evaluating the condition of a machine (assembly, sub-assembly, or component) in an indirect way, without dismantling it. It is based on measuring the generated diagnostic signals (symptoms) and comparing them with the nominal values.

***Exploitation***, as understood nowadays, comprises all purpose-oriented, organisational, technical and economic actions taken by people while dealing with technical objects. The concept also covers the interrelations between those actions, from the moment a device is deployed for operational use until it is shut down and intended for recycling.

***Surface Engineering*** covers all aspects of research and technical activities aimed at design, construction, reconstruction, and also investigations and applications of technological and functional surface layers that have different, i.e. better properties that the core (substrate). Those include mainly anti-abrasive, anti-corrosive, anti-fatigue, and also decorative properties. Others are optical, thermo-physical, electrical, magnetic, adhesive, ablative, bio-compatible and diffusive properties. Surface engineering is an autonomous science and technology discipline. Since 1994 it has been recognised by Poland's Committee for Scientific Research as one of the fifteen most innovative disciplines in the technology category. Surface engineering is one of manufacturing technologies (like welding, casting, also thermal, plastic and regular machining and others), in which a product of materials technology receives different surface properties.

The development of surface engineering is connected with the construction of new devices and a very complex apparatus. For those working in the field of surface engineering that means it is necessary to get continuous training and to develop their expertise and skills.

The present monograph is devoted to the issues of machine engineering and operation. The monograph comprises three chapters. The first chapter deals with diagnostics and exploitation. The second one concerns surface engineering and focuses mainly on the manufacturing of technological surface layers. The third chapter provides a collection of experimental results obtained with methods in which concentrated energy fluxes are employed. Presented in this chapter, electro-spark and laser machining are categorised as welding technologies.

The material contained in the monograph provides updated, though not fully comprehensive picture of research activities in the field of exploitation, diagnostics and surface engineering.

As a scientific editor of the monograph, I am convinced that the works included have been properly selected. They well represent the achievements of this part of the research community who deal primarily with machine engineering.

I believe the present monograph can be a valuable source of information for students of mainly mechanical engineering, young researchers, and also employees of different industries who want to broaden their knowledge in exploitation, diagnostics and surface engineering, or are interested in finding a solution to particular technical problems.

Norbert Radek

# 1 INSPECTION AND MAINTENANCE

## 1.1. ANALYSIS OF DIAGNOSTIC SYSTEMS IN WHEELED TRACTORS

*Ryszard Michalski, Michał Janulin*

### 1.1.1. INTRODUCTION

A wheeled tractor is a vehicle designed for transporting machines and devices without a self-propelled drive system (such as trailers) and for propelling machines without an engine with the use of a power take off or a hydraulic coupling. Tractors are classified as single axle and tandem axle machines. A 4K2 tandem axle tractor with a powered rear axle (4-wheeled, 2-wheel drive) is the most popular structural solution. Compatible machines and devices are attached to the tractor using a three-point hitch. Subject to need, a wheeled tractor can perform different functions. Technical diagnostics is a vital tool for assessing:

- functionality during transport and operation,
- work performance,
- operating safety in field and road driving modes,
- exhaust gas emissions.

The importance of technical diagnostics is frequently underestimated by both manufacturers and users. The use of diagnostic systems in modern wheeled tractors and precision farming applications should be examined in greater depth.


***Fig. 1.1.*** *John Deere wheeled tractor, model 7930*

This paper analyzes the diagnostic system in a John Deere wheeled tractor which supports an assessment of the vehicle's functionality, performance, operating safety and exhaust gas emissions. The diagnostic system was analyzed on the example of a John Deere tractor, model 7930, which supports the monitoring of a wide range of operating parameters.

Tractor JD 7930 is equipped with a simple and highly functional on-board computer which is easy to operate for beginners. Operating parameters are set manually. The operator presses icons on the control panel to open the applications menu where engine parameters can be adjusted by rotating the dial. This solution enables the operator to quickly change engine parameters without having to learn complex menu functions.

The tractor's key parameters are presented in Table 1.1.

***Table 1.1.*** *Key technical parameters of a John Deere 7930 tractor*

| MODEL | 7930 |
|---|---|
| **ENGINE PERFORMANCE** | |
| Power rating (97/68 EC) | 220 KM (162 kW) |
| Maximum rating (97/68 EC) | 243 KM (179 kW) |
| Power rating (Intelligent Power Management) according to 97/68EC (transport and PTO during operation) | 250 KM (184 kW) |
| **ENGINE CHARACTERISTICS** | |
| Rated RPMs | 2100 |
| Type | PowerTech Plus, Common Rail injection system, 4 valves per cylinder, Euro IIIA emission compliant |
| Aspiration | Variable-geometry turbocharger with intercooler and exhaust gas recirculation (EGR) |
| Cooling | Engine fan with a thermostatically controlled viscous clutch |
| Fuel tank capacity | 392 liters; 358 liters by right-hand door |
| **TRANSMISSION** | |
| AutoQuad Plus | Four powershiftable gears with variable reverse and switch control, speed adjustment, Softshift and Field Cruise |
| Speed range | 20F/20R – versions from 2.4 to 42 km/h, 42 km/h EcoShift or 50 km/h |

| | |
|---|---|
| **PTO – REAR AND FRONT** | Electrohydraulic, controlled from the truck cabin, engaged and disengaged by an oil cooled multiple disc clutch |
| Type – rear | 45 mm, 20-groove, 1000 rpm or 45 mm, 1000 rpm +/– set : 35 mm 540/1000 rpm |
| Engine rpm at PTO rotational speed during start-up | 540/1000 : 1950 rpm |
| Type – front PTO | Type 1-1000 rpm, direction of rotation: counterclockwise (all models), Type 2-1000 rpm, direction of rotation: clockwise (only 7730) or Type 3 : 1000 rpm, direction of rotation: clockwise (7830/7930) |
| **HYDRAULICS** | With pressure and flow rate compensation, subject to load, and a separate axial piston pump |
| Max. number of SCV valves | 4 x rear + 3 x front (central block), total of 7 |
| **3-POINT HITCH** | Category III N/III, lower links with hook implements |
| Rear suspension | Electrohydraulic control, electronically controlled resistance at lower links. Damping system. External control push-buttons. |
| Maximum hook lifting capacity | Standard: 7493 kg (73.5 kN), optional: 9177 kg (90.0 kN) |
| Lifting capacity (OECD) at the height of 610 mm | Standard: 6324 kg (62.0 kN), optional: 7560 kg (74.0 kN) |
| Front suspension | Category III N, lower links with hook implements, lifting capacity: 5200 kg (49.0 kN) (OECD compliant, at 610 mm: 3175 kg) |
| **FRONT AXLE** | |
| Suspension | Passive, hydropneumatic, triple link with drag bar and hydraulic cylinder |
| Power range and cylinders | 100 mm, 2 double acting cylinders with shock absorber function |
| **CABIN** | |
| Type | CommiView with ComfortCommi or Active Seat; Pulpit CommiARM in models with AutoPower steering gear |
| Noise reduction/ noise level | Passive noise reduction, noise inside cabin: 72 dB(A) |
| Display | Display screen on the Commi Center terminal and the center pillar, Hydraulic TouchSet screen with ISO-compliant GreenStar 2 color display is optionally available |
| **DIMENSIONS AND WEIGHT** | |
| Width x height x length | 2.44 x 3.18 x 5.50 m |
| Tires | 600/70R30 and 710/70R42 |
| Gross weight load at 40 km/h | 13 100 kg |

### 1.1.2. EVALUATION OF DIAGNOSTIC FUNCTIONS IN A WHEELED TRACTOR

A diagnostic system has to provide the user with information about the vehicle's basic functions. The elements that control tractor functions are divided into two groups: the first controls the engine and the gearbox, and the second monitors the hydraulic system. A view of the operator's cabin and the armrest control unit is displayed in Figure 1.2.

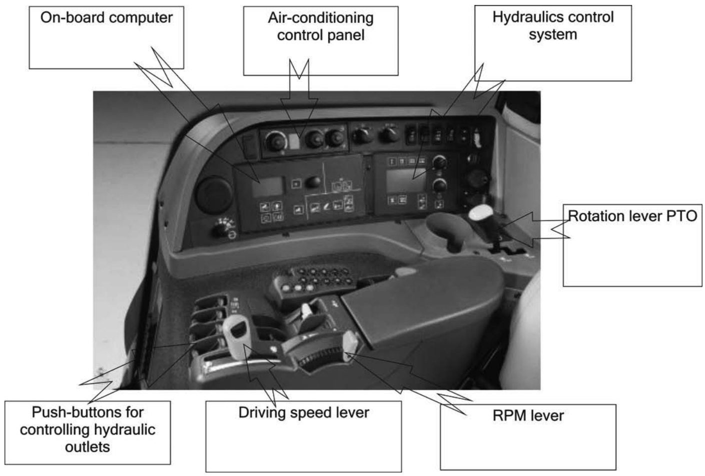


***Fig. 1.2.*** *Cabin controls in a John Deere tractor*

A view of the hydraulics control system is shown in Figure 1.3. The computer controls six hydraulic outlets which are marked with Roman numerals I to VI on the panel (Fig. 1.3).

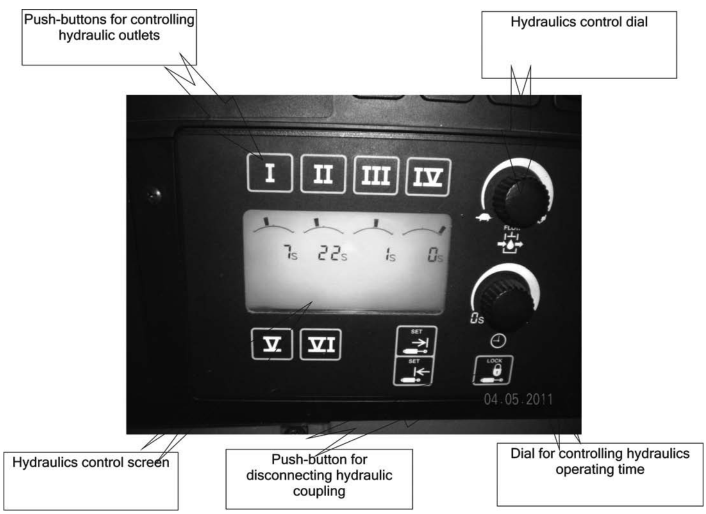


***Fig. 1.3.*** *View of the on-board computer and the control panel*

The operator can control the performance and operating time of each outlet by pressing the respective numeral. The outlets can be programmed to operate in a desired sequence, and this is a highly useful option when the tractor is operated with attachments. By pressing the respective icons on the control panel, the operator can block the rear power lift or activate the transport mode, in which case the power lift will act as a shock absorber to minimize dynamic load caused by sudden vibration of the transported machines.

Malfunctions are color coded and displayed on the screen. During normal operation, two parameters are displayed, and they can be configured by the user. The panel also features four push-buttons for changing the type of displayed parameters (Fig. 1.4). Dials for controlling cabin temperature are placed above the display.

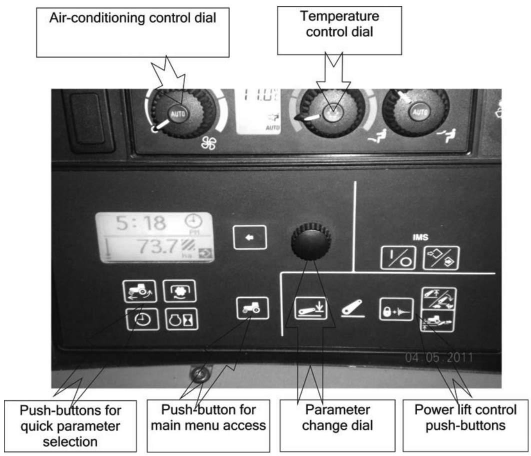


***Fig. 1.4.*** *View of the panel for controlling the tractor's operating parameters*

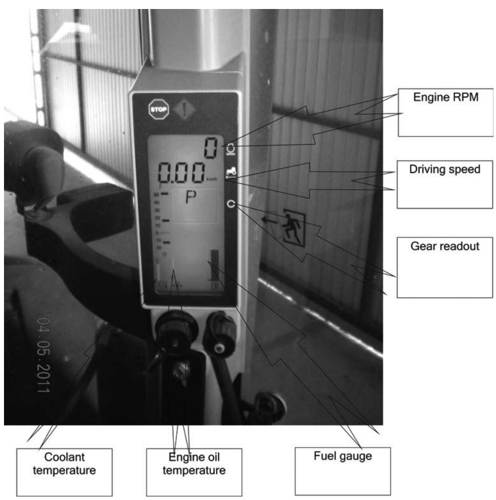


***Fig. 1.5.*** *Hierarchical structure of the parameter monitoring system in a John Deere tractor, model 7930*

The hierarchical structure of the tractor's parameter monitoring system is shown in Figure 1.5.

The main menu for monitoring operating parameters in a John Deere tractor has the following features: implement selection, enable RPTO, gearbox, automatic activation of PTO, diagnostics, system error codes, controls, CAN statistics, maintenance interval.

The following operating parameters are shown on the main display: maximum engine rotation, power management (power consumption indicator), set speed, slip, engine rotational speed, engine hours until next service, coolant temperature, engine oil pressure, battery voltage, power lift height, PTO rotational speed, width of implement, fuel consumption in l/h. The key parameters monitored by the on-board computer in the discussed tractor are:

– functionality during transport and operation,

– work performance parameters.

Less emphasis is placed on exhaust gas parameters during operation – the on-board computer monitors the quantity of consumed fuel and engine rotational speed, but the purity of exhaust gas is not verified. Operator safety in field and road traffic has been generally disregarded, and the system focuses mainly on protecting tractor subassemblies from damage caused by overheating or seizure.

Table 1.2 provides examples of error codes displayed on the main on-board computer screen.

***Table 1.2.*** *Examples of displayed error messages*

| | |
|---|---|
| **ACU 00158.04** | ACU switched supply voltage low |
| **ACU 00177.17** | Low transmission oil temperature |
| **ACU 000581.07** | Transmission not responding to command |
| **ACU 000974.02** | Hand throttle sensor circuit voltage problem |
| **ACU 000974.04** | Rear PTO voltage problem |
| **ACU 001080.02** | ACU sensor supply 2 voltage problem |
| **ACU 002000.09** | ECU message missing |
| **ACU 002003.09** | PTI message missing |
| **ACU 002020.09** | SFA message missing |
| **ACU 523775.02** | Single lever control problem |
| **ACU 523923.02** | SCV control lever switch problem |
| **ACU 523954.07** | Speed band adjustment fault |
| **ACU 523955.31** | Engine overload in manual mode |
| **ACU 523960.17** | Operator not in seat |

As shown in Table 1.2, the diagnostic system monitors mainly operator controls and electrical circuits in the tractor. The supplied information enables the support service to identify the malfunction, but it does not signal the cause of the problem. The tractor's diagnostic system has been designed to monitor the electronic system, whereas mechanical defects that underlie the diagnosed faults are largely neglected. Tractor malfunctions can be classified into four categories: exhaust gas, engine performance, functional performance and operating safety. The diagnostic system in the analyzed John Deere tractor focuses mainly on functional problems and defects that affect engine performance, whereas exhaust gas problems and threats to operating safety are signaled in less detail. The system detects defects which increase exhaust gas emissions by collecting data about the engine's input parameters, but the type of substances emitted to ambient air is not analyzed. Information about the composition and smokiness of exhaust gas is not obtained from the exhaust system, even though such data would be highly useful in diagnosing malfunctions that lead to excessive exhaust gas emissions. As regards operating safety, the diagnostic system does not monitor basic parameters such as brake lining wear or clearance in kinematic pairs of the steering system. The availability of the above parameters would significantly improve operator safety, in particular when towing heavy machines or trailers. The discussed tractor would greatly benefit from a new diagnostic system which would identify the remaining categories of defects and where problems would be diagnosed earlier than in standard OBD II. In the above standard, a malfunction is identified when the measured value exceeds the standard value by 50%. This solution causes a significant delay in diagnosing defects, and it can result in costly repairs.

Conclusions:

Our analysis indicates that diagnostic systems in modern wheeled tractors focus on selected subassemblies and parameters that are vital for engine control. As regards exhaust system defects, the system monitors only those engine parameters that could suggest excessive toxicity levels, but the composition or smokiness of exhaust gas is not analyzed. Exhaust system defects are identified based on algorithms that account for selected operating parameters, and standard OBD II detects a malfunction only when the measured value exceeds the standard value by 50%. The above solution causes significant delays in diagnosing defects, and it could lead to serious damages that are difficult to repair.

This study was supported by research grant No. N N504513740

# 1.2. STRUCTURAL ANALYSIS OF A WHEELED TRACTOR ORIENTED TOWARDS DAMAGE DIAGNOSTICS

*Ryszard Michalski, Jarosław Gonera, Michał Janulin, Ryszard Arendt*

## 1.2.1. INTRODUCTION

A wheeled tractor is a vehicle designed for transporting machines and devices without a self-propelled drive system (such as trailers) and for propelling machines without an engine with the use of a power takeoff or a hydraulic coupling. Tractors are classified as single axle and tandem axle machines. A 4K2 tandem axle tractor with a powered rear axle (4-wheeled, 2-wheel drive) is the most popular structural solution. Compatible machines and devices are attached to the tractor using a three-point hitch. Subject to need, a wheeled tractor can perform different functions. Technical diagnostics is a vital tool for assessing:

- functionality during transport and operation,
- performance parameters,
- operating safety in field and road driving modes,
- exhaust gas emissions.

The importance of technical diagnostics is frequently underestimated by both manufacturers and users. The use of diagnostic systems in modern wheeled tractors and precision farming applications should be examined in greater depth.

The monitoring of operating parameters of wheeled tractors used in agriculture, construction and forestry supports:

- the search for energy efficient production technologies,
- an assessment of energy losses associated with a tractor's traction properties,
- reduced exhaust gas emissions.

During a technical inspection, the operation and performance of a wheeled tractor is diagnosed, and damaged components are identified and localized. Periodic inspections in service stations do not always deliver optimal results due to limited service time, restricted scope of the inspection and the absence of working load during the diagnostic process. Based on the generated consequences, defects can be classified into the following groups:

- functional defects ($u_f$) which inhibit performance (torque, towing force, working speed, fuel consumption),
- exhaust defects ($u_e$) which increase toxic emissions (and noise) and fuel consumption due to a malfunction of the fuel supply system, layout of the diesel engine and the power transmission system,
- defects that jeopardize driving safety ($u_s$) can affect the following tractor systems: brake, suspension, steering and lights,
- defects that affect engine performance ($u_d$) and driving parameters in a tractor, including decreased acceleration, delayed response to changes in movement parameters, unequal power levels, significant loss of power and moment of force.

The presence of a malfunction should be signaled, and the operator should be provided with information about the type of defect, the affected subassembly and component.

This study analyzes the structure of a wheeled tractor for the needs of monitoring malfunctions caused by defects that impair the vehicle's functionality, exhaust gas emissions, driving safety and engine performance. The structure of a wheeled tractor will be analyzed in view of the following evaluation criteria:

- determination of valuable diagnostic information which is available to the user,
- adoption of an effective diagnostic model for monitoring the tractor's performance (ability to detect and localize defects with 10% risk),
- availability and versatility of structural solutions for a given class of tractors,
- standard diagnostic procedures for detecting the analyzed categories of defects,
- diagnostic knowledge base and inference algorithms.

### 1.2.2. EVALUATION OF DIAGNOSTIC SOLUTIONS IN MODERN WHEELED TRACTORS

Tractor diagnostics is not a new problem, and leading tractor manufacturers have been analyzing and improving their diagnostic tools for many years. In most cases, however, diagnostic measures are reduced to periodic inspections in service stations and the monitoring of the tractor's selected functional parameters during operation.

***Table 1.3.*** *Selected diagnostic trouble codes in a John Deere tractor*

| Diagnostic Trouble Codes John Deere – Engine (200.000-) | | | | | | | | |
|---|---|---|---|---|---|---|---|---|
| No | Suspect Parameter Number (SPN) * | Failure Mode Identifier (FMI) * | Digit Codes | Fault classification based on consequences | | | | Description |
| Significance | Represents the system or component at fault. | Represents the type of fault, e.g. exceeded value | Service code | emission | driving safety | engine performance | functionality | |
| 1 | 28 | 3 | 115 | | | | + | Throttle #3 position (C) high (throttle position measured with a potentiometer) |
| 2 | 28 | 4 | 116 | | | | + | Throttle #3 position (C) low (throttle position measured with a potentiometer) |
| 3 | 29 | 3 | 13 | | | | + | Throttle # 2 position (B) high (throttle position measured with a potentiometer) |

| | | | | | | | | |
|---|---|---|---|---|---|---|---|---|
| 4 | 29 | 4 | 14 | | | | + | Throttle #2 position (B) low (throttle position measured with a potentiometer) |
| 5 | 91 | 3 | 11 | | | | + | Throttle #1 position (A) high (throttle position measured with a potentiometer) |
| 6 | 91 | 4 | 12 | | | | + | Throttle #1 position (A) low (throttle position measured with a potentiometer) |
| 7 | 94 | 3 | 127 | | | | + | Fuel rail pressure input voltage high |
| 8 | 94 | 4 | 129 | | | | + | Fuel rail pressure input voltage low |
| 9 | 94 | 10 | 171 | | | | + | Fuel rail pressure loss detected |
| 10 | 94 | 17 | 172 | | | | + | Fuel rail pressure not developed |
| 11 | 97 | 3 | 176 | | | | + | Water in fuel input voltage high |
| 12 | 97 | 4 | 176 | | | | + | Water in fuel input voltage low |
| 13 | 97 | 16 | 175 | | | | + | Water in fuel detected |
| 14 | 100 | 1 | 65 | | | | + | Engine oil pressure extremely low |
| 15 | 100 | 3 | – | | | | + | Oil pressure sensor input voltage high |
| 16 | 100 | 4 | – | | | | + | Oil pressure sensor input voltage low |
| 17 | 100 | 18 | 64 | | | | + | Engine oil pressure moderately low |
| 18 | 105 | 3 | 23 | | | | + | Manifold air temperature sensor input voltage high |
| 19 | 105 | 4 | 24 | | | | + | Manifold air temperature sensor input voltage low |
| 20 | 105 | 16 | 66 | | | | + | Manifold air temperature moderately high |
| 21 | 107 | 31 | 120 | | | | + | Air filter restriction high |
| 22 | 110 | 0 | 63 | | | | + | Coolant temperature extremely high |
| 23 | 110 | 3 | 25 | | | | + | Coolant temperature sensor input voltage high |
| 24 | 110 | 4 | 26 | | | | + | Coolant temperature sensor input voltage low |
| 25 | 110 | 16 | 62 | | | | + | Coolant temperature moderately high |

| | | | | | | | | |
|---|---|---|---|---|---|---|---|---|
| 26 | 111 | 1 | 61 | | | | + | Engine coolant level low |
| 27 | 158 | 17 | 84 | | | | + | ECU power level down |
| 28 | 174 | 3 | 37 | | | | + | Fuel temperature sensor input value high |
| 29 | 174 | 4 | 38 | | | | + | Fuel temperature sensor input value low |
| 30 | 174 | 16 | 81 | | | | + | Fuel temperature moderately high |
| 31 | 611 | 3 | 98 | | | | + | Injector wiring shorted to power source |
| 32 | 611 | 4 | 99 | | | | + | Injector wiring shorted to ground |
| 33 | 620 | 3 | 21 | | | | + | Sensor power supply open/short to B+ |
| 34 | 620 | 4 | 22 | | | | + | Sensor power supply short to ground |
| 35 | 627 | 1 | 97 | | | | + | Injector supply voltage problem |
| 36 | 629 | 13 | 28 | | | | + | Watchdog trip failure |
| 37 | 636 | 2 | 144 | | | | + | Pump position sensor/cam position sensor input noise |
| 38 | 636 | 8 | 143 | | | | + | Pump position sensor/cam position sensor input missing |
| 39 | 636 | 10 | 144 | | | | + | Pump position sensor/camp position sensor input pattern error |
| 40 | 637 | 2 | 142 | | | | + | Crank position input noise |
| 41 | 637 | 7 | 145 | | | | + | Crank position/cam position out of synchronization |
| 42 | 637 | 8 | 141 | | | | + | Crank position input missing |
| 43 | 637 | 10 | 142 | | | | + | Crank position sensor input pattern error |
| 44 | 639 | 13 | 55 | | | | + | Bus CAN error |
| 45 | 651 | 5 | 131 | | | | + | Cylinder #1 circuit open |
| 46 | 651 | 6 | 91 | | | | + | Cylinder #1 circuit shorted |
| 47 | 652 | 5 | 132 | | | | + | Cylinder #2 circuit open |
| 48 | 652 | 6 | 92 | | | | + | Cylinder #2 circuit shorted |
| 49 | 653 | 5 | 133 | | | | + | Cylinder #3 circuit open |
| 50 | 653 | 6 | 93 | | | | + | Cylinder #3 circuit shorted |

| | | | | | | | | |
|---|---|---|---|---|---|---|---|---|
| 51 | 654 | 5 | 134 | | | | + | Cylinder #4 circuit open |
| 52 | 654 | 6 | 94 | | | | + | Cylinder #4 circuit shorted |
| 53 | 655 | 5 | 135 | | | | + | Cylinder #5 circuit open |
| 54 | 655 | 6 | 95 | | | | + | Cylinder #5 circuit shorted |
| 55 | 656 | 5 | 136 | | | | + | Cylinder #6 circuit open |
| 56 | 656 | 6 | 96 | | | | + | Cylinder #6 circuit shorted |
| 57 | 1080 | 3 | 173 | | | | + | Sensor #2 supply voltage high |
| 58 | 1080 | 4 | 174 | | | | + | Sensor #2 supply voltage low |
| 59 | 1110 | 31 | – | | | | + | Engine shutdown |
| 60 | 1347 | 5 | 177 | | | | + | Pump control valve #1 error/mismatch |
| 61 | 1347 | 7 | 178 | | | | + | Fuel rail pressure control error |
| 62 | 1348 | 5 | 179 | | | | + | Pump control valve #2 error/mismatch |
| 63 | 1568 | 2 | 29 | | | | + | Torque curve selection invalid |
| 64 | 1569 | 31 | 68 | | | | + | Fuel derate |

* *Defective components and type of defect are described based on a John Deere tractor manual.*

Modern tractors are equipped with diagnostic systems which monitor mainly operator controls and electrical circuits in the vehicle. The supplied information enables the support service to identify the malfunction, but it does not signal the cause of the problem. The tractor's diagnostic system has been designed to monitor the electronic system, whereas mechanical defects that underlie the diagnosed faults are largely neglected (Michalski and Janulin 2011). Tractor malfunctions can be classified into four categories: exhaust gas, engine performance, functional performance and operating safety. Diagnostic systems in modern tractors focus mainly on functional problems and defects that affect engine performance (refer to Table 1.3), whereas exhaust gas problems and threats to operating safety are signaled in less detail. The list of functional defects which are signaled by the most advanced diagnostic systems in John Deere tractors is presented in Table 1.3.

The system detects defects which increase exhaust gas emissions by collecting data about the engine's input parameters, but the type of substances emitted to ambient air is not analyzed. Information about the composition and smokiness of exhaust gas is not obtained from the exhaust system, even though such data would be highly useful in diagnosing malfunctions that lead to excessive exhaust gas emissions. As regards operating safety, the diagnostic system does not monitor basic parameters such as brake lining wear or clearance in kinematic pairs of the steering system. The availability of the above parameters would significantly improve operator safety, in particular when towing heavy machines or trailers. Wheeled tractors would greatly benefit from diagnostic systems which identify the remaining categories of defects and support early fault detection. The existing diagnostic tools in wheeled tractors measure engine parameters and fluid levels (Fig. 1.6).

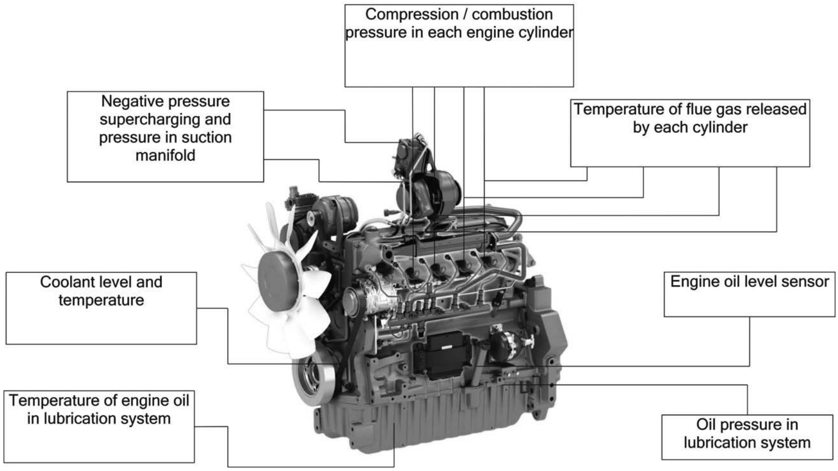


***Fig. 1.6.*** *Engine parameters measured in a wheeled tractor*

A tractor's performance parameters are evaluated by using the following equation to calculate the power transferred from the engine to the wheels:

$$N_e = F_n \cdot V \tag{1.1}$$

where:

$$F_n = \frac{M_s \cdot i_c \cdot \eta_c}{r_d} \tag{1.2}$$

$$V_{rz} = V_t(1 - s) \tag{1.3}$$

and based on the first law of motion:

$$F_n = F_f + F_u \tag{1.4}$$

Slip is closely related to the adhesive force between the wheel and the ground:

$$s = f(F_{opr}) \tag{1.5}$$

The correlation between the adhesion coefficient and wheel slip *s* is determined based on measurement results.

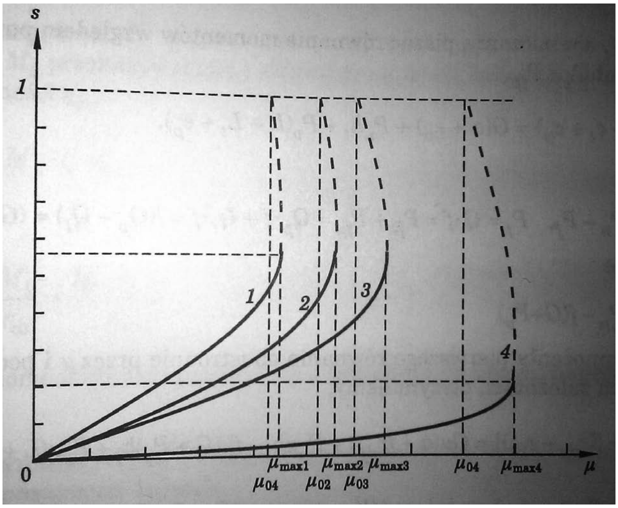


*Fig. 1.7. Correlation between wheel slip (s) and adhesion coefficient (μ) on various types of ground*

Characteristics of a wheeled tractor's drawbar pull (Fig. 1.8).

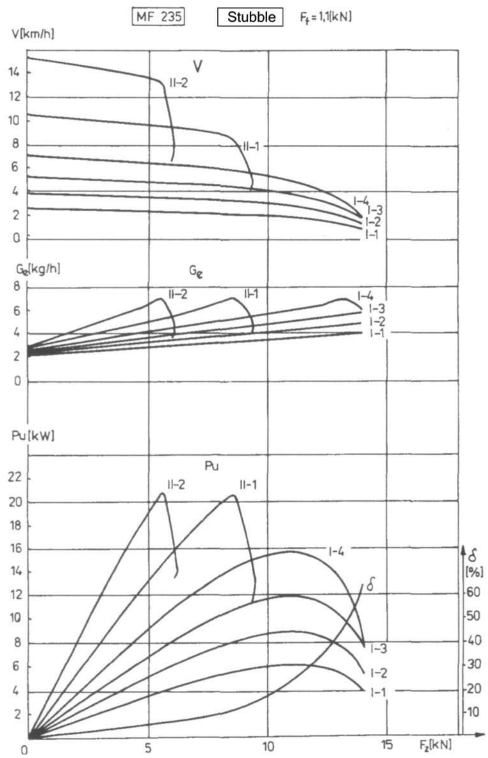


*Fig. 1.8. Drawbar pull of a tractor working on soft ground, where: $F_z$ – drawbar pull at the hitch, $P_u$ – drawbar horsepower, $G_e$ – hourly fuel consumption, $g_e$ – specific fuel consumption, V – velocity, $\delta = s$ – slip*

$$F_u = F_n - F_f \tag{1.6}$$

$$F_u = \frac{M_e \cdot i_c \cdot \eta_c}{r_d} - F_f \tag{1.7}$$

Wheel slip is practically impossible to control "intuitively" within a relatively narrow, recommended range of $s$ = 0.1-0.15 for trailed implements and $s$ = 0.13-0.15 for suspended implements. Excessive or insufficient wheel slip results in up to 30% loss of drawbar horsepower, it increases fuel consumption and tire wear. Subject to the type of operation performed, field working speed is set at $V_a$ = 2-10 km/h and transport speed at $V_t$ = 7-40 km/h

Advanced tractors are provided with new-generation electric and electronic systems which control the operation of actuator systems. Such sophisticated solutions require an on-board computer for online monitoring of functional performance, exhaust gas emissions, safety and operating parameters. Modern tractors would greatly benefit from a diagnostic system which would identify the remaining categories of defects and where problems would be diagnosed earlier than in standard OBD II. Mechatronic diagnostic systems identify the machine's actual operating load in different operating modes and under specific circumstances. By monitoring the tractor's parameters, the operator can reduce fuel consumption by adjusting engine power to the required working speed and load.

A tractor's hourly fuel demand can be determined with the use of the below formula:

$$Q_{pal} = \frac{g_e(n_e) \cdot N_z}{1000 \cdot \rho_{pal}} \frac{\mathrm{dm}^3}{\mathrm{h}} \tag{1.8}$$

where: $g_e(n_e)$ – specific fuel consumption [g/kWh] determined based on the engine's RPM at driving speed $V$ and overall gear ratio $i_k$; $\rho_{pal}$ – fuel viscosity [kg/dm$^3$]; $N_z$ – power demand [kW].

At constant crankshaft speed, the power required by a tractor to overcome rolling resistance, subject to driving speed $V$, can be determined using the following formula:

$$N_z = \left[ m \cdot g \cdot (f + \sin\alpha) + \frac{\rho \cdot A \cdot C_x \cdot (V - V_w)^2}{2} + m \cdot a + R \right] \cdot \frac{V}{\eta} + N_{od} + N_{WOM} \tag{1.9}$$

where: $m$ – tractor's mass [kg]; $f$ – coefficient of rolling resistance; $\alpha$ – ground inclination; $\rho$ – air density [kg/m$^3$]; $A$ – area of the tractor's front face [m$^2$]; $C_x$ – coefficient of aerodynamic drag; $V$ – driving speed [m/s]; $V_w$ – wind speed [m/s]; $\eta$ – power transmission efficiency; $R$ – machine and implement resistance [N]; $N_{od}$ – power consumption of on-board systems (e.g. power steering, air-conditioning, lighting, etc.); $N_{WOM}$ – power demand of a PTO-driven implement.

The tractor's velocity in given gear can be calculated based on the below formula:

$$V = \frac{\pi \cdot r_d \cdot n_e}{30 \cdot i_k} \frac{\mathrm{m}}{\mathrm{s}} \tag{1.10}$$

where: $r_d$ – rolling radius of wheel [m]; $i_k$ – gear ratio in $i^{\text{th}}$ gear; $n_e$ – crankshaft rotational speed [rpm].

A tractor's field speed is generally low, therefore aerodynamic drag can be omitted.

Diagnostic systems in modern wheeled tractors do not make full use of the relations between diagnostic symptoms and parameters. Damaged components in a given assembly are not specifically identified. To illustrate, a message informing the operator about the failure of a Diesel engine does not specify that the defective component is the injector on the third cylinder. The existing diagnostic systems are not equipped with a sufficient number of sensors, and they fail to monitor many important parameters.

An effective on-board control system should analyze the diagnostic relations between the tractor's performance parameters, fuel consumption and defect category: functional defects ($u_f$), exhaust defects ($u_e$), defects that jeopardize safety ($u_s$) and defects that affect performance ($u_d$).

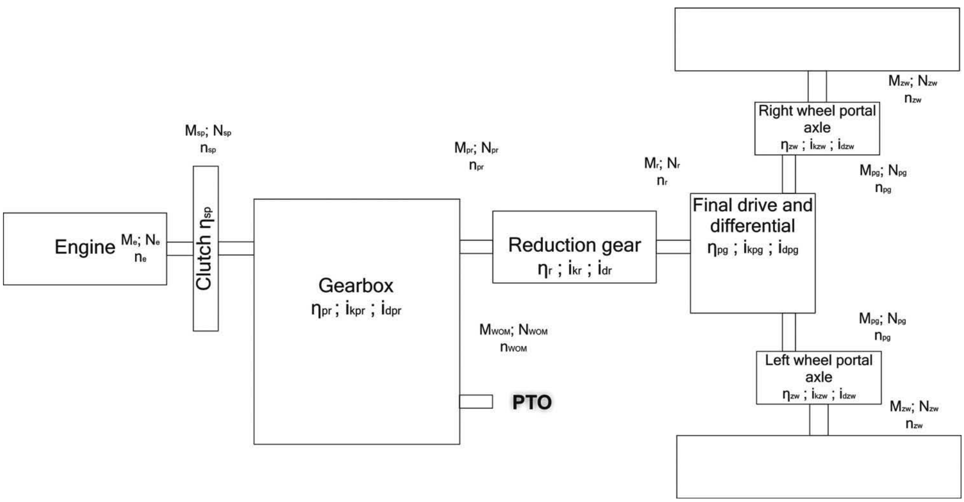


***Fig. 1.9.*** *Diagram of a power transmission system in a wheeled tractor with technical specifications*

### 1.2.3. BUILDING DIAGNOSTIC RELATIONS

The presented model of a wheeled tractor relies on traction values which describe the vehicle's operational phenomena and determine its wear in a given load cycle (Fig. 1.10).

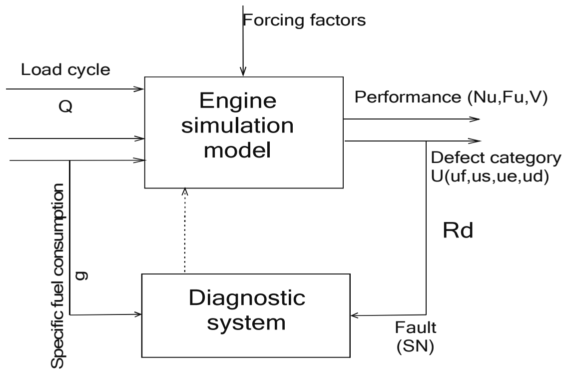


***Fig. 1.10.*** *Diagnostic diagram of a wheeled tractor based on diagnostic relations, where: g – specific fuel consumption,* $S_N$ *– fault, u – defect category*

The processes noted in a tractor's complex kinematic systems are dynamic processes that result from the conversion of chemical to mechanical energy in the engine and energy dissipation in the remaining components of the power transmission system. This energy is required to power implements that are attached to (transport) and suspended on the tractor.

The tractor's status, i.e. its actual load cycle, will be modeled for every instantaneous velocity $V(t)$ and values of motion resistance and gear ratio in the power transmission system. The above correlations will presented in the form of the tractor's nominal drawbar pull. Torque and rotational speed will be analyzed to provide a multi-dimensional description of the tractor's operating status.

A tractor's operating status is determined by: driving speed, resistance to motion (of the tractor and implements), mass, gear ratio in the power transmission system, layout of the power transmission system, rolling radius of drive wheels, etc. The severity of damage to a tractor's parts and assemblies is determined by the load cycle and material strength.

In this analysis, failure is defined as every event which deteriorates a tractor's performance quality and effectiveness, and which should be detected in the diagnostic process (Michalski 2004). Therefore, a tractor's fault ($S_N$) results from one of the four defect categories ($u_f$, $u_s$, $u_e$, $u_d$), and it can be expressed in the form of the following relation:

$$S_N \Rightarrow \left(u_f \cap u_s \cap u_e \cap u_d\right) \neq 0 \tag{1.11}$$

Defect diagnostics is a process of detecting, isolating and describing malfunctions (Kościelny 2001):

- detection of defects, i.e. tracing down (observing) defects in an object and determining the moment of damage,
- localization of defects, i.e. determining the type and place of damage,
- identification of defects, i.e. determining the magnitude and variability of damage over time.

A description of defects in a tractor constitutes a basis for evaluating the severity of a fault. A defective vehicle can be serviced, repaired or scrapped.

A defect is reported when at least one of the measurable or immeasurable features characterizing the tractor's technical condition ceases to support correct functioning of the machine. A defect is defined as the loss of the tractor's ability to perform the assigned functions [PN-93/N-50191]. A malfunction can be analyzed at different levels of complexity, including systems, kinematic pairs and components. A machine defect results from damage to its components, regardless of the analyzed level. By monitoring the tractor's physical parameters, the operator can observe the damage not only based on the symptoms (as a random event), but also based on the results of the entire damage process (consequences).

The most frequent types of machine damage are sudden damage (overload) and gradual damage (wear) (Michalski 2001). Sudden damage results from a rapid change in the analyzed component's parameters. It may be caused by cracking due to thermal shock and overloading. In this type of defect, the probability of damage is independent of the vehicle's runtime. Catastrophic damage is a variant of sudden damage which renders the machine completely unfit for operation. Gradual damage is caused by wear, corrosion, fatigue, material creep, etc.

Each of the above defect groups can be further broken down into parametric damage and emergency damage. In parametric damage, the system is transformed from a fully operational state (parametric ability) to a non-operational state (parametric failure). Parametric wear damage implies that maximum wear values have been exceeded. In emergency damage, the system is transformed from an operational state (in special cases, if the system had previously undergone parametric damage – from a non-operational state) to a state of functional failure, i.e. complete technical failure. Emergency wear damage implies that maximum wear values have been exceeded. Based on the type of threat to a tractor's operational safety, defects can be classified as (PN-93/N-50191):

- **critical defects** which pose a threat to humans, generate significant material losses and other irreversible consequences,
- **non-critical defects** which do not pose a threat to humans and do not generate significant material losses.

Another category of malfunctions are **degradation defects** which imply gradual and partial damage (tractor's selected functions are preserved).

Knowledge engineering techniques have not yet been developed in the process of diagnosing a tractor's defects, but they seem to offer almost endless possibilities. Diagnostic knowledge is composed of facts, relations and procedures. In a mathematical approach, the diagnostic process involves the search for relations R between defects (faults) and specific diagnostic symptoms. There exists a cause and effect relationship between a malfunction $f_i \subset F$ of tractor components and symptoms $s_j$ represented by set $S$. This relationship can take on one of the following forms:

$R: \{s_j\} \Rightarrow f_i$ – one-to-one relationship (a set of symptoms identifies a given state);

$R: \{s_j\} \Rightarrow \{f_i\}$ – one-to-many relationship.

Knowledge engineering techniques rely on symbolic representations of knowledge (inherited and expert knowledge) as well as automatic inference mechanisms. They involve numerical models, uncertain, incomplete, fuzzy and qualitative knowledge. All diagnostic knowledge engineering methods rely on mathematical logic, in particular the theory of relations (Moszner 1967).

In most applications, the process of developing diagnostic relations involves a dialogue between an expert and a knowledge engineer. The number of available knowledge sources is, however, much greater. In this approach to knowledge acquisition in the process of developing diagnostic relations, the appropriate methods are selected based on:

- specialist technical information supplied by manufacturers and operators,
- experimental tests to determine symptoms of machine damage,
- expert tests to determine symptoms of machine damage,
- physical models of mechanical systems oriented towards damage diagnostics.
- identified mathematical models oriented towards damage detection.

The development of diagnostic relations based on different methods and information sources will foster the growth of reliable declarative knowledge which comprises facts and state-symptom diagnostic relations, as well as procedural knowledge which underlies diagnostic inference.

If we assume that knowledge is an organized data set, the acquisition of (diagnostic) knowledge is a process of gathering diagnostic information (data set) and developing models that support the most effective use of that information (ordering a data set). In a wheeled tractor, the following symptoms are associated with the discussed categories of defects (Michalski, Gonera 2011):

- **functional defects**: overheating or slipping of friction clutch, gearbox overheating, reduction gear overheating, final drive and differential overheating, overheating of rear wheel portal axles, loss of air in front and rear axle tires, leak in induction system, engine overheating, unequal power levels in cylinders, incorrect oil pressure reading, significant bushing clearance in the crankshaft and piston assembly, abnormal oil pressure drop in the engine lubrication system;
- **exhaust defects**: overheating or slipping of friction clutch, uncontrolled loss of air in front and rear axle tires, engine overheating, loss of coolant, unequal power levels in cylinders, loss of engine oil, engine oil burning;
- **defects that jeopardize safety**: excessive clearance in steering system, light bulb damage in the lighting system, wiper malfunction, horn malfunction, loss of brake fluid, reduced brake force, reduced pressure in brake system, uncontrolled loss of air in front and rear axle wheels, oil pump damage;

– **defects that affect performance**: overheating or slipping of friction clutch, gearbox overheating, overheating of reduction gear, overheating of final drive and differential, overheating of drive wheel portal axles, loss of gear oil, uncontrolled loss of air in front and rear axle tires, engine overheating, unequal power levels in cylinders.

There is a certain delay between the moment when a given component is diagnosed as defective and the tractor's response, i.e. the appearance of changes in functional parameters as a symptom of the defect. Defects that affect the machine's performance are most quickly diagnosed and remedied. Exhaust defects, functional defects and defects that jeopardize driving safety do not generate noticeable symptoms or may be manifested only in critical situations.

The above suggests that **exhaust defects and defects that jeopardize driving safety** are not effectively monitored. During operation, those types of malfunctions may progress due to natural wear of a tractor's components, and the available methods, technical and legal solutions do not support their detection. In standard OBD II (On-Board Diagnostics), a malfunction which can increase toxic emissions from the exhaust or fuel injection system is identified as significant when the measured value exceeds the standard applicable to a given vehicle type by 50% (Merkisz 2002).

Diagnostic information about a tractor's status can be presented in the following form:

$$f_i \Rightarrow U_\rho ; U_i = \{u_{n,i}\} \tag{1.12}$$

where: $U_i$ – set of parameters characteristic of the $i^{th}$ fault (defect), $u_{n,i}$ – $n^{th}$ parameter characteristic of the $i^{th}$ fault (defect).

Relation $R_{XF}$ can be described by the Cartesian product of sets $F$ and $X$:

$$R_{XF} \subset X \times F \tag{1.13}$$

where: $X$ – set of process variables, $F$ – machine's state space.

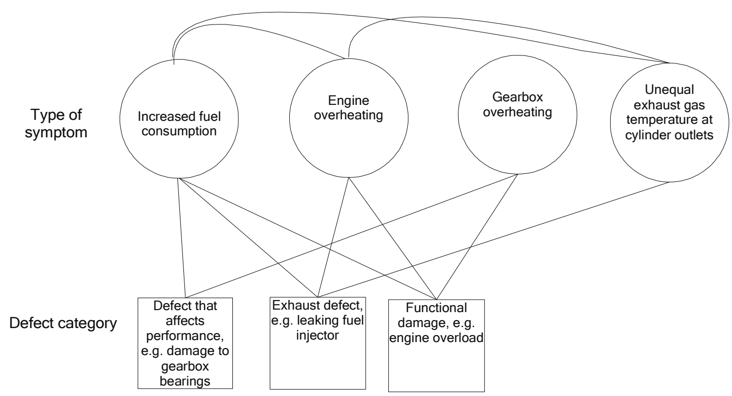


***Fig. 1.11.*** *Diagram illustrating the relation between defects and symptoms*

Tests should be carried out to determine a tractor's diagnostic relations in relation to a given defect category. In this case, the space of process variable values is mapped as a function of the machine's state space *F*. In machines, the diagnostic process examines various relations between a vehicle's state (defect) and the observed symptoms. In most cases, there are two types of relations:

- classical equivalence relations $R_k$ which have the features of reflexive, symmetric and transitive relations with characteristic function $\mu_R \in [0,1]$

$$\mu_R(x_1, x_2, ..., x_n) = \begin{Bmatrix} 1 & \text{when} & (x_1,...,x_n) \in R \\ \\ 0 & \text{when} & (x_1,...,x_n) \notin R \end{Bmatrix} \tag{1.14}$$

i.e. a total ordering relation $\leq$;

- fuzzy relations whose range is expanded to the [0,1] interval, written as a set of pairs

$$\mu_R(x_1,...,x_n)/(x_1,...,x_n) \tag{1.15}$$

then:

$$R = \sum \mu_R(X,f)/(X,f) \tag{1.16}$$

The relation is between different membership functions ($\subseteq$ partial order) which satisfies the first two conditions of the equivalence (reflexive and symmetric) relation. The classical relation concept is a special case of a fuzzy relation when the membership function can take on only two values: 0 or 1 (Yager and Filer 1997).

The weakness of classical quantitative methods for describing complex phenomena has been used by L. Zadeh to formulate the principle of incompatibility. This area of research deals with diagnostic knowledge engineering which is based on the relations between defects and symptoms:

$$R \subset \left[ (x_{i,1}, U_i) \wedge (x_{i,2}, U_2) .. (x_{i,n}, U_i) \Rightarrow (f_i, y_{i,w}) \right] \tag{1.17}$$

where: $R$ – set of relations, $U_n$ – set of parameters characteristic of the $n^{\text{th}}$ parameter, $x_{i,n}$ – $n^{\text{th}}$ element of the set of process variables of the $i^{\text{th}}$ fault, $f_i$ – machine's $i^{\text{th}}$ state, $y_{i,w}$ – evaluation of the $i^{\text{th}}$ stated based on the adopted criteria.

A system for monitoring the performance of a wheeled tractor should be developed in two stages:

- development of a model system for monitoring various types of defects in a wheeled tractor to support the existing diagnostic knowledge base and inference algorithms,

– testing a tractor's monitoring system and developing technical and legal standards for mechatronic systems for monitoring the condition of a wheeled tractor.

Conclusions:

This paper discusses the diagnostic system of a wheeled tractor which supports the identification of four types of defects based on a structural analysis of modern tractors. The results of our analysis suggest that the diagnostic range of most monitoring systems is restricted to the operating parameters of the engine and other key components in a wheeled tractor. As regards exhaust system defects, the system monitors only those engine parameters that could suggest excessive toxicity levels, but the composition or smokiness of exhaust gas is not analyzed. Exhaust system defects are identified based on algorithms that account for selected operating parameters, and standard OBD II detects a malfunction only when the measured value exceeds the standard value by 50% (Merkisz 2002). The above solution causes significant delays in diagnosing defects, and it could lead to serious damages that are difficult to repair. A tractor's diagnostic system should identify the vehicle's technical condition online and provide the operator with information about functional, exhaust, performance and safety defects in reference to the actual operating load.

Acknowledgements: This study was supported by research grant No. N N504513740

# 1.3. THE INFLUENCE OF WASTE ADDITIVES ON THE MATERIAL OPERATIONAL PROPERTIES

*Jolanta Latosińska, Norbert Radek, Łukasz J. Orman*

## 1.3.1. INTRODUCTION

Ceramic materials are commonly used in many types of industries for example in the building industry as construction materials or their constituents. The possibilities of the use of ceramics are mostly related to their microscopic and macroscopic properties. At the same time, waste products are more and more often reused worldwide and can be applied for ceramic materials production. As a result, problems related to the utilisation of possibly hazardous substances are avoided. Moreover, additional economical benefis might be achieved in this way. These are linked to the substitution of conventional fuels with waste or to the reuse of waste such as sewage sludge, which would otherwise be landfilled or treated in a different and sometimes much more expensive way. This could not only generate some unnecessary costs, but it might also pose a serious threat to the environment and people. For example landfilling, which is generally most prevalent especially in Poland, can lead to ground water contamination with leachate, sanitary problems and spreading of diseases or biogas emissions. Biogas might cause fire or explosion hazards if it gathers in enclosed spaces but also – if it is released to the atmosphere – contributes to the global warming phenomenon just as carbon dioxide.

Liew et al. [17] studied the physical parameters of bricks made with the addition of sewage sludge. It was reported that the increase in sewage sludge concentration resulted in lowered shrinkage, density and compressive strength of bricks (which was lowest for the 40% sludge concentration). The content of dried sewage sludge varied from 10% to 40% by weight. It was observed that the leachability of metals from the produced bricks was very low.

Wiebusch and Seyfried [18] focused their analysis on the brick samples produced with ashes generated during the process of sewage sludge incineration. The maximal ash concentration reached 40% by weight. The authors proved a considerable influence of the ash content as well as of the sintering temperature. Its value had to be generally 1060$^{o}$C in order to provide the maximal strength value. The ashes of different chemical compositions and sintering temperatures from 1000$^{o}$C to 1060$^{o}$C were considered. The most favourable content of the waste material was 10% in view of the compressive strength value, which reached almost 150MPa.

Lin and Weng [19] experimentally studied chosen parameters of bricks made from incinerated sewage sludge ash and clay. It was concluded that the optimal ash content amounted to 20% (by weight) so that good bonding properties could be provided. While the optimal firing temperature that led to the maximal compressive strength was 1000$^{o}$C. The data indicate that the addition of 20% ash and firing temperature of 1000$^{o}$C let to the best strength properties. The compressive strength value at this temperature was higher than that of the brick with 0%, 10%, 30%, 40% as well as 50% ash – which proved to be the least advantageous composition.

Latosińska and Żygadło [20-21] found out during their experimental analyses that sewage sludge from sewage treatment plants can be used as an ingredient in the production of keramsite. The content of the organic matter present in the sludge is quite significant. Consequently, the produced materials tend to have a lot of pores in their structure. The porosity improves thermal insulation properties, which is crucial in view of their possible use in buildings as a constituent of wall materials.

Lin et al. [22] experimentally considered properties of water treatment sludge as well as bottom ash from the municipal solid waste incinerator. Sludge was mixed with ash and, afterwards, samples in the form of blocks were formed. These were sintered at the temperatures 900$^{o}$C-1200$^{o}$C. It turned out that increased bottom ash concentration led to a lower value of compressive strength. It was also proven that generally the compressive strength rose with sintering temperature for samples produced with the use of sludge.

Stegemann and Buenfeld [23] discussed the unconfined compressive strength of the materials containing waste as a function of mix composition. They used neural networks for the analysis and literature data of Portland cement containing real industrial wastes. The authors considered different types of waste e.g. different kinds of dust, municipal solid waste incinerator fly ash, sludges and its ashes as well as others.

However, in the literature some contradictory information on operational parameters of the materials can also be found. Tay et al. [24] indicate that there are significant discrepancies in the test results of the compressive strength of materials produced with sewage sludge or with ashes generated during its incineration. It is related to the research methods, the kind of clay used for the tests and the dimensions of the bricks. Besides, the addition of sewage sludge could not be very advantageous in view of the properties of the products – for example sewage sludge used as an ingredient in bricks' production may lead to problems with shrinkage or soaking, as presented in Figure 1.12.

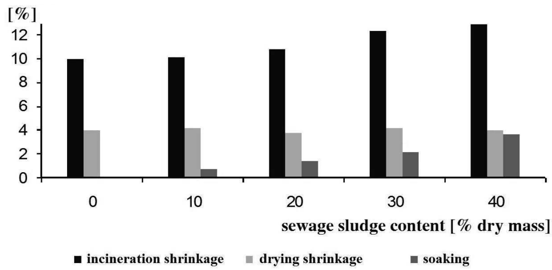


***Fig. 1.12.*** *Shrinkage and soaking as a function of sewage sludge content [24]*

The authors' own research projects conducted so far on the discussed issue have mainly focused on the impact which the acid rain might have on buildings, and in particular on the strength of ceramic materials produced from clay and clay with the addition of fly ash (20% by weight). The obtained test results of the compressive strength of samples treated and untreated with acid seem to prove the existence of the impact of this factor with respect to the composition of the material [25].

### 1.3.2. MATERIAL AND METHOD

#### Sample preparation

The ceramic specimens of different component compositions (considered by weight) were tested, namely: 100% clay, 80% clay and 20% fly ash, 80% clay and 20% sewage sludge as well as 60% clay, 20% fly ash and 20% sewage sludge. The samples' dimensions were about 26 mm x 26 mm x 10 mm. They were sintered in a laboratory furnace at two different temperatures: 850$^{o}$C and 900$^{o}$C, chosen basing on the literature data considering this subject. The specimens were kept in the furnace for about 8 hours, including 1 hour at the maximal sintering temperature. After the sintering process, the products remained in the device until their temperature dropped to about 100$^{o}$C. Afterwards, they were removed and left for cooling.

#### Test results

The outer surfaces of the produced samples were investigated basing on the images generated by the scanning electron microscope (SEM) in order to get an insight into their surface structure. The magnification of 500 times was used in this study. The test results have been presented in the figures below: 1.13a-b (for 100% clay sample), 1.14a-b (sample with clay and 20% sewage sludge), 1.15a-b (sample with clay and 20% fly ash) and 1.16a-b (sample with clay and 20% sewage sludge and 20% fly ash).

a) b)

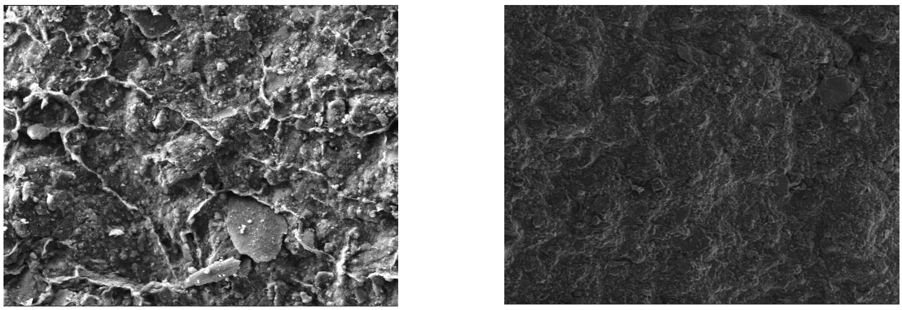

***Fig. 1.13.*** *SEM image of the outer surface of the sample of 100% clay. Sintering temperature: a) 850°C, b) 900°C*

a) b)

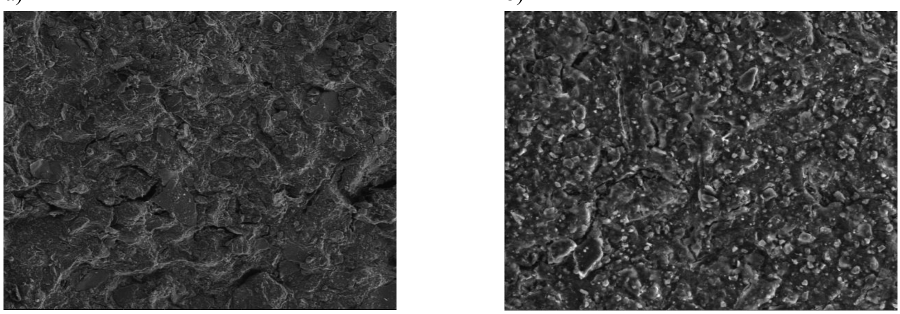

***Fig. 1.14***. *SEM image of the outer surface of the sample of clay with 20% sewage sludge addition. Sintering temperature: a) 850°C, b) 900°C*

a) b)

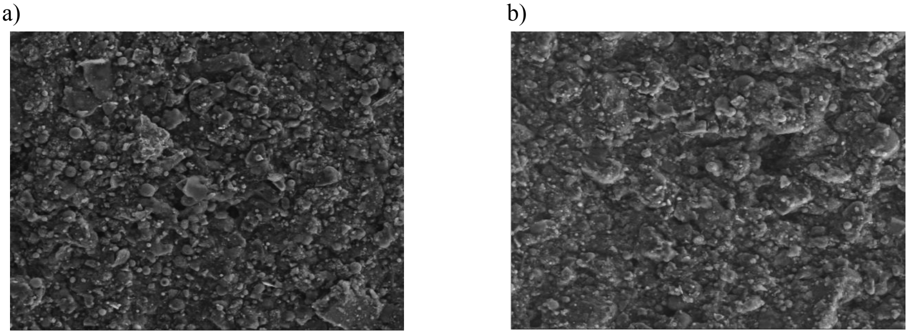

***Fig. 1.15.*** *SEM image of the outer surface of the sample of clay with 20% fly ash addition. Sintering temperature: a) 850°C, b) 900°C*

a) b)

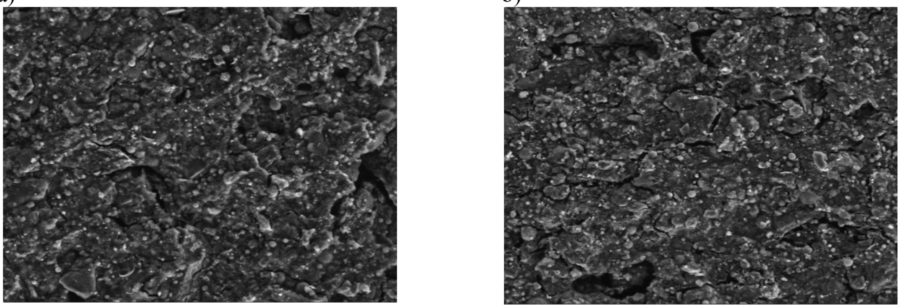

*__Fig. 1.16.__ SEM image of the outer surface of the sample of clay with 20% sewage sludge and 20% fly ash additions. Sintering temperature: a) 850$^oC$, b) 900$^oC$*

Additionally, the material composition of the samples was investigated. The results have been presented in Table 1.4. While figures below show elementary analysis determined in the course of the experiment for samples with clay (Fig. 1.17a), clay with sewage sludge (Fig. 1.17b) and clay with fly ash (Fig. 1.17c).

a)

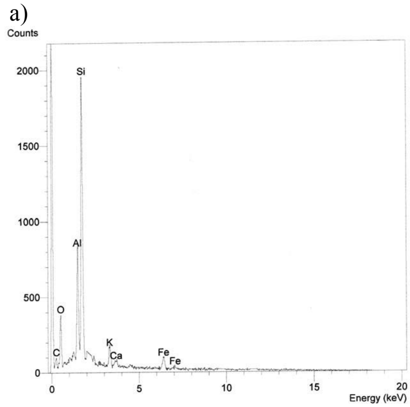


b)

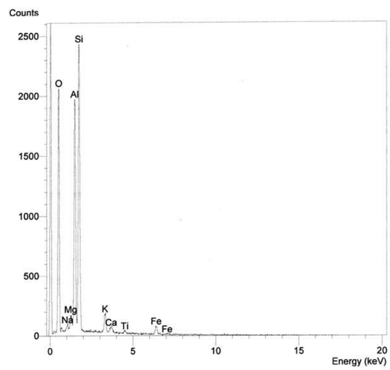


c)

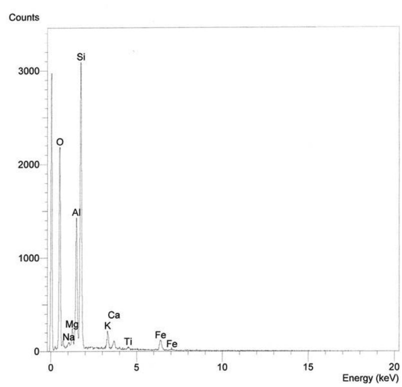


*__Fig. 1.17.__ Elementary analysis of the sample: a) of clay, b) of clay and sludge, c) of fly and ash*

***Table 1.4.*** *Composition of elements (in %) in the samples sintered at 850°C*

| Element | Clay | Clay with sewage sludge | Clay with fly ash |
|---|---|---|---|
| Na | – | 1.30 | 1.16 |
| Mg | – | 2.01 | 1.13 |
| Al | 7.12 | 13.79 | 19.69 |
| Si | 18.62 | 34.77 | 29.67 |
| K | 1.88 | 2.70 | 2.55 |
| Ca | 0.49 | 1.29 | 0.86 |
| Ti | – | 0.50 | 0.47 |
| Fe | 2.92 | 4.33 | 2.66 |
| O | 68.98 | 39.31 | 41.82 |

### 1.3.3. DISCUSSION OF RESULTS AND CONCLUSIONS

Basing on the conducted research data, conclusions can be drawn about the influence of the material composition on the outer surface of the produced ceramic elements. The products from clay have a concise structure, while specimens with the addition of sewage sludge contain the glass phase. The samples of clay and fly ash have spherical ash particles. The same is observed in the case of clay and both sewage sludge and fly ash additives. The surface of the samples produced with the use of clay and waste materials have more surface cracks in relation to the samples from clay. The introduction of calcium and iron oxides (Tab. 1.4) from sewage sludge and ash led to the creation of areas of consise structure. While the organic compounds degassed during sintering and cracks got created in the produced porous structure.

If the volumetric porosity of the products is also increased, better thermal insulation properties might be anticipated as a result. However, at the same time material strength could be affected in the negative way. Generally, no significant impact is observed in terms of sintering temperature in the studied range of this parameter.

The obtained results might be extended to include higher number of samples with different concentrations of the waste materials as well as the compressive strength of materials tests or thermal conductivity analyses. Consequently, the optimal parameters of the material composition and process conditions can be found, which would lead to a practical application of the test results even in the industrial scale.

The authors have already begun conducting compressive strength tests of ceramic samples. The tests were carried out on samples produced from clay and clay with the addition of fly ash (20% by weight) after curing in distilled water and acid solution (which was used to simulate the impact of acid rain on the ceramic materials as building components). The results have been presented in Table 1.5 [25].

*Table 1.5.* Compressive strength of ceramic samples after curing in water and acid [25]

| No. | Ceramic sample | Compressive strength, MPa |
|---|---|---|
| 1. | clay sample – cured in distilled water | 45.1 |
| 2. | clay sample – cured in acid | 41.1 |
| 3. | sample with clay and fly ash – cured in distilled water | 24.9 |
| 4. | sample with clay and fly ash – cured in acid | 34.8 |

# 1.4. THE OPERATIONAL AND ECONOMIC ASPECTS OF USING COBALT IN METALLIC-DIAMOND TOOLS

*Jan Lachowski*

## 1.4.1. METALLIC-DIAMOND TOOLS

In the industry of metallic-diamond tools for cutting natural stones and building materials, circular saws with a working layer in the form of segments soldered to a steel disc between special cuts are used (Fig. 1.18). The segments constitute the working elements of a saw are produced by means of the technology of powder metallurgy.

The process of producing metallic-diamond sinters consists in mixing the powder constituting the metallic matrix (Fig. 1.19) with the diamond powder, synthetic or natural (Fig. 1.20), pressing fittings, and then sintering or hot pressing them. As a result of those operations one receives sinters commonly known as metallic-diamond segments. The segments are soldered to steel disks (Fig. 1.18) and they constitute cutting elements of circular saws used for cutting materials [26, 27].

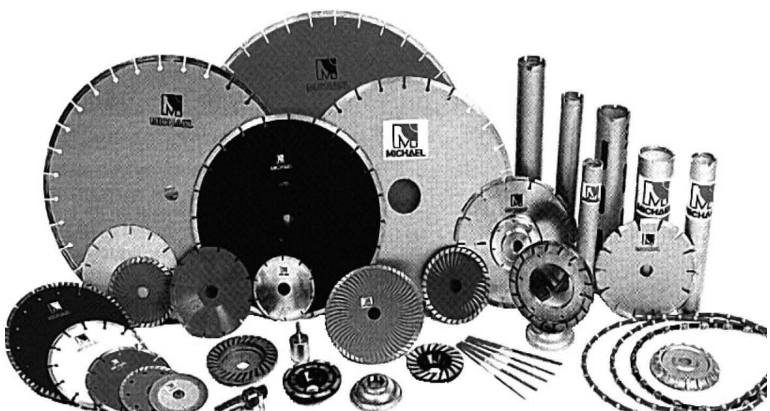

***Fig. 1.18.*** *Modern metallic-diamond tools [26, 27]*

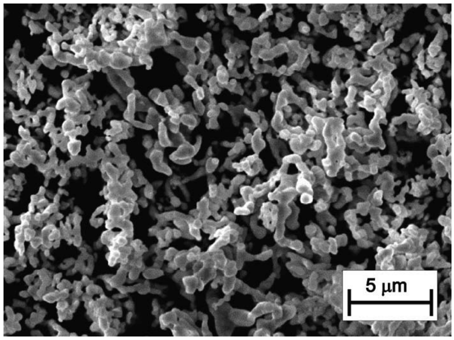


***Fig. 1.19.*** *Powder of SMS cobalt [26, 27]*

Technological progress in the production of modern metallic-diamond tools is expressed in the producers' striving for producing tools of better and better functional properties with the use of lower production costs. Good quality of a tool is influenced mainly by:

- suitable structure of a tool,
- proper choice of the matrix material,
- proper choice and location of diamond particles in the matrix material.

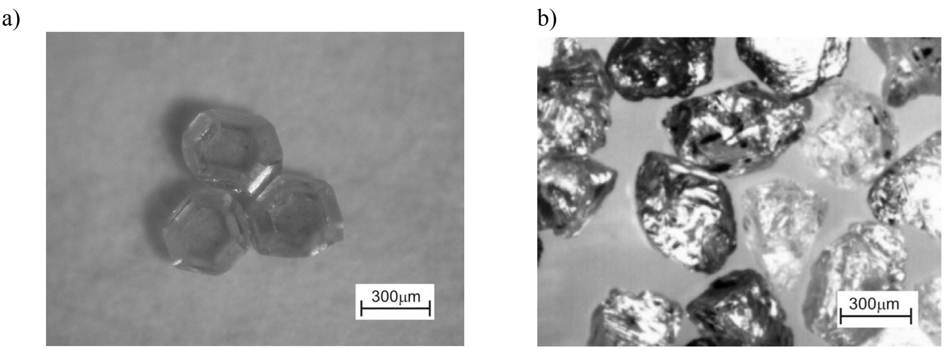


***Fig. 1.20.*** *a) Synthetic diamonds, b) natural diamonds [26, 27]*

Cobalt is the material that is most often used for the matrix of metallic-diamond sinters. However the price of that material is high and at the same time unstable. The economic situation forces producers to seek possibilities to replace cobalt with other, cheaper material, which as a matrix material would ensure similar functional properties of tools with lower costs of their production.

### 1.4.2. USING DIAMONDS FOR THE PRODUCTION OF TOOLS

The content of diamond in a segment of a tool is specified by the so called concentration which can be defined as follows: concentration of 100 corresponds to 4.4 carats (0.2 g) of diamond in 1 $cm^3$, which constitutes 25% of volume. Other values of the concentration of diamond are determined proportionately to the basic value of 100 [26]. In the production of tools most often the concentration of 20-25 is used.

In the past the use of diamond as a tool material was limited to its natural variant (Fig. 1.20b). As a result of crushing and sorting of diamond bort, diamond powders of different particle sizes were obtained.

The possibility of producing synthetic diamond allowed for controlled modification of the shape and properties of particles, from very fine-grained, used for grinding and polishing, to large, strong crystals of the regular, multifaceted shape (Fig. 1.20a), used for cutting the stones and ceramic materials that are most difficult for processing.

The technology of the production of synthetic diamonds was mastered in at least 15 countries [28]. Due to the price, synthetic diamonds constitute more than 90% of all industrial diamonds, despite they posses worse functional properties.

### 1.4.3. RETENTION OF DIAMOND PARTICLES IN METALLIC MATRIX

A significant property of the matrix material is retention – i.e. maintaining (Fig. 1.21) particles of a diamond during the work of a metallic-diamond tool. Diamond particles are maintained in a matrix thanks to mechanical or chemical connections, or by both of those connections simultaneously [26, 29].

a) b)

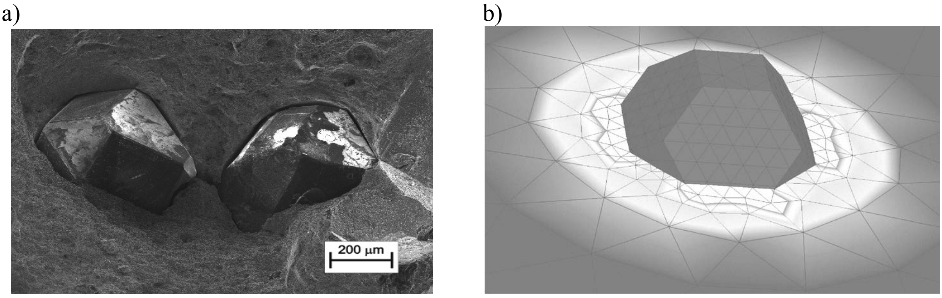


***Fig 1.21.*** *Fractured surface of a segment with diamond particles: a) numerical model of a diamond particle with the surrounding plastic sphere b) [29, 30]*

Mechanical connection is obtained during the cooling after the process of hot pressing. Because diamonds have a very small coefficient of thermal expansion in relation to metals, diamond particles are pressed by the shrinking matrix [30]. Maintaining appropriate mechanical connection depends on elastic and plastic properties of the matrix material. The analysis of the retention of diamond particle in relation to mechanical properties of the matrix was conducted in papers [29, 31, 32, 33]. The most significant parameters of the assessment of efficiency of retention are elastic strain energy and plastic energy of the deformed matrix around a diamond particle (Fig. 1.21b) [34].

### 1.4.4. THE LEVEL OF MINING AND PRODUCTION OF COBALT IN 1900-2010

Statistical data concerning the production and the prices of cobalt have been collected since 1900 [35]. Analysing the production (Fig. 1.22) and the consumption (Fig. 1.23) of cobalt one can observe two periods. In the period from 1900 to 1938 the production and the consumption of cobalt was not high. Then since 1939 (the outbreak of World War II) there has appeared a quick increase of the production and the consumption of cobalt.

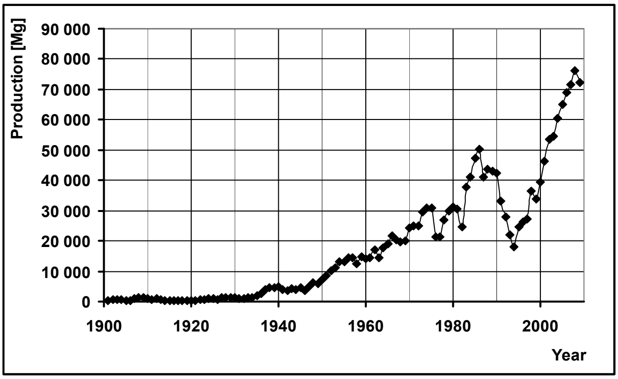


***Fig. 1.22.*** *The world mine production of cobalt in the years 1900-2009 [27]*

From the moment when the technology of obtaining synthetic diamonds on an industrial scale was developed, the use of metallic-diamond tools increased significantly [27] as the price of synthetic diamonds is definitely lower from the price of natural diamonds. That caused a further increase in the demand for cobalt; the production and the consumption of cobalt increased rapidly. If in the period to 1938 the average consumption in the USA amounted to about 200 tonnes per year, then in the years 1950-2009 the average value amounted to about 8000 tonnes (Fig. 1.23).

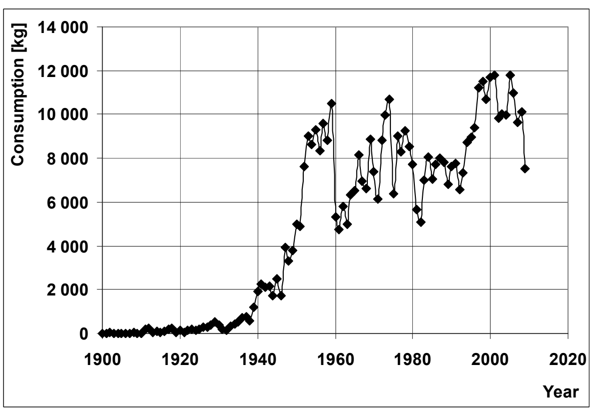


***Fig. 1.23.*** *The amount of the consumption of cobalt in the USA (in tonnes) starting in 1900 [27]*

The mining of cobalt in 2009 in total amounted to 72.3 thousands of tonnes and it was focused on a small group of countries, mainly in: Congo, Russia, China, Zambia, Australia, Canada and Cuba. The participation of individual countries in the mining is shown in Figure 1.24 and Table 1.6. In 2010 there appeared a further strong increase in the mining which is estimated at 88 thousands of tonnes.

***Table 1.6.*** *Cobalt mining [Mg] in 2009*

| Congo | Russia | China | Zambia | Australia | Canada | Cuba |
|---|---|---|---|---|---|---|
| 35500 | 6100 | 6000 | 5000 | 4600 | 41000 | 3500 |

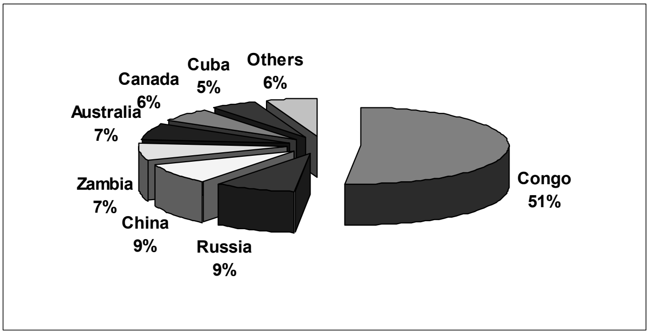


***Fig. 1.24.*** *The percentage share of individual countries in the mining of cobalt*

The fastest increase in the mining of cobalt in the last decade was noted in Congo (Fig. 1.25). From approximate 10 thousands of tonnes in the years 2002-2003, to the estimated 45 thousands of tonnes in 2010. In 1994-1995 the mining in that region amounted to approximate only 3.4 thousands of tonnes.

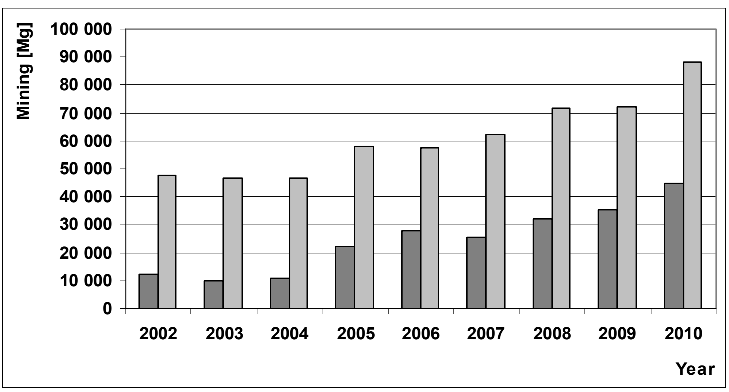


***Fig. 1.25.*** *The dynamics of the mining of cobalt in Congo (dark bars) in the last decade, comparing with the world mining (grey bars)*

Apart from large players in the mining of cobalt, also the producers of metallic cobalt are significant. Approximately 31% of the production of metallic cobalt takes place in the countries in which there is no mining. Those countries include: Finland, Norway and Belgium. Nowadays China is the first producer of cobalt metal in the world (Fig. 1.26).

The confirmed world resources of cobalt amount to approximately 15 millions of tonnes. The majority of those resources is located in Australia, Canada, Russia, Congo and Zambia [28]. Large amounts of cobalt also occur at the bottom of the Pacific Ocean [36, 37] in metallic manganese nodules, but their mining is unprofitable with the currently used technologies. The oceanic resources of cobalt are estimated at 2.5-10 millions of tonnes [37].

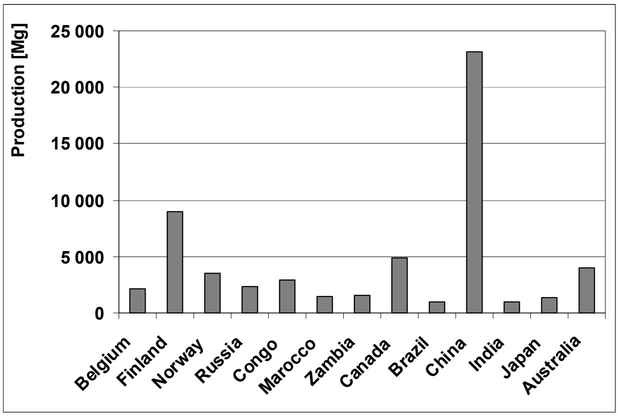


***Fig. 1.26.*** *Production of cobalt metal in 2009 year*

## 1.4.5. THE LEVEL OF PRICES OF COBALT IN 1900-2010

In the first considered period (to 1938) the price of cobalt showed greater stability and fluctuated around an average value amounting to 4000 $/tonne. After World War II the price of cobalt further fluctuated on a balanced level, until the mid 1970s when the price increased rapidly (Fig. 1.27).

The price of cobalt has shown strong fluctuations since 1977 till the present moment (Fig. 1.27). Political events occurring in the regions connected with the mining of cobalt had a significant impact on its price. In the years 1977-1978 there was a rebellion in the Katanga province in Congo (Zair) [38]. The rebels based in Angola carried out a series of attacks on Katanga. The rebellion was brought under control with the help of French and Belgian troops.

In 1996 ethnic conflict between the Hutu and Tutsi tribes in the neighbouring Rwanda spread onto the area of Zair. The military activities called the First Congo War led to overthrowing the president Mobutu and the return to the previous name of Congo (*Democratic Republic of Congo*). These events led to a strong increase in the prices of cobalt in the mid 1990s (Fig. 1.27).

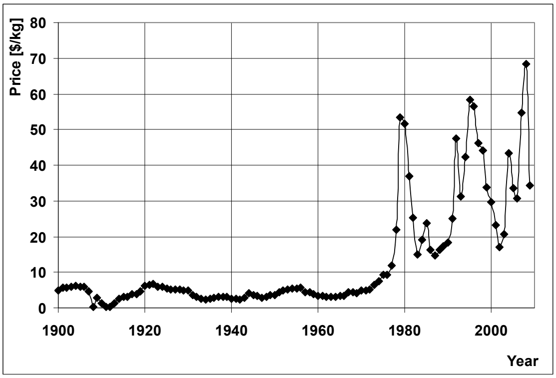


*Fig. 1.27. Dynamics of the price of cobalt in the years 1900-2009*

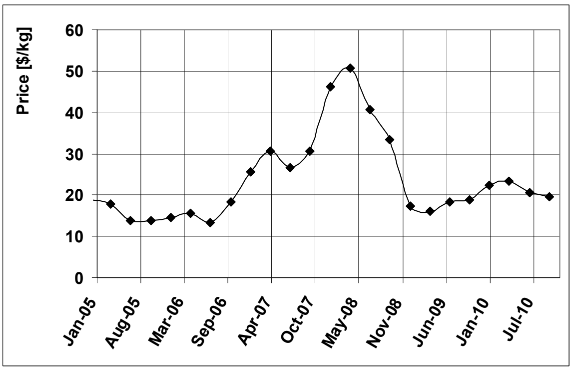


*Fig. 1.28. Quarterly fluctuations of the price of cobalt ($/kg) in the years 2005-2010 [36]*

In the years 2007-2008 there was again a strong increase in the prices of cobalt (Fig. 1.27). The price tripled, and then decreased to the previous level [36]. In the years 2009-2010 the price was more stable, yet it still showed fluctuations. Monthly changes in the price indicate constant uncertainty as to the supply and demand of cobalt [36] (Fig. 1.28).

Conclusions:

Since 1977 both the increase as well as strong fluctuations of the price of cobalt have been observed. However, in contrast with the price of cobalt, there has been observed a constant decrease in the price of synthetic diamonds.

Indeed, the costs of producing metallic-diamond tools are influenced by the costs of metallic matrix. That is why new materials are being sought for the matrix of the metallic-diamond segments in order to decrease the cost of producing metallic-diamond tools. Works are conducted in that direction to replace cobalt with other cheaper alloys of metals, among others, sinters of cobalt with copper are used as matrices [39]. Copper enables to decrease the temperature of sintering or hot pressing, and hence the reduction of costs of the production of tool segments.

The global use of cobalt in 2009 was as follows [37]: lithium batteries – 25%, superalloys – 20%, hard materials – 18%, catalysts – 10%, other applications – 27% (Fig. 1.29). The demand for cobalt will remain high, especially for applications in electric batteries. Lithium batteries, used in hybrid electric vehicles, contain large amounts of cobalt. Signalled by large automotive companies (Hitachi, General Motors, Honda) [37], the increase of production of hybrid vehicles will be an additional factor forcing the price of cobalt in the future.

Considering the above, it should be stated that it is appropriate to seek new materials for the matrix of metallic-diamond tools to free the production of those tools from cobalt.

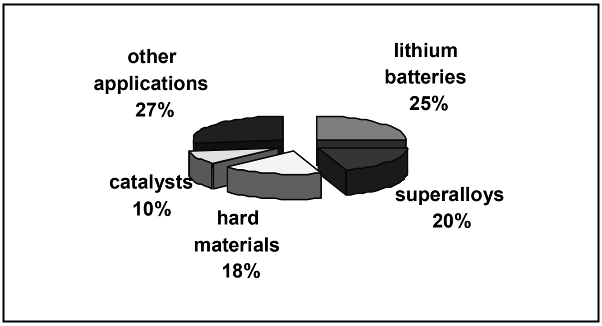


***Fig. 1.29.*** *The global use of cobalt in 2009 [37]*

# 1.5. REVERSE ENGINEERING IN MAINTENANCE AND MANUFACTURING PROCESSES

*Sławomir Błasiak, Jerzy Bochnia*

## 1.5.1. GENERAL INFORMATION ABOUT REVERSE ENGINEERING

Software assisting technology design is commonly used in all industries. Integrated systems supporting design and manufacture which can be described as "virtual technologies" considerably accelerate the introduction of new solutions or improvements in manufacturing processes, and thereby significantly reduce costs of new product implementation. This becomes particularly important for small and medium-sized enterprises involved in the production of individual components or small-scale production performed periodically.

Improved efficiency can be achieved by using 3D scanning technology which allows fast and accurate transfer of physical object's three-dimensional geometry to the computer. The result is a complete digital model that can then be measured, compared with the constructional model, edited and processed by CAD/CAM software for prototyping, visualization or animation [40].

Computer-aided design is a process that starts with an idea which is transformed into a virtual model, and then by means of computer-aided manufacturing system into a material object.

In reverse engineering material is measured and digitized measurement data are converted into a virtual model. In the next stage of the process computer-aided manufacturing system enables constructing the material object which is a reconstruction of the measured model. In other words, "traditional" engineering transforms engineering concept and model into material object model while the reverse engineering transforms material object into model and concept [45].

Digitization or in English *data acquisition* is the first stage of reverse engineering.

The English phrase data acquisition is usually associated with digital processing of analog signals. The process discussed in the paper also comprises this type of transformation since the purpose of digitization in reverse engineering is to convert analog signal (the shape of mapped object) into a digital signal (object's virtual model in computer modeling system). The digitization process can be compared to analog-to-digital-converter, in particular, to two important operations taking place in converter, namely digitizing (or sampling) and quantization [46, 47].

It should be noted that in the process of object mapping by means of reverse engineering methods two transformations take place: analog-to-digital (model digitization) and digital-to-analog element construction. Both of them result in recovery process errors. Reverse engineering is used to solve numerous technical problems [46, 48].

For example, it can be used to prepare technical documentation of an existing element if such documentation is not available. What is more the documentation can then be used to modify the project. Reverse engineering is also used when the product design involves construction of a material model, namely, in the automotive industry after a life-size model of the car is made, it is digitized so that it can be used in computer-aided manufacturing system. Another field of reverse engineering application is biomedical engineering, for example, mapping bone shape on the basis of tomographic images and then designig prosthesis adapted to the patient's anatomical characteristics.

In the measurement of geometrical quantities of machine elements the coordinate measuring technique begins to dominate. It allows determining dimensions of spatially shaped machine parts with relatively high accuracy and in time adjusted to rate of their manufacture. The technique qualitatively different from existing measurement methods, is characterized by the measurement procedures based on coordinate values of localized measurement points which provide the basis for determination of all geometric figures that constitute machine part. For example, hole diameter is determined by setting the value of at least four points of a circle in locations freely but relatively evenly distributed. Mean square approximation of the circle allows to determine its diameter or radius and coordinates of its center thereby reducing measurement time when compared to classical methods. This is shown by the case of measuring probes where it was necessary to position the measuring tip in the axis of the measured hole which made measurement process labor-consuming since it was based on determining the diameter as the distance between the tip and the opposite walls of the hole [43].

Both description and performance characteristics of measurement tools are important as they are used to present and appropriately formulate their suitability to conduct measurements regardless of value range of the quantities examined and expected accuracy. Coordinate measuring technique used in measuring machines consists in determining the coordinates of points (xi, yi, zi) forming the actual outline set relative to the coordinate system (x, y, z) of the measuring machine. [44]. Since coordinate measuring technique has changed the philosophy of measurement relating to classical methods it should be incorporated into the basic education of a modern engineer dealing with machine construction, automation, robotics, and especially metrology [43].

### 1.5.2. 3-D SCANNER WORKING PRINCIPLE

The operation of ATOS II optical scanner is based on triangulation. The projector head makes the projection of a sequence of moire patterns onto the measured object and two cameras record their distribution. By solving optical transformation equations the system calculates the coordinates for each single camera pixel with a set accuracy. The result of each measurement is a cloud of points whose number is dependent upon camera resolution (from 0.8 to 8 mln points). Measuring a given item the system "assemblies" individual point clouds (Fig. 1.30), basing on reference points (Fig. 1.31). The distances between points do not change during measurements.

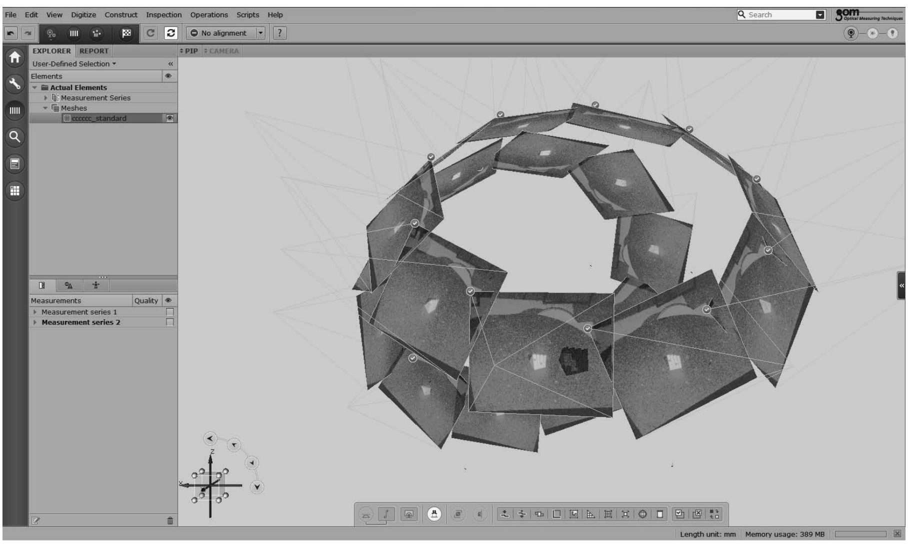


***Fig. 1.30.*** *Sequence of two measurement series*

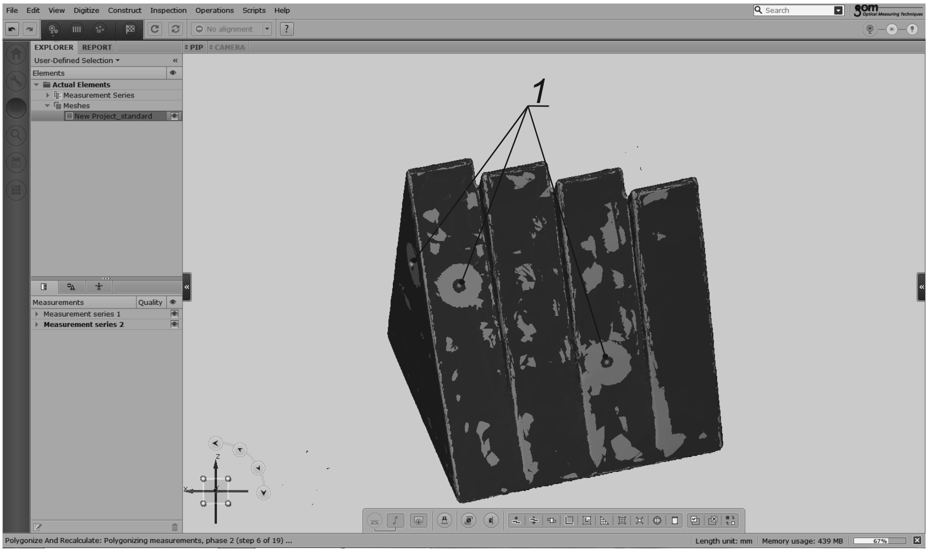


***Fig. 1.31.*** *Image of connected point clouds: 1 – reference points*

The Figure 1.32 shows the obtained solid model together with the image from one of the scanning head cameras.

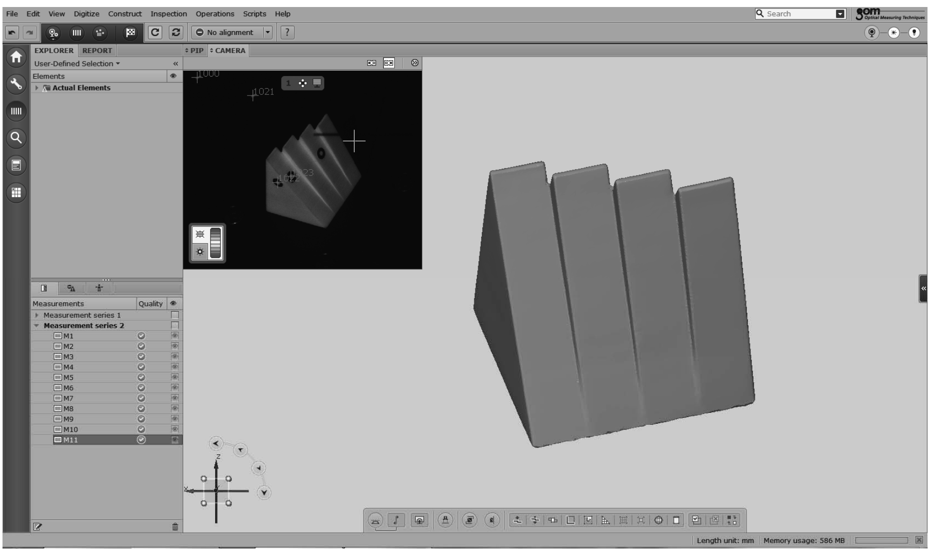


***Fig. 1.32.*** *Solid model after triangulation*

After conducting a series of measurements ("scans") poligonization process takes place. The result is a surface model consisting of a triangle mesh.

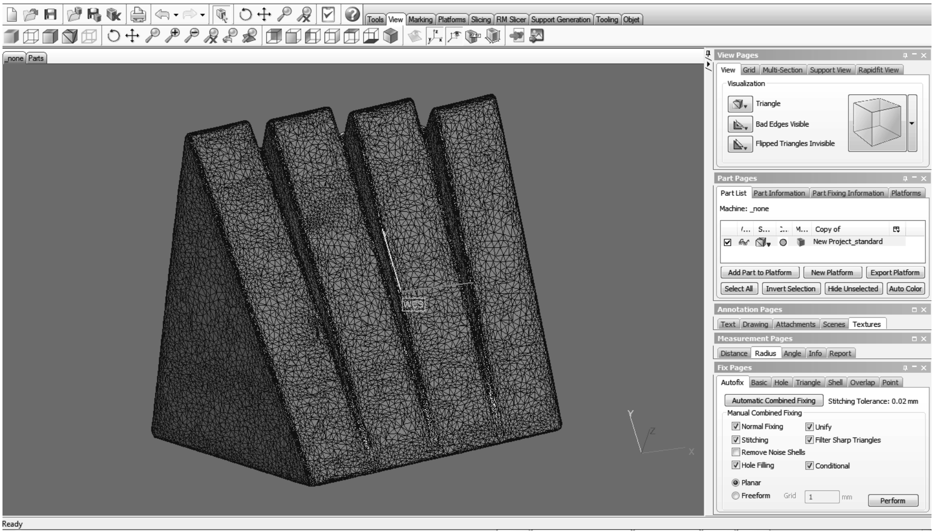


***Fig. 1.33.*** *View of triangle mesh in Magics software*

The geometric model can be either analyzed by comparing it with the CAD model or prepared for 3-D printing.

### 1.5.3. SCANNER STRUCTURE

A 3-D optical scanner (Fig. 1.34) consists of the following parts: measuring head (1), dedicated software (3) allowing scan processing, the control computer (4) of a 64-bit architecture and a tripod (2) adapted to measuring task [41].

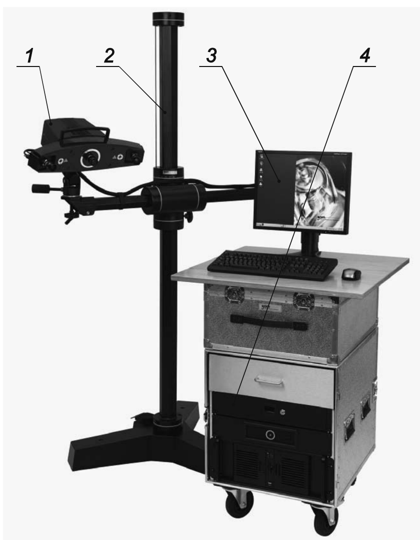


***Fig. 1.34.*** *ATOS II [41] scanning system*

As an additional equipment GOM mbH company provides a set of measuring probes (Fig. 1.35).

***Fig. 1.35.*** *A set of measuring probes [41]*

## 1.5.4. 3-D SCANNER APPLICATIONS

3-D scanning allows, among others, conducting precise measurements obtained from a large number of measurement points located over the entire surface of the product and direct comparison of the measurements with CAD solid model which is a fundamental advantage of optical measurement method.

The measurement results obtained by ATOS scanner are presented as optimized triangle mesh in *. STL format (Fig. 1.36a).

a) b)

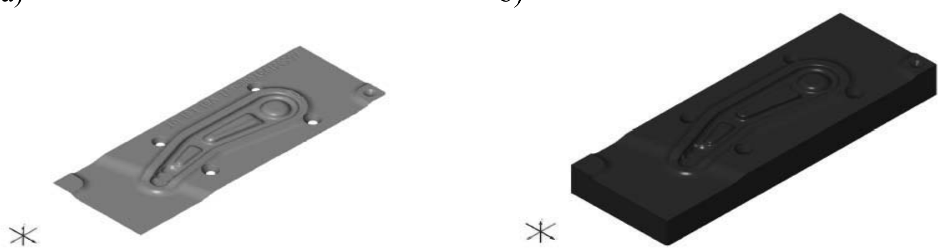

***Fig. 1.36.*** *a) Scan results, b) CAD drawing [41]*

Then to ATOS software CAD data determining the measured detail (eg. the best fit) can be imported (Fig. 1.36b). The comparison of measurement data with CAD ones results in a fully readable and easy for interpretation color deviation map (Fig. 1.37).

While cool colors indicate that there is a loss of material in comparison to CAD model warm ones imply surplus material. Additionaly, the map can be extended by the inspection points attached in optional places and informing about the numerical value of the deviation.

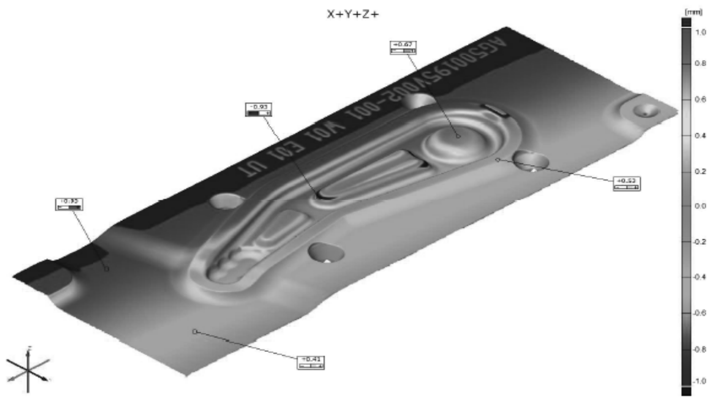


***Fig. 1.37.*** *Results of comparison with solid model [41]*

There is also a possibility of measuring the most important properties of a detail by 2D drawing (angles, distances, hole spacing etc.). The analysis may result in professionally written measurement report which can be exported to popular formats (*. pdf, html, *. doc, etc.) [41].

Other applications of 3D scanner include:

- quality control,
- reverse engineering,
- Rapid Prototyping,
- virtual assembly,
- milling with STL.

The system is not limited by the size of the scanned items and digitization in two measuring ranges (38 x 29 mm) and (2000 x 1500 mm) is possible.

As it has already been mentioned modern methods of product design and manufacturing technology require computer-aided software, namely, CAD (Computer Aided Design) and CAM (Computer Aided Manufacturing). In other words, product design is first created by computer modeling software and then used to determine product's manufacturing technology. The traditional design method based on using drawing boards has already passed into history as the computer systems significantly reduce the time required for production preparation which is crucial when customers demand newer and newer products, and market competition creates mounting pressure on price decline.

An interesting example is the automotive market. While in the sixties of the twentieth century the same car model was produced even for several years, now car companies offer a new model every six years and frequently changes in the design and appearance of the car are made during production process. To be competitive on the market, manufacturers try to decrease costs by reducing the costs of design preparation. At this point the question arises: what if products were designed in the form of the model, for example, by an industrial design artist who has not saved them in electronic form; does it mean that it is impossible to use execute a design by means of computer design and manufacturing systems? Here, a good example is automotive industry where specialist companies prepare a design of car body in the form of the model. The model has to be converted into electronic form, in other words "digitized" because only this form of design allows determining car body production technology. The solution to this problem is reverse engineering which offers tools for the transformation: a model of the product – an electronic (virtual model) – the product. The origins of reverse (reconstructive) engineering can be attributed to the construction of milling machines-copiers that allow a simple representation of the product model. The term reverse engineering is widely known in computer applications where it refers to the analysis of computer system aiming at construction of a similar system as close to the original as possible.

Summing up it can be concluded as follows:

- two methods are dominant in digitization,
- measurement by means of scanners (or vision systems),
- measurement by means of coordinate measuring technique.

The authors of numerous works present various methods of point cloud filtering whose main purpose is to reduce the number of points and thereby reduce the requirements for memory size and improve the computational efficiency of the computer system aiding the design.

In addition, digitized points are subject to measurement error called "noise". The attempts can be made to filter it out. It should be emphasized that with growing efficiency of computer systems their price decreases, so it seems that the problem of filtration, which until recently was one of the most important problems of reverse engineering, is of secondary importance. In filtration process performed so far the number of points was reduced at the expense of losing accuracy of the mapped object. Now filtration is conducted within the scanning measurement error in order to remove measurement "noise" and consequently does not reduce the accuracy of mapping.

In some papers the attempts have been made to fit curved surfaces to point clouds, but in most cases, the point cloud triangulation is made. It consists in constructing a surface consisting of adjacent triangles whose vertices are cloud points. Methods of stretching space on point clouds obtained by scans or coordinate measurements have reached a considerable degree of development but no substantial progress has been noted. Point cloud triangulation algorithms with separate product cross-sections show high degree of complexity and significantly increase the cost of the software.

There is no unambiguous method to assess the accuracy of elements mapped by means of reverse engineering. The reason is the need to compare curved surfaces – reverse engineering is applied to map objects digitized by diagnostic imaging methods (computer tomography, magnetic resonance imaging) but lacks a clear description of methods detecting edges of the depicted objects. For edge detection image analysis methods are used and since they have not been devised for reverse engineering they do not provide accuracy assessment of such mappings.

Conclusions:

The paper presents only a few areas of optical 3D scanners application. One of their biggest advantages is the possibility of carrying out measurements for high density of measurement points collected in a short time (about 1 million points in 1 second). Optical measurement methods using coordinate measurement techniques reduce time of both measurement and subsequent analysis and do not require machine programming. Most importantly the amount of data for the metrological analysis of the measured element is incomparably greater than in traditional methods of measurement. Inspection activities that follow the process provide comprehensive information on element geometry and its deviation from the nominal profile. All these features determine effective and justified application of optical tools using coordinate measurement technique for geometric measurements of manufactured parts. For complex items, such as moldings and stampings, measurement by classical coordinate measuring machine can last up to several days. Thanks to the use of 3D scanners the process can be shortened to hours.

## 1.6. THE TECHNOLOGY OF OVERHAULING A CIRCULATING PUMP IN THE REFRIGERATING CYCLE OF THE CONDENSER OF A HEAT AND POWER GENERATING PLANT

*Andrzej Korczak, Grzegorz Peczkis*

### 1.6.1. THE EFFICIENCY OF THE CLAUSIUS-RANKIENE CYCLE IN A HEAT AND POWER GENERATING PLANT

The circulation in a heating plant with a superheater in the boiler, called Clausius-Rankine's cycle, in the coordinate system i.s. is to be seen in Figure 1.39. This circulation is related to the flux of the medium following through the high-pressure part of the steam turbine and through its low-pressure part NP. The total thermal efficiency of the heat and power generating plant is higher than the C-R cycle, because the heat from the exchanger is passed entirely to the heated medium.

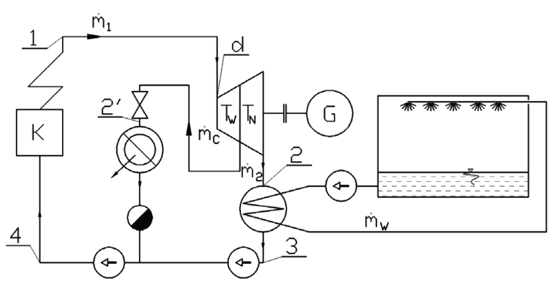


***Fig. 1.38.*** *Simplified diagram of a heat and power generating plant*

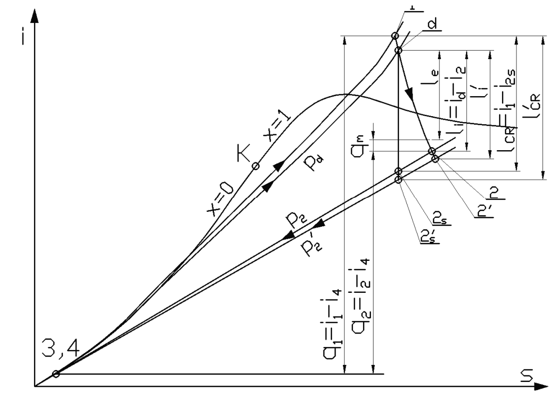

*Fig. 1.39.* *Clausius-Rankine's circulation in a classical steam electric power station in the i.s. system*

In the considered example of a heat and power generating plant the flux of steam from the boiler is passed to the high-pressure part of the bleeder turbine. The steam flux $m_c$ from the bleed of the turbine gives off in the heat exchanger and after its condensation it is passed to the pipeline of the condensate before entering feeding the steam boiler. Therefore the thermal efficiency of the unit is higher than the efficiency of the classical C-R cycle. The remaining flux of the steam $m_2$ releases its energy in the low-pressure part of the turbine and its is condenser taken over by the cooling water, which passes the heat to the cooling tower.

The power of the condensing turbine depends on the enthalpy $i_j$ of the steam fluxes: $m_1$ – which is passed to the turbine and m2which flows through the low-pressure part of the turbine, as well as the enthalpy of the wet steam in the condenser. As the present publication concerns the modernization of the cooling circulations of the condenser, it deals witch the balance and efficiency of the unit witch respect to the flux of steam and condensate $m_2$. The efficiency of the Clausius-Rankine cycle, referred to the steam flux $m_2 = m_1 - m_c$, flowing through the high-pressure and low-pressure part of the turbines, is expressed by the quotient:

$$\eta_{CR} = \frac{i_1 - i_{2s}}{i_1 - i_4} \tag{1.18}$$

The quantities contained in the formula have been shown in the Figure 1.39. In order to determina the thermal efficiency of the power station, also the thermodynamic efficiency of the pipeline must by taken onto consideration:

$$\eta_r = \frac{i_d - i_{ws}}{i_l - i_{2S}} \tag{1.19}$$

As well as the indicated efficiency of the turbine:

$$\eta = \frac{i_d - i_w}{i_d - i_{ws}} \tag{1.20}$$

The thermal efficiency of the cycle is determined by the ratio of the indicated power, achieved in the cycle, to the heat which is passed to the medium circulating in the boiler, as expressed by the formula:

$$\eta_{ob} = \frac{N_{iob}}{Q_d} = \eta_{CR}\eta_r\eta_i \tag{1.21}$$

The diagram in Figure 1.39 indicates that a reduction of pressure in the condenser from $p_2$ to $p_2$' results in an increased drop of enthalpy in the turbine, both the isentropic and the actual enthalpy, as well as in an increases of energy supplied to it. The indicated thermal efficiency grows only imperceptibly, whereas the efficiency of the cycle C-R and the thermal efficiency increases considerably. Wukałowicz's /1/ diagram MP shows that the isentropic change of the enthalpy of wet steam per unit in the change of pressure is much larger than in the case of superheated steam.

Therefore, the so-called "vacuum in the condenser", depending on the amount of heat taken over by the cooling water and then passed to the cooling tower is of much importance. The steady state depends to a large extent on the flux of cooling water, the circulation of which is excited by a circulating pump. A decrease of the parameters of operation, and hence also the efficiency of the circulating pump of the cooling water involve, therefore, a considerable reduction of the indicated efficiency of the turbine in relation to the flux of steam $m_2$.

### Methods of increasing the thermal efficiency of the C-R cycle in a CHP plant (heat and power generating plant)

A thermo-electric unit with a low-pressure condensation turbine includes two couple cycles in which the thermal energy is supplied to the circulating medium in a steam boiler. One of them produces electricity, the other one supplied heat to external consumers. Steam for heating or technological purposes can be obtained either before entering the turbine or – as in the considered case – from the bleed of the turbine. The Clausius-Rankine cycle concerns the flux of steam $m_2$, flowing through the whole turbine and them passed behind the stage of condensation to the condenser. The efficiency of the C-R cycle can by increased, first of all, by expanding the extreme temperatures of the circulation and by its so-called improvement of the thermal efficiency to bring it nearer to the ideal Carnot cycle.

The lowest possible temperature in the condenser is maintained by an efficiently operating cooling system (1.18). We have to do with an improved efficiency of the unit with nominal parameters and with its reconstruction, e.g. after a long time of exploitation, in order to restore the initial nominal parameters. The present paper concerns the reconstruction of the cooling cycle of a condenser. The efficiency of a heat and power generating unit depends, of course, on its technical states and the possibility of attaining the nominal parameters of operation of all its machines and installations. The efficiency of the EC unit can also be improved in relation to the final efficiency by replacing its worn elements by more efficient ones, or by adding new elements, e.g. preheaters of water in the draught of combustion gases, reducing their temperature at the outlet.

### 1.6.2. ASSESSMENT OF THE TECHNICAL STATE OF THE COOLING CYCLE IN THE CONDENSER, BASING ON ITS PIEZOMETRIC DIAGRAM

Every hydraulic cycle, and thus also the considered cooling cycle of the condenser may by diagnosed by constructing and analyzing a piezometric diagram. This diagram is plotted on the diagram of the cycle. Figure 1.40 present the diagram of the cooling cycle of a condenser, and Figure 1.41. It′s piezometric diagram, the parameters of operation having been determined previously to the overhauling of the pump and condenser.

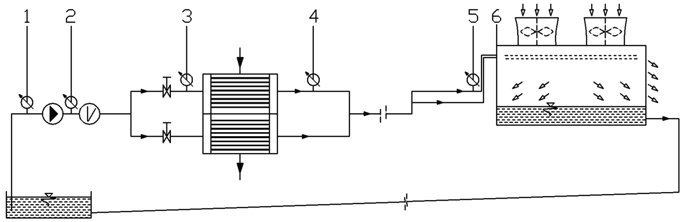


***Fig. 1.40.*** *Cooling cycle of the condenser*

The piezometric diagram shown in Figure 1.41 was plotted basing on measurements of the pressure in the pipeline and the geometrical heads in the cross sections marked in Figure 1.40. Moreover, the flux of water in this pipeline was measured by means of an ultrasonic flow-meter, and thus also the efficiency of the circulating pump (1.21).

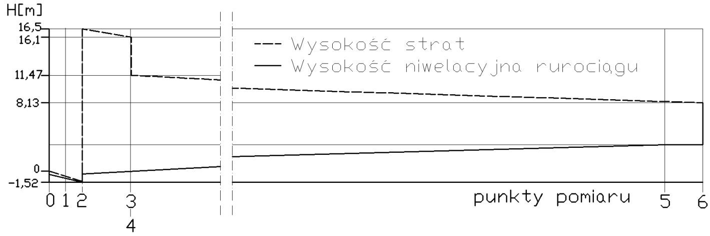


***Fig. 1.41.*** *Piezometric diagram of the circulating of cooling water in the condenser*

Considering a heat and power generating plant, after about fifty years of exploatation of the pump of cooling water in condenser, the result of the corrosion and flow erosion is degradation of its flow duct. The ducts walls roughness and wideness of the slot sealing is extended. The average wideness of slots increases from 0.3 mm to about 3 mm. The consequence of that is significant increase of volumetric losses and decrease of the pump's efficiency, what is shown in the diagram.

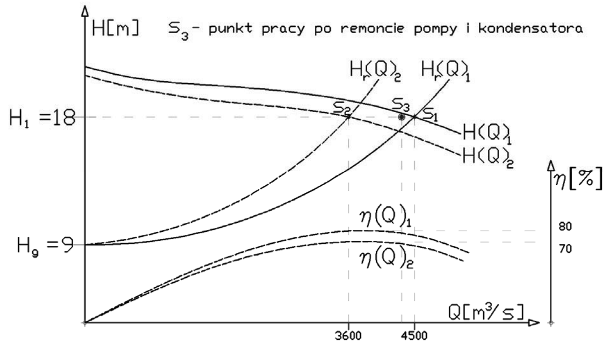


***Fig. 1.42.*** *Flow characteristic of the pump and pipeline of the circulating of cooling water in the condenser. $H(Q_1)$, $H(Q_2)$ – characteristics of the new pump before and after overhauling. $H(Q_1)$, $H(Q_2)$ – characteristic of the new pipelines previous to the repair of the condenser*

### 1.6.3. DESCRIPTION OF THE STRUCTURE AND TECHNICAL STATE OF THE CIRCULATING PUMP OF WATER COOLING THE CONDENSER

The structure of the circulating pump of the water cooling the condenser results from tts parameters. The casing of the pump is divided in the horizontal plane, and the inlet and outlet ferrule are connected with the bottom of the casing. The double suction impellers cooperate with centrifugal stators.

The nominal operating parameters of the pump, quoted in catalogues, are: Efficiency $Q$ = 4500 m$^3$/hour = 1.25 m$^3$/sec.; High of lift $H$ = 18 m. A single-suction pump with the same parameters would be a high-speed mixed flow or propeller pump. In order to determine the specific speed, like in the case of high-speed centrifugal pumps, a system of three parallelly operating double-suction impellers were applied, as shown in Figure 1.43.

***Fig. 1.43.*** *View of circulating pump of water cooling the condenser, without the upper part (cover) of the casing*

The specific speed of the pump, related to the single-suction impeller, i.e. 1/6 of the efficiency of the pump, amounts to:

$$n_q = n\frac{(0.166Q)^{1/2}}{H^{3/4}} = 50.8 \tag{1.22}$$

This is the specific speed of a high-speed centrifugal pump. Pumps with such a specific speed attain the highest efficiency (1.20). After sixty years of exploitation the circulating pump of water cooling the condenser displayed lower parameters of operation and reduced characteristics $H(Q)2$ than those quoted in Figure 1.42. The main reason for the reduction of the parameters was the increased counter-flow in the pump due to the widening of the ports (slits, interstices?) sealing the necks of the impellers. The flux of the counter-flow passing the slot which seals the neck of the impeller can be calculated basing on the determined height of the pressure drop in the slot and on its dimensions. The height of the pressure drop in the slot of the impeller is determined basing on the degree of reaction of the impeller and the additional drop of pressure caused by the spinning (swirling) of the liquid between the impeller and the casing. In the considered case the height of the pressure drop in the slot of impeller neck has been assumed to be $H_{SZ}$ = 12 m. Before the overhaul of the pump the dimensions of the slots sealing the necks of the impellers were as follows mean diameter of the slots $d_{SZ}$ = 404 mm, mean width of the slots $b_{SZ}$ = 3 mm, length of the slots $l_{SZ}$ = 12 m. The transformation of Darcy Weisbach's formula permits to calculate the mean velocity of flow of the liquid in the slot /3/:

$$v = \sqrt{\frac{2g\Delta H_{SZ}}{\lambda l/2b_{SZ} + \zeta_{wyl}}} \tag{1.23}$$

Substituting numerical values in this formula, we get $v$ = 12.2 m/sec. Thus, the average flux flowing through one slot can be calculated, viz.:

$$q_1 = \Pi d_{SZ} b_{SZ} v = 0.046 \text{ m}^3/\text{s} \tag{1.24}$$

The total volumetric loss is however, six times larger, amounting to $q_l$ = 0.278 $m^3/s$, which is about 22% of the nominal efficiency of the pump. Moreover, due to the fact that the hydraulic losses in the cooling cycle of the condenser increased considerably in result of clogging in the leaking pipes of the exchanger, the characteristics of the circulation of Hr(Q)2 are steeper, in result of which the efficiency of the circulation of the cooling water was reduced to 3679 $m^3/h$ and the temperature in the condenser rose to 55°C, corresponding to its boiling pressure.

## 1.6.4. THE TECHNIQUE OF REPAIRING A CIRCULATING PUMP OF WATER COOLING THE CONDENSER

The fundamental reason for the drop of the parameters of a pump of cooling water was the increased roughness of the walls in the ducts, and still more the widening of the slots tightening the necks of the impellers. The possibility of smoothing then was not taken into consideration of volumetric losses of the counter-flow through the slots sealing the necks of the impellers high improve considerably the characteristics of the pumps and approximate this process to the characteristics of a new pump. As the pump is rather heavy and installed beyond the reach of the overhead travelling crane, only the gyrating part was overhauled in the factory whereas the casing was repaired on the spot.

### The repair of the pump casing

The first thing that had to be done in order to feature the state of the casing was to measure the diameter of its cylindrical walls, forming together with the necks of the impellers the sealing slots. The width of the slots between the surface of the auxiliary disc with a diameter of 400.02 mm and the cylindrical surfaces of the walls of the casing was measured by means of a slot gauge. The disc was mounted on a steel bar situated on the pitch surface of the casing and aligned along the axis of the casing.

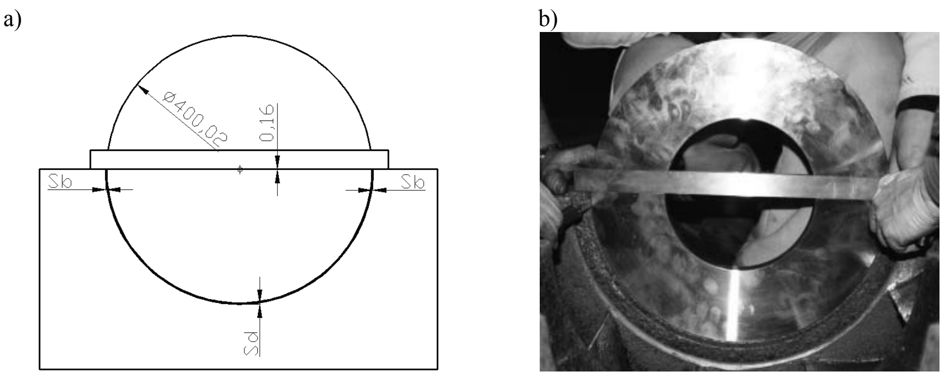


*Fig. 1.44. a) Dimensions of the auxiliary disc supported by the bottom half of the pump casing, b) measurement of the geometry of the cylindrical surface of the casing cooperating with the neck of the impeller by means of a slot gauge*

Measurements of the dimensions of the cylindrical diameters of the wall of the casing, forming jointly with the impeller necks sealing slot, indicated their scatter exceeding 3 mm and their ovality therefore these surfaces were verified as individual dimensions, restricting their treatment to an indispensable minimum. Due to such a assumption, this operation had to be completed previous to the final treatment of the impellers of the pump which had to be repaired when both halves of the pump casing have been assembled, the surfaces of the sealing slot of each of both parts was stepwise redressed until the entire widhthand circumference of the surface has been corrected. The redressing was accomplished by means of the shaft of the pump with its mounted head equipped with two lathe tools. The structure of the head is to be seen in Figures 1.45 and 1.46 present view on the work-stand.

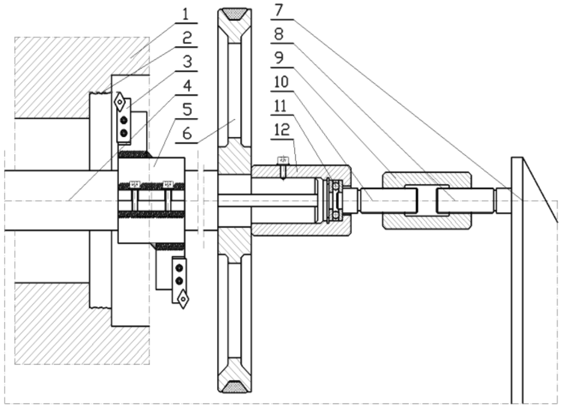


***Fig. 1.45.*** *Diagram of the device used to redress the casing of the pump: 1 – Casing, 2 – Treated worked surface, 3 – Lathe with replaceable pads, 4 – Shaft of the pump, 5 – Lathe head, adjusted for this repair, 6 – Driving belt pulley, 7 – Cantilever fastened to the foundation, 8, 9, 10 – Bolt, 11 – Longitudinal base, 12 – Mounting of the head, realizing the longitudinal shift of the shaft*

***Fig. 1.46.*** *View of the device redreeing the casing of the pump at the work – stand*

The shaft of this device was driven by a motor with a power rating of 75 kW making use of an inverter and belt transmission. This permitted to apply a rotational speed of 30 RPM and more. The feed of the cutting tool was achieved by repelling the shaft by means of a Roam screw. The material of the casing was scooped to a depth of about 2.5 mm. The dimensions of the respective slots differ from each other. After the treatments the diameters were measured by means of a rod gauge.

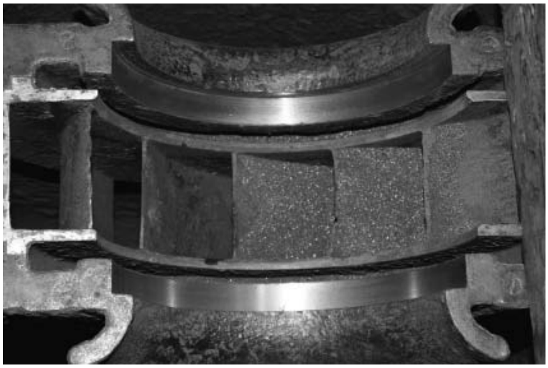

***Fig. 1.47.*** *View of the redressed cylindrical surfaces of the bottom half of the pump casing*

## Repairs of the impellers of the pump

In the factory of pumps the decrements and damages of the flow ducts in the impellers were padded and worked manually. The rings assigned for the verification of the impeller necks were cast of bronze BA1044 and after their treatment and the treatment of the impeller necks they were assembled by forcing them in. Next the external surfaces of the respective dimensions of the diameters, so that the slots sealing the impeller necks in the pump would be identical with a width of 0.4 mm. The impellers were then statically balanced and mounted on the shaft. Figure 1.48 shows a worked and statically balanced impeller, and Figure 1.49 presents the assembled gyrating set of a pump before its delivery to the heat and power generating plan.

***Fig. 1.48.*** *A statically balanced, regenerated impeller of a pump*

***Fig. 1.49.*** *Gyrating assembly after its regeneration*

Conclusions:

In the course of overhauling the pump of water cooling the condenser, the width of its slot sealing the necks of the impellers was reduced. Instead of irregularly shaped slots with various widths of the about 3 mm, slot were obtained with an averaged width of 0.4 mm and uniformly treated surfaces. The flux of the counter-flow through one slot sealing the neck of the impeller, calculated by means of the formulae 6 and 7 amounts after the repair to $q_2 = 0.0044$ m$^3$/s which is 2.1% of the efficiency of the pump. This means that the volumetric loss in the pump has been reduced tenfold. The efficiency of the pump increased of the pump increased by about 15%. After the overhaul the characteristic $H(Q)$ of the pump approximated the $H_1(Q)$ characteristic of the new pump presented in Figure 1.42. Thanks to the repair of the pump and condenser the flux of cooling water increased to 4326 m$^3$/h, caused by the reduction of temperature in the condenser. The most important effect of overhauling the cooling system of the condenser is the increased power rating of the turbine and the reduction of the unit costs of the production of electricity, so that the costs of the overhaul deal with in this paper were reimbursed in the course of less than one year.

## 1.7. PHOTOVOLTAIC CELL-DC MOTOR COOPERATION: OPERATIONAL ISSUES

*Wacław Orlewski*

### 1.7.1. HANDLING AND STORAGE OF SOLAR ENERGY

The photovoltaic cells have recently become the commonly used energy sources for typical application. In the cell, the solar energy is straightforwardly transformed to the DC electric current that enables both industrial and household devices be directly powered, in case DC current is needed, or, with the help of energoelectronic intermediate circuits, when AC current is required. To prolong the solar energy usage time as well as to stabilize the electric energy parameters, either the batteries, but also mechanical means to store energy can be utilized, e.g. water pools with the pump storage system [53]. The machine presented in the paper, in particular the motor, can serve both as a pump drive, powered by DC current from photovoltaic cell and used to transport water to the pool, and as a AC power generator, after the simple switching of the winding.

### 1.7.2. SUPPLY CIRCUIT CHARACTERISTICS

The presented machine, together with the battery of photovoltaic cells, can serve as a DC power drive to transfer the solar energy to the gravitational potential energy of water stored, e.g. in pump storage generating station pool. This energy can then be transferred to the electric current energy by means of AC generator built from the same machine, after the small winding modification.

The load of a machine working as a DC drive should be adjusted so, Figure 1.50a, that the power conveyed to the motor is maximal under the given sun irradiance. Thus, the current and voltage should coincide with the parameters defining the gray region on Figure 1.50a; here $I_K$ is the short circuit current and $U_{OC}$ is the open circuit voltage. The I-V characteristics of the typical photovoltaic solar cell (amorphous silicon cell) is shown on Figure 1.50b for different sun irradiances.

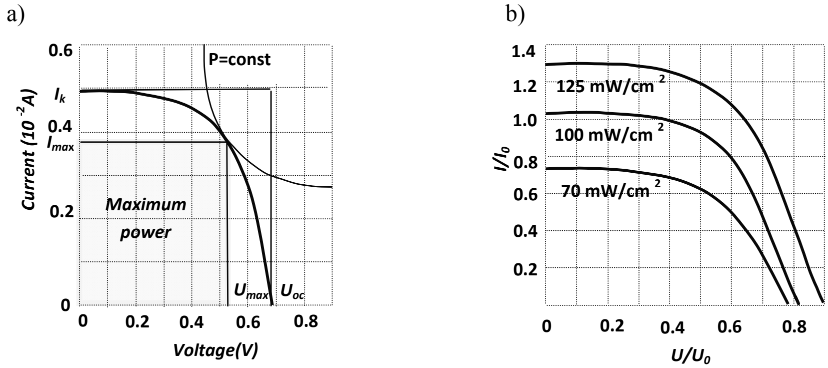


***Fig. 1.50.*** *Photo voltaic cell characteristics: a) current-voltage characteristics with the maximum power conditions shown as a gray region.* $U_{max}$ *and* $I_{max}$ *refer to the optimal power conditions, b) the characteristics under different solar irradiance (after [54])*

The cell has its energy maximum that rises with the sun light intensity (Fig. 1.51), but lowers with increasing temperature (Fig. 1.52). Since temperature usually rises with increasing sun irradiance, energy supplied by photovoltaic cell may be considered roughly time independent. The motor presented below should thus be compatible with such an requirement: the work to be done, transporting water to the pumped storage generating station pool, should also be performed with the constant power. This can be achieved by the change of turbine blades angle that affects motor angular velocity and intake current, and, consequently, the torque.

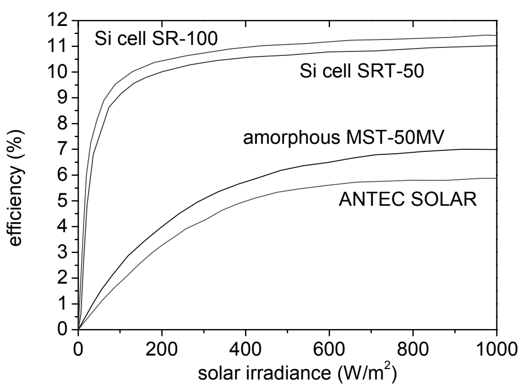


***Fig. 1.51.*** *Selected solar cell efficiencies as a function of solar irradiance at 25 ℃ (after [55], page 102)*

Once the solar daily energy is stored in the water tank, the proposed motor can be adjusted to serve as the power AC generator. The way the winding of such a double-function machine is constructed and changed when the power drive is converted to a generator, will be presented belove.

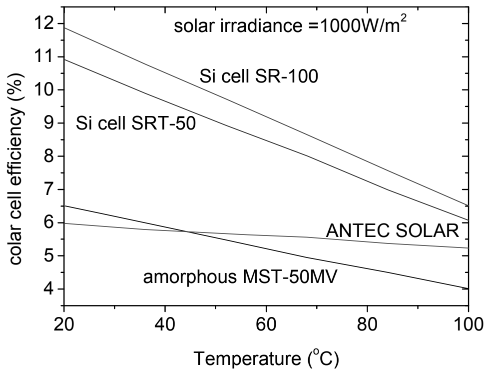


*Fig. 1.52. Selected solar cell efficiencies as a function of temperature under a solar irradiance of 1000 W/m$^2$. Note that for monocrystalline Si cells (SR-100 and SRT-50) the efficiency drop is as large as 50% from t = 20°C to 100°C, (after [55], page 103)*

## 1.7.3. SERIES CONVERTER TYPE MOTOR CONSTRUCTION

As stated above, the aim of the present paper is to propose the efficient way to store solar energy and, when needed, to convert this energy to AC current. This is realized by the synchronous machine with thyristor current converter (Converted Type Motor, CTM).

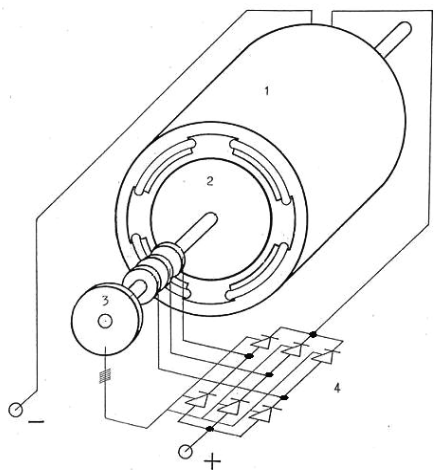


*Fig. 1.53. Series brushless DC motor schematics (after [56]), where: 1 – stator, 2 – rotor, 3 – sensoreless adjustable – electronic commutator, 4 – thyristor current converter*

The construction of such a motor capable of transforming to AC generator is shown on Figure 1.53 [55]; this is based on a special inverted synchronous machine with 3-phase rotor. The salient-poled stator with the cage and with 4 poles is powered by a thyristor current converter co-operating with sensoreless electronic commutator. The commutation process is internal and the machine uses its stator winding as a choke in DC current inverter from which it is powered. This type of a machine can be started from DC power supply.

### 1.7.4. MOTOR BLOCK DIAGRAM

In case the role of a rotor and a stator in a converter type synchronous machine is reversed, it is possible to change the stator winding configuration from series to separately excited one. This enables the change of the machine operation mode from energoelectronic series DC motor to a synchronous generator that can co-operate with the power grid. The excitation circuit of a synchronous machine is then powered from the grid with the thyristor rectifier. Such a machine can thus be used both as a motor (powered by the photovoltaic cell) used to fill the pumped storage generating station reservoir and, later after the rewinding, as an AC current generator driven by the stored water.

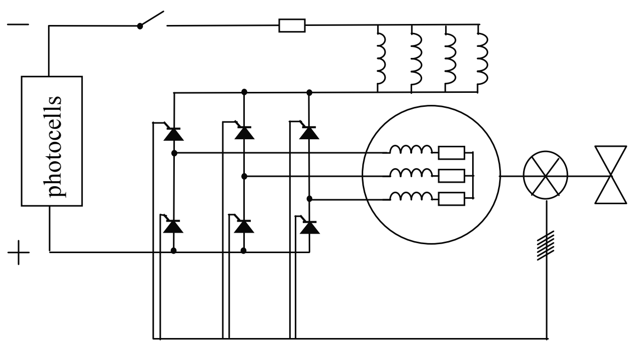


***Fig. 1.54.*** *DC motor diagram (before rewinding)*

The diagram of the machine working as a DC motor is presented on Figure 1.54. Due to the required low resistance of an excitation winding in the machine working as a DC drive, the individual pole windings should be connected in parallel. On the contrary, in a separately excited synchronous generator the excitation winding resistance is higher. Thus, in order to change the machine mode from motor to generator, the circuit rewinding to series connection is required resulting in 16 times larger winding resistance coinciding with large difference in excitation currents of both machines. For this reason, the additional winding switching of the proposed machine stator is needed, as shown on Figure 1.55 and, in the whole setup, on Figure 1.56.

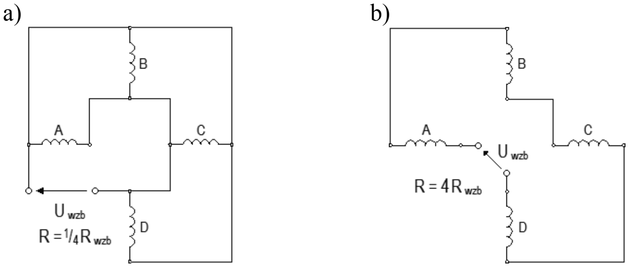


***Fig. 1.55.*** *a) The scheme of induction winding poles connection in a series DC motor, b) the scheme of induction winding poles connection in a synchronous generator*

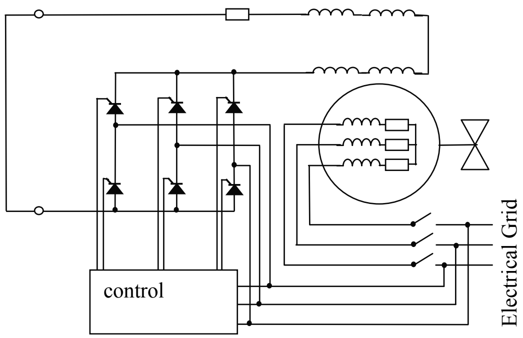


***Fig. 1.56.*** *Generator diagram (after rewinding of the synchronous machine)*

## 1.7.5. OPERATIONAL PARAMETERS

In the current converter intermediate circuit the additional excitation winding of a synchronous machine was implemented that acts as an circuit choke (Fig. 1.54). By this means, the series power structure of this machine was realized. The experiments of the startup and stable operational states of such a machine were performed on the bench model and proved the correct operation of such a reconfigured converter type machine as well as efficiency of its series type connection [56]. In the bench model experiments the mechanical characteristics of the drive powered from the separately excited DC high power generator were measured. The experimental results, as a load torque and angular velocity vs. intermediate circuit current are shown on Figures 1.57 and 1.58 together with the linear simulation of a series DC motor operation.

The motor presented above can also be controlled by the proper commutator angle θ setting. The motor characteristics at different supply voltages and for some stable commutator angle $\theta_1$ are shown on Figure 1.59, while Figures. 1.60 and 1.61 present the relevant characteristics for two different commutator angles for supply voltage $U_d/U_{dN} = 1$ (Fig. 1.61) and $U_d/U_{dN} = 0.75$ (Fig. 1.61). Apart from the relatively easy control system, the additional advantage of the presented motor is that the commutation angle is very stable, independent on load current (Fig. 1.62).

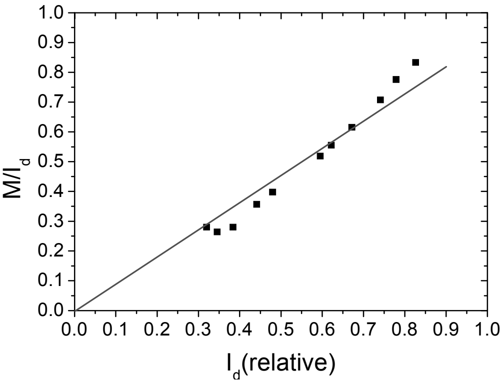


***Fig. 1.57.*** *Experimental characteristics for the bench model of the series converter type motor with the relevant computer simulation. Here the torque, as M/$I_1$, vs. $I_1$ current (in relative units) is presented [57]*

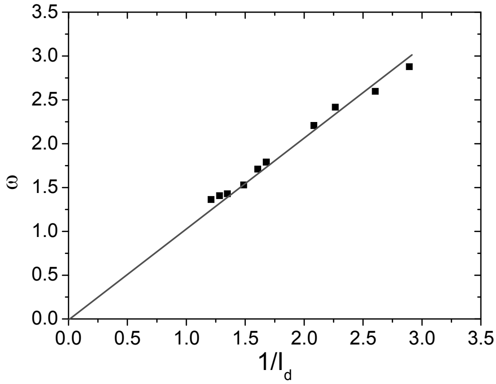


***Fig. 1.58.*** *Experimental results of the bench model tests; same as in Figure 1.54, but here the angular velocity ω as a function of inverse current $I_1$ (in relative units) is shown [57]*

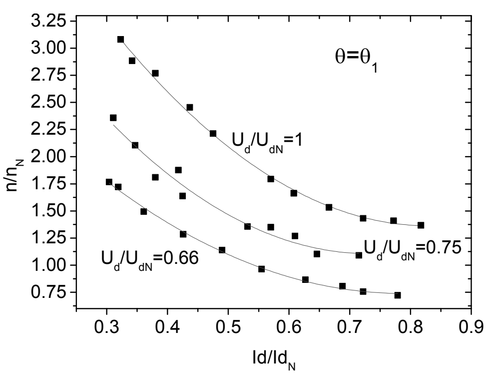


***Fig. 1.59.*** *Motor characteristics at different supply voltages (for the stable commutator angle $\theta_1$)*

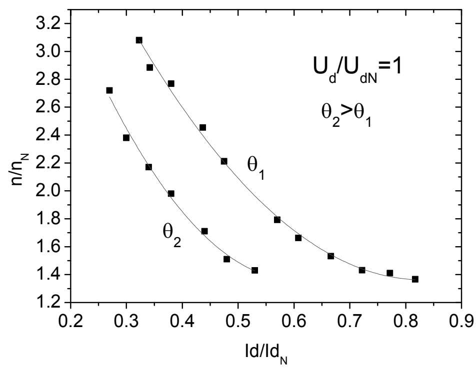


***Fig. 1.60.*** *Motor characteristics at different commutator angles $\theta$ (for the stable supply voltage $U_d/U_{dN} = 1$)*

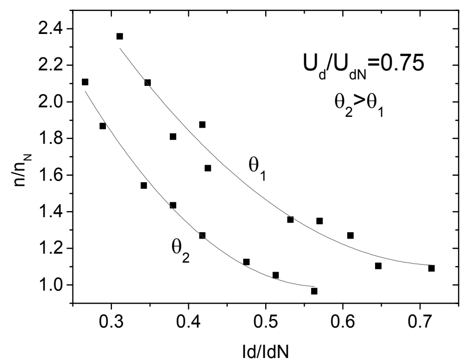


***Fig. 1.61.*** *Motor characteristics at different commutator angles $\theta$ (for the stable supply voltage $U_d/U_{dN} = 0.75$)*

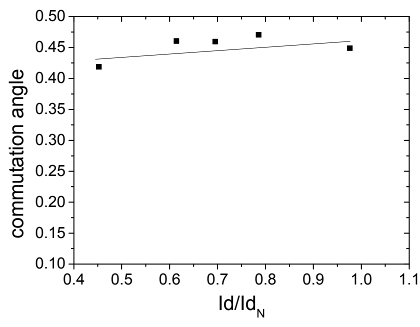


***Fig. 1.62.*** *The results of the thirystor test angle commutation as a function of current $I_d$ (in relative units) is shown*

The additional experiments to test co-operation of the machine with photovoltaic cell (and not a DC generator, as in the present experiment) as well as with a load element (simulating the water pump) are needed. In case the cell works at elevated temperature and sun irradiance, the change of current-voltage characteristics of the cell should be taken into account.

The series converter type motor presented above possesses the capability of self-excitation and self-adjustment when powered from DC power source. To optimize the whole system (solar cell, motor and water pump) performance, the optimization of load to maintain constant power requirement is needed, as stated above. This can be realized by the turbine blade angle adjustment maintaining the constant water intake for particular vertical distance; in this situation, the maximal efficiency condition will be realized [58].

Conclusions:

The system presented above enables the conversion of solar energy to the potential energy of water. This is realized by the co-operation of solar cell battery with DC power drive that pumps water to the pumped storage generating station water pool. The reverse conversion of water potential energy to AC current is realized by the water-turbine-powered synchronous generator; this generator can cooperate with the transformer and electrical grid.

The specially constructed machine can both be used to pump the water and to generate AC current: the machine windings can be easily switched between motor and generator modes, co-operating with a single water turbine, which is the essential extension of motor functions, in comparison to those presented in refs. [53, 56, 57]. The machine is a series converter type motor, that can be self-triggered and powered by a single DC power source. The energoelectric brushless thyristor commutator enables the machine commutation using relatively high currents. The processes undergoing in the machine allow for high DC power conversion and collaboration with electrical grid. No additional DC to AC current converters, other than electromechanical and commutation processes in the machine, are required.

In conclusion, the alternative solution to the energy transfer from renewable energy source (sun), via DC current to, ultimately, AC current is presented.

## REFERENCES


[1] Michalski R.: *Mechatroniczny system monitorowania stanu ciągnika kołowego*. Biuletyn WAT, Vol. LX, nr 1, 2011.

[2] Michalski R. (red): *Diagnostyka maszyn roboczych*.Wydawnictwo ITE, Radom 2004.

[3] Instrukcje obsługi ciągnika John Deere i dokumentacja kodów usterek.

[4] Merkisz J., Mazurek S.: *Pokładowe systemy diagnostyczne pojazdów samochodowych.* WKiŁ, Warszawa 2000, s. 127-138.

[5] Bączewski J., Krysztofiak A.: *Metoda optymalizacji typoszeregu ciągników rolniczych w aspekcie obniżenia energo- i materiałochłonności prac ciągnikowych*. Prace Przemysłowego Instytutu Maszyn Rolniczych, Poznań 1999, nr 4, s. 54-57.

[6] Chancellor W.J., Thai N.C.: *Automatic Control of Tractor Transmission Ratio and Engine Speed*. Transactions of the ASAE, No 3 (27), 1984, pp. 642-646.

[7] De Souza E.G., Santa Catarina A.: *Optimum Warking Curve for Diesel Engines*. Transactions of the ASAE, No 42, 1999, pp. 559-563.

[8] Hansson P.A., Noren O., Bohm M.: *Effects of Specific Operational Weighting Factors on Standardized Measurements of Tractor Engine Emissions*. Journal Agricultural Engineering Research, No 741, 1999, pp. 347-353.
[9] Kim J.H., Kim K.U., Wu Y.G.: *Analysis of transmission load of agricultural Tractors*. Journal of Terramechanics, No 37, 2000, pp. 113-125.
[10] Kościelny J.M.: *Diagnostyka zautomatyzowanych procesów przemysłowych.* Akademicka Oficyna Wydawnicza EXIT, Warszawa 2001, s. 18.
[11] Merkisz J., Mazurek S.: *Pokładowe systemy diagnostyczne pojazdów samochodowych*. WKiŁ, Warszawa 2000, s. 127-138.
[12] Michalski R.: *Diagnostyka maszyn roboczych*. Wydawnictwo ITE, Radom – Olsztyn 2004.
[13] Michalski R.: *Mechatroniczny system monitorowania stanu ciągnika kołowego*. Biuletyn WAT, Vol. LX, nr 1, 2011.
[14] Michalski R.: *Pokładowy system nadzoru on-line stanu technicznego kombajnu zbożowego wspomagany metodami sztucznej inteligencji*. Projekt KBN nr 7TO7B00711, (sprawozdanie).
[15] Michalski R., Gonera J.: *Monitorowanie pracy ciągnika kołowego.* Kielce 2011 (in print).
[16] Michalski R., Janulin M.: *Analiza diagnostyki użytkowej ciągników kołowych*. Kielce 2011 (in print).
[17] Liew A.G., Idris A., Samad A.A., Wong C.H.K., Jaafar M.S., Baki A.M.: *Reusability of sewage in clay bricks*. J. Mater Cycles Waste Manag, 6 (2004), pp. 41-47.
[18] Wiebusch B., Seyfried C.F.: *Utilization of sewage sludge ashes in the brick and tile industry*. Wat. Sci. Tech. 36, 11 (1997), pp. 251-258.
[19] Lin D.-F., Weng C.-H.: *Use of sewage sludge ash as brick material*. Journal of Environmental Engineering, Vol. 127, 10 (2001), pp. 0922-0927.
[20] Latosińska J., Żygadło M.: *Modyfikacja cech kruszywa keramzytowego odpadowym dodatkiem surowcowym*. Ceramika, 91/2 (2005), pp. 1283-1290.
[21] Latosińska J., Żygadło M.: *The application of sewage sludge as an expanding agent in the production of lightweight expanded clay aggregate mass.* Environmental Technology, 32:13, pp. 1471-1478.
[22] Lin C.-F., Wu C.-H., Ho H.-M.: *Recovery of municipal waste incineration bottom ash and water treatment sludge to water permeable pavement materials*. Waste Management, 26 (2006), pp. 970-978.
[23] Stegemann J.A., Buenfeld N.R.: *Prediction of unconfined compressive strength of cement paste containing industrial wastes*. Waste Management, 23 (2003), pp. 321-332.
[24] Tay J-H., Show K-Y.: *Resource recovery of sludge as a building and construction material – a future trend in sludge management*. Wat. Sci. Tech. 36, 11 (1997), pp. 259-266.
[25] Gawdzik J., Latosińska J., Orman Ł.J., Radek N.: *Wpływ składu surowcowego materiałów konstrukcyjnych na ich właściwości eksploatacyjne*. Materiały Konferencyjne „Terotechniologia 2009", Zeszyty Naukowe PŚk: Nauki techniczne – budowa
i eksploatacja maszyn, Kielce 2009, s. 142-146.
[26] Konstanty J.: *Powder Metallurgy Diamond Tools*. Elsevier, Oxford 2005.

[27] Konstanty J.: *Producton and Applications of PM Diamond Tools*. International Powder Metallurgy Directory, 12/2006.

[28] US Department of Interior, US Geological Survey. URL: http://minerals.usgs.gov/minerals/pubs/commodity/diamond.

[29] Lachowski J., Borowiecka-Jamrozek J.: *Modelowanie komputerowe retencji i pracy cząstki diamentu w osnowie kobaltu*. Sympozjum Terotechnologie, Kielce, wrzesień 2005, s. 29-37.

[30] Borowiecka-Jamrozek J., Lachowski J.: *Własności mechaniczne, termiczne i atomowe kobaltu – osnowy narzędzi metaliczno-diamentowych*. Sympozjum Terotechnologie, Kielce, wrzesień 2005, s. 39-46.

[31] Romański A., Lachowski J., Konstanty J.: *Diamond retention capacity – evaluation of stress field generated in a matrix by a diamond crystal*. Industrial Diamond Review, Vol. 66, No. 3, 2006, pp. 43-45.

[32] Romański A., Lachowski J.: *Modelowanie stanu naprężeń i odkształceń w spiekanych materiałach narzędziowych metaliczno-diamentowych*. „Rudy i metale nieżelazne", R52, nr 7, 2007, s. 402-409.

[33] Lachowski J., Romański A.: *Modelowanie retencji i pracy cząstki diamentu w osnowie metalicznej*. I Kongres Mechaniki Polskiej, Warszawa 28-31.08.2007.

[34] Romański A., Lachowski J., Frydrych H.: *Is energy of plastic deformation a good estimator of the retentive properties of metal matrix in diamond impregnated tools?* 2nd International Industrial Diamond Conference, 19-20th April 2007, Rome, Italy.

[35] US Department of Interior, US Geological Survey; URL: http://minerals.usgs.gov /minerals/ pubs/commodity/cobalt.

[36] World Mineral Production 2005-09, British Geological Survey, Keyworth, Nottingham, 2011; URL: http://www.bgs.ac.uk/mineralsuk

[37] Cobalt Development Institute; URL: http://www.thecdi.com

[38] www.en.wikipedia.org, access 10mar2011

[39] Romanski A., Lachowski J.: *Effect of friction coefficient and mechanical properties of the matrix on its diamond retention capabilities*. 5th International Powder Metallurgy Conference, October 8-12 2008, Ankara, Turkey, pp. 298-307.

[40] http://www.skaner3d.com.pl. (10.2011)

[41] http://www.ita-polska.com.pl/optyczneskanery3d i materiały powierzone przez firmę ITA Polska.

[42] Augustyniak M., Barczewski M., Andrzejewski J.: *Wykorzystanie optycznych narzędzi współrzędnościowej techniki pomiarowej w badaniach deformacji występujących w przetwórstwie tworzyw polimerowych.* "Postępy nauki i techniki", Nr 6, 2011.

[43] Ratajczyk E.: *Współrzędnościowa technika pomiarowa*. Oficyna Wydawnicza Politechniki Warszawskiej, Warszawa 1994, s. 7.

[44] Adamczak S.: *Pomiary geometryczne powierzchni*. Wydawnictwo Naukowo-Techniczne, Warszawa 2008, s. 219, 269.

[45] Varady T., Martin R.R., Cox J.: *Reverse engineering of geometric models -an introduction*. Computer-Aided Design, Vol. 29, No. 4, 1997, pp. 255-68.

[46] Smith S.W.: *Cyfrowe przetwarzanie sygnałów*. Wydawnictwo BTC, Warszawa 2007.

[47] Zieliński T.P.: *Cyfrowe przetwarzanie sygnałów. Od teorii do zastosowań*. WKiŁ, Warszawa 2007.

[48] Motavalli S.: *Review of reverse engineering approaches*. Computers ind. Engng., Vol. 35, No. 1-2, 1998, pp. 25-28.

[49] Ochęduszko S., Szargut J., Górniak H., Guzik A., Wilk S.: *Zbiór zadań z termodynamiki technicznej*. PWN, Warszawa 1975, s. 603.

[50] Jędral W.: *Pompy wirowe*. PWN, Warszawa 2001, s. 404.

[51] Marcinkowski W., Kundera Cz: *Teoria konstrukcji uszczelnień bezstykowych*. Podręcznik akademicki, Wydawnictwo Politechniki Świętokrzyskiej, Kielce 2008, s. 443.

[52] Mieszkowski M. (red): *Pomiary cieplne i energetyczne*. WNT, Warszawa 1981, s. 653.

[53] Orlewski W., Siwek A.: *Elektrownia wodna na przepływie wody użytkowej*. Rynek Energii, 6 (2010), s. 87-91.

[54] Lewandowski W.M.: *Proekologiczne źródła energii odnawialnej*. WNT, Warszawa 2002.

[55] Jastrzębska G.: *Odnawialne źródła energii i pojazdy proekologiczne*. WNT, Warszawa 2007, s. 102-103.

[56] Orlewski W.: *Analysis of Thyristor Commutation of Series Converter-Type Motor*. 7$^{th}$ European Conference on Power Electronics and Applications, Trondheim, Norway 1997, pp. 3663-3667.

[57] Orlewski W.: *Analiza statycznych charakterystyk szeregowego silnika przekształtnikowego*. Zeszyty Naukowe AGH, Elektrotechnika i Elektronika, T. 18, Z. nr 3/4 (1999), s. 146-149.

[58] Zarzycki M., Rduch J.: *Pompy wirowe śmigłowe w ruchu turbinowym dla małych elektrowni wodnych.* VIII Ogólnopolskie Forum Odnawialnych Źródeł Energii – 2002. Międzybrodzie Żywieckie, 15-17 maj 2002, pp. 314-323.

# 2 SURFACE ENGINEERING

## 2.1. INTERACTION OF N-(2-CHLOROBENZYLIDENE)-4-ACETYLANILINE WITH SURFACE OF X5CrNi18-10 AUSTENIC STAINLESS STEEL

*Joanna Trela, Mieczysław Scendo*

### 2.1.1. INTRODUCTION

The development of classic and nuclear energetic, the rocket technique and chemistry requires application stainless steels which are materials about the highest corrosion resistance [1-3]. Stainless steel containing about 10.5% Cr. Chrome creates the passive surface layer of the steel. Stainless steels show corrosion resistance on acting nitric(V) acid, very dilute sulphuric(VI) acid, many organic acids as well as acetic acid (except glacial acetic acid), alkalis, and also unfavorable atmospheric conditions. The breakdown of passive films on steel surfaces exposed to acids: hydrochloric, hydrobromic, formic and sorrel [1, 3, 4]. The stainless steels are wide use in different fields of industry. The study of effective method of protection stainless steel before corrosion is very important. The most often applied and effective method is addition to the corrosive environment of inhibitors which even small concentration considerably reduce the speed of corrosion. The effectiveness of any corrosion inhibitor is dependent on the type of metal and properties of the corrosive environment. Most of the well-known organic inhibitors are heterocyclic compounds containing π-electrons, heteroatom and aromatic rings. New inhibitors are demanding still. Inhibitors have to fulfill the row of principal requirements: (i) they have to be nontoxic, (ii) the best natural origin, (iii) biodegradable (iv) they should be cheap and possibly easy to synthesis. This type substances were named *green inhibitors*. The effectiveness of working is very important feature of this type of substances, mainly in acid environment (pH 1-4). The efficiency of the inhibitor depends on the adsorption properties. Corrosion inhibitors are needed to isolation of metal from corrosive environment and reduce the corrosion rates [5-7].

Imines which be called the *Schiff bases* contain in their particle the atoms of nitrogen and oxygen. With this reason they are the good corrosion inhibitors of metals [8-13]. These substances found application in many fields of biochemistry and chemistry.

The present work reported our attempt to use potentiodynamic polarization to investigate the influence of the concentration of *N*-(2-chlorobenzylidene)-4-acetylaniline (CBAA) on the corrosion of X5CrNi18-10 austenic stainless steel in chloride acid solutions.

## 2.1.2. EXPERIMENTAL METHODS

**Solutions**. The electrolytes were prepared using of the NaCl and HCl analytical grade reagents (Merck) The corrosive medium 1.2 M $Cl^{-}$ was prepared from a stock of NaCl and 1.0 M HCl solution. All solutions were prepared from double distilled water. The pH of all solutions had 1.5 the value. For each experiment a freshly made solution was used. All test have been performed in naturally aerated electrolytes.

**Inhibitor**. The *N*-(2-chlorobenzylidene)-4-acetylaniline (CBAA) (> 98%) was purchased from ALDRICH and was used without father purification. The structure of *N*-(2-chlorobenzylidene)-4-acetylaniline is given in Figure 2.1. The CBAA is flat molecule and is stable in air, water and in majority organic solvents. The *N*-(2-chlorobenzylidene)-4-acetylaniline was dissolved at concentrations in the range of 0-20 mM in corrosive acid chloride solutions, which were mixed with magnetic stirrer. For each experiment a freshly prepared electrolyte was used.

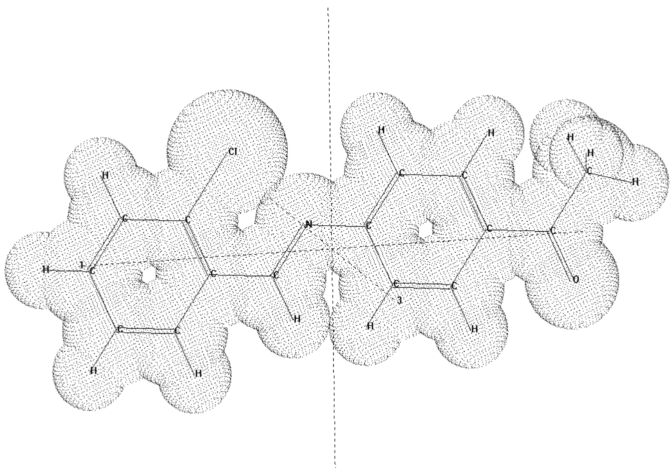

***Fig. 2.1.*** *Molecular structure of N-(2-chlorobenzylidene)-4-acetylaniline (CBAA) obtained after a geometric optimization procedure using a HyperChem 7.5 software*

All solutions were prepared from double redistilled water. For all experiments were used a naturally aerated solutions.

**Electrodes and apparatus**. Experiments were carried out in a three-electrode glass cell with a 200 $cm^3$ capacity. The working electrode was prepared from stainless steel in the shape of rectangle which had a surface area of 4.11 $cm^2$. The elements compositions of working electrode is show in Table 2.1.

***Table 2.1.*** *The elements compositions at weight percentages (%) of X5CrNi18-10 austenitic stainless steel*

| C | Si | Mn | Cr | Ni | N | S | P |
|---|---|---|---|---|---|---|---|
| <0.07 | <1.0 | <2.0 | 17-19.5 | 8-10.5 | <0.11 | <0.015 | <0.045 |

Prior to each experiment, the working electrode surface was treated with 800, 1200, and 2000 grade emery paper to give a mirror like surface finish, and then thoroughly rinsed with double distilled water. After this the electrode was degreased with ethanol in an ultrasonic bath (~5 min) and then rinsed with double distilled water. The electrode was taken immersed in the test electrolyte.

Electrode potentials were measured and reported against the external saturated calomel electrode (SCE) connected to the cell via a Luggin probe. The capillary tip was opposite to the end of the working electrode and about 3 mm from it.

A platinum wire was used as an auxiliary electrode. Reference and auxiliary electrodes were individually isolated from the test solution by glass frits.

All voltammetric experiments were performed using a potentiostat ATLAS 0531 (Atlas, Gdansk) with AtlasLab software the same firm. The scheme of measuring apparatus is showed in Figure 2.2.

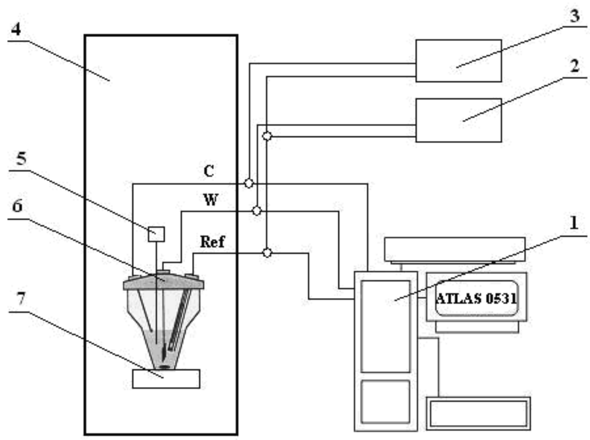


***Fig. 2.2.*** *Scheme of measuring apparatus: C – auxiliary, W – working, and Ref – reference electrode. Moreover: 1 – electrochemical analyzer from outside devices, 2 and 3 – digital voltmeters, 4 – air thermostat, 5 – digital thermometer, and 7 – magnetic stirrer with heating plate*

The values reported in the paper represent mean values of at least three replicate measurements. Moreover, experiments were carried out at suitably temperature (25 ±0.5°C) in an air thermostat with the forced air circulation.

### 2.1.3. RESULTS AND DISCUSSION

Polarization curves

The electrochemical behaviour of X5CrNi18-10 austenic stainless steel in 1.2 M $Cl^-$ solutions were studied. The pH of solution was 1.5. The electrode potential was changed from –800 to +400 mV, scan rate 1 mV $s^{-1}$. The polarization curve is presented in Figure 2.3.

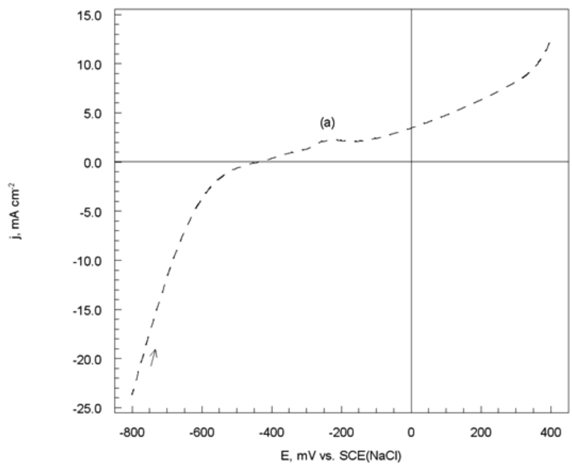


***Fig. 2.3.*** *The polarization curve for X5CrNi18-10 austenic stainless steel. The solution contained 1.2 M Cl⁻, dE/dt 1 mV s⁻¹*

The curve is characteristic for passive metals. The cathodic polarization curve (*a*) concerns the reaction connected with reduction of the hydrogen which run according to following mechanism:

$$Fe + H^+ = (FeH^+)_{ads} \tag{2.1}$$

$$(FeH^+)_{ads} \rightarrow (FeH)_{ads} - e^- \tag{2.2}$$

$$(FeH^+)_{ads} + H^+ \rightarrow Fe + H - 2e^- \tag{2.3}$$

At potential –350 mV (curve (*a*)) the characteristic peak develops. The peak is connected with oxygenation the material of electrode:

$$Fe + H^+ + ½O_2 = (FeOH^-)_{ads} \tag{2.4}$$

$$(FeOH^-)_{ads} = (FeOH)_{ads} + e^- \tag{2.5}$$

$$(FeOH)_{ads} + H^+ + ½O_2 = (FeOH)_{2,s} + 3e^- \tag{2.6}$$

$$(FeOH)_{2,s} + H^+ + ½O_2 \rightarrow FeOOH_s + H_2O + 2e^- \tag{2.7}$$

$$2FeOOH_s \rightarrow Fe_2O_3, s + H_2O \tag{2.8}$$

Moreover, forming passive layer be enriched in result following oxides:

$$2Cr + 2H^+ + 2O_2 \rightarrow Cr_2O_3 + H_2O + 14e^- \tag{2.9}$$

$$Ni + 2H^+ + O_2 \rightarrow NiO + H_2O + 6e^- \tag{2.10}$$

The metal react with the ions $Cl^-$ according reaction:

$$Fe + Cl^- = (FeCl^-)_{ads} \tag{2.11}$$

$$(FeCl^-)_{ads} = (FeCl)_{ads} + e^- \tag{2.12}$$

Formed the $(FeCl)_{ads}$ comes in composition of passive layer. Because the pH of electrolyte is acid, therefore layer $(FeCl)_{ads}$ undergoes dissolution:

$$(FeCl)_{ads} \rightarrow (FeCl^+) + e^- \tag{2.13}$$

$$(FeCl^+) = Fe^{2+} + Cl^- \tag{2.14}$$

The Figure 2.4 shows that the cathodic and anodic currents decrease with an increase the concentration of *N*-(2-chlorobenzylidene)-4-acetylaniline (curves (*b*) – (*e*)). This indicates that the addition of CBAA affects both the cathodic and anodic reactions, therefore the compounds act as a mixed-type inhibitors.

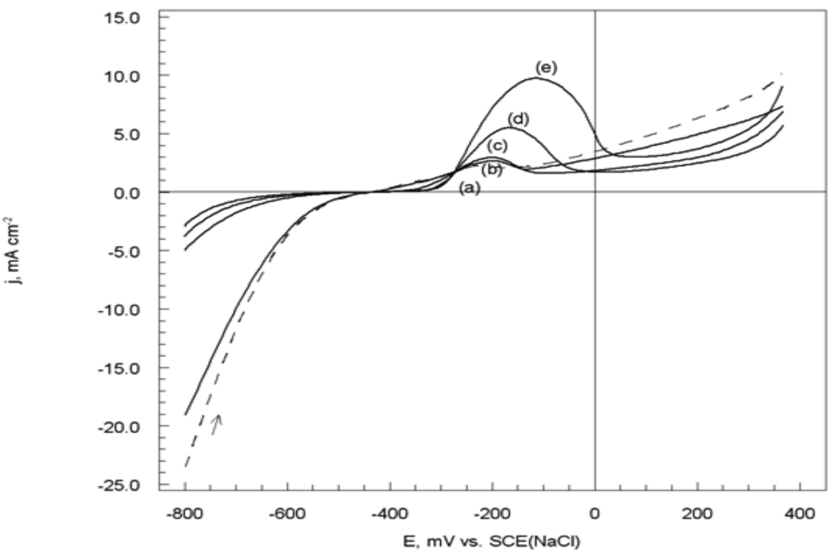


***Fig. 2.4.*** *The polarization curves for X5CrNi18-10 austenic stainless steel. The solutions contained 1.2 M $Cl^-$ and (a) 0, (b) 1, (c) 10, (d) 15, and (e) 20 mM of N-(2-chlorobenzylidene)-4-acetylaniline, dE/dt 1 mV $s^{-1}$*

The increase of the dissolution peak current density with the increase of *N*-(2-chlorobenzylidene)-4-acetylaniline concentration was observed. This mean, that CBAA takes part in formation of adsorbed film.

Electrochemical corrosion kinetic parameters were calculated on the basis of cathodic and anodic potential versus current characteristics in the Tafel potential region, Figure 2.5.

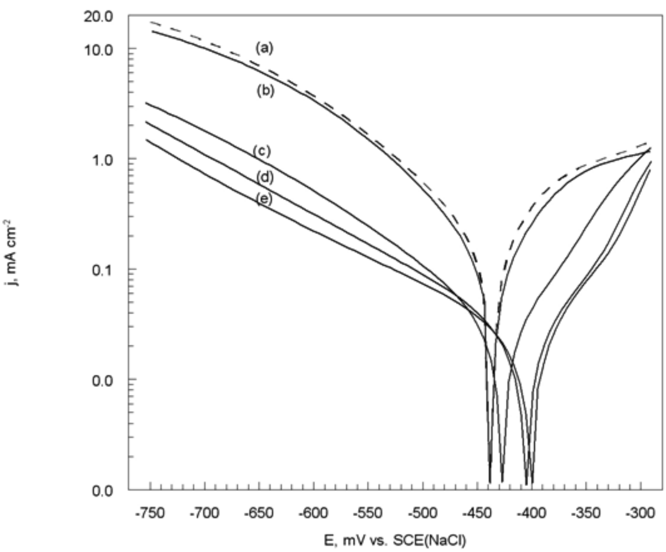


***Fig. 2.5.*** *Tafel plots for X5CrNi18-10 austenic stainless steel. Solution containing 1.2 M $Cl^-$ (a) 0, (b) 1, (c) 10, (d) 15, and (e) 20 M of N-(2-chlorobenzylidene)-4-acetylaniline, dE/dt 1 mV $s^{-1}$*

The corrosion parameters such as corrosion potential ($E_{corr}$), corrosion current density ($j_{corr}$), cathodic ($b_c$) and anodic ($b_a$) Tafel slope are listed in Table 2.2.

***Table 2.2.*** *Corrosion parameters for X5CrNi18-10 austenic stainless steel. The solutions contained 1.2 M $Cl^-$ and of N-(2-chlorobenzylidene)-4-acetylaniline, at temperature 25 ℃*

| Concentration CBAA mM | $E_{corr}$ mV | $j_{corr}$ mA $cm^{-2}$ | $b_a$ | $-b_c$ |
|---|---|---|---|---|
| | | | mV/dec | |
| Blank | –442 | 0.24 | 35 | 55 |
| 1 | –438 | 0.13 | 30 | 57 |
| 5 | –430 | 0.074 | 28 | 57 |
| 10 | –425 | 0.028 | 25 | 60 |
| 15 | –414 | 0.025 | 23 | 68 |
| 20 | –408 | 0.022 | 20 | 70 |

It should be noted that $E_{corr}$ changes imperceptibly. This is characteristic for mixed inhibitors. The corrosion current density ($j_{corr}$) decreased when the concentration of *N*-(2-chlorobenzylidene)-4-acetylaniline was increased which indicates the inhibiting effect of CBAA. Moreover, change both cathodic ($b_c$) and anodic ($b_a$) Tafel slopes (Tab. 2.1) indicated that increased concentration of CBAA change the corrosion of mechanism.

The polarization resistance values ($R_p$) for austenic stainless steel increased with an increase in the concentration of an inhibitor, Figure 2.6.

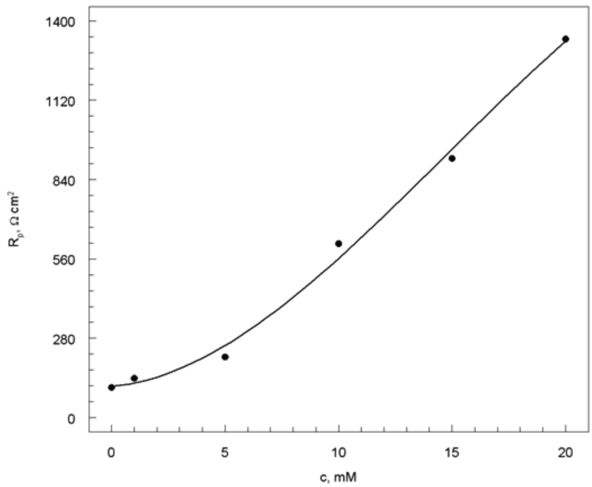


***Fig. 2.6.*** *Influence concentration of N-(2-chlorobenzylidene)-4-acetylaniline on resistance values for X5CrNi18-10 austenic stainless steel*

The results show an increase in the degree of surface coverage of electrode by adsorption *N*-(2-chlorobenzylidene)-4-acetylaniline.

## Inhibition efficiency

Inhibition efficiency for solutions containing different concentration of *N*-(2-chlorobenzylidene)-4-acetylaniline is showed in Figure 2.7.

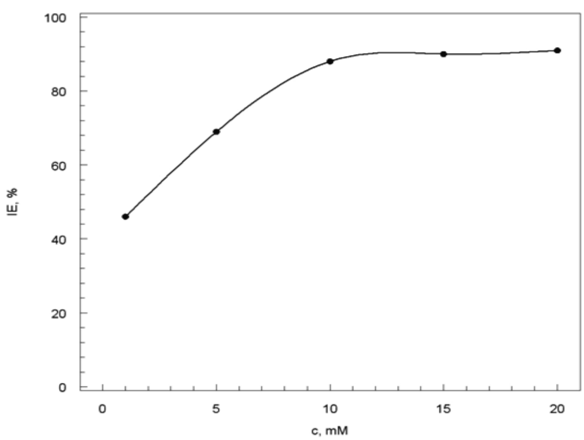


***Fig. 2.7.*** *Inhibition efficiency for X5CrNi18-10 austenic stainless steel. The solutions containing 1.2 M* $Cl^-$ *and N-(2-chlorobenzylidene)-4-acetylaniline*

The inhibition efficiency increased with the concentration of *N*-(2-chlorobenzylidene)-4-acetylaniline. The largest growth of inhibition efficiency was observed for small concentrations inhibitor, about 10 mM. Enlarging part of CBAA in solution of electrolyte doesn't cause the essential growth of value *IE*.

## Adsorption isotherm

The efficiency of organic molecules as good corrosion inhibitors mainly depends on their adsorption ability on the metal surface. Basic information about the interaction between inhibitor and metal can be provided by the adsorption isotherm. The investigation of the relation between corrosion inhibition and adsorption of inhibitor is of great importance. In aim of qualification of mechanism the influence of *N*-(2-chlorobenzylidene)-4-acetylaniline from steel surface isotherm of adsorption was prepared, Figure 2.8.

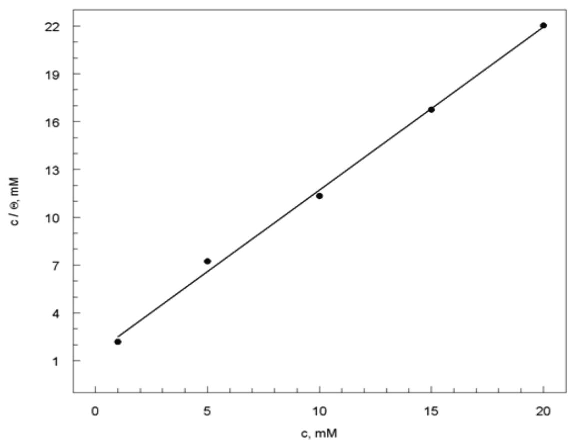


***Fig. 2.8.*** *The isotherm of adsorption for N-(2-chlorobenzylidene)-4-acetylaniline on X5CrNi18-10 austenic stainless steel surface*

The Langmuir adsorption isotherm [13] was applied to investigate the adsorption of CBAA on X5CrNi18-10 stainless steel surface in chloride solutions given by the following equation:

$$c/\Theta = 1/K_{ads} + c \tag{2.15}$$

where: $K_{ads}$ is the adsorption equilibrium constant, $c$ is the concentration of inhibitor.

A graph of $c/\Theta$ against $c$ leads to values $K_{ads}$:

$$K_{ads} = A\ exp\,(-\Delta G^0_{ads}/RT) \tag{2.16}$$

The standard free energy of adsorption, $\Delta G^0_{ads}$, were calculated from the adsorption equilibrium constant using the equation:

$$\Delta G^0_{ads} = -RT\ ln\ (55.5 \times K_{ads}) \tag{2.17}$$

where: $A$ is the reverse of concentration of solvent, $\Delta G^0_{ads}$ is the standard free energy of adsorption, $K_{ads}$ is the equilibrium constant of adsorption, $R$ is the universal gas constant, $T$ is the absolute temperature, and the value of 55.5 is concentration of water in the solution.

The standard free energy of adsorption were calculated and are given in Table 2.3. The Langmuir isotherm assumes that:

- Adsorption of *N*-(2-chlorobenzylidene)-4-acetylaniline sets on the *active centers* steel, according to mechanism:

$$CBAA_{sol} + H_2O_{ads} \leftrightarrow CBAA_{ads} + H_2O_{sol} \tag{2.18}$$

- The steel surface contains a fixed number of adsorption sites, and each site holds one molecule of CBAA (adsorbate).
- The adsorbents do not interact with one another, i.e. there is no effect of lateral interaction of the adsorbents on $\Delta G^{0}_{ads}$.
- The negative value of $\Delta G^{0}_{ads}$ indicate spontaneous adsorption of Schiff base on austenic stainless steel surface.

***Table 2.3.*** *The coefficient of linear adjustment, slope, equilibrium constant of adsorption, and standard free energy of adsorption of N-(2-chlorobenzylidene)-4-acetylaniline on austenic stainless steel surface*

| $r$ | $b$ | $K_{ads} \times 10^2$, $M^{-1}$ | $-\Delta G^0_{ads}$, kJ $mol^{-1}$ |
|---|---|---|---|
| 0.9986 | 1.02 | 6.84 | –26.15 |

Generally the standard free energy of adsorption values of –20 kJ $mol^{-1}$ or less negative are associated with an electrostatic interaction between charged metal surface (physical adsorption), those of –40 kJ $mol^{-1}$ or more negative involves charge sharing or transfer from the inhibitor molecules to the metal surface to form a co-ordinate covalent bond (chemical adsorption) [14-18]. For investigated Schiff base inhibitor, on can see that calculated $\Delta G^{0}_{ads}$ values, equals –26.15 kJ $mol^{-1}$. This mark, that particle of *N*-(2-chlorobenzylidene)-4-acetylaniline strongly affect from surface stainless steel. Moreover, CBAA undergoes mixed adsorption creating protective layer on surface of X5CrNi18-10 austenic stainless steel.

Conclusions:

1. The X5CrNi18-10 austenic stainless steel undergoes the passivation in acid solutions.

2. The polarization curves indicated that of *N*-(2-chlorobenzylidene)-4-acetylaniline behave as mixed type corrosion inhibitor by inhibiting both cathodic hydrogen evolution and anodic metal dissolution reactions.
3. The inhibition efficiency of CBAA increased with increase concentration inhibitor in solution.
4. The adsorption of the investigated compound was confirmed to follow the Langmuir adsorption isotherm.
5. The inhibition is due to the formation of an insoluble stable film through the process of adsorption of the inhibitor molecules on the steel surface.

This work was supported by the ESF Human Capital Operational Programme grant 6/1/8.2.1./POKL 2009

# 2.2. THE SUPERFICIAL LAYER FORMING BY ELECTROEROSION-MECHANICAL MACHINING WITH A FLEXIBLE ELECTRODE

*Sławomir Spadło*

## 2.2.1. THE FIELD OF APPLICATION OF BEDMD METHOD

Due to the present trend in constructing machines, alloys of special properties are often used. These materials are characterised by mechanical durability and high resistance to abrasion and corrosion. Cutting such materials may prove difficult because most of them are hard to cut. The process is made even more difficult by the fact that parts made of these alloys are of complex shapes. In these circumstances it is advisable to use BEDMM (Brush Electro-Discharge Mechanical Machining) as the surface finishing process.

BEDMM involves gradual removal of the extra material from the surface of the part being machined by electro-erosive, electro-chemical and mechanical processes. Apart from the removal of the material, mass exchange processes between the hot electrode and the machined part take place, being the result of the mixing of the partially melted electrodes and diffusion processes. As a result of those processes the chemical composition and geometrical structure of the superficial layer of the part is formed. Consequently, the resulting layer exhibits new properties [20, 23, 25 and 28].

## 2.2.2. EXPERIMENTAL INVESTIGATIONS

The investigations aim is to explain the phenomena occurring in the process of electrodischarge mechanical machining with the brush electrode as well as to determine the influence of the machining conditions on the surface layer conditions.

The following factors (Fig. 2.9) influencing the machining results have been examined:

– kinematics parameters ($v_0$ – rotational speed of the brush electrode, $v_f$ – feed-rate),
– electric parameters ($U$ – voltage, $E$ – impulse energy, $\tau$ – impulse time duration),
– material of brush electrodes (tungsten, molybdenum, chromium-nickel steel) and diameter of wires,
– value of the deflection ($\Delta$) of the hot electrode components.

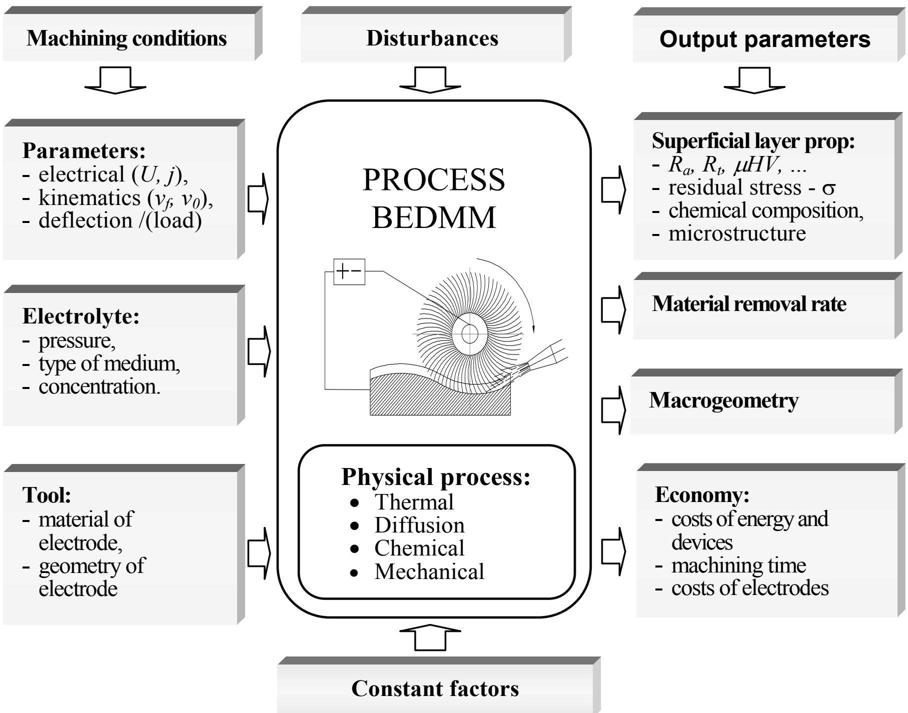


***Fig. 2.9.*** *BEDMM process as a subject investigation*

The layer is shaped by the energetic effect of the discharge on the electrodes and the following phenomena are caused by such a discharge:
– superficial melting of the anode and cathode,
– expulsion of the material into the inter-electrode area and its consequent solidification,
– transfer of the melted material from the hot electrode onto the part surface,
– mixing and diffusion of the particles of the transferred material into the workpiece material,
– temperature increase of the surrounding layers,
– very fast cooling of the superficial layer due to the heat transfer through the part core.

The above factors have influenced the following output parameters:

- productivity,
- parameters describing the geometry of the surface layer ($R_a$, $R_t$, $S_m$, $D_q$, $W_a$, $W_t$, $W_{sm}$),
- surface texture,
- metallographic structure of the superficial layer,
- superficial layer chemical composition,
- microhardness distribution in the superficial layer.

In the BEDMM process [20] a rotating metal brush is used as a tool and the process is performed in the presence of a machining fluid, which is water-glass in water solution with composition ratio lower than that used in erosion-mechanical cutting (<10%). The position of the brush should be properly chosen, as shown in (Fig. 2.10a) to ensure deflection (Δ) of the tool components big enough to allow mechanical rupture of the anodic layer on the surface of the workpiece and an initiation of an electrical discharge. After the initiation is achieved and the plasma channel is built a rapid local increase in temperature occurs on the peak of roughness which causes melting, evaporation and metal removal. Figure 2.10b shows the principle of this process. Electrochemical, electrodischarge and mechanical phenomena and their interaction can be found in BEDMM.

In electrical discharge machining spark discharges is the main factor influencing the formation of the superficial layer. As a result of single discharges local melting and material evaporation occur, resulting in roughening of the surface in the form of craters. They are determined, but as the craters overlap and are randomly distributed their structure must be random in nature.

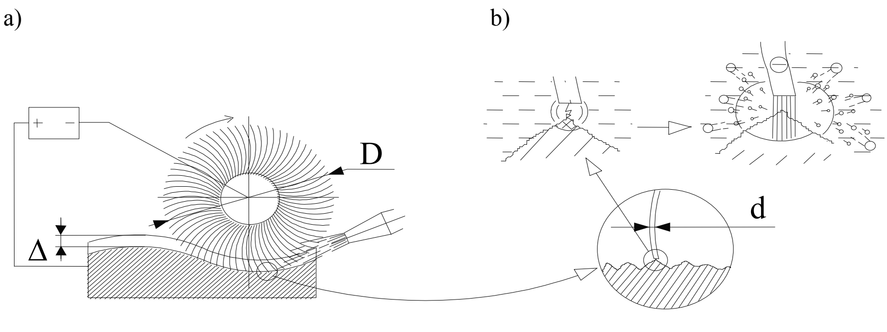


***Fig. 2.10.*** *Electrical discharge ocurses in BEDMM process*

With typical parameters of machining the mechanical contact of the brush with the melted metal can cause the liquid metal to spread over the machined surface, as a result of which the peaks of roughness are flattened. An increase in pressure, with low voltage applied, can cause the depassivated layer to be torn off. Eventually it leads to a direct contact of the electrodes and the fading of the discharges. That, in turn, changes the nature of the process to electromechanical. In these circumstances the main process that forms the geometrical structure of the surface layer is furrowing the surface with each part of the brush.

Detailed examinations of the superficial layer carried out by means of X-ray diffraction microanalysis have shown that apart from the removal of the material from the machined surface, particles of the hot electrode are transferred to the machined part. As a result of these processes a 5-10 μm thick modified layer is created. When molybdenum, tungsten or chromium nickel steel electrodes are used, the concentration level of these elements in the superficial layer increases up to 10%.

Some wires affect the surface by electrical discharges and by the above described process of mass transfer from the cathode to the anode and thermochemical modification of the superficial layer. Other wires affect the surface in an electromechanical way [19]. The mechanical contact of the wires with the machined surface is accompanied by an electric current without any discharges. This electromechanical influence results in smoothing the roughness peaks created by the electric discharges and in the temperature increase of the machined surface.

The electrical erosion phenomena, which occur during machining with the brush electrode, are accompanied by a mechanical contact of the elastic brush wires, which are pressed against the machined surface and move at high speed. It results in removing the machined part particles, which do not adhere closely to the surface and cause surface smoothing.

a) b)

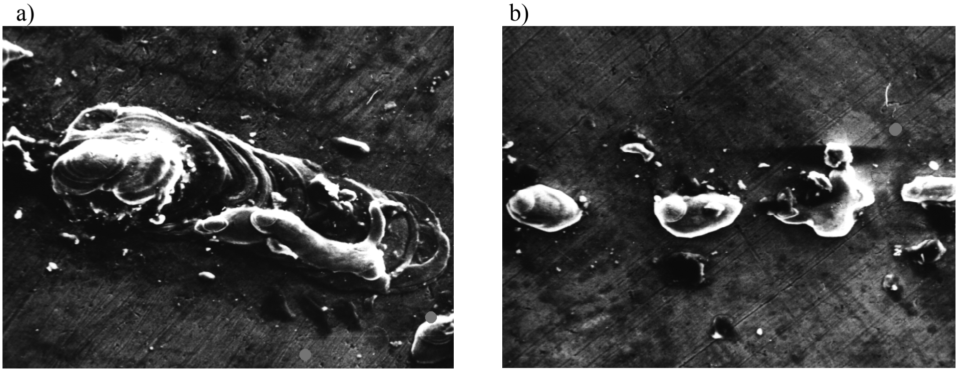

***Fig. 2.11.*** *SEM photograph of the BEDMM machined surface with a visible trace of the discharges: a) U = 8 V (voltage) and b) U = 4 V (voltage) at magnification 300x. Process parameters: d = 0.185 mm (single wire diameter),* $v_o = 0.7$ *m/s (tangential velocity)*

The surface texture is random and consists of micro-craters covered by micro-irregularities resulting from the dynamic effects of the melted metals particles transfer, thermocapillary waves, etc. with the distinct summit levelling due to the mechanical effect of the brush elements.

The final effect of the process is shown in Figure 2.12. It is a surface machined with voltage applied $U = 12$ V. The results of the research have been supplemented by the profilogram of a surface machined in the BEDMM process (Fig. 2.13). Its analysis shows that removal of material occurs mainly at the peaks of the roughness.

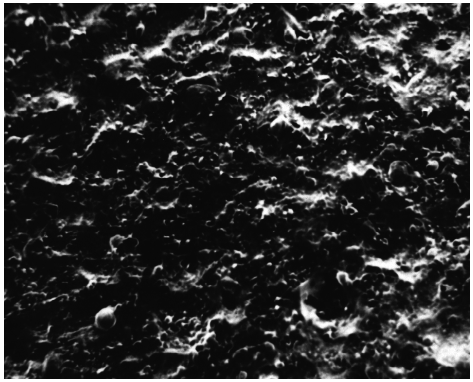

*Fig. 2.12.* *SEM photograph of surface layer after being BEDMM machined at magnification 300x. Process parameters: U = 12V (voltage), d = 0.3 mm (single wire diameter), $v_o$ = 3.6 m/s (tangential velocity), $v_f$ = 12 mm/min (feed rate)*

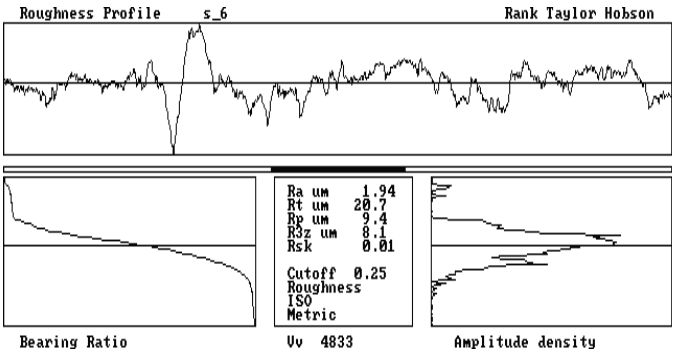


*Fig. 2.13.* *Profilogram of surface layer after being BEDMM machined. Process parameters: U = 12 V (voltage), d = 0.3 mm (single wire diameter), $v_o$ = 3.6 m/s (tangential velocity), $v_f$ = 12 mm/min (feed rate)*

On closer inspection [23] the surface roughness profile above appears to be asymmetrical. Two structures can be distinguished, the primary one, being the result of spark discharges and seen as craters in the shape of spherical caps, and the secondary one, being the result of mechanical and electrochemical processes, mainly seen at the peaks of roughness. The peaks being flat, the roughness of the layer has an advantageous profile.

The range of roughness produced by the BEDMM process (Fig. 2.14) is $R_a$ = 0.5-5 μm, the lower values being comparable to the values produced by grinding.

Residual stresses in the superficial layer usually occur as a result of the melting and solidifying of the superficial layer. Examinations carried out using the Philips-Weisman method have demonstrated that the stresses are positive. They occur at a depth of no more than 100 μm. After BEDMM roughening machining (*U* = 16 V) maximum tensile stress achieved 1500 MPa. Applying mechanical machining with a rotating brush to a part that has been BEDMM-machined creates compressive (negative) stresses in the superficial layer about 500 MPa. For example, in Figure 2.15 result of performed investigation is presented.

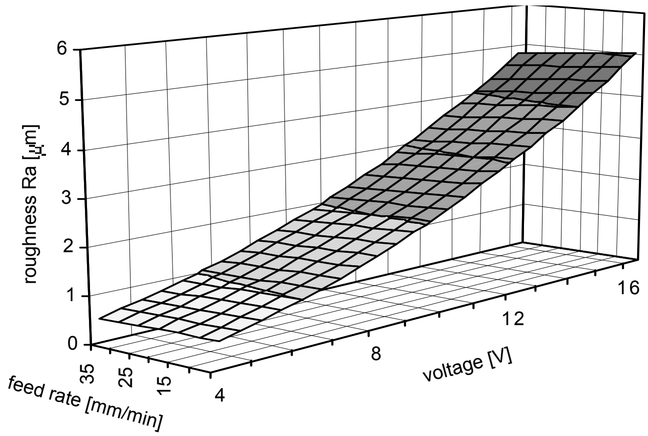


***Fig. 2.14.*** *The effect of the voltage and tangential velocity of the hot electrode on $R_a$, with chromium cast-iron are being the machined alloy. Process parameters: d = 0.3 mm (single wire diameter), $\Delta$ = 0.4 m/s (deflection), $v_f$ = 12 mm/min (feed rate)*

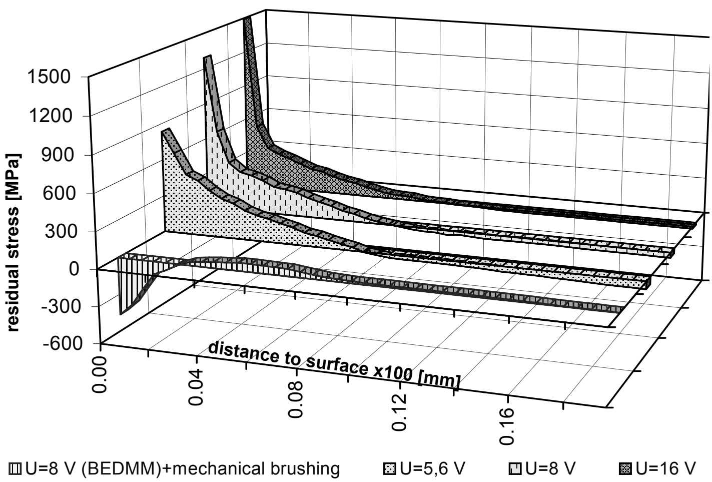


***Fig. 2.15.*** *Residual stresess after BEDMM machined carbon steel C45 (0.45 %C) workpieces. Process parameters: U = 5.6, 8, 16 V (voltage), $\Delta$ = 1 mm (deflection), $v_0$ = 3.6 m/s (tangential velocity), $v_f$ = 12 mm/min (feed rate)*

The metallographic structure (Fig. 2.16) shows features typical of a surface machined by BEDMM. Superficial layer has a gradient structure with an increase of chromium and nickel content. At the top, a molten and resolidifier layer, called recast layer, is observed. This layer is usually present because material removal in BEDMM is mainly based on melting process of the workpiece material. In the recast layer in BEDMM condition mixing and diffusion of material working electrode and workpart can occur due to temporary, directly contact electrodes. Below the recast layer a heat affected zone is present. This zone comprises the workpart material which has undergone an influence by heat and has not been molten. In case of applied steel it's usually hardened [21].

Microhardness distribution in a crossection of the surface layer after the BEDMM process ($U$ = 16 V) shows Figure 2.17, as a material of workpiece hardened steel (NC 10) was selected.

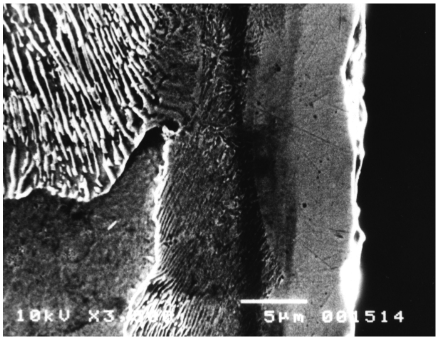


*Fig. 2.16. SEM photographs of the metallographic microstructures of the surface layers after the machining process (U = 8 V) using chromium nickel steel X6CrNiTi18-10 (1H18N9T) electrode; material of workpiece carbon steel C45 (0.45%C), magnification 3500x*

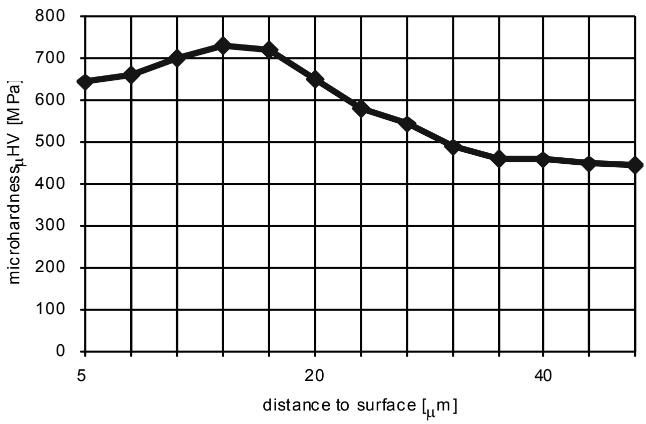


*Fig. 2.17. Microhardness distribution of crossection of the surface layer after the BEDMM process (U = 16 V), hardened steel X153CrMoV12 (NC 10)*

X-ray diffraction pattern obtained from the surface layer after the BEDMM process using a chromium nickel steel electrode shows Figure 2.18. The chemical composition of the superficial layer after the BEDMM process ($U$ = 8 V, DC current generator) using chromium nickel steel X6CrNiTi18-10 (1H18N9T) obtained by an X-ray diffraction analysis:

- workpiece – native material steel C45 (0.45% C), Cr 0.09%, Ni 0.08%,
- superficial layer machined by X6CrNiTi18-10 (1H18N9T) – steel electrode Cr 9.91%, Ni 5.25%,

– chemical composition hot electrode X6CrNiTi18-10 (1H18N9T) – steel electrode Cr 18.0%, Ni 9.0%.

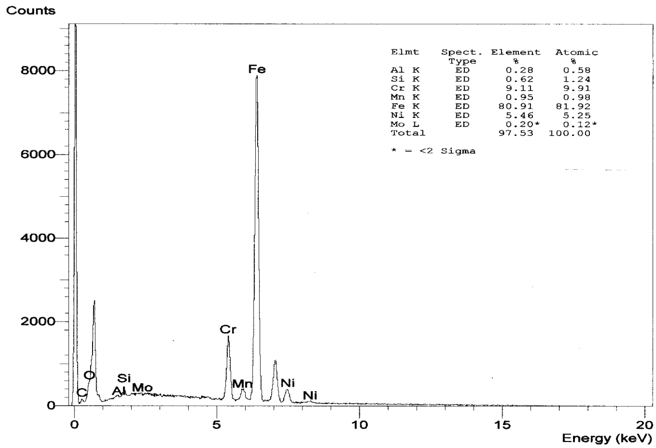


***Fig. 2.18.*** *X-ray diffraction pattern obtained from the surface layer after the BEDMM process using a chromium nickel steel X6CrNiTi18-10 (1H18N9T) electrode (U = 8 V)*

Figure 2.19a shows microstructure and line scan of X-ray diffraction microanalysis of the surface layer after the BEDMM process using a chromium nickel steel electrode. Figure 2.19b shows chemical elements distribution in the superficial layer with an increase of chromium and nickel content.

a) b)

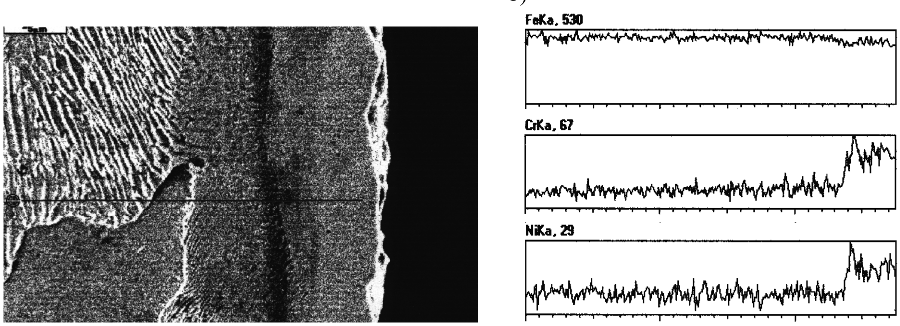


***Fig. 2.19.*** *X-ray line scan of the superficial layer after the BEDMM process (U = 8 V) using chromium nickel steel X6CrNiTi18-10 (1H18N9T) electrode: a) SEM photograph showing microstructure of sub-surface layer (magnification 3500x); b) chemical elements distribution in the sub-surface layer*

Conclusions:

The investigations into electrodischarge machining with rotating brush electrodes have shown that:

1. The surface layer subjected to the BEDMM process contains chemical components of the hot electrode (cathode).

2. Analysis of the molten and resolidified layer shows an increase of chromium (up to 10%) and nickel (up to 5%) content.
3. Thickness recast layer achieved about 5-10 micrometers.
4. The metallographic structure of the superficial layer reveals properties that are typical of electroerosion discharge machining.
5. The physical properties of the hot electrode and level of voltage significantly influence the machining process and its results.
6. If the process is well controlled higher hardness, higher wear resistance of the superficial layer can be achieved.

Praca powstała dzięki wsparciu finansowemu Ministerstwa Nauki i Szkolnictwa Wyższego w ramach projektu badawczego własnego pt. "Modelowanie i symulacja komputerowa procesów wymiany ciepła i masy w obróbce elektrozyjno-mechanicznej" realizowanego w Politechnice Świętokrzyskiej.

## 2.3. HEATING SURFACE LASER TEXTURING IN STUDIES OF HEAT TRANSFER IN MINICHANNELS

*Magdalena Piasecka*

### 2.3.1. TO HEAT TRANSFER ISSUES IN MINI GAPS

Transferring large heat fluxes is one of the most significant issues of today's technology. An increasing number of high-tech heat exchange devices are based on heat transfer to fluid during flow boiling in minichannels of various geometry and spatial orientation. Owing to the change of state that accompanies boiling, it is possible at the same time to meet two contradictory demands: to obtain the largest possible heat flux at small temperature difference between the heating surface and the saturated liquid, and to keep small dimensions of heat transfer systems. Boiling incipience, a fundamental problem in boiling heat transfer, is also a practical problem in terms of ensuring that the used equipment remains safe and operational. It is known that under certain circumstances, the wall of the system can reach a temperature that exceeds the saturation temperature of liquid before boiling begins. Under certain conditions, the temperature level required to initiate boiling may be larger than the allowable maximum wall temperature of the system, which can result in the destruction of the object being cooled, as early as the single-phase regime. This "temperature overshoot" called "nucleation hysteresis", is conspicuous when highly wetting dielectric fluids are used. Thus the heat transfer coefficient, the accompanying incipience of nucleate boiling in minichannels, and its behaviour under certain conditions constitute some of the most important issues of heat transfer mechanism. The knowledge of boiling incipience guarantees safe operation of devices. The investigated heat transfer during flow boiling in minichannel can be applied to cooling, thermostabilization and thermoregulation of those devices which generate large heat fluxes, especially for heat exchangers and electronic devices equipped with microscale cooling systems.

Following the classification by Kandlikar et al. minichannels are channels with small hydraulic diameter between 200 μm and 3 mm [34]. On the basis of the literature review undertaken by [35, 36], it can be stated that although much has been written recently on flow boiling heat transfer in minichannels, there is a large scatter in the local heat transfer coefficient values obtained as a result of experimental investigations and theoretical analyses. The available results are incoherent and, frequently, conflicting. The literature does not offer any generalized, universal criterial equations which would help predict heat transfer for various minichannel geometries. Correlations for determining heat transfer coefficients in minichannels, proposed by some researchers, are usually verified experimentally for channel systems heated by smooth heaters. Therefore the research focused on porous structure systems seems interesting due to their theoretical potential of further heat transfer enhancement.

### 2.3.2. EXPERIMENTAL SET-UP

The main loop

The main loop of the experimental stand (Fig. 2.20) with the test section (1) consists of the following elements: 2a – a rotary pump, 3 – a compensating tank (pressure regulator), 4 – a tube type heat exchanger, with water as the coolant, 5a – a filter, 6 – rotameters and 7a – a deaerator. Two pressure converters are installed on the inlet and outlet of the minichannel (8). Before the boiling heat transfer experiment starts, a closed-loop calibration circuit is actuated, with water circulating inside it. The circuit is made up of another rotary pump (2b), a heater with an electric heater element (9), two filters (5b) and an additional deaerator (7b). The heating foil, acting as the heating surface in the minichannel, is provided with electric current by an inverter welder (10) as a current regulated DC power supply (up to 300 A). Regulation and control of the system are provided by: 11 – a shunt, 12 – an ammeter, 13 – a voltmeter and, for the calibration loop, an autotransformer (14).

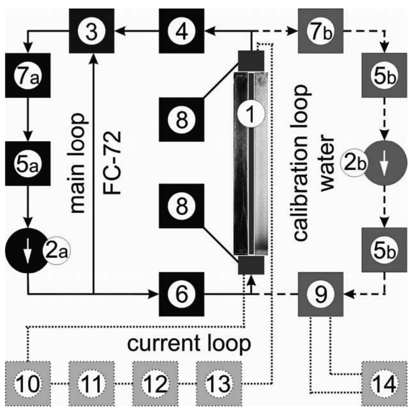


*Fig. 2.20. The schematic diagrams of the main loops at the experimental stand: 1 – test section with a minichannel; 2a,b – rotary pump; 3 – compensating tank/pressure regulator; 4 – tube-type heat exchanger, 5a,b – filter 6 – rotameters; 7a,b – deaerator, 8 – pressure regulator, 9 – a heater with an electric heater element, 10 – inverter welder, 11 – shunt, 12 – ammeter, 13 – voltemeter, 14 – autotransformer*

The experimental data and image acquisition system is shown in Figure 2.21. It consists of the following elements: lighting systems, two digital cameras, data acquisition system and a computer with the specialist software. The use of thermography has been made possible thanks to the colour image acquisition system which includes the Canon G11 camera and two fluorescent lamps and 2 LED lamps emitting “cool white light”. On the other side of the minichannel, the Canon Eos 550D digital SLR camera is used to observe flow structures. The lighting system uses two powerful 2 x 1 kW halogen reflectors with forced air cooling and heat resistant casing. Measurement data is recorded with DaqBoard 2000 data acquisition station equipped with DASYLab software installed on a laptop.

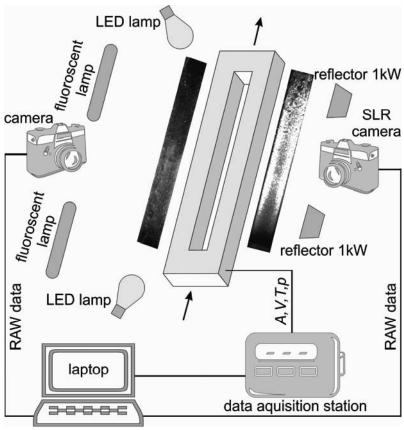


***Fig. 2.21.*** *The diagram of the experimental data and image acquisition system*

## Test section

The test section (Fig. 2.22) with a minichannel of 1 mm depth, 40 mm width, 360 mm length, is the most important part of the experimental stand. The test section is set at various angles to the horizontal plane. The article presents results for the minichannel oriented horizontally, with the unbent side upward. The heating element for the working fluid (FC-72) flowing along the minichannel is an alloy foil (2) stretched between the front cover (6) and the channel body (5). This thin foil (0.004’’ depth-approx. 0.1 mm) designated as Haynes-230, made of Ni-Cr-W-Mo high-temperature alloy constitutes one of the minichannel surfaces of the rectangular section. The foil is supplied with the direct current of controlled intensity. It is possible to observe both surfaces of the minichannel through two openings covered with glass plates. One plate (4a) allows observing changes in the temperature of the foil surface. It is a plain side of the heating foil (between the foil and the glass) and is covered with thermosensitive liquid crystal paint (3). Two dimensional temperature field on the foil surface is determined on the hue distribution on this surface thanks to liquid crystal thermography. The opposite surface of the minichannel (from the enhanced side of the heating foil) can be observed through the other glass plate (4b), which helps recognize the vapour-liquid two-phase flow patterns. K-type thermocouples (7) are installed in the inlet and outlet of the minichannel and on the glass plate near the minichannel outlet.

The channel body (5) and the front cover (6) of the test section are made of PA6 duralumin. Teflon separator forms lateral surfaces of the minichannel. The thickness of the separator determined the depth of the minichannal (variable in the range from 0.5 mm to 1.5 mm; 1 mm separator was used). Two electrodes (9) are copper elements energize the heating foil.

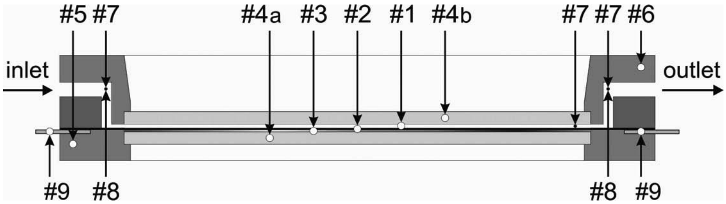


*Fig. 2.22. The schematic diagrams of the test section: 1 – minichannel, 2 – heating foil, 3 – liquid crystal layer, 4a,b – glass plate, 5 – channel body, 6 – front cover, 7 – thermocouple, 8 – enhanced side of the foil with mini-reentrant cavities, 9 – copper element*

The surface was textured on the heating foil from the side of fluid in the minichannel. Thus, microcavities were distributed uniformly on the selected area of the foil (40 x 40 mm), as shown in Figure 2.23a. They were performed with a laser drilling with the diode pumped Nd:YAG laser producing UV radiation of the wavelength of 355 nm. The microcavities are 50 μm in diameter and 1 μm deep, their total height is about 6 μm. They are evenly distributed every 100 μm in both axes (Fig. 2.23b). A 4-5 μm high layer of melted metal accumulates annularly around the cavities. The photo and 3D topography of the sample of the foil with micro-reentrant cavities are presented in Figure 2.23c,d. The figures also show the photo and 3D topography of a single cavity, Figure 2.23e,f. 3D surface topographies were obtained by Form Talysurf PGI-1200 measurement system manufactured by Taylor Hobson. The study was conducted in Geometric Computer Measurement Laboratory at the Kielce University of Technology.

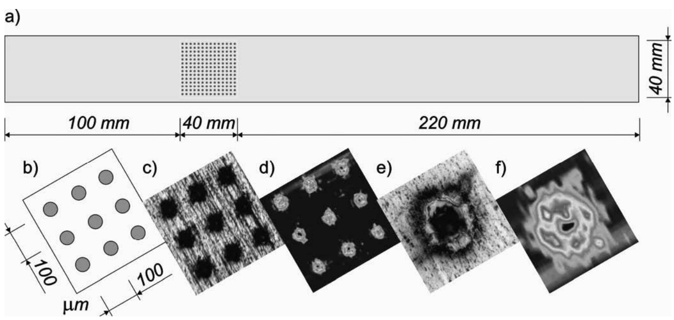


*Fig. 2.23. a) Heating foil with the selected enhanced area; b) magnification of the sample enhanced area; c, e) photos of the enhanced foil with micro-reentrant cavities; d, f) 3D topography of enhanced foil with micro-reentrant cavities*

### 2.3.3. EXPERIMENTAL RESEARCH

#### Experimental data

*Quantities set:*

- heat source capacity (heat flux volumetric density) $q_V$ supplied to the heating wall, derived from the formula:

$$q_V = \frac{I \cdot \Delta U}{A_F \cdot \delta_F} \tag{2.19}$$

*Quantities measured*

Thermal and flow parameters:

- local temperature of the heating foil $T_F(x)$, determined from the hue distribution on the surface;
- temperature of the investigated fluid at the channel inlet and outlet;
- volumetric rate of flow (rotameter readings);
- positive gauge pressure at the inlet $p_{inlet}$ and outlet of the minichannel $p_{outlet}$ (pressure converters readings);

*Electrical parameters:*

- voltage drop over a definite heating foil length $\Delta U$;
- current supplied to the heating foil $I$.

#### Error analyses

Evaluation of the accuracy of heating foil temperature measurements with liquid crystals thermography and heat source efficiency measurement error in the same) experimental set up and studies employing rectangular vertical minichannel with plain heating foil were discussed in [35]. Mean temperature measurement error of heating foil by liquid crystal thermography $\Delta T_F$ = 0.86 K was obtained. The value of the relative heat source efficiency measurement amounted to 3.5%. The data can be assumed as representative for the example under study because conditions of the investigation and the application of enhanced heating foil in the study does not affect error analyses.

#### Experimental procedure

The calibration procedure has to precede the boiling heat transfer investigation. Its aim is to assign corresponding temperature values to the hues observed on the surface covered with liquid crystals. In the degassed system, during the calibration process, the water of the pre-set temperature is fed to the minichannel in the closed cycle, see Figure 2.20. The water is heated while passing through the heater with an electric heater element (9) equipped with autotransformer (14) for smooth power adjustment. The image of temperature distribution on the surface is registered by a digital camera, Figure 2.21. Water temperature at the inlet and outlet to the minichannel is controlled with the measurement data acquisition station equipped with DASYLab software. Liquid crystal thermography technique and the procedure of surface hue calibration against temperature was discussed in [35].

After the calibration process, the main closed flow loop with FC-72 is actuated once the fluid is degassed. Then the gradual increase in the electric power supplied to the foil results in an increased heat flux transferred to the flowing fluid.

The liquid crystal colour images of the heating foil are presented for the horizontal minichannel with heating surface laser texturing on the selected area (Fig. 2.24).

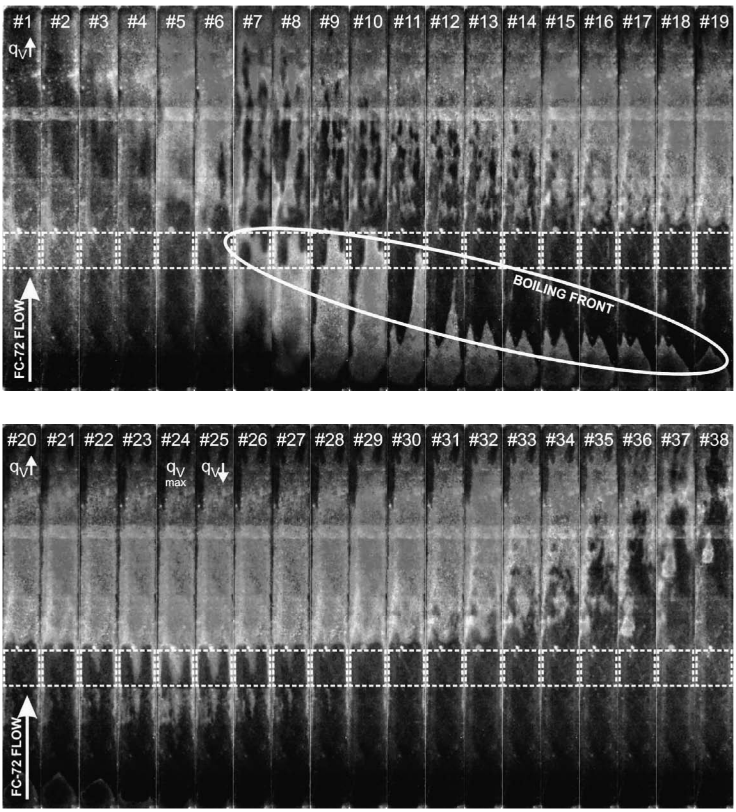


***Fig. 2.24.*** *Colour heating foil images while increasing and later decreasing heat flux supplied to the heating surface using enhanced foil on the selected area marked with dotted line, experimental parameters:* $u = 0.14$ *m/s,* $G = 240$ *kg/(m²s),* $p_{inlet} = 124$ *kPa,* $\Delta T_{sub} = 48$ *K,* $q_V = 9.44\ 104 \div 2.79\ 105$ *kW/m³,* $q_w = 9.59 \div 28.38$ *kW/m²*

At the beginning, when the liquid flows along the minichannel, an increase in the electric power supplied to the heating foil causes flow boiling incipience (images from 7 up to 22). Owing to the liquid crystal layer located on the heating wall contacting the glass, it is possible to observe a "boiling front" and measure temperature distribution on the heating wall. The "boiling front" is recognizable as the hue sequence pattern, which indicates a gradual hue changes of the liquid crystals (in accordance with the spectrum sequence) and then sharp hue changes of the liquid crystals (inversely to the spectrum sequence). Out-of-sensitivity-range temperatures are shown in black. The boiling incipience is identified with the maximum value of the heating surface temperature in “boiling front” image. A sharp temperature drop follows further out. The “boiling front” moves in the direction opposite to the direction of the liquid flow in the channel with increasing of the heat flux supplied to the foil. This phenomenon of the occurrence of nucleation hysteresis was discussed in [35-37].

When the heat flux continues to increase, a new hue sequence appears in the upper parts of images (images up to 7). This occurs when developed nucleate boiling is in progress in the minichannel. Then the current supplied to the foil is gradually reduced following the occurrence of saturated navy blue hue on the foil surface (images from 25 up to 38). Mild hue changes, in the direction opposite to the spectrum sequence are observed to accompany the decrease in the current supplied to the foil. As a result, heat transfer returns to single phase forced convection. This experiment is accomplished when the black colour of the background paint is seen which means that the temperature of the heating foil is lower than the bottom limit of the active range of liquid crystals.

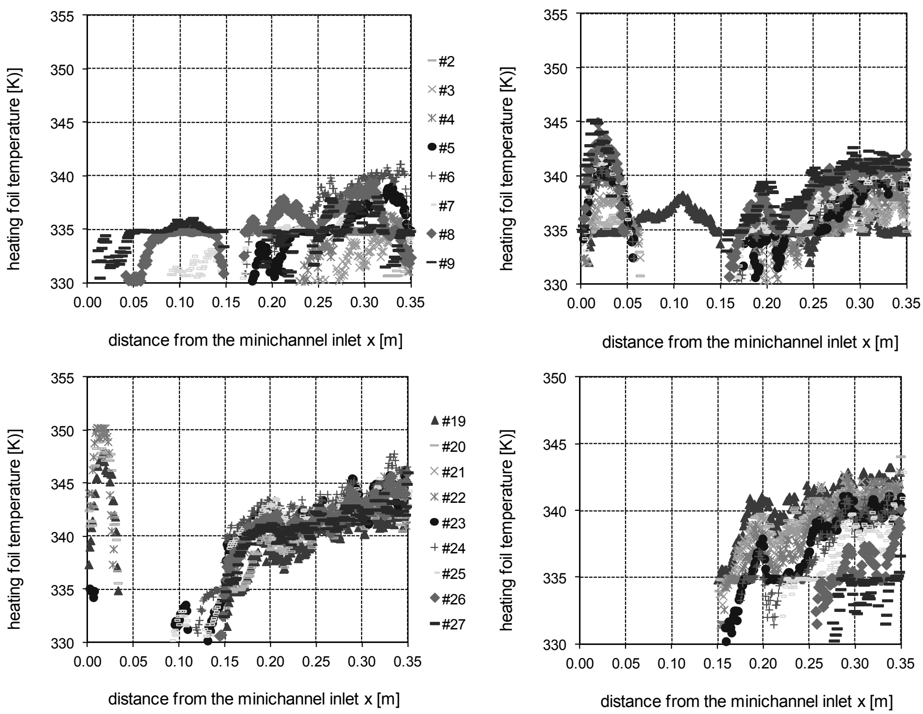


*Fig. 2.25. Heating foil dependence on the distance along the minichannel length, experimental data as for Figure 2.24*

Results of the heating foil temperature distribution obtained on the basis of hue distribution due to liquid crystal thermography are presented in the form of foil temperature dependence on the distance along the channel length in the Figure 2.25.

### Monochrome images of flow structures analyses

The analyses of flow structure cover the minichannel with foil enhanced in the selected area. It was based on the monochrome images of flow structures with an SLR camera of heating foil, obtained on the side coming into contact with fluid flowing in a minichannel. They were processed using Corel graphics software. After the photos had been binarized, which helped determine the boundary between the liquid and the vapour; the analysis of phase volumes was developed in Techystem Globe software. The software made it possible to obtain volumes of two phases in the select cross-section for the chosen area.

Three settings for increasing heat fluxes supplied to the heating surface: 8, 16 and 24 (Fig. 2.24) – were selected for analyses. Colour images were employed for the analysis (Fig. 2.26a) and accompanied by flow structure images (Fig. 2.26b). In the case of four cross-sections marked as I, II, III of each image (5 x 40 mm) the void fraction is determined. Cross-sections are placed at the distance of 90 mm (I), 133 mm (II) and 270 (III) from the inlet to the minichannel. They are marked with black lines on to the images. Subsequent cross-sections of images (Fig. 2.26c,d) and the binarized image of two-phase flow structure image (black and white) adopted for analysis in Techsystem Globe (Fig. 2.26e) are also shown in the Figure 2.26.

It was observed that bubble structure was prevalent at the boiling incipience and early development, but further development of boiling was dominated by cork structure with short and evenly distributed bubble agglomerates.

The void fraction was determined according to the following formula:

$$\Phi = \frac{V_v}{V_l + V_v} = \frac{A_v \cdot A_{ch}}{(A_l + A_v) \cdot \delta_{ch}} = \frac{A_v}{A_l + A_v} \tag{2.20}$$

Liquid and vapour cross-section areas were obtained from phase image analysis performed by means of Techsystems Globe software. The results were presented in the Figure 2.27 as void fraction dependence along the minichannel length.

An analysis of the two-phase flow images confirmed that the increase in void fraction takes place together with the increase in the heat flux from the value of approx. 0% (for boiling incipience) to the value of approx. 35% (for the developed nucleate boiling). If the cross-section farther from the inlet were selected, the void fraction would be higher.

The use of liquid crystal thermography with helped reveal the “boiling front” at the boiling incipience in the flow of FC-72 through a horizontal minichannel with the heating surface in the form of a single-sided alloy foil enhanced in the selected area. The boiling front was accompanied by “nucleation hysteresis” a considerable heating surface temperature drop.

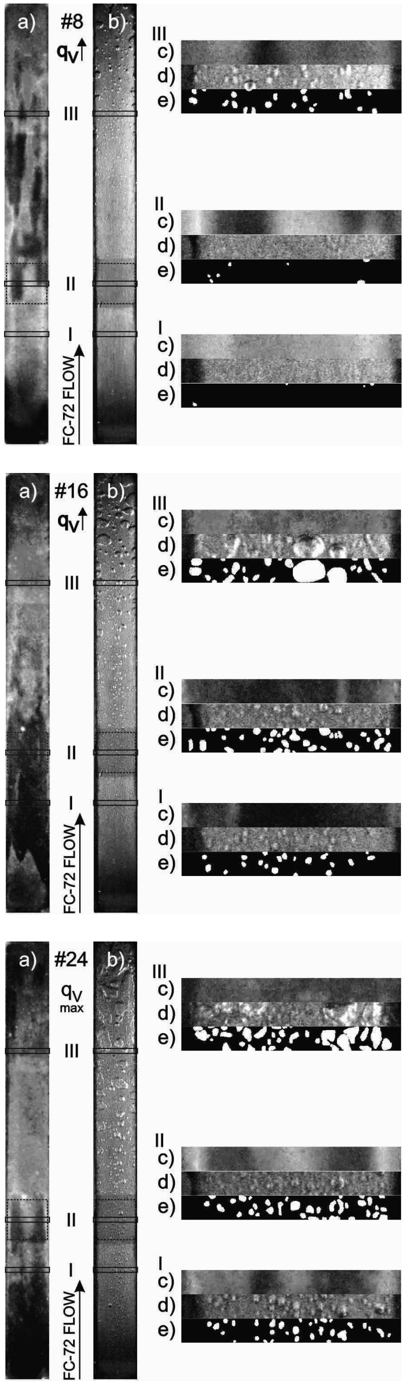


***Fig. 2.26.*** *Selected colour heating foil images for settings 8, 16 and 24 (a) and the corresponding two-phase flow structure images (b) with enlarged real (vertically arranged) cross-sections (c, d) and binarized phase images (e), experimental data as for Figure 2.24*

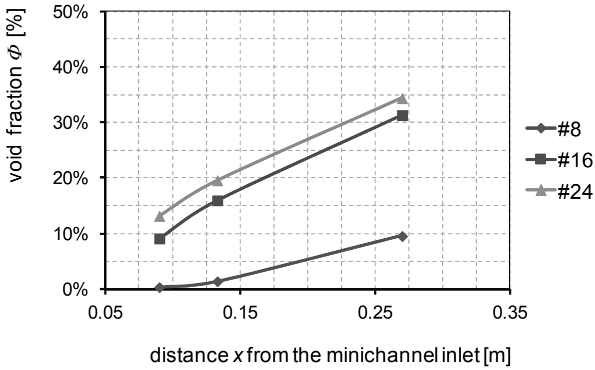


***Fig. 2.27.*** *Void fraction dependence along the minichannel length for selected cross sections for settings: 8, 16 and 24, experimental data as for Figure 2.24*

The observations have confirmed that in the research that boiling incipience occurs in lower heat flux supplied to the enhanced foil which constitutes a heating surface of the minichannel in comparison to results from the studies on similar minichannels employing the plain foil [35-37]. Thus the heating surfaces with the proposed arrangement of micro-reentrant cavities make it possible to provide a large number of nucleation sites. This leads to intensification of the heat flux transferred from the investigated surfaces and prior occurrence of the boiling incipience.

It was observed that bubble structure was prevalent at the boiling incipience and early development, but further development of boiling was dominated by cork structure with short and evenly distributed bubble agglomerates.

An analysis of the two-phase flow images confirmed that the increase in void fraction takes place together with the increase in the heat flux.

The research has been financially supported by the Polish Ministry of Science and Higher Education, Grant No. N N 512 354037 for the years 2009-2012.

## Nomenclature

$A$ – cross section area, m$^2$

$BI$ – boiling incipience

$G$ – mass flux, kg/(m$^2$s)

*hue* – component of the system HSI

$I$ – current supplied to the heating foil, A

$p$ – pressure, N/m$^2$

$q_V$ – volumetric heat flux, (capacity of internal heat source), W/m$^3$

$q_w$ – heat flux density, W/m$^2$

$T$ – temperature, K

$u$ – velocity, m/s

$V$ – volume, m$^3$

$x$ – distance from the minichannel inlet, m

**Greek**

$\Delta T_F$ – mean temperature measurement error of heating foil by liquid crystal thermography, K

$\Delta T_{sub}$ – inlet liquid subcooling, $(T_{sat} - T_l)_{inlet}$, K

$\Delta U$ – the voltage drop across the heating foil, V

$\Phi$ – void fraction, %

$\delta$ – depth, m

**Subscripts**

| | |
|---|---|
| *ch* – minichanel | *l* – liquid |
| *F* – foil | *sat* – saturation |
| *f* – fluid | *v* – vapour |
| *inlet* – at the inlet | *w* – wall |

# 2.4. ELECTROEROSIVE ALLOYING MODES OPTIMIZATION AT FORMATION OF A SPECIAL MICRORELIEF ON BRONZE SLIDING BEARINGS FRICTION SURFACES

*Vasyl S. Martsynkovskyi, Vyacheslav B. Tarelnik,*
*Ievgen V. Konoplianchenko*

## 2.4.1. STATEMENT OF A PROBLEM

Failure of the machines parts which are being contact at maintenance, is consequence of different kinds physical depreciation: fatigue failures, creep of materials, mechanical depreciation, corrosion, erosion, cavitation, ageing of a material, etc.

The most widespread cause defunctionability of parts and machines end-effector is not breakage, this cause is deterioration and damage of their working surfaces. Thus, products life cycle directly depends on quality of their surfaces which is defined by geometrical characteristics and physicomechanical properties of a surface layer.

In [38] is offered the method of coatingon on bronze plain bearings liners (PBL) alignment coverings of structure: silver + copper + babbit. Alignment coverings are coatingon by a electroerosive alloying method (EEA) with the purpose of durability PBL increase.

In [39] is developed the technique of optimization EEA modes which are necessary for formation on PBL surfaces alignment coverings above specified structure.

In [40] is offered the new way of formation on PBL friction surfaces, by EEA method, the special relief which increasing reliability of work due to increase carrying capacity ability of the combined electroerosive covering (CEEC). The way is realized as follows.

On PBL working surface (Fig. 2.28), by EEA method and means of an electrode-tool, plate electroerosive covering from silver, copper and tin babbit. Thus parameters such as energy of discharge and productivity EEA get out of the Table 2.4.

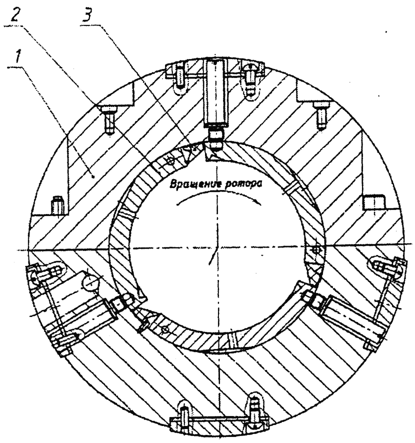


*__Fig. 2.28.__ The damping pedestal bearing, top view: 1 – bearing body, 2 – PBL, 3 – scrapers*

***Table 2.4.*** *Optimum modes EEA and layers thickness at formation CEEC of structure: silver + copper + babbit*

| № | Electrode material | Energy of discharge $W_p$, J | Productivity EEA $T$, min/cm$^2$ | Layers thickness $h_l$, mkm |
|---|---|---|---|---|
| 1. | silver | 0.2 | 1.3 | 15 |
| 2. | copper | 0.17 | 1.35 | 16 |
| 3. | babbit B 83 | 0.02 | 2.2 | 30 |

As per offered method the layers of electroerosive coverings PBL plate in different directions – lengthways, across and the least corner to a surface of the liner (Fig. 2.29).

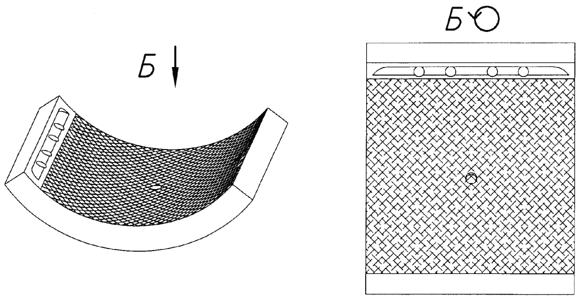


*__Fig. 2.29.__ PBL with a special microrelief of a surface*

It is necessary to note, formation of a special regular microrelief is being by process EEA.

Besides at sides and entrances edges are formed the lines of an additional microrelief (Fig. 2.30).

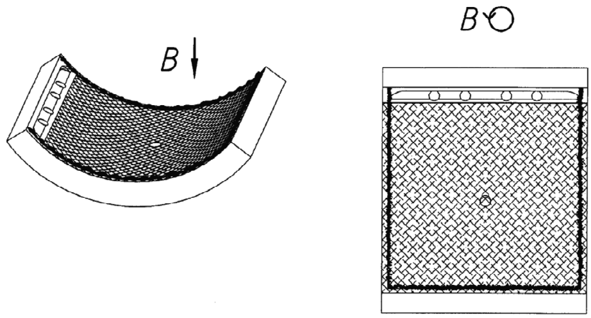


*Fig. 2.30. The bearing liner with a additional lines of microrelief*

Increase of carrying capacity is explained by curves of pressure in the bearing, where the line a – is pressure on PBL with a smooth surface before plate CEEC, b – pressure on PBL with CEEC and with the generated microrelief, c – pressure on PBL with CEEC, which is generated by a microrelief and with additional lines of a microrelief on edges (Fig. 2.31).

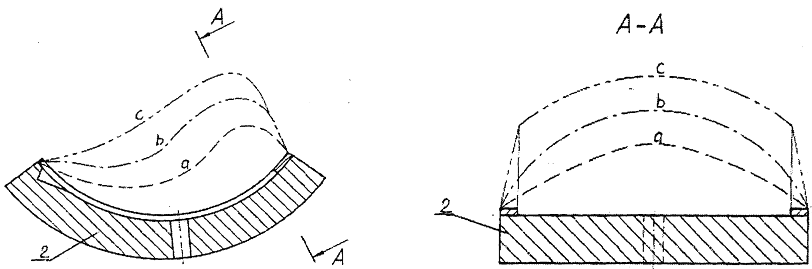


*Fig. 2.31. The curves of pressure in the sliding bearing with a different variants of manufacturing PBL*

Apparently in last variant type PBL we have upper pressure, that promotes increase carrying capacity ability

Optimization of EEA modes at CEEC plate is in detail enough described in [39] and the received optimum modes are resulted in Table 2.4.

Thus, **the purpose** of present article is EEA modes optimization for formation at sides and entrances edges PBL the lines of an additional microrelief.

## 2.4.2. TECHNIQUE OF RESEARCHES

Researches were spent on equipment EEA of model «EIL-8A» with use of samples sizes 10 x 10 x 8 mm from bronze OSC 5-5-5. Thickness of a covering layer measured by a micrometer, and a surface roughness measured on the device profilograph-roughness indicator models “201” of a factory "Calibre" by removal and processings profile records. Productivity of process (T) EEA defined as necessary time of 100% continuity coverings at surface of the sample 10 x 10 mm. At EEA bronze samples used electrodes from soft antifrictional materials: silver, copper and babbit B83.

### 2.4.3. RESULTS OF RESEARCHES

Results of dependence of a surface roughness ($R$a), layer covering thickness ($h_l$) and EEA process productivity ($T$) from energy of discharge ($W_p$), at plate babbit on bronze PBL with a covering from silver and copper, which have been generated according to modes in Table 2.4, are presented in Table 2.5. Besides in Table 2.5 are presented results of the same parameters (Ra, $h_l$ and $T$) after babbit coverings burnishing by electrode from silver at $W_p$ = 0.04 J. In this case babbit, as more fusible material, is melt and fill the grains and microroughnesses, before generated covering, reducing a roughness and thickness of a covering layer.

***Table 2.5.*** *Dependence Ra, $h_l$ and T at babbit plate on bronze samples with a covering from silver and copper with next burnishing by silver from energy of discharge $W_p$*

| Parameter | Electrode material | Energy of discharge $W_p$, J | | | |
|---|---|---|---|---|---|
| | | 0.01 | 0.02 | 0.04 | 0,1 |
| Ra, mkm | babbit B83 | 0.9 | 1.6 | 2.5 | 4 |
| $h_l$, mkm | | 20 | 30 | 41 | 48 |
| $T$, min/cm$^2$ | | 2.5 | 2.2 | 1.8 | 1.2 |
| | silver | $W_p$ = 0.04 J | | | |
| Ra, mkm | | 0.8 | 1.4 | 1.8 | 2.7 |
| $h_l$, mkm | | 19 | 28 | 35 | 39 |
| $T$, min/cm$^2$ | | 2.7 | 2.7 | 2.7 | 2.7 |

a)

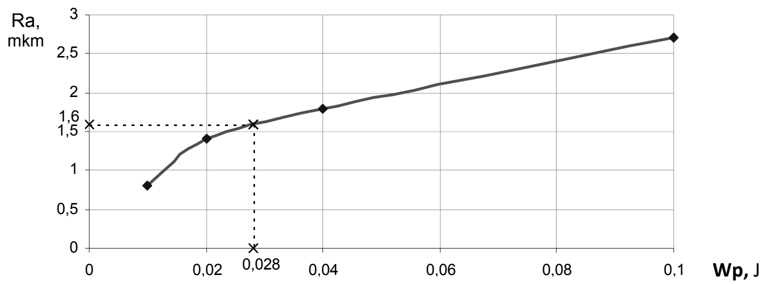


b)

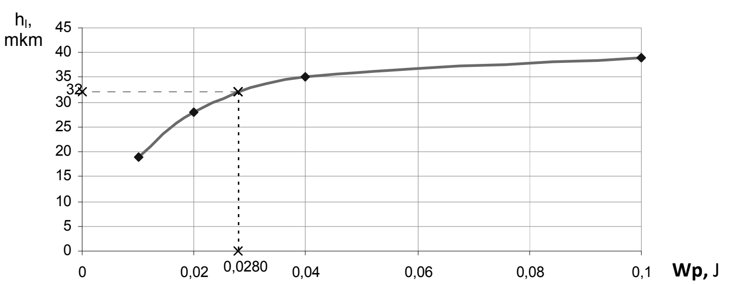


***Fig. 2.32.*** *Dependences Ra and $h_l$ from $W_p$ at silver burnishing of a bronze surface sample with CEEC from silver, copper and babbit*

On Figure 2.32 are presented dependences of a surface roughness (a) and layer thickness (b) from energy of discharge at silver burnishing of a bronze surface sample with CEEC from silver, copper and babbit.

Above the graph (Fig. 2.32) it is possible to define energy of discharge and the covering thickness which corresponds roughness Ra = 1.6 microns.

On the received energy of discharge (Fig. 2.33) we define a surface roughness (a). layer thickness (b) and productivity EEA (c) at plate a covering from babbit.

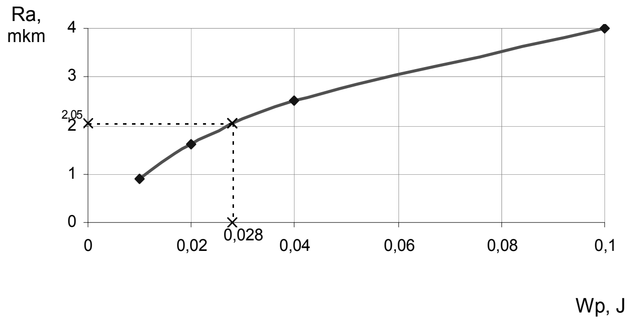


a

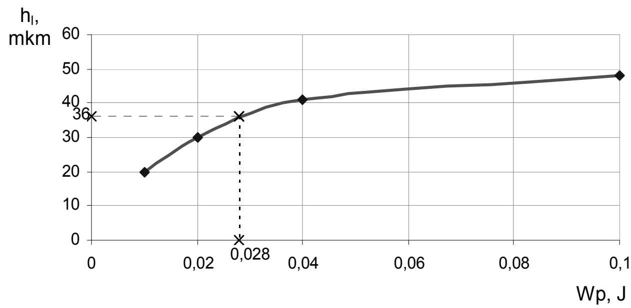


b

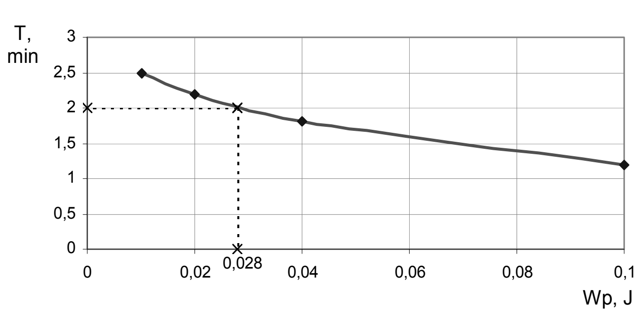


c

***Fig. 2.33.*** *Dependences a surface roughness (a), layer thickness (b) and productivity EEA (c) at plate a babbit covering from energy of discharge*

Results of the lead researches are presented in Table 2.6.

***Table 2.6.*** *Optimum modes EEA and layers thickness at formation CEEC of structure: silver + copper + babbit + silver*

| № | Electrode material | Energy of discharge $W_p$, J | Productivity EEA $T$, min/cm$^2$ | Layers thickness $h_l$, mkm |
|---|---|---|---|---|
| 1. | silver | 0.2 | 1.3 | 15 |
| 2. | copper | 0.17 | 1.35 | 16 |
| 3. | babbit B 83 | 0.028 | 2.0 | 36 |
| 4. | silver | 0.04 | 2.7 | 32 |

Thus, the technique of optimum modes definition of formation at side and entrance edges of a bronze bearing surface the lines of additional microrelief can be presented in the form of algorithm.

The essence of algorithm consists in the following:

1. Experimental dependences Ra = $f(W_p)$ and $T = f(W_p)$ are by defined at EEA bronze by silver.
2. Under dependence Ra = $f(W_p)$ graph is defined the optimum energy of discharge $W_p$ corresponding roughness Ra = of 1.6 microns.
3. Under dependence $T = f(W_p)$ graph we define productivity EAA, which corresponds optimum energy of discharge $W_p$.
4. By experimental we define dependences Ra = $f(W_p)$ and $T = f(W_p)$ at EEA plate silver by copper.
5. Under dependence Ra = $f(W_p)$ graph is defined the optimum energy of discharge $W_p$ corresponding roughness Ra = of 1.6 microns.
6. Under dependence $T = f(W_p)$ graph we define productivity EAA, which corresponds optimum energy of discharge $W_p$.
7. By experimental we define dependences Ra = $f(W_p)$ and $T = f(W_p)$ at EEA plate silver by babbit B83.
8. Under dependence graph Ra and $h_l$ from $W_p$, at silver burnishing of a bronze surface sample with CEEC from silver, copper and babbit we can define energy of discharge and thickness of a covering which corresponds to roughness Ra = 1.6 microns.
9. On the received energy of discharge we define productivity EAA and layers thickness at plate a covering from babbit.

Conclusions:

On the basis of the lead researches it is possible to draw following conclusions:

1. The technique and the algorithm is developed of optimum modes definition of formation at side and entrance edges of a bronze bearing surface the additional microrelief consisting of the combined electroerosive covering of structure is made: silver + copper + babbit + silver.
2. The thickness of the combined electroerosive covering, which corresponding electroerosive alloying optimum modes is defined.

# 2.5. LASER PROCESSING OF HIGH STRENGTH ALUMINIUM ALLOYS VIA ADDITIVE MANUFACTURING TECHNIQUE

*Konrad Bartkowiak, Norbert Radek*

## 2.5.1. INTRODUCTION

Selective Laser Melting (SLM) is an additive manufacturing technology, which is capable of producing very complex 3D parts characterized by thin structural walls. This technique offers additional geometric degrees of freedom for designers compared to conventional manufacturing technologies. Unlike in milling or casting, complexity of shape is negligible as a cost factor in SLM. These preconditions might especially be capitalized on by producing topology optimized or functionally integrated lightweight parts for vehicles via SLM. Established lightweight construction materials namely in the automotive or aerospace industries are aluminium alloys with high strength-to-weight ratios. Currently only casting alloys are available for SLM, such as AlSi12 and AlSi10Mg, with tensile strengths below 355 MPa [41-44]. For example, the dimensional stability, geometric features and accuracy of AlSi10Mg parts under pre-heating and without pre-heating conditions manufactured via SLM technique were already discussed [45]. Other developments have been done with Al 6061 alloy to fabricate and characterize heat sinks [46]. This alloy has been also investigated in comparison with AlSi12. In this paper the negative phenomenon of oxide films that appeared during the SLM process has been noticed. Another report shows methods for increasing the density of parts fabricated via SLM [47]. Further developments show feasibility of manufacturing components by using copper powders [48]. In another work the analysis of mechanical properties (strength and hardness) scandium modified Al alloy in comparison with Al 7050 was investigated [49]. The literature review shows records of aluminium alloys parts manufactured by SLM, but they are mainly limited to AlSi10Mg, AlSi12, Al 6061 and Scalmalloy alloys. Review of the state-of the art in the research field has failed to show current research efforts in SLM of high-strength and super-high strength aluminium materials, but the initial work has been demonstrated [50]. It should be also mentioned here that wrought Al-alloys reach tensile strengths from 400 to 570 MPa after forming precipitations by age hardening. Laser material processing of these alloys seems to be a challenge, because they are considered hard to weld.

## 2.5.2. EXPERIMENTAL INVESTIGATIONS

The aim of this work is to investigate the opportunities of introducing novel ready blended high strength Al powder compositions to the SLM technique based on low average power Ytterbium fiber laser (IPG, YLR-200 SM). The laser source was characterized by a central wavelength of $\lambda$ = 1070 nm and a minimum laser spot size $d$ = 10 µm. The laser beam was fibre delivered to a 4 axis laser workstation (XYZ, $n$ – rotation), which is illustrated in Figure 2.34.

The powder layer thickness was varied between $s$ = 30, 60, 90, 120 and 150 µm. A commercial film applicator with gap clearance of $s$ = 30, 60, 90 and 120 µm was used for initial powder distribution experiments. To achieve a dense and homogenous powder layer with the thickness of 150 µm, a special manual powder distribution system was designed and built up. The powder layer was distributed on 50 mm x 30 mm x 1 mm Al substrate (EN AW 6082, T651). The experiments were carried out under a protective inert gas atmosphere. To achieve minimal oxygen content in the processing chamber during the laser irradiation, different positions of the argon input set-up were tested before SLM experiments. The argon atmosphere was controlled by oxygen sensor with accuracy of ±0.1% and within measuring range from 0.0 to 100.0% $O_2$ concentration.

a)

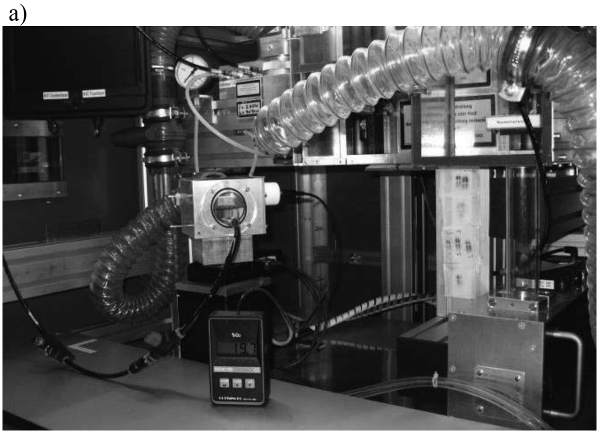

b)

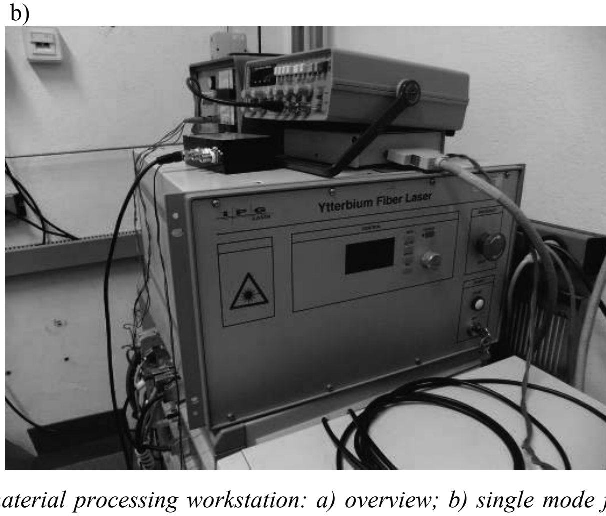


***Fig. 2.34.*** *Laser material processing workstation: a) overview; b) single mode fiber laser YLR-200 SM (IPG)*

The applied workstation was not a pure SLM machine, because it was almost impossible to automatically deposit a new powder layer on top of the solidified layer and also scan speed was limited to 250 mm/s (linear axis). In this case studies were limited to analysis of fabricated single laser track formations.

The SLM process investigations were performed on the following high strength aluminium powder alloys: EN AW 2024, EN AW 2618 and EN AW 7075. All were produced by the air atomisation method. For example, in Figure 2.35 the first mentioned Al powder is illustrated. It is cold age-hardened alloy characterized by AlCu4Mg1 composition. The powder particles have a median size between 25-45 µm. The SEM micrograph below shows spherical shape particles.

The major alloying element is copper with a content of 3.8-4 wt.%. Moreover, magnesium with 1.2-1.5 wt.% and manganese with 0.3-0.4 wt.% are also included. This alloy is distinguished by a good strength/mass ratio, high static and dynamic strength and a good fatigue resistance. It shows for the heat treatment condition T4 a tensile strength of Rm = 460 MPa and a hardness of about 126 HV. This is a commonly used alloy in the aerospace sector [51].

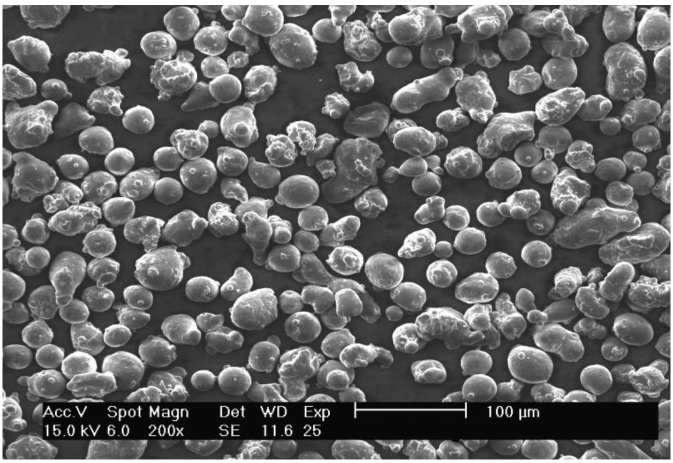


***Fig. 2.35**. SEM micrograph of aluminium alloy powder Al 2024*

In Figure 2.36 Al 2618 alloy powder is illustrated. The particles are characterized by spherical shape and grain size of 25-45 µm, which is similar to the previous Al 2024 powder. The major alloying elements of this aluminium alloy are copper with 1.5-2.7 wt.% and magnesium with 1.3-1.8 wt.%. Other included elements are iron with 0.9-1.3 wt.% and nickel with 0.9-1.2 wt.%. It is hot age-hardened material characterized by AlCu2Mg1.5Ni composition. This alloy is distinguished by a high tensile strength and by high temperature strength. The achievable tensile strength value is Rm = 440 MPa within the hardness about 120 HV, which is related to the heat treatment condition T6. It is mainly used for applications in the aerospace sector, engineering and turbine constructions [51].

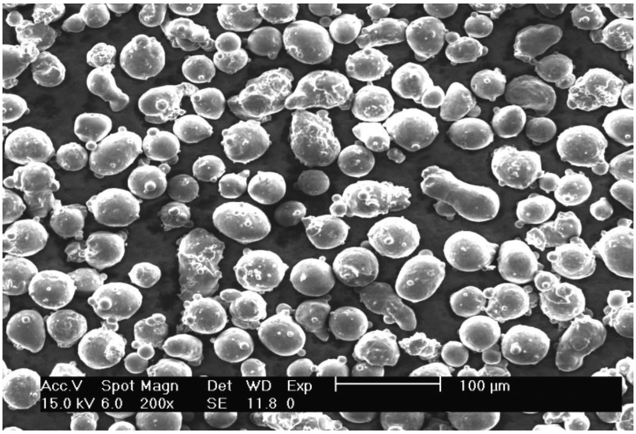


***Fig. 2.36.*** *SEM micrograph of aluminium alloy powder Al 2618*

In Figure 2.37a SEM micrograph of Al 7075 alloy powder is show. The chemical composition of this hot age-hardened alloy is AlZn5.5MgCu. In this alloy the main addition is zinc with 5.1-6.1 wt.%. Further important components are magnesium with 2.4-2.9 wt.%, copper with 1.2-2.0 wt.% with less than 0.5 wt.% of the other elements. The powder has a median particle size between 25-45 µm. It was noticed that Al 7075 powder is characterized by more longitudinal shape particles in comparison with the previous analysed Al-Cu powders (Al 2024 and Al 2618). EN AW 7075 is a super-high-strength aluminium alloy, which achieves a tensile strength of Rm = 570 MPa. The hardness of this material reached values about 170 HV (heat treatment condition T6). There are many industrial applications because of the good mechanical properties. This alloy can be successfully applied in the space, defence, automotive industry where its use in lightweight constructions should be taken into account [51].

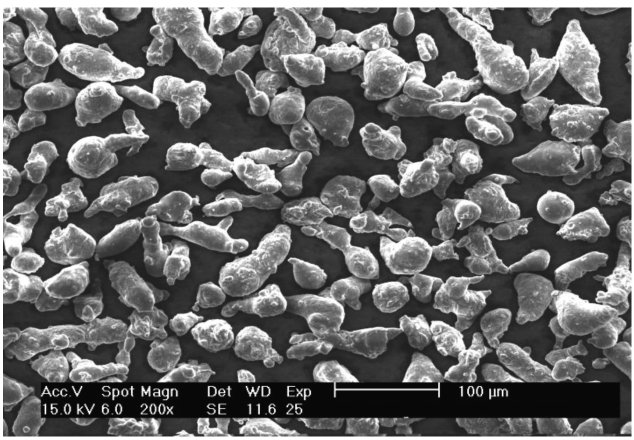


***Fig. 2.37.*** *SEM micrograph of aluminium alloy powder Al 7075*

After laser material processing of reactive Al metal powders, metallographic micro-sections of a number of samples were prepared. The sections were taken perpendicular and longitudinally to the fabricated tracks and to the direction of the laser beam displacement on the sample. The macroscopic visual observation of the single laser track formations was performed using a Leitz Aristomet microscope and the Keyence VHX-1000. To get a higher magnification of the microstructure, some chosen samples were investigated under the Scanning Electron Microscope (SEM, Philips XL 30). The micro-hardness (HV 0.002) was measured using a Fischerscope HCU micro-hardness tester. Micro-hardness distributions through the cross-section depth of the fabricated tracks were then determined.

Metallographic results are presented and discussed below. For example in Figure 2.38 a fabricated single laser track formation of Al2024 is illustrated. The first picture shows a longitudinal micro-section (Fig. 2.38a). It was observed that manufactured laser track formation was almost fully fused to the substrate.

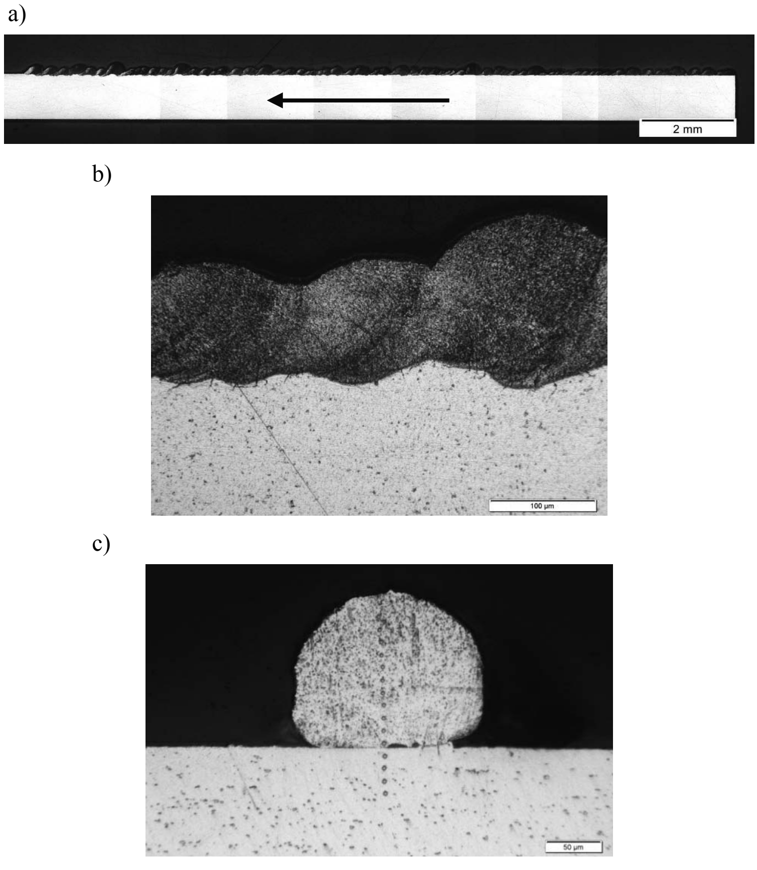


*Fig. 2.38.* *EN AW 2024 single laser track formation on EN AW 6082 substrate after SLM process: a-b) micrograph of longitudinal micro-section; c) micrograph of perpendicular micro-section after micro-hardness measurement. Applied laser processing parameters: P = 108 W, v = 30 mm/s, d = 40 µm, p (Ar) = 1 bar, s = 150 µm*

However some interruptions by imperfections and an irregular weld seam were noticed. The black arrow marked on the sample (Fig. 2.38a) shows direction of the laser beam displacement on the sample.

The micrographs taken at higher magnification (Fig. 2.38b) illustrate this shape more clearly. The dark appearance of the molten structure depends upon etching time. The presented micrographs above show a dense and pore-free structure of the single laser track formation. The structures visible as black shapes suggest that there are some cracks. However, further investigations proved that these structures belong to the grain boundaries. In Figure 2.38c a micrograph of a single laser track formation after the micro-hardness measurement is depicted. In following Figure 2.39 the results of the micro-hardness measurement of a melted single laser track formation are shown. In this case the introduced energy per length to the processed sample was 1.32 J/mm. The micro-hardness of the Al 2024 fabricated structure is 178 ±6.5 HV0.002, which is ca. 50 ±13.8 HV 0.002 higher than the substrate. The Al 2024 micro-hardness is also 52 HV 0.002 higher than conventionally semi-manufactured parts mentioned in the literature [51].

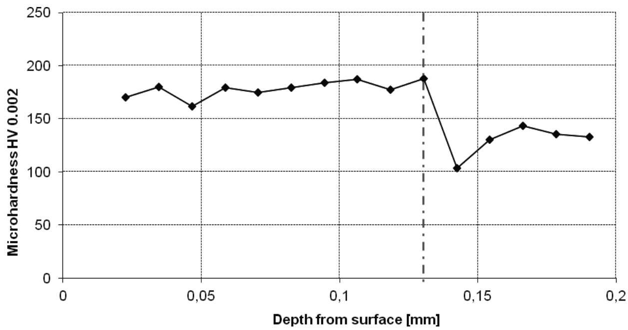


***Fig. 2.39.*** *Micro-hardness distribution (HV 0.002) of EN AW 2024 single laser track formation on EN AW 6082 substrate after SLM process. Applied laser processing parameters: P = 98 W, v = 75 mm/s, d = 40 µm, p(Ar) = 1 bar, s = 150 µm*

The other sample of Al 2618 single laser track formation after SLM process is illustrated in Figure 2.40. the first micrograph (Fig. 2.40a) shows an overview of the longitudinal micro-section.

The fabricated single laser track formation is characterized by irregular weld seam. However there are no cracks observed. The fabricated track shows very little marginal porosity (Fig. 2.40b). In Figure 2.40c a micrograph of single laser track formation after the micro-hardness measurement (perpendicular micro-section) is presented. In the following Figure 2.41 the micro-hardness distribution of Al 2618 single laser track formation is depicted. In this case an increase of the micro-hardness after SLM processing was also noticed. Applied energy per length to the workpiece was about 1.61 J/mm. The measured values are 232 ±11 HV 0.002, which is about 62 HV 0.002 higher than parts mentioned in the literature than the standard conventionally semi-manufactured wrought parts after heat treatment T6 [51].

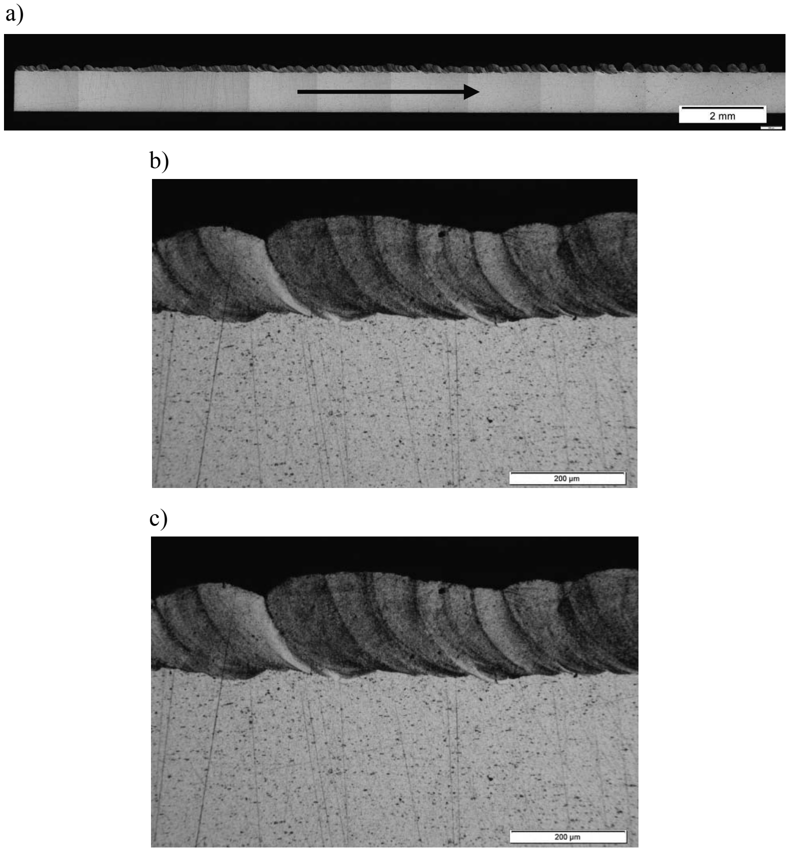


*Fig. 2.40.* EN AW 2618 single laser track formation on EN AW 6082 substrate after SLM process: a-b) micrograph of longitudinal micro-section; c) micrograph of perpendicular micro-section after micro-hardness measurement. Applied laser processing parameters: P = 128 W, v = 100 mm/s, d = 40 µm, p(Ar) = 1 bar, s = 150 µm

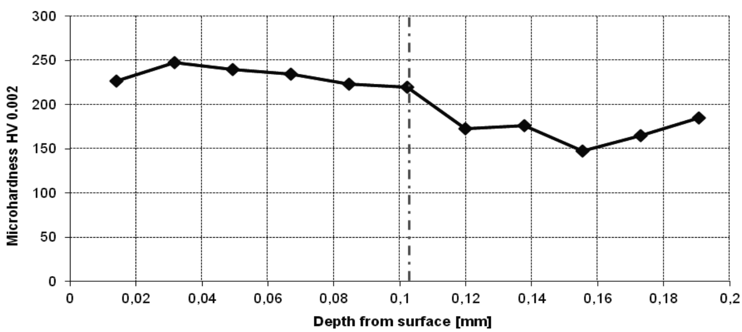


*Fig. 2.41.* Micro-hardness distribution (HV 0.002) of EN AW 2618 single laser track formation on EN AW 6082 substrate after SLM process. Applied laser processing parameters like in Figure 2.40

In Figure 2.42 the other sample of Al 7075 single laser track formation after SLM process is illustrated. The first micrograph (Fig. 2.42a) shows an overview of the longitudinal micro-section. In this case the fabricated laser track was fully fused to the substrate material. In this case good weld seam was produced. In Figure 2.42b the micrograph of longitudinal micro-section under higher magnification is presented. This picture shows that the fabricated track is characterized by a good density, pore and crack free structure. A micrograph of the perpendicular micro-section of the single laser track formation shows a fully fused track to the substrate (Fig. 2.42c). The results of the micro-hardness distribution are depicted in Figure 2.43. In this case the applied energy per length to the work piece was 0.944 J/mm. This sample is characterized by micro-hardness of 207 ±15 HV 0.002, which is about 75 HV 0.002 higher than conventionally semi-manufactured parts mentioned in the literature [51].

a)

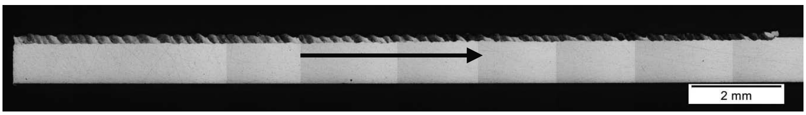


b)

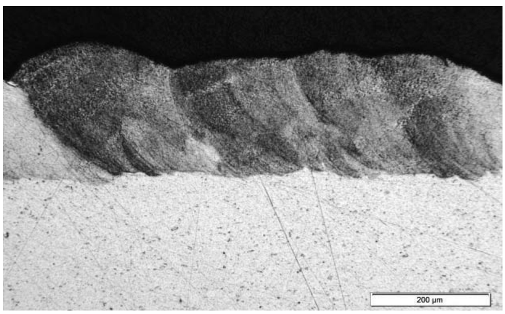


c)

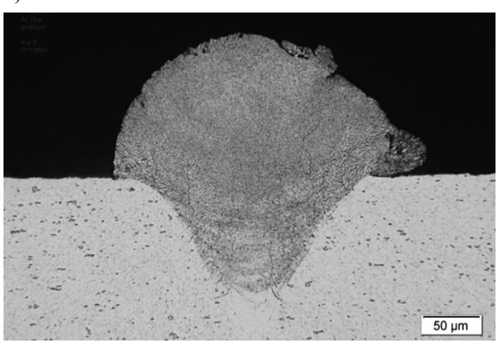


***Fig. 2.42.*** *EN AW 7075 single laser track formation on EN AW 6082 substrate after SLM process: a-b) micrograph of longitudinal micro-section; c) micrograph of perpendicular micro-section. Applied laser processing parameters P = 118 W, v = 125 mm/s, d = 40 µm, p(Ar) = 1 bar, s = 150 µm*

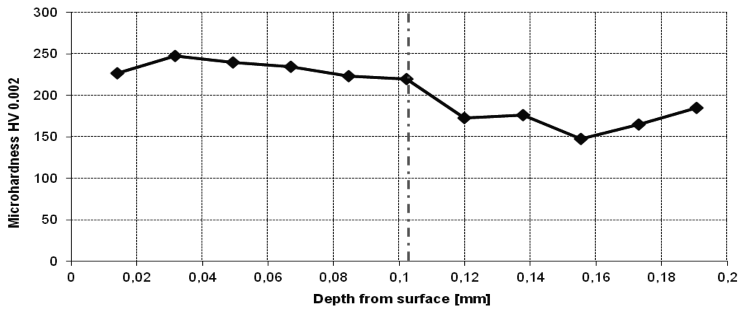


***Fig. 2.43.*** *Micro-hardness distribution (HV 0.002) of EN AW 7075 single laser track formation on EN AW 6082 substrate after SLM process. Applied laser process parameters: P = 118 W, v = 125 mm/s, d = 40 μm, p(Ar) = 1 bar , s = 150 μm*

Conclusions:

Based on empirical tests including hardness measurement, observation under a microscope as well as observations of powders/samples of high strength aluminium alloys EN AW 2024 (Al 2024), EN AW 2618 (Al 2618) and EN AW 7075 (Al 7075) using scanning electron microscope (SEM), it can be stated that:

1. Metallographic analysis demonstrates a crack free and dense microstructure of fabricated single track formations. Especially, the ready blended powder alloys, which contains zn element (al 7075) are characterized by a crack free structure and no porosity.
2. The analysis also indicates that there is no brittle hard oxidation upper layer, which could be a problem for further development of multi-layer additive manufacturing process of reactive materials.
3. Micro-hardness measurements indicated the mechanical properties of the fabricated structures. Laser processing al powder alloys are characterized by much higher hardness values in comparison with conventional fabricated parts compared with declared data in the standard literature [51]. Hardness, as a result of laser processing, of alloy en aw 2024 increased from a level of 129 ±19 hv 0.002 to a level of 178 ±6 hv 0.002 (increase of 38%). The hardness of the slm processed zones of the alloy en aw 2618 was increased from a level of 170 ±18 hv 0.002 to a level of 232 ±11 hv 0.002 (increase of 36%). Micro-hardness measurements of the en aw 7075 single laser track formations shows an increase from a level of 132 ±23 hv 0.002 to 207 ±15 hv 0.002 (increase of 57%).
4. More accurate analysis of the micro-structures could give information on the exact composition of content of the slm processed track formation. Edx analysis could show the precise amount of the solidified alloying elements and their distribution.
5. The determined laser material processing parameters window can be used for further developments. Obtained results give fundamental information about laser material processing of the new al-cu and al-zn powder

compositions. The experimental data can be applied to further research of the slm process in order to fabricate 3d samples based on high strength and super-high strength aluminium alloys.

# 2.6. ANTIWEAR LAYERS WC-Co CARRIED OUT ON DIAMOND – IMPREGNATED SEGMENTS FOR CIRCULAR SAWING OF HARD MATERIALS

*Joanna Borowiecka-Jamrozek*

## 2.6.1. DIAMOND-IMPRENATED SEGMENTS

Detonation spraying is a thermal spray process whereby high density, hard and high adhesion coatings can be deposited on a substrate material in order to increase its resistance to wear [52-54]. The process consists in using repeated gas explosions to heat and accelerate particles of a suitable powder material through a detonation gun barrel and to throw them at a high velocity onto the substrate located adjacent to the outlet of the barrel [55]. By careful pre-treatment of the substrate surface and control of the spraying regimes it is possible to deposit metallic coatings of a predetermined thickness and microstructure [56].

The main objective of the present work is to implement the detonation spraying technology to reinforce the sides of uniform diamond-impregnated segments located on the circumference of circular saw blades used for cutting natural stone, concrete, brickwork and other ceramic materials.

The diamond-impregnated segments are exclusively produced by powder metallurgy in a variety of shapes and internal structures that may greatly affect the tool life and its cutting behavior [57, 58]. Although uniform and simple-shaped segments are cheaper to manufacture, the application requirements often justify selection of complex designs. A three-layer (sandwich type) structure of segments has been found the best choice for most of the circular sawing applications. As the outer layers differ from the inner one in their susceptibility to wear a desirable saddle-like wear profile is being developed at work on the working face of each segment (Fig. 2.44) which imparts a self-guiding characteristic to the saw blade and prevents it from deviating in the cut.

The sandwich structure of the segment is produced by cold pressing the three layers of suitably prepared diamond grit-matrix powder mixtures. The green segments are subsequently hot pressed to near-full density in graphite moulds [57, 58].

As the production of thin sandwich segments for small saw blades is arduous and expensive the application of detonation spraying to reinforce the sides of uniform segments by deposition of wear resistant WC-Co coatings has been proposed as an alternative technology.

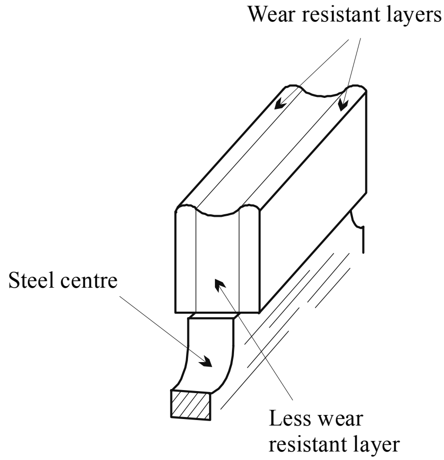


***Fig. 2.44.*** *Wear pattern of a sandwich type diamond-impregnated segment*

## 2.6.2. EXPERIMENTAL PROCEDURE

A commercial *Extrafine* cobalt powder (Umicore, Belgium), having Fisher sub-sieve size of around 1.5 µm, was used to manufacture the target material for the detonation spraying experiments. The powder is shown in Figure 2.45.

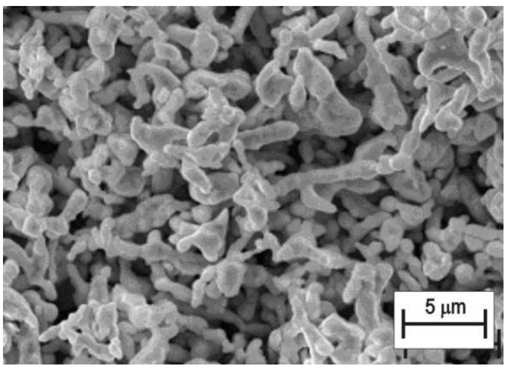


***Fig. 2.45.*** *Extrafine cobalt powder*

The substrate specimens were prepared by means of hot pressing the cobalt powder in a graphite mould at 850ºC for 2 minutes under a pressure of 35 MPa. Portions of WC-8wt% Co powder, having a narrow range of particle sizes between 22-45 µm, were repeatedly ejected at 4 Hz for 6 minutes from a 580 mm barrel at a velocity of around 1000 m/s to be deposited on the cobalt target positioned 300 mm head of the barrel outlet.

The coated specimens were subsequently used to prepare metallographic transverse sections for metallographic examination by means of scanning electron microscopy and light microscopy (LM), as well as for microhardness tests.

### 2.6.3. RESULTS AND DISCUSSION

A typical microstructure of the WC-8%Co coating deposited on a cobalt substrate is presented in Figures 2.46 and 2.47. The average coating thickness after 6 minutes of detonation spraying was estimated at 40.3 ±11.4 μm.

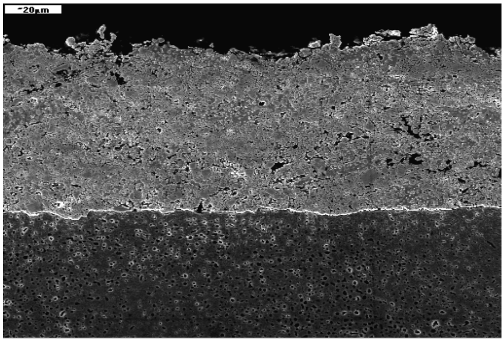

***Fig. 2.46.*** *Thickness of WC-8%Co coating after 6 minutes of detonation spraying at 4 Hz*

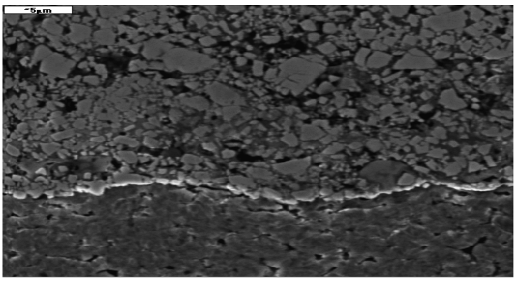

***Fig. 2.47.*** *SEM micrograph showing good coating adhesion to the substrate*

Figures 2.48 and 2.49 show microhardness impressions of the Vickers diamond pyramid left on the surfaces of the coating, the substrate material and at the interface area. As it is evident from Figure 2.48 the sub-surface layer of the cobalt substrate was strain hardened by the coating powder particles colliding with the target at high velocities. Thus the microhardness of cobalt in the close proximity with the coating increased to around 280 $HV_{0.05}$ and was markedly higher than the average Vickers microhardness number of the as-hot pressed material which was 161 $HV_{0.05}$. The microhardness of the coating was ranging between 770 and 796 $HV_{0.05}$.

The experimental work has shown that, by the correct selection of the process parameters, it is possible to deposit hard and good adhesion WC-8%Co coatings on a PM cobalt substrate by means of detonation spraying in a relatively rapid and cost effective manner. With detonations initiated at 4 Hz the coating thickness increases by 7-8 μm per minute. By observing the shape of the diamond pyramid impressions in the coating it is clearly seen that the coating is characterised by a relatively high toughness and is firmly bonded to the target surface.

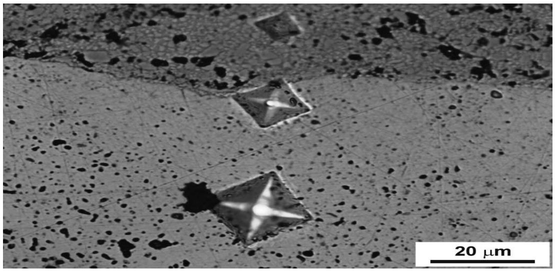


***Fig. 2.48.*** *Vickers microhardness impressions in the substrate and in the coating*

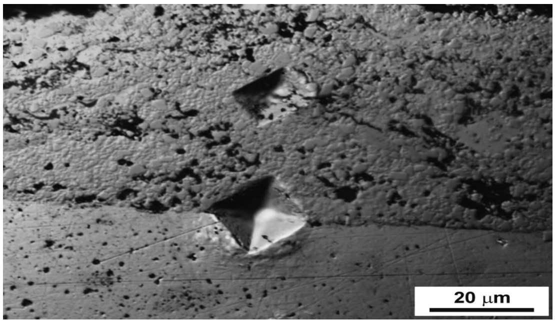


***Fig. 2.49.*** *Vickers microhardness impressions in the coating and at the boundary between the substrate and the coating*

Conclusions

The main conclusions of the present work on detonation spraying of WC-8%Co coatings on PM cobalt substrate may be described as follows:

1. The coating deposition rate at the firing frequency of 4 Hz ranges between 7-8 μm/min. The local coating thickness may differ up to ±25% from its mean value.
2. The coatings have a porous microstructure. Their microhardness ranges between 770-796 $HV_{0.05}$.
3. The process of coating deposition induces, by its nature, a considerable strain hardening of the sub-surface layer of the cobalt substrate.
4. The absence of microcracks around the impressions left by a Vickers diamond pyramid testifies to good ductility of the coatings.
5. The absence of decohesion induced by forcing a Vickers diamond pyramid between the substrate and the coating testifies to good adherence of the coating to the substrate.

Currently, coating powders containing up to 20wt% Co are being deposited on cobalt in order to decrease the porosity level in the coating and thereby to increase its hardness. Additionally, investigations are underway into implementation of techniques that would enable quantitative evaluation of the level of coating adhesion to the substrate.

# 2.7. SHAPE MEASUREMENTS OF SURFACES WITH GEOMETRICAL TEXTURE MADE ON SiC RINGS

*Piotr Sęk, Bogdan Antoszewski*

## 2.7.1. LASER SURFACE TEXTURING (LST)

Current technology has very high requirements for reliability, durability and performance of sliding friction pairs. For that reason new technologies were developed for forming and shaping the micro and macrogeometry of sliding surfaces. Thats why the manufacturing of surface geometrical texture became so important. Geometrical surface texture are regular, repeatable micro geometrical formations on the surface like micropores, grooves or cavities. The application of surface texturing has influence on:

- reducing the friction resistance both during movement and in rest state,
- widens the range of permissible values of friction node loads,
- assures a lower temperature of friction node in comparison to untextured one,
- restricts the wear and tear of friction pair elements,

can be beneficial with other wear types like for example with fretting [59-61].

Laser surface texturing belongs to group of technologies called laser microprocessing and is recommended everywhere where one wants to obtain high performance and precision. Laser surface texturing is a technology of giving surface chosen geometrical shape and properties.

Laser beam, as an electromagnetic wave is koherent, allows high concentration of energy. In laser microprocessing the area of laser influence on material is defined by the size of laser beam dot or mask wich allows processing of only uncovered parts of material. In cases where while processing we need high surface energy density, several different optical elements are used for focusing the laser beam.

Laser beam of diameter $D$ and wave lenght of $\lambda$ theoreticaly can be focused in focal point, wich minimal diameter depends on occurring of the phenomena of diffraction and its given by formula:

$$d = 2.44\frac{f}{D}\lambda \tag{2.21}$$

where: $f$ – FD of used optical focusing element.

Wave length $\lambda$ is essential not only because of possibility to obtain high focus of laser beam, but also because of possibility of absorbing the radiation by processed material. In laser microprocessing very crucial is the aspect of duration of laser pulse, because depending on exposure time and intesification of laser radiation we can use different methods of influence on processed material. Pulses of duration over 1 ns are called long pulses. In case the pulses last from 1 ps to 1 ns they are called short, and impulses with duration shorter then 1 ps are called ultrashort pulses.

Laser material processing using long pulses leaves explicit marks of melting and changes in material structure due to heat influence. Ablation caused with pikosecond and femtosecond is cold the cold ablation, because in the processed material we cant observe the area of heat influence in its traditional meaning.

When producing surface geometrical texture, identification of obtained structures and their physical properties is a crucial step. This paper analyses methods of topography measurements.

Surface geometrical texture due to its regularity can be easily described using few mathematical values like: total operations area ($A_n$), summary area of all made modifications ($A_t$), area of single modification ($a_t$),distance between micropores centers ($L$), micropore diameter($d$) and micropore density ($S_p$), wich is the ratio of $A_t/A_n$.

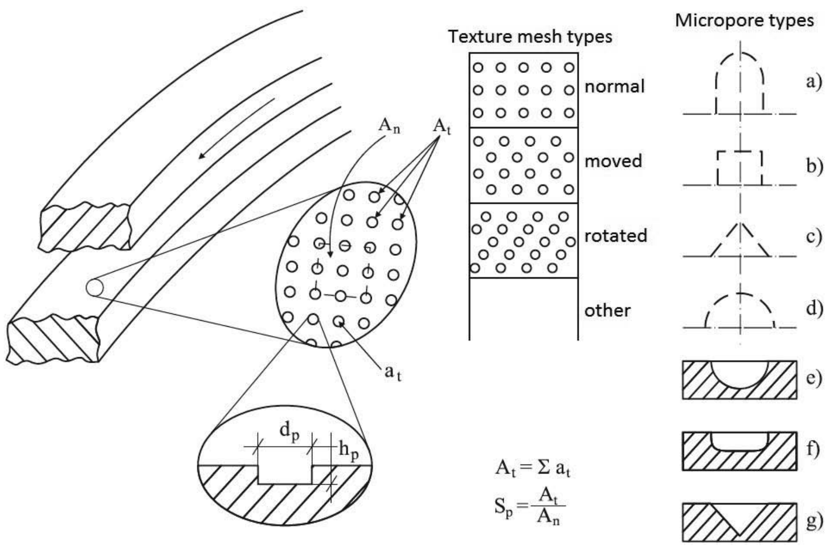


***Fig. 2.50.*** *Values characterizing surface geometrical textures and types of textures*

## 2.7.2. TEST OBJECTS

The tests were conducted on surface geometrical textures made on SiC rings of dimensions 35 x 25 x 7. Geometrical texture was made using laser device ESI *Model 5200 μVIA DRILL.* Its a Nd:YAG laser, diode pumped with maximal beam power 2 W, emitting ultraviolet radiation of wave lenght 355 nm. Other crucial laser parameters are impuls width 30 ns for 3 kHz, frequency 100 Hz÷20 kHz. Laser is equipped with scaner optics of working area 533 mm x 635 mm. Micropores were made using standard scaner software. Surface texturing procedure consisted of two steps, firstly puncture eroding over a spiral and second profiling the micropore with laser beam of diameter equal to assumed.

Table 2.7 shows obtained surface texture parameters and on Figure 2.51 shows an example view obtained using Scanning microscope.

*Table 2.7. Studied surface texture parameters*

| Sample no. | Micropore diameter $d$ [μm] | Distance between micropores centers $L$ [μm] | Micropore depth [μm] | Micropore density [%] |
|---|---|---|---|---|
| 1 | 78 | 162 | 13 | 18.2 |
| 2 | 134 | 279 | 13 | 17.9 |
| 3 | 78 | 106 | 13 | 42.5 |
| 4 | 134 | 183 | 13 | 41.8 |
| 5 | 150 | 256 | 13 | 27.4 |
| 6 | 70 | 119 | 13 | 27.1 |
| 7 | 102 | 128 | 13 | 49.9 |
| 8 | 102 | 233 | 13 | 15.1 |
| 9 | 102 | 174 | 13 | 26.9 |
| 10 | 102 | 174 | 13 | 26.9 |

a) b)

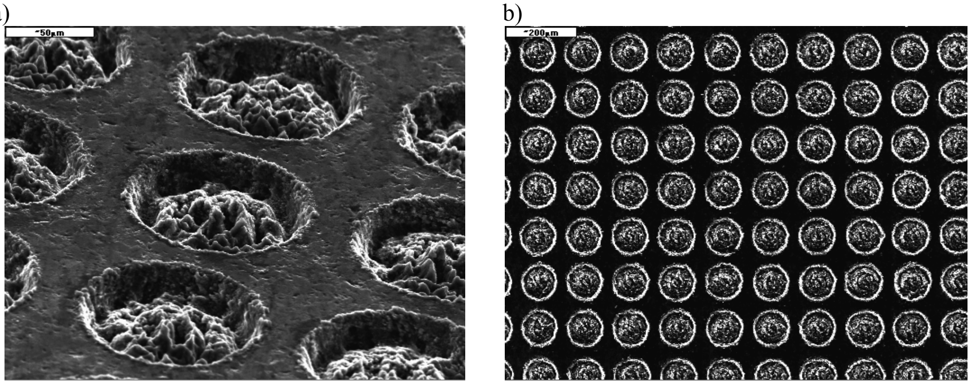

***Fig. 2.51.*** *View of surface geometrical texture on SiC ring a) view of single micropore (zoom 500x), b) view of studied surface (micropore density 42%, zoom 100x)*

## 2.7.3. RESEARCH METHODOLOGY

The aim of research was identification of capabilities of modern digitalized profilometers. All measurement were made in Laboratory of Computer Geometrical Dimension Measurements on Kielce University of Technology using contact profilometer Form Talysurf PGI 1230 and optical profilometer Talysurf CCI – Lite Non-contact 3D Profiler with 50 mm lens. Measurement using AFM method was not possibile due to to wide dimensions of tested sample and too high roughness of micropores bottom. Next pictures (Fig. 2.52-2.57) show chosen measurements results.

***Table 2.8.*** *Merits and flaws of optical and contact profilometers*

| | **Merits** | **Flaws** |
|---|---|---|
| **Contact measurement** | – No unmeasured spots<br>– High probing density (0.125 mm)<br>– Surface parameters don't influence the measurement results | – Measurement of low toughness material is not possible<br>– Long time of 3D measurement<br>– High level of own murmur |
| **Optical measurement** | – No interaction with studied surface<br>– Low level of own murmur<br>– Very quick measurement<br>– High resolution on Z axis – 10pm | – High influence of studied surface optical properties on measurement results<br>– Weak penetration of measured surface ("optical needle" angle of 120 degrees)<br>– False results when measuring surfaces with sharp edges<br>– Low resolution on X/Y axis |

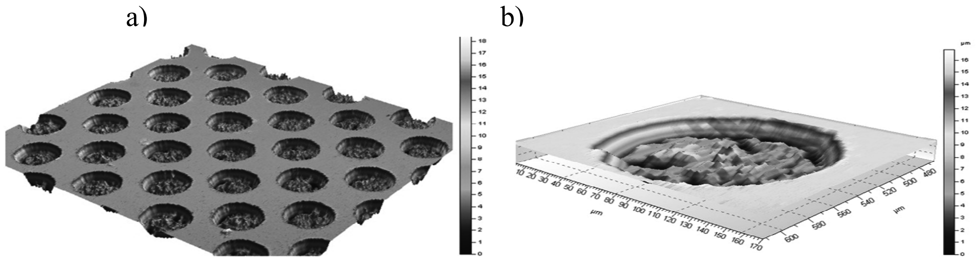


***Fig. 2.52.*** *a) 3D view of studied surface, b) 3D view of single micropore obtained using contact profilometer Form Talysurf PGI 1230*

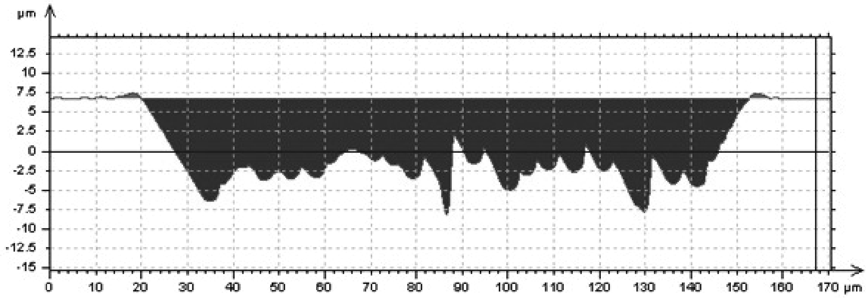


***Fig. 2.53.*** *Profile of single micropore obtained using contact profilometer Form Talysurf PGI 1230. Maximum micropore depth 14.9143 µm, maximum outflow height 0.7297 µm, total micropore volume 122376.6 µm$^3$, outflow volume 508.146 µm$^3$*

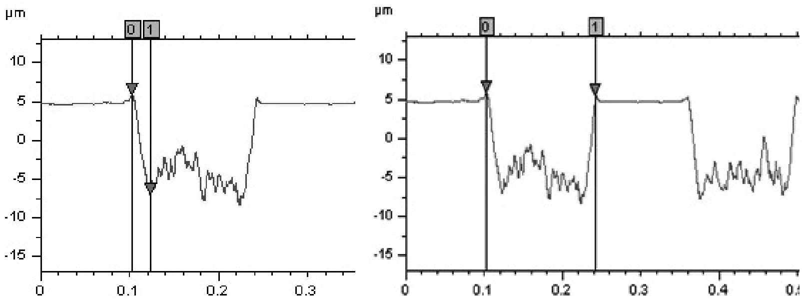


*__Fig. 2.54.__ Profile of single micropore obtained using contact profilometer Form Talysurf PGI 1230. Micropore diameter 140.001 µm, slope angle 31.6116°*

a) b)

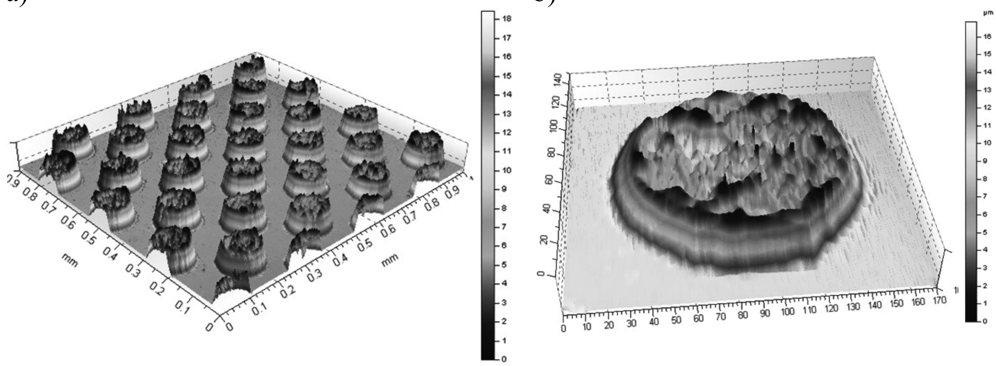


*__Fig. 2.55.__ a) 3D view (reverse) of studied surface obtained using contact profilometer Form Talysurf PGI 1230 b) 3D view (reverse) of single micropore obtained using contact profilometer Form Talysurf PGI 1230*

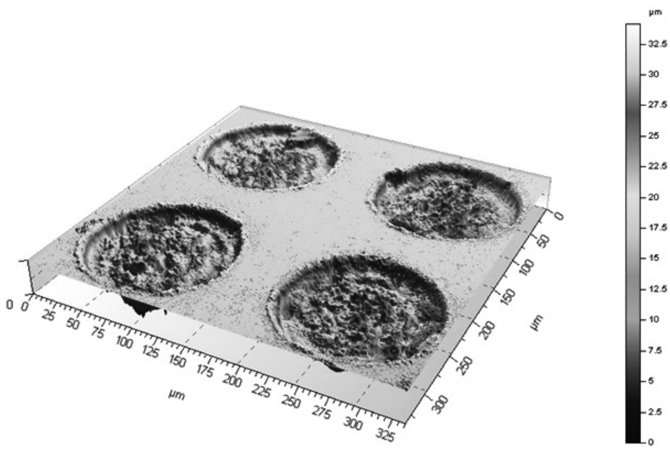


*__Fig. 2.56.__ 3D view of surface obtained using optical profilometer Talysurf CCI – Lite Non-contact 3D Profiler with 50 mm lens*

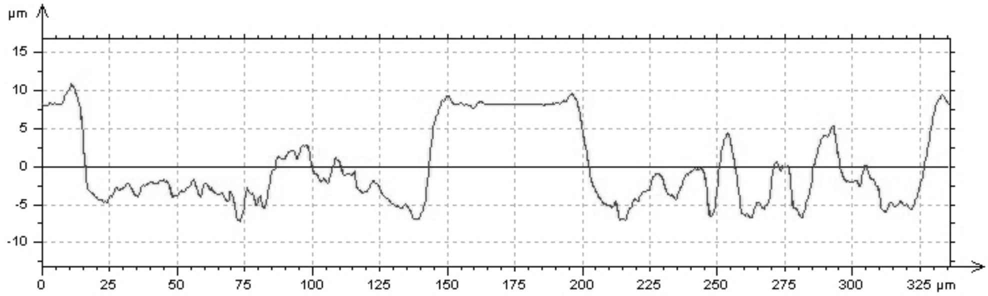


***Fig. 2.57.*** *Profile of two micropores obtained using optical profilometer Talysurf CCI – Lite Non-contact 3D Profiler with 50 mm lens*

Conclusions:

1. Analised measurement methods using optical and contact profilometers can be used for measuring surface texture parameters.
2. By using optical and contact profilers one can measure the diameter and depth of micropores, distance between them, angle of slope, roughness, coarseness of micropores bottom, outflows height, relation between outflows volume and micropores total volume.
3. Results can be used for optimalization of surface texture geometry.
4. Results can be used for choosing a laser device with suitable wave lenght in order to upgrade the precision of laser discreet processing.

## REFERENCES


[1] Krakowiak S.: *Korozja wżerowa stali stopowych*. Wydawnictwo Politechniki Gdańskiej, Gdańsk 2007.

[2] Przybyłowicz K.: *Metaloznawstwo*. WNT, Warszawa 1992.

[3] Surowska B.: *Wybrane zagadnienia z korozji i ochrony przed korozją*. Wydawnictwo Politechniki Lubelskiej, Lublin 2002.

[4] Baszkiewicz J., Kamiński M.: *Korozja materiałów*. Oficyna Wydawnicza Politechniki Warszawskiej, Warszawa 2006.

[5] Leçe H.D., Emregül K.C., Atakol O.: *Difference in the inhibitive effect of some Schiff base compounds containing oxygen, nitrogen and sulfur donors*. Corrosion Science, 50 (2008), pp. 1460-1468.

[6] Wang L.: *Inhibition of mild steel corrosion in phosphoric acid solution by triazole derivatives.* Corrosion Science, 48 (2006), pp. 608-616.

[7] Cruz J., Martinez R., Genesca J., Garcia-Ochoa E.: *Experimental and theoretical study of 1-(2-ethylamino)-2-methylimidazoline as an inhibitor of carbon steel corrosion in acid media.* Journal of Electroanalytical Chemistry, 566 (2004), pp. 111-121.

[8] Jacob K.S., Parameswaran G.: *Corrosion inhibition of mild steel in hydrochloric acid solution by Schiff base furoin thiosemicarbazone*. Corrosion Science, 52 (2010), pp. 224-228.

[9] Prabhu R.A., Venkatesha T.V., Shanbhag A.V., Kulkarni G.M., Kalkhambakr R.G.: *Inhibition effects of some Schiff's bases on the corrosion of mild steel in hydrochloric acid solution*. Corrosion Science*,* 50 (2008), pp. 3356-3362.

[10] Ali S.A., Al-Muallem H.A., Rahman S.U., Saeed M.T.: *Bis-isoxazolidines: A new class of corrosion inhibitors of mild steel in acidic media*. Corrosion Science*,* 50 (2008), pp. 3070-3077.

[11] Bahpour M., Ghoreishi S.M., Mohammadi N., Soltani N., Salavati-Niasari M.: *Investigation of some Schiff base compounds containing disulfide bond as HCl corrosion inhibitors for mild steel. Corrosion Science,* 52 (2010), pp. 4046-4057.

[12] Li Z., Miao X., Xin H., Deng W.: *Synthesis, crystal structures, photophysical properties and self-assembly of fluorene-based bis-Schiff bases.* Materials Chemistry and Physics, 124 (2010), pp. 1105-1112.

[13] Scendo M.: *Działanie wybranych inhibitorów korozji miedzi w wodnych roztworach chlorków.* Wydawnictwo Akademii Świętokrzyskiej, Kielce 2006.

[14] Emergül K.C., Düzgün E., Atakol O.: *The application of some polydentate Schiff base compounds containing aminic nitrogens as corrosion inhibitors for mild steel in acidic media.* Corrosion Science*,* 48 (2006), pp. 3243-3260.

[15] Scendo M.: *Inhibition of copper corrosion in sodium nitrate solutions with nontoxic inhibitors.* Corrosion Science*,* 50 (2008), pp. 1584-1592.

[16] Ahamad I., Quarishi M.A.: *Mebendazole: New and efficient corrosion inhibitor for mild steel in acid medium*. Corrosion Science*,* 52 (2010), pp. 651-656.

[17] Ahamad I., Prasad R., Quraishi M.A.: *Experimental and quantum chemical characterization of the adsorption of some Schiff base compounds of phthaloyl thiocarbohydrazide on the mild steel in acid solutions.* Materials Chemistry and Physics, 124 (2010), pp. 1155-1165.

[18] Migahed M.A., Farag A.A., Elsaed S.M., Kamal R., Mostfa M., Abd El-Bary H.: *Synthesis of a new family of Schiff base nonionic surfactants and evaluation of their corrosion inhibition effect on X-65 type tubing steel in deep oil wells formation water.* Materials Chemistry and Physics, 125 (2011), pp. 125-135.

[19] Davydov A.D., Kozak J.: *Physico-Chemical Principles of Electrochemical Discharge Machining.* Surface Engineering and Applied Electrochemistry, 3, 1991, USA.

[20] Nowicki B., Spadło S.: *Brush Electro-Discharge Mechanical Machining BEDMM.* Proceedings International Symposium for Electromachinning – ISEM-11, Lausanne, Switzerland, April 1995, ISBN 2-88074-291-9, pp. 191-201.

[21] Nowicki B., Pierzynowski R. Spadło S.: *The Ectrodischarge – Based Surface Alloying Process Using Brush Electrode*. Proceedings International Symposium for Electromachinning – ISEM-12, Aachen, Germany, May 1998, pp. 289-298.

[22] Spadło S.: *Sposób obróbki gładkościowej powierzchni, zwłaszcza o złożonych kształtach*. Patent PL 172559, Departament Wydawnictw UPRP 10/97, Warszawa 1997, s. 1-4.

[23] Nowicki B., Pierzynowski R., Spadło S.: *New Possibilities of Machining and Electrodischarge of Free-Form Surfaces.* Journal of Materials Processing Technology, Vol. 109, No. 3/2001, ISSN 0924-0136, pp. 371-376.

[24] Nowicki B., Pierzynowski R., Spadło S.: *The superficial layer of parts machined by brush electro discharge mechanical machining (BEDMM).* Journal Engineering Manufacture. Vol. 218, part B, 2004, ISSN 0954-4054, pp. 9-15.

[25] Nowicki B., Pierzynowski R., Spadło S.: *Comparative Investigation Into The Brush Electrodischarge Alloying With The Electrodes Of Alloy Steel And Tungsten.* International Journal for Manufacturing Science and Technology, Vol. 4, No. 2003 (1), ISSN 1524-1548, pp. 44-54.

[26] Nowicki B., Pierzynowski R., Spadło S.: *Investigation of electro-discharge mechanical dressing (EDMD) of diamond abrasive wheels with conductive bonds using brush electrodes.* Journal Engineering Manufacture. Proc. IMechE Vol. 220, part B, 2006, pp. 421-428.

[27] Radek N., Antoszewski B.: *Influence of laser treatment on the properties of electro-spark deposited coatings.* Kovove Materialy-Metallic Materials, Vol. 47, No. 1 (2009), pp. 31-38.

[28] Radek N., Wajs E., Luchka M.: *The WC-Co electrospark alloying coatings modified by laser treatment*. Powder Metallurgy and Metal Ceramics, Vol. 47, No. 3-4/2008, pp. 197-201.

[29] Radek N.: *Determining the operational properties of steel beaters after electrospark deposition.* "Eksploatacja i Niezawodność – Maintenance and Reliability", No. 4/2009, pp. 10-16.

[30] Spadło S., Dudek D.: *Analyzing the technical characteristics of EDM tools*. Proceedings of conference 8th Europen Conference of Young Research and Scientific Workers – Transcom 2009, Žilina, pp. 193-196.

[31] Spadło S.: *The analysis of brushing tool characteristics*. Archives of Civil and Mechanical Engineering. Quarterly Polish Academy of Sciences, Committee of Civil and Mechanical Engineering, Vol. IV, No. 4/2004, ISSN 1644-9665, pp. 27-40.

[32] Spadło S.: *Teoretyczno-eksperymentalne aspekty obróbki elektroerozyjno-mechanicznej*. Monografie, Studia, Rozprawy, Z. 52, Wydawnictwo Politechniki Świętokrzyskiej, PL ISSN 0239-4979, Kielce 2006, s. 195.

[33] Spadło S.: *Selected Problems of Modeling and Control in Mechanics*. *The analysis of mechanical characteristics of filament brush tool.* ed. Adamczak S., Radziszewski L.: Monografie, Studia, Rozprawy, M. 19, Wydawnictwo Politechniki Świętokrzyskiej, Kielce 2011, pp 135-146.

[34] Kandlikar S.G., Grande W.J.: *Evolution of Microchannel Flow Passages – Thermohydraulic Performance and Fabrication Technology*. Heat Transfer Eng. 25 (2002), pp. 3-17.

[35] Piasecka M., Maciejewska B.: *The study of boiling heat transfer in vertically and horizontally oriented rectangular minichannels and the solution to the inverse heat transfer problem with the use of the Beck method and Trefftz functions.* Exp. Thermal Fluid. Sci., 38 (2012), DOI 10.1016/j.expthermflusci, 2011.11.02, pp. 19-32 (in print).

[36] Hożejowska S., Piasecka M., Poniewski M.E.: *Boiling Heat Transfer in Vertical Minichannels.* Liquid Crystal Experiments and Numerical Investigations, Int. J. of Thermal Sc., 48 (2009), pp. 1049-1059.

[37] Piasecka M., Poniewski M.E.: *Hysteresis phenomena at the onset of subcooled nucleate flow boiling in microchannels*, Heat Transfer Eng., 25 (2004), pp. 44-51.

[38] Martsynkovskyi V.S., Tarelnik V.B., Pchelintsev V.A.: *Method of plain bearings liners machining.* Patent of Ukraine № 78155 A, B23H1/00, 3/00, 5/00, Published 15.02.2007, Bulletin of inventions №2.

[39] Martsynkovskyi V.S.: *Electroerosive alloying modes optimization for formation of a wear-in coverings on bronze plain bearings liners*//Compressor and power mechanical engineering. – № 2 (8), 2007, pp. 15-22.

[40] Martsynkovskyi V.S.: *Method of plain bearings liners machining.* Patent of Ukraine № 77906, B23H1/00, 3/00, 5/00, Published 15.01.2007, Bulletin of inventions №1.

[41] Brandl E. et al.: *Additive manufactured AlSi10Mg samples using Selective Laser Melting (SLM): Microstructure, high cycle fatigue, and fracture behaviour*. Materials & Design, Vol. 34, February 2012, pp. 159-169.

[42] Buchbinder D. et al.: *Rapid Manufacturing von Aluminiumbauteilen für die Serienproduktion durch Selectives Laser Melting (SLM)*. Euro-uRapid 2007, International User´s Conference on Rapid Prototyping & Rapid Tooling & Rapid Manufacturing, December 3-4, 2007, Frankfurt.

[43] Buchbinder D. et al.: *High Power Selective Laser Melting (HP SLM) of Aluminium.* Parts: Lasers in Manufacturing 2011 – Proceedings of the Sixth International WLT Conference on Lasers in Manufacturing, 2011, pp. 271-278.

[44] Vilaro T. et al.: *Direct manufacturing of technical parts using selective laser*. Proceedings of 12$^{th}$ European Forum on Rapid Prototyping, March 5-6, 2008, Paris, France.

[45] Buchbinder D. et al.: *Generative Fertigung von Aluminiumbauteilen mit minimalem Verzug*, Fraunhofer ILT, Jahresbericht, 2008.

[46] Wong M. et al.: *Selective laser melting of heat transfer devices*. Rapid Prototyping Journal, 13 (5), 2007, pp. 291-297.

[47] Louvis E. et al.: *Selective laser melting of aluminium components*. Journal of Materials Processing Technology 211, 2011, pp. 257-284.

[48] Becker D. et al.: *Components made from copper powder open up new opportunities*, Press Release, Aachen 2011.

[49] Schmidtke K. et al.: *Process and Mechanical Properties: Applicability of a Scandium modified Al-alloy for Laser Additive Manufacturing*. Physics Procedia, Vol. 12, Lasers in Manufacturing ,2011 (LIM2011), pp. 369-374.

[50] Bartkowiak K. et al.: *New developments of laser processing aluminium alloys via additive manufacturing technique.* Physics Procedia, 2011, Vol. 12, P. 1, pp. 393-401.

[51] Ostermann F.: *Anwendungstechnologie Aluminium*. 2. Auflage, Springer-Verlag, Heidelberg, Berlin, New York 2007.

[52] Antoszewski B.: *Natryskiwanie cieplne. Metody, własności, zastosowanie.* „Mechanika", 75, s. 47-56.

[53] Sobiecki J., Ewertowski J., Babul. T., Wierzchoń T.: *Influence of Surface Preparation onthe Properties of Tungsten Carbide Coatings Produced by Gas-Detonation Method*. Materials Science Forum, 426-432 (2003), pp. 2587-2592.

[54] Hao, Du., Hua Weigang, Liu, Jiangang, Gong, Jun., Sun, Chao Wen., Lishi.: *Influence of process variable on the qualities of detonation gun sprayed WC-Co coatings*. "Materials Science and Engineering", A408 (2005), pp. 202-210.

[55] Poorman R.: US Patent 2964420, 1960.

[56] Jeziorski L., Jasiński J., Babul T., Tatar M.: *Powłoki z węglika wolframu wytwarzane metodą detonacyjną*. "Inżynieria Materiałowa", 5 (2005), s. 711-713.

[57] Konstanty J.: *Cobalt as a Matrix in Diamond Impregnated Tools for Stone Sawing Applications*. 2nd Edition, AGH UWNT, Kraków 2003.

[58] Konstanty J.: *Powder Metallurgy Diamond Tools*. Elsevier, Oxford 2005.

[59] Kovalchenko A., Ajayi A., Erdemir A., Fenske G., Etison I.: *The effect of laser surface texturing on transitions in lubrication regimes during unidirectional sliding contact.* Tribology International, 38 (2005), pp. 219-225.

[60] Manabu Wakuda, Yukihiko Yamauchi, Shuzo Kanazaki, Yoshirteru Yasuda: *Effect of surface texturing on friction reduction between ceramic and steel materials under lubricated sliding contact*. *Wear*. 254 (2003), pp. 356-363.

[61] X.Q Yu., S.He., R.L.Cai.: *Frictional characteristics of mechanical seals with a laser textured seal face.* Journal of Materials Processing Technology, 129 (2002), pp. 463-466.

# 3 WELDING TECHNOLOGIES IN SURFACE ENGINEERING

## 3.1. THE PROPERTIES AND APPLICATIONS OF ELECTRO-SPARK DEPOSITED COATINGS

*Norbert Radek*

### 3.1.1. INTRODUCTION

The origin of electrical discharge machining (EDM) dates back to 1770 when English scientist Joseph Priestly discovered the erosive effect of electrical discharges. During the 1930s, attempts were made for the first time to machine metals and diamonds with electrical discharges. Erosion was caused by intermittent arc discharges occuring in air between the tool electrode and workpiece connected to a DC power supply. These processes were not very precise due to overheating of the machining area and may be defined as „arc machining" rather than „spark machining" [1].

By controlling polarity, it is possible to remove or replace material.

The process of material removal involving erosion of the stock subjected to electric discharges is called electrical discharge machining (EDM). The surface layer forming on the product improves its operational properties [2-4].

The process of material growth resulting from electroerosion is known as electro-spark alloying (ESA) or electro-spark deposition (ESD). The erosion of the anode and the spark discharges between the electrodes result in the formation of a surface layer with properties different from those of the base material [5-6].

Electro-spark alloying is one of the methods that require concentrated energy flux. The method was first used in the USSR in the 1940s almost simultaneously with the destructive electrical discharge machining. The ESA technique was studied intensively in the 60s. In the next decade, it was commonly applied to deposit hard-melting materials on selected metals and alloys, mainly steel. Polish scientists became interested in electro-spark alloying of coatings as early as in the 80s.

Electro-spark deposition (ESD) is a cheap high-energy process. Developed in the post-war period, the technology has been frequently modified. Its main advantages are the ability to select precisely the area to be modified, the ability to select the coating thickness, which may range from several to several dozen micrometers, good adhesion of a coating to the substrate, and finally, cheap and simple equipment for coating deposition.

The processes of coating formation on metal parts including electro-spark deposition involve mass and energy transport accompanied by chemical, electrochemical and electrothermal reactions. Today, different electro-spark deposition techniques are used; they are suitable for coating formation and surface microgeometry formation [7-9].

Coatings produced by electro-spark deposition are applied:

- to protect new elements,
- to recover the properties of worn elements.

Electro-spark alloying is becoming more and more popular as a surface processing technology. Electro-spark deposited coatings are frequently applied in industry, for example, to produce implants or cutting tool inserts. The coatings are deposited with manually operated equipment or robotized systems.

Research on this technology is being conducted all over the world, and the companies interested in applying it include NASA and the US Navy [10-11].

As electro-spark coatings are reported to be resistant to wear and corrosion, they can be applied, for instance, to:

- ship propeller components,
- casting moulds,
- fuel supply system components,
- exhaust system components.

The electro-spark deposition coating is characterized by non etching structure. It is stay white after etching. The surface layer is constituted in environment of local high temperature and high pressure. The fundamental value parameters of electro-machining are as following [2]:

- shock wave pressure comes from electric spark is (2-7)$10^3$ GPa,
- temperature rich (5-40)$10^3$ Celsius degree value.

How the surface layer was generating by electro-spark deposition process is depicted in details in Figure 3.1. To understand this scheme below is necessary to list accurate descriptions, i.e.: 1 – material of base (cathode), 2 – working electrode (anode), 3 – created coating with established operational features, 4 – plasma, 5 – diffusive or reactive-diffusive zone, 6 – nearer surrounding (shielding gas), 7 – further surrounding (air), 8 – electrode holder with channels supplying gas, IR – infrared radiation, UV ultraviolet radiation.

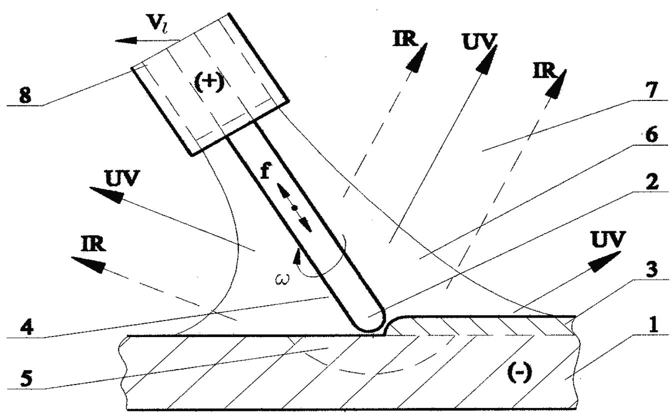


*Fig. 3.1. Scheme of surface layer forming by electro-spark deposition method*

### 3.1.2. PHYSICAL BASIS OF ELECTRO-SPARK ALLOYING

Since B.R. Lazarenko and N.I. Lazarenko patented electro-spark machining of materials in 1946 [12], the investigations into the physics of the process of electric erosion of materials in removal machining (EDM – Electro Discharge Machining) and increment machining (ESA – Electro-Spark Alloying) have been conducted by research teams all over the world.

According to literature [13-14], the occurrence of three areas is characteristic of the erosion process caused by an electric discharge:

- area adjacent to the anode,
- discharge channel (presently termed a plasma channel),
- area adjacent to the cathode.

B.N. Zolotych [14] claims that in order to learn about the processes of electric erosion, it is necessary to specify the mechanism of the transfer of energy delivered in a pulse to the areas directly participating in the discharge process, namely electrodes, dielectric liquid or gases. The energy causes the erosion of electrodes. The character of energy transfer to the anode and the cathode is different and depends mainly on the current carriers. On the anode, the whole current is carried by electrons, whereas on the cathode, it is carried by ions and electrons. As a result of the model of electric discharge adopted by B.N. Zolotych, the processes on the anode and the cathode are considered separately.

The energy of a pulse can be expressed as follows [14]:

$$W_i = \int_0^{t_i} U(t) I(t) dt \tag{3.1}$$

where: $W_i$ – pulse energy, $U(t)$ – pulse voltage, $I(t)$ – pulse current intensity, $t_i$ – pulse duration.

The energy of a pulse, in its simplified form, can be calculated from the dependence [14]:

$$W_i = U_r \cdot I_r \cdot t_i \tag{3.2}$$

where: $W_i$ – pulse energy, $U_r$ – amplitude of the working voltage, $I_r$ – amplitude of the intensity of the working current, $t_i$ – pulse duration.

The energy supplied to the electrode (anode and cathode) surfaces in the electro-spark alloying is written by B.N. Zolotych [14] as a sum:

$$W_E = W_A + W_K \tag{3.3}$$

where: $W_E$ – energy transferred to the electrodes, $W_A$ – energy transferred to the anode, $W_K$ – energy transferred to the cathode.

In turn, the energy of the pulse [14] can be presented as follows:

$$W_i = W_E + W_W \tag{3.4}$$

where: $W_i$ – pulse energy, $W_E$ – energy transferred to the electrodes, $W_W$ – energy acting in the discharge channel.

Energy transfer to the electrodes can be achieved by means of the following processes [2, 14-15]:

- the cathode bombardment by ions due to the action of the electric field in the zones adjacent to the electrodes and the anode bombardment by electrons,
- the discharge channel radiation,
- thermal, i.e. gas kinetic bombardment by particles contained in the discharge channel,
- for small thicknesses of the gap between the electrodes, energy transfer between the electrodes can proceed because of the action of vapour streams produced on the anode and the cathode,
- Electro-spark alloying can be applied to all the materials that are current conductors regardless of their hardness, shape or toughness [16].

### Polarity of electrodes

The polarity of electrodes decides about the character of the machining process, namely whether it is removal machining (EDM) or increment machining (ESA). The concept was used for the first time by B.R. Lazarenko [17], and defined by B.N. Zolotych in work [14]. According to B.R. Lazarenko [17], the polarity effect depended on the melting point of the electrodes, but B.N. Zolotych [14] demonstrated it also depended on the pulse energy and pulse discharge time.

In electro-spark alloying, the eroded material is transferred from the anode to the cathode, and consequently a layer is formed on the cathode surface. The layer consists of either pure anode material or results from the interaction of the materials of the electrodes and the interelectrode medium which is usually air. The intensity of the process of the material transfer depends on many factors [6].

An important factor that influences the effect of polar transfer of the material is the phenomenon of simultaneous erosion of the anode and the cathode. This effect is expressed by the polarisation coefficient $K_n$ [15, 19]:

$$K_n = \frac{\gamma_k}{\gamma_a} \tag{3.5}$$

where: $K_n$ – polarisation coefficient, $\gamma_k$ – cathode erosion [g], $\gamma_a$ – anode erosion [g].

For the case when $K_n < 1$, the transfer of the material occurs (positive polarity), if $K_n > 1$ the transfer of the material virtually does not take place (negative polarity).

The following conditions are true for a majority of electrodes:

- if $(T_t)_k \geq (T_t)_a$, $K_n < 1$,
- if $(T_t)_k \leq (T_t)_a$, $K_n > 1$.

where: $(T_t)_a$ – anode melting point, $(T_t)_k$ – cathode melting point.

The polarisation coefficient $K_n$ depends on the pulse discharge time and energy, and for electrodes made of the same materials, on their thermal conductivity.

According to the author of work [15], the polarisation coefficient can be expressed as follows:

$$K_n = \frac{Q_k(k,t_i,W_i)\cdot\psi_a(T_t,c,q_t)}{Q_a(k,t_i,W_i)\cdot\psi_k(T_t,c,q_t)} \tag{3.6}$$

where: $K_n$ – polarisation coefficient, $Q_{k,a}$ – amount of heat released on the cathode and the anode, $\psi_{k,a}$ – total heat of the phase change of both electrodes, $k$ – thermal conductivity, $W_i$ – pulse energy, $t_i$ – pulse duration, $T_t$ – electrode melting point, $c$ – electrode heat capacity, $q_t$ – electrode heat of fusion.

The above dependence on polarisation coefficient $K_n$ takes into account basic thermal processes that proceed in the discharge channel and on the surface of electrodes.

In work [19], the author demonstrated that for $K_n$ much higher than unity, the transfer of the material to the cathode takes place, but simultaneously the cathode mass decrement occurs.

According to works [19-20], the polar transfer of mass is affected by the properties of the gaseous environment, in which the electric erosion process takes place. Other factors that influence the transfer include the size of the interelectrode gap and changes in the properties of electrode surfaces when those interact in the pulse discharge [15, 21].

### 3.1.3. EXPERIMENTAL

The coatings were deposited on the C45 grade plain-carbon steel by the ESD method using a portable EIL-8A electro-spark deposition facility (TRIZ, Ukraine). The electrodes, of composition 85% WC, 10% Co and 5% $Al_2O_3$, were produced using the powder metallurgy hot pressing route [22]. The main characteristics of the powders used in this work are included in Table 3.1.

*__Table 3.1.__ Powders used to manufacture electrodes*

| Powder | Particle Size, μm | Producer |
|---|---|---|
| WC | ~0.2 | OMG |
| Co | ~1.4 | Umicore |
| $Al_2O_3$ | 18÷60 | Sulcer-Metco |

The powders were mixed for 30 minutes in the chaotic motion *Turbula T2C* mixer. The mixture was then poured into rectangular cavities of a graphite mould, each 6 × 40 mm in cross section, and consolidated by passing an electric current through the mould under uniaxial compressive load. A 3 minute hold at 950°C and under a pressure of 40 MPa permitted obtaining electrodes of porosity <10% and strength sufficient to maintain integrity when installed in the electrode holder.

The equipment used for electro-spark alloying was an EIL-8A model. Basing on the results of previous research as well as instructions given by the producer, the following parameters were assumed to be optimal for ESA:

- voltage, $U = 230$ V,
- capacitor volume, $C = 150$ μF,
- current intensity, $I = 2.4$ A.

In Figure 3.2 the electro-spark deposition equipment is illustrated.

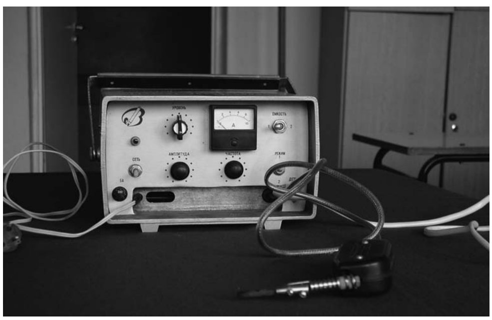

***Fig. 3.2.** View of EIL-8A electro-spark deposition – equipment*

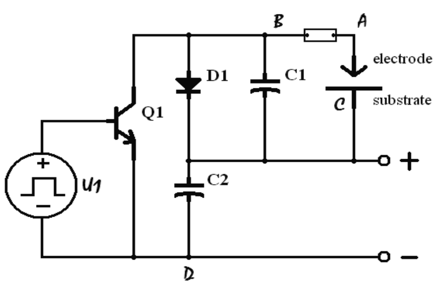


***Fig. 3.3.** Schematic diagram of a pulse generation system*

The quality of electro-spark deposition depends mainly on the shape, duration, and average value of current or pulse power. An average value of current is directly proportional to the number of generators operating in parallel. Figure 3.3 shows a schematic diagram of a single pulse generator and following Figure 3.4 presents current impulse shape from this device.

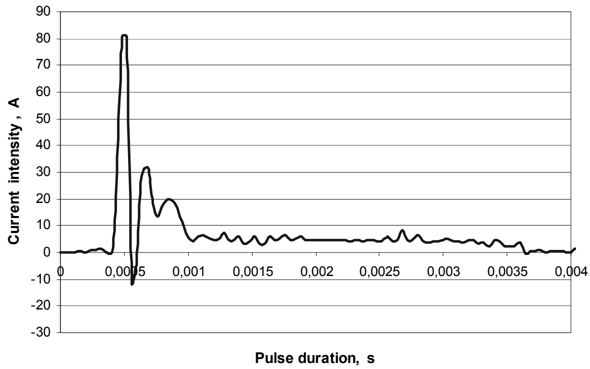


***Fig. 3.4.*** *Shape of a current impulse*

Electrical energy stored in capacitor C2 is transmitted to the circuit: substrate – electrode in the form of a spark discharge and current flow. The process is initiated by switching on/of a transistor Q1. The switching frequency of the transistor is of the order of several to several dozen kHz. The capacitor C1 allows changing the shape and duration of an impulse as well as affecting the pulse-duty while setting pulse frequency of transistor Q1.

### 3.1.4. RESULTS AND DISCUSSION

Microstructure and X-Ray diffraction analysis

A characteristic feature of any electro-spark deposited coating is that the new layer has a difficult-to-etch structure – it remains white. Similar layers are produced by grinding and lapping. What the processes have in common is high temperature and high loads applied locally. Electro-spark deposition differs from grinding and lapping in the process intensity: the pressure of the shock wave from an electric spark discharge is $(2\div7)\cdot10^6$ N/mm$^2$ and the temperature reaches values of the order of $(5\div40)\cdot10^3$°C (in grinding it does not exceed 1000°C).

The temperature during an electro-spark discharge increases locally and it is much higher than the boiling point of the materials the electrodes are made of. A high heat transfer rate causes that the temperature within the layer falls rapidly to the solidifying point, the thickness of the coating being of the order of several micrometers. The processes of crystallization, phase transition and chemical interaction occur in the solid phase. Electro-spark deposited coatings are fine-grain non-equilibrium structures, which are heterogeneous in composition, structure and properties. They are characterized by very high adhesion to the underlying substrate, which is a result of the diffusion or reaction-diffusion processes.

A microstructure analysis were conducted for WC-Co-$Al_2O_3$ coatings using a Joel JSM-5400 scanning electron microscope and a Neophot 2 light microscopy.

In Figure 3.5 selected view of the surface microstructure of an electro-spark alloying WC-Co-$Al_2O_3$ coating is illustrated. It is clear that the thickness of the obtained layers was 60 to 70 μm, whereas the heat affected zone (HAZ) ranged approximately 30 to 40 μm into the substrate, one can see a Figure 3.5 also reveals a clear boundary between the coating and the substrate and pores within microcracks are observed.

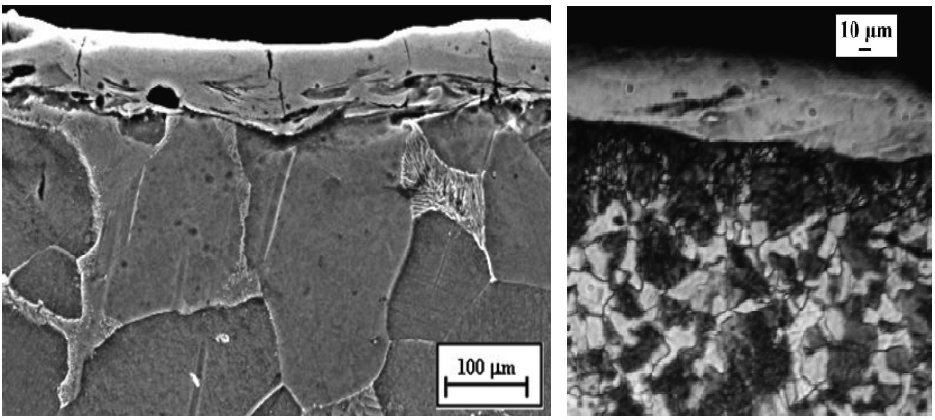


*__Fig. 3.5.__ SEM (left) and LM (right) micrographs of the polished cross section throug a WC-Co-$Al_2O_3$ ESD coating on C45 steel substrate*

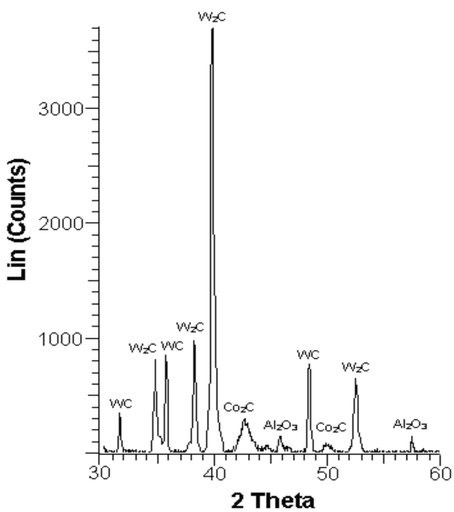


*__Fig. 3.6.__ X-ray diffraction pattern of the WC-Co-$Al_2O_3$ coating*

A Philips PW 1830 X-ray diffractometer with CuK$\alpha$ radiation, operating at 40 kV and 30 mA, was used for phase(s) identification. According to the structure X-ray analysis of the WC-Co-$Al_2O_3$ coating on the C45 steel substrate, as shown in Figure 3.6, the superficial layer of the coating consists of WC and $W_2C$ besides a small amount of $Co_2C$ and $Al_2O_3$. The semi-carbide $W_2C$ is known to appear as an intermediate during the formation and dissolution of WC. Besides, it has been found that peaks from the $W_2C$ phase are the most intense.

## Microgeometry Measurements

One of the main disadvantages of the coatings produced by electro-spark alloying is high roughness of the finished surface. By reviewing the literature and analyzing the latest developments in this technology, one can notice that the surface generation process involves erosion of the base material and formation of microcraters and ridges by the particles leaving the electrode. The surface is regular with rounded microroughness peaks. The effect of the process parameters on the formation of surface roughness has been described in numerous publications. By controlling these parameters, it is possible to obtain surfaces with pre-determined microgeometry. Electro-spark alloying allows producing surfaces with enhanced roughness called surface relief.

The roughness of the WC-Co-$Al_2O_3$ coatings was measured at the Laboratory for Measurement of Geometric Quantities of the Kielce University of Technology using a TALYSURF CCI equipped.

The roughness was measured in two directions perpendicular to each other. Then, the average value was calculated: Ra = 4.99÷5.66 μm.

The without coatings steel specimens (C45) had a roughness from 0.46 to 0.53 μm.

Figure 3.7 presents an example three dimensional surface microgeometry measurement of the WC-Co-$Al_2O_3$ coatings.

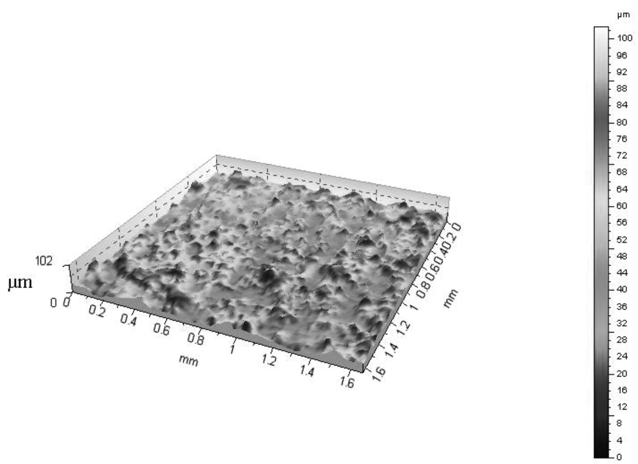


***Fig. 3.7.*** *Three dimensional surface microgeometry of the WC-Co-$Al_2O_3$ coating deposited*

## Microhardness And Adhesion Tests

The microhardness of the specimens with WC-Co-$Al_2O_3$ coatings was analyzed applying a load of 0.4 N and using the Vickers method. The indentation was made consecutively in three zones: the coating, the heat affected zone (HAZ) and the base material. The results are given in Table 3.2. The process of electro-spark alloying resulted in certain changes in the material structure.

***Table 3.2.*** *Results of the microhardness tests for the WC-Co-$Al_2O_3$ coating*

| Measured zones | Microhardness HV0.4 | | | Mean value HV0.4 |
|---|---|---|---|---|
| | Measurement number | | | |
| | 1 | 2 | 3 | |
| **Coating** | 877 | 931 | 911 | 906 |
| **HAZ** | 391 | 388 | 372 | 384 |
| **Substrate** | 270 | 288 | 279 | 279 |

The average microhardness of the base material after ESA was 279 HV0.4. The value was the same as that at the initial state. The average microhardness of the WC-Co-$Al_2O_3$ coating was 906 HV0.4. Thus, there was a 225 percent increase compared to that of the base material. The microhardness of the heat affected zone after electro-spark alloying was 38 % higher in relation to that of the base material.

A scratch test was conducted to measure the adhesion of the WC-Co-$Al_2O_3$ coatings. Adhesion tests were conducted using REVETEST instrument (CSEM, Switzerland). The diagram showing the operation of the tester is presented in Figure 3.8. The measurements were performed at a load increase rate of 103.2 N/min; a table feed rate of 9.77 mm/min and a scratch length of 9.5 mm.

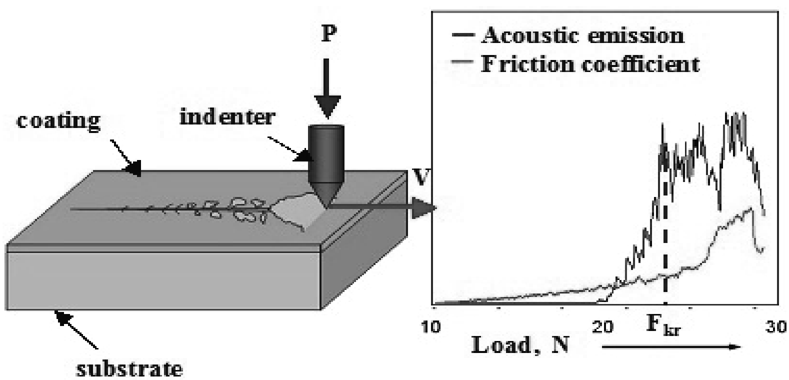


***Fig. 3.8.*** *Diagram of the stand for scratch tests of coating adhesion together with an idealized graph used to indicate the value of the critical force on the basis of the profile of acoustic emission signal and the friction force*

A special indenter – a Rockwell diamond cone with a corner radius of 200 μm, was used to scratch the samples at a gradually increasing normal force (load). The information about the cracking or peeling of layers was obtained basing on the measurements of the material resistance (tangential force) and the registration of acoustic emission signals. The lowest normal force causing a loss of adhesion of the coating to the substrate is called critical force and is assumed to be the measure of adhesion.

The critical force was determined basing on the records of changes in the acoustic emission signals and the tangential force as well as on the results of observations with an optical microscope fitted in the REVETEST tester. The values of the critical force were established by comparing the scratches left by the indenter with the responses of acoustic emission signals. Table 3.3 shows the values of the critical force obtained from three measurements of a given sample, the force mean values and standard deviations. The mean value of the critical force of the WC-Co-$Al_2O_3$ coating calculated from three measurements was 7.64 N.

***Table 3.3.*** *Results of the adhesion test*

| Coating | Critical force, N | | | Mean value, N |
|---|---|---|---|---|
| | Measurement number | | | |
| | 1 | 2 | 3 | |
| **WC-Co-$Al_2O_3$** | 8.65 | 7.94 | 6.32 | 7.64 |

Measurements with PG-2/200 shape analyser made it possible to observe transverse profile of scratches in the examined coatings. Exemplary image of a scratched specimen is shown in Figure 3.9. Observations indicate that coating scratching with diamond probe is accompanied by plastic deformation of the substrate. It can be evidenced by substantial material pile-up along the groove drawn. As a result of plastic deformation, a furrow (wave) of deformed material is formed in front of the moving indenter. In accordance with the author's observations, and also tests described by Hebda [23] and Kupczyk [24], the height of the deformed material depends on the material yield point. The lower is the yield point, the greater is the wave height.

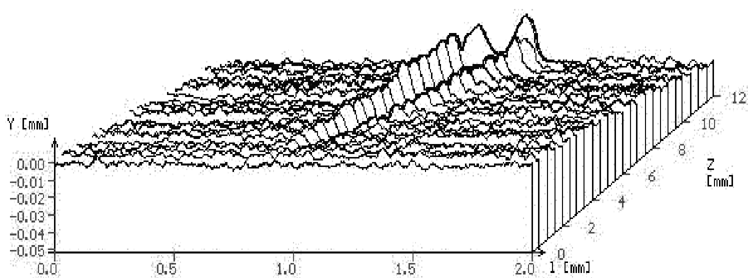


***Fig. 3.9.*** *Spatial image of the scratched WC-Co-$Al_2O_3$ coating*

## Corrosion Resistance Tests

The corrosion resistance of the $WC\text{-}Co\text{-}Al_2O_3$ coatings and the underlying substrate was analyzed using a computerized system for electrochemical tests, Atlas'99, produced by Atlas-Sollich. The potentiodynamic method was applied, because it is reported to be one of the most effective methods of electrochemical testing.

The cathode polarization curve and the anode polarization curve were determined by polarizing the samples with a potential shift rate of 0.2 mV/s in the range of ±200 mV of the corrosive potential, and with 0.4 mV/s in the range of higher potentials. Samples with a marked area of 10 mm in diameter were polarized up to a potential of 800 mV. The polarization curves were drawn for samples exposed for 24 hours to a 3.5% NaCl solution so that the corrosive potential could be established. The tests were performed at a room temperature of 21°C (±1°C).

The results are summarised in Table 3.4. A diagram of the three-electrode chamber for electrochemical corrosion testing is presented in Figure 3.10.

***Table 3.4.*** *Corrosion current densities of the tested materials*

| Material | Corrosion current density ($I_k$), μA/cm$^2$ |
|---|---|
| **C45** | 35.4 |
| **$WC\text{-}Co\text{-}Al_2O_3$** | 16.8 |

The $WC\text{-}Co\text{-}Al_2O_3$ coating was reported to have the highest corrosion resistance. The corrosion current density of the coating was 16.8 μA/cm$^2$, while that of the C45 steel substrate was 35.4 μA/cm$^2$. Applying the $WC\text{-}Co\text{-}Al_2O$ coating improved the sample corrosion resistance by approx 100%. The fusion of the coating and the substrate resulted in a considerable heterogeneity of electrochemical potentials on the coating surface. The microcracks in the surface layer also contributed to the intensification of the corrosion processes.

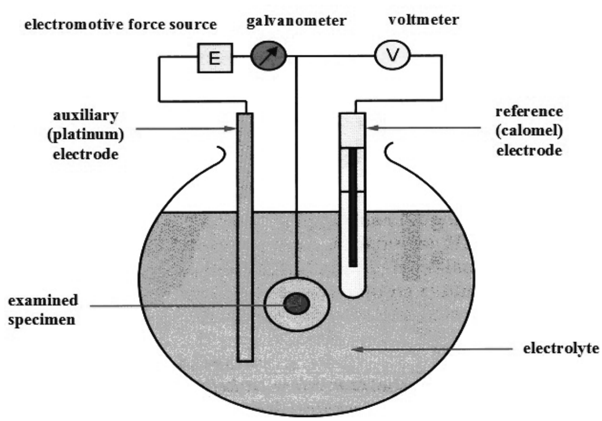


***Fig. 3.10.*** *Diagram of three-electrode chamber for tests of the corrosion resistance of materials [25]*

Wear Resistance Of Beaters

In the experiment, the coatings were electro-spark deposited on hammer faces made of carbon steel C45 (Fig. 3.11) – the cathode – using a WC-Co-$Al_2O_3$ electrode.

There were sixteen specimens measured: eight with electro-spark deposited WC-Co-$Al_2O_3$ coatings and eight uncoated ones.

***Fig. 3.11.*** *Working surface of an unworn specimen before the deposition of a WC-Co-$Al_2O_3$ coating*

All the specimens were weighed for the first time before the tests. Then, eight of them were coated with WC-Co-$Al_2O_3$ and weighed again. It should be noted that only the working surfaces were strengthened. The next stage involved mounting the beaters in a hammer mill operating in Nordiska Ekofiber Polska Ltd. (Fig. 3.12). The eighteen beaters were placed symmetrically along the mill shaft. After 250 hours of operation, all of them were weighed again. The data are shown in Tables 3.5 and 3.6.

***Table 3.5.*** *Mass of the beaters with WC-Co-$Al_2O_3$ coatings*

| Specimen number | Measurement number | | | Mass loss |
|---|---|---|---|---|
| | I [g] | II [g] | III [g] | [g] |
| **1 N** | 936.43 | 936.49 | 936.31 | 0.18 |
| **2 N** | 947.62 | 947.66 | 947.43 | 0.23 |
| **3 N** | 969.13 | 969.15 | 969.03 | 0.12 |
| **4 N** | 949.87 | 949.92 | 949.71 | 0.21 |
| **5 N** | 937.69 | 937.71 | 937.47 | 0.24 |
| **6 N** | 929.75 | 929.79 | 929.64 | 0.15 |
| **7 N** | 958.32 | 958.37 | 958.21 | 0.16 |
| **8 N** | 967.28 | 967.32 | 967.11 | 0.21 |
| | | | **average value** | **0.19** |

Table 3.5 presents measurement results for the specimens with WC-Co-$Al_2O_3$ coatings. Column I shows the mass of the beaters before electro-spark alloying; in column II we have the mass of the beaters with electro-spark deposited

WC-Co-$Al_2O_3$ coatings, and in column III the mass of the beaters after 250 h of operation in the mill. Table 3.6 contains results for the uncoated specimens before use (column I), and after 250 hours of operation in the mill (column II).

***Table 3.6.*** *Mass of the beaters without coatings*

| Specimen number | Measurement number | | Mass loss |
|---|---|---|---|
| | I [g] | II [g] | [g] |
| **1 W** | 937.72 | 937.48 | 0.24 |
| **2 W** | 934.19 | 933.54 | 0.65 |
| **3 W** | 948.86 | 948.64 | 0.22 |
| **4 W** | 965.72 | 965.29 | 0.43 |
| **5 W** | 953.78 | 953.31 | 0.47 |
| **6 W** | 943.33 | 942.89 | 0.44 |
| **7 W** | 921.18 | 920.45 | 0.73 |
| **8 W** | 972.83 | 972.62 | 0.21 |
| | | **average value** | **0.42** |

The mass loss analysis showed that the beaters with the WC-Co-$Al_2O_3$ coatings had a lower wear rate than the uncoated beaters. The latter are predicted to operate for approximately 2-3 years. The investigations will be continued as there is not enough data confirming that the application of WC-Co-$Al_2O_3$ coatings improves the long-term wear resistance of beaters.

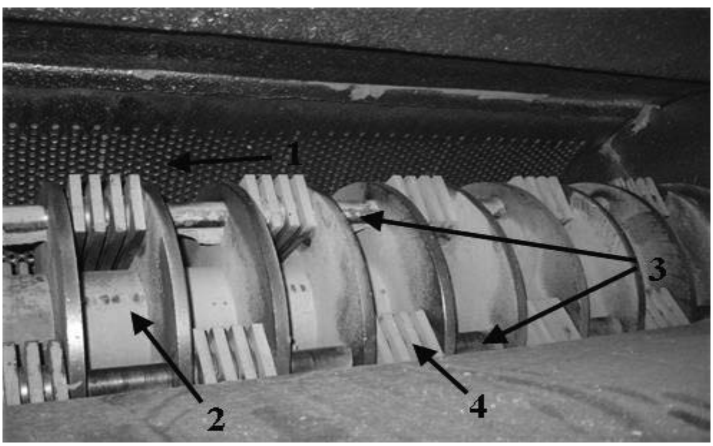


***Fig. 3.12.*** *A view of the inside of the mill for waste paper grinding: 1 – sieve, 2 – main shaft, 3 – fixing pivots, 4 – beaters*

Electric pulse measurements

Electric pulses of the electro-spark alloying are generated in the system presented in Figure 3.13.

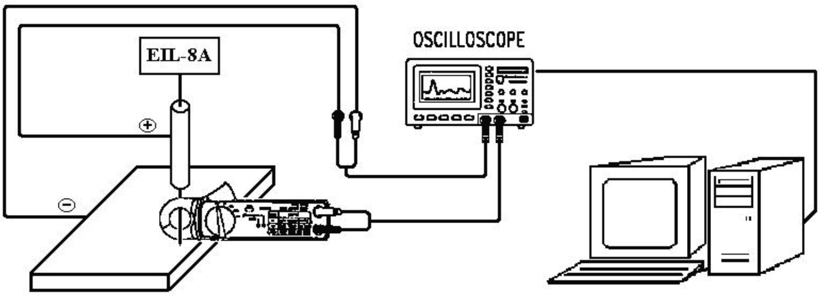


***Fig. 3.13.*** *The measurement system [26]*

While conducting investigations into the process of electro-spark alloying, it is necessary to take measurements of the current intensity and the power of electric pulses used. Transistor pulse generation system is energised from the power source, which is a power capacitor. The way of taking measurements is presented in Figure 3.13.

For current measurements, a CM-05 digital probe by Prova Instruments Inc. was employed. The probe, which has jaws, is current-to-voltage transducer based on a Hall sensor. The probe measures AC/DC current in the bar and ensures that the measuring and high current systems are galvanically separated. The probe voltage output signal is fed directly to the TDS 210 digital oscilloscope (Tektronix). In the other channel of the oscilloscope, the voltage between the electrode and the machined workpiece is measured. The measurement data are transferred to the computer via TDSCM communications module. Measured quantities are also available as a file in ASCII format.

In order to determine the patterns of current and voltage of electric discharge in the ESA process, a measurement stand comprising Hewlett-Packard 54602A digital oscilloscope, current probe and IBM PC was used. The stand makes it possible to record instantaneous values of the current and spark discharge voltage. Digital oscilloscope accounts for simultaneous measurements of voltage and current. Buffer memory allows remembering 500 samples, which makes it possible to record a few discharge cycles (at appropriately selected time base). 8-bit resolution of the amplitude measurements may seem too low, yet the results obtained are satisfactory. The system suffers from a minor drawback due to the fact that it is possible to record only two patterns. The parameters of the process of electro-spark alloying were selected experimentally.

Exemplary patterns of current and electric discharge voltage recorded in electro-spark alloying are presented in graphs (Fig. 3.14-3.15).

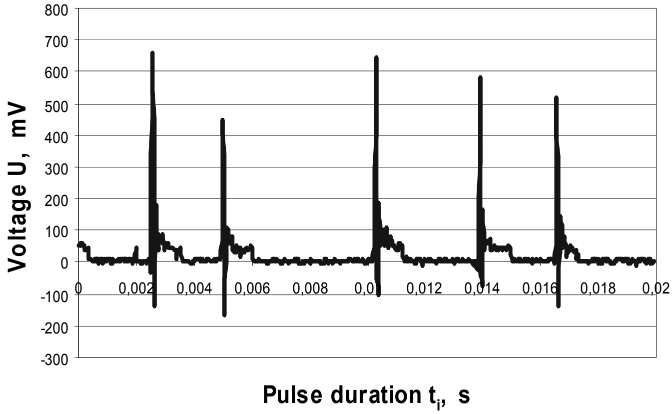


***Fig. 3.14.*** *Pattern of changes in voltage parameters (I = 0.4 A; C = 150 μF)*

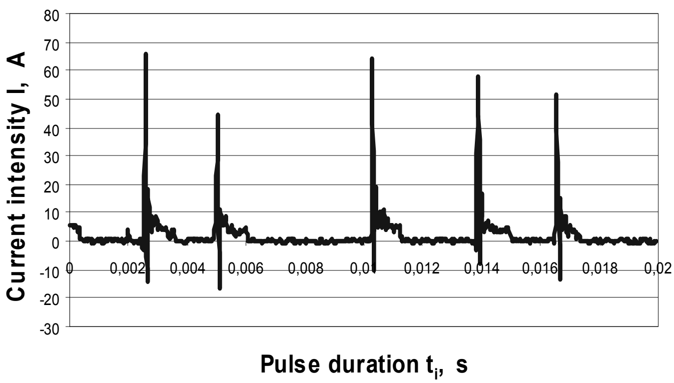


***Fig. 3.15.*** *Pattern of changes in current parameters (I = 0.4 A; C = 150 μF)*

Basic electric quantities in a discharge, i.e. current $i(t)$ and voltage $u(t)$ of an electric pulse can be read form the graphs. After digital processing of those quantities, it is possible to compute, e.g. instantaneous power of an electric pulse, which is expressed by formula $p(t) = u(t) \bullet i(t)$. Additionally, the duration of the spark discharge pulse can be read. If current, voltage and the duration of the spark discharge pulse are given, an instantaneous energy of an electric pulse can be calculated. From the literature, it is known that the thickness of the deposited coating and its functional properties are influenced to the greatest extent by the pulse energy. The current and voltage characteristics obtained could be used to optimise the ESA process, so that the coatings with desirable functional properties could be designed.

Conclusions:

The following conclusions can be drawn from the analysis and test results.

1. The microstructure analysis revealed that the coating thickness was 60÷70 μm, whereas the heat affected zone ranged approximately 30÷40 μm. The coatings possessed microcracks and pores.
2. A significant increase in roughness Ra was reported for specimens with WC-Co-$Al_2O_3$ coatings. Higher roughness, however, is not always considered a disadvantage. Under certain circumstances, valleys in the roughness profile act as lubricant reservoirs, which increases the rate of heat transfer and that of catalysis.
3. The microhardness of the WC-Co-$Al_2O_3$ coating produced by electro-spark alloying was 906 HV0.4, while that of the base material – C45 steel – was 279 HV0.4.
4. The mean value of the critical force of the WC-Co-$Al_2O_3$ coating calculated from three measurements was 7.64 N.
5. The obtained $I_k$ values indicate over 100% increase in corrosion resistance of the ESD coated sample compared to uncoated C45 steel substrate.
6. The coating surface is composed of WC and $W_2C$ besides a small amount of $Co_2C$ and $Al_2O_3$.
7. The durability of beaters was studied under real conditions; the specimens with WC-Co-$Al_2O_3$ coatings were reported to be more wear resistant than the uncoated ones.
8. Further research will be targeted at determining the long-term wear resistance of beaters with WC-Co-SiC and $TiB_2$-Co-$Al_2O_3$ coatings produced by electro-spark alloying.
9. The measurement system that was constructed includes: the EIL-8A device, the TDS 210 digital oscilloscope (Tektronix) and CM-05 digital probe. The system makes it possible to take measurements of the basic electric quantities, i.e. current $i(t)$ and voltage $u(t)$ of an electric pulse. The system can also digitally process those quantities, which includes determining additional electric quantities, e.g. instantaneous power of an electric pulse $p(t) = u(t) \bullet i(t)$.
10. The shortcoming of the measurement system used consists in the recording of only two patters, and also a relatively slow data transmission from the oscilloscope to the computer. Additionally, digital oscilloscope employed for measurements is based on 8-bit convertors, which diminishes measurement accuracy. An alternative solution is to replace the oscilloscope with a multi-channel 14-bit control-measurement card. Due to FIFO buffer or DMA channel, it ensures high speed and accuracy of A/D processing.

# 3.2. THE SURFACE GEOMETRIC STRUCTURE AND TRIBOLOGICAL PROPERTIES OF THE ELECTRO-SPARK DEPOSITED WC-Cu COATINGS BEFORE AND AFTER LASER TREATMENT

*Norbert Radek*

## 3.2.1. ESD AND LBM – MODIFICATION METHODS

There are many methods for producing surface coatings, such as electroplating and plasma spraying. Very thin layers can be deposited by vapour deposition. Various surface treatment techniques have been developed to improve the desired properties of the deposited layers, based on the substrate material. Some of these methods are expensive and should be used only for unique applications, where the high cost is justified. However, for most applications, there is a need for low cost coatings of good properties. This study is an attempt to improve a widely used low cost method of electro-spark deposition (ESD). It has been already recognized as an economically effective surface coating [27-29]. ESD is also widely used for its relative low cost equipment required for this process. The deposition of the coating is achieved by an electrical circuit, which generates sparks between the electrode and the work-piece. Electrical pulses of high frequency and high direct current between the electrode (anode) and work-piece (cathode) release very hot micro-particles of electrode material, resulting in continuous micro-welding coating on the work-piece surface. Important advantage is that the coating is bonded with relatively low heat. This energy saving is because only the micro particles are heated, while the body of the work-piece remains at low temperature. ESD has been known by several other terms such as spark hardening, electric spark toughening, and electro-spark alloying (ESA).

Electro-spark deposited coatings have some disadvantages but these can be easily eliminated. One of the methods is laser beam machining (LBM); a laser beam is used for surface polishing, surface geometry formation, surface sealing or for homogenizing the chemical composition of the coatings deposited [30-33].

It is envisaged that the advantages of laser-treated electro-spark coatings will include:

- lower roughness,
- lower porosity,
- better adhesion to the substrate,
- higher wear and seizure resistance,
- higher fatigue strength due to the occurrence of compressive stresses on the surface,
- higher resistance to corrosion.

The work discusses the properties of electro-spark deposited WC-Cu coatings subjected to laser treatment. The properties of the coatings after laser treatment were assessed based on following methods: microstructure and X-ray diffraction analysis, surface geometric structure and roughness measurement, microhardness tests and tribological studies.

### 3.2.2. PHYSICAL PROCESSES THAT OCCUR IN LASER BEAM MACHINING OF ELECTRO-SPARK COATINGS

In laser machining of electro-spark coatings the following can occur most frequently:

1. With a high-melting coating, the substrate melts and the coating does not.
2. Only the coating melts.
3. Both the coating and the substrate melt.
4. The coating is vaporised and plasma is generated.

Thermal conductivity – k is an important parameter that decides about the thermal effects in laser beam machining of electro spark coatings. The literature on the subject [34] states that 90% of the energy absorbed by the material due to the action of a laser beam is transferred into the material by means of thermal conduction and approx. 10% is radiated through the surface layer.

In the diagram of a laser beam action on the electro spark coating, which is presented below (Fig. 3.16), coating, diffusion and the substrate material zones can be differentiated. Each zone has different thermal conductivity ($k_1 \neq k_2 \neq k_3$). The values of k primarily depend on the materials of the coating and the substrate that are used. In laser treatment of electro spark coatings, thermal resistances on the concrete – substrate boundary do not occur because the diffusion link between the two zones does not hamper the heat transfer.

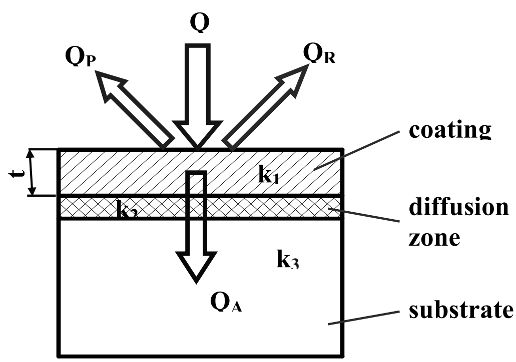


***Fig. 3.16.*** *Diagram of laser beam action on the electro spark coatings: $k_1$, $k_2$, $k_3$ – thermal conductivities, t – coating thickness, Q – total power of laser-emitted radiation, $Q_A$ – total power absorbed by the material surface, $Q_R$ – total power reflected by the material surface, $Q_P$ – total power transferred by radiation*

The carrying away of the heat is low for thin coatings (it depends mainly on thermal conductivity), as a result, after a laser exposure, the site affected by a laser beam may remain in the liquid phase [35]. For higher coating thicknesses, the melted area dwindles (crystallisation occurs) already during the action of a laser beam when the volume of the unmelted material is seven times greater than the volume of the melted material [36]. The phenomena mentioned above should be experimentally validated for laser treatment of electro spark coatings (coating thickness 8÷60 μm).

Non-uniform thickness of coatings can influence the effects of laser treatment to a large extent. For the same power density, different effects may be produced at different sites of the treated coating, including those disadvantageous ones, like, e.g. the coating vaporisation.

When the meting point of the layers deposited by electro spark treatment (e.g. WC, $TiB_2$, Mo, Ti) is higher than that of the steel substrate (e.g. C45 steel), it is possible that local partial meltings of the substrate under the unmelted layer will occur. After the molten metal solidifies, column or equiaxial (depending on the rate of cooling) crystals are formed, orientated with the direction of heat carrying away. Also, martensitic and bainitic structures, and phases and compounds that have refined grain structure are formed.

With appropriately selected parameters of laser treatment, melting proceeds only in the electrospark coating. For coatings that have high thermal conductivity (e.g. copper), the solidification of the metal molten area already starts when the laser beam is still operating, because of heat being intensively carried away into the material. As regards metal coatings that have low thermal conductivity (e.g. Ti) heat transfer is slow, thus the solidification of the molten metal will take longer. On the surface of laser irradiated materials that have low thermal conductivity vaporisation begins before the impulse intensity reaches the maximum value, which may lead to the vaporisation of a thin coat.

The melting of an electro spark coating results in an increase of its density, which leads to reduced porosity and elimination of surface defects, such as hairline cracks, delamination, cracks or open pores. In some cases the smoothing of the surface may occur.

At very high rates of cooling, the viscosity of the liquid metal increases so much that crystallisation nuclei are not able to form. The molten metal does not crystallise but it solidifies in a disordered manner forming an amorphous layer. Such layers can, among others, form metal – refractory metal compounds (e.g. Cu, Co, Fe with WC, $Al_2O_3$, $TiB_2$).

Laser beam melting of an electro spark coating deposited on the steel substrate can cause simultaneous melting and mixing of both materials (laser alloying). The action of the laser beam makes the materials melt. The molten pool of the materials is formed, in which they mix together vigorously, because of convective and gravitational motion and the pressure of the laser beam. The melting process starts at the coat and spreads (through convection and conduction) to the surface layer of the substrate. In addition, the alloying material (coating) entirely melts in the substrate material. A diffusion zone is formed on the boundary of the solid state and the liquid state. After the action of the beam stops, the alloy solidifies and the substrate material in the neighbourhood of the alloy becomes hardened.

In deep melting of the thin coating by a laser beam, the coating vaporisation and plasma generation often occur (for the power density above $10^7$ W/cm$^2$). Metal vapours and plasma acting on the molten metal produce different physical processes than it is the case when no vapours are present. A pit is formed in the liquid metal at the site of the laser beam penetration into the material due to the pressure exerted by the vapour. This process is disregarded in the models of thin layer melting, even though the action of vapours can significantly affect the shape of the surface after solidification. Vapour, among others, cools the molten material, which accelerates its solidification. Vaporisation and plasma generation phenomena are undesirable in laser treatment of thin electro spark coatings because the coating will be removed or damaged, which will affect the service properties of the technological surface layer. Such phenomena are eliminated by appropriately selecting the parameters of the treatment.

The action of the shock laser (power density up to $10^8 \div 10^{10}$ W/cm$^2$) on a thin coating can cause changes in the structure of the coating and the substrate material, fracture or bursting of the coating and its rapid vaporisation accompanied by plasma generation. A major advantage of the shock laser, which employs both shock wave energy and a mechanical impulse, is the occurrence of compressive stresses in the top layer and the elimination of micro-cracks. A disadvantage involves the formation of a crater, and thus deterioration of the quality of the surface irradiated with the laser.

In the surface engineering, a laser beam can be used for ablation, often treated as vaporisation. The ablation process takes place due to the impulse action of a high power density laser beam on the material in short time intervals, usually in nanoseconds. For thin coatings, laser ablation can be used for removing a part of the coating material (even in the atomic scale) and for reinforcing the remaining part of the coating due to shock wave phenomenon. Very high heating and cooling rates cause grain refinement and the formation of amorphous and nanocrystalline structures. Laser ablation can be used to improve service properties of thin coatings, namely to reduce roughness, heal pores and microcracks, increase the resistance to wear, increase the microhardness, etc.

### 3.2.3. PRODUCTION OF ESD ELECTRODES BY THE POWDER METALLURGY HOT PRESSING ROUTE

The electrodes used to deposit coatings by means of the electro-spark deposition (ESD) method are produced using the powder metallurgy (PM) hot pressing route [37].

### Powder mixing and granulating

Basically, the electrode preparation consists in mixing the selected component powders so as to achieve the pre-determined chemical composition, and particle shape and size distribution considering the final product application. This operation is often carried out using chaotic motion mixers (Fig. 3.17).

***Fig. 3.17.*** *2 litre Turbula T2C mixer*

Binding agents and/or lubricants, e.g. paraffin oil, monoethylene glycol, etc., may often added to the powder at this stage, in amounts up to 2 wt.%, so as to reduce dust and prevent segregation when the powder is subsequently handled or processed; but also to minimise wear of steel dies and to reduce oxides during subsequent cold and hot pressing operations, respectively.

When the powder is to be cold compacted on a press working on a volumetric die filling principle, a further granulation treatment is necessary to obtain required flow and packing characteristics of the powder (Fig. 3.18). Granulation may be carried out in a variety of ways [38-42] but, practically, the fluidised-bed method and techniques based on mixing, sieving and rolling have became widespread.

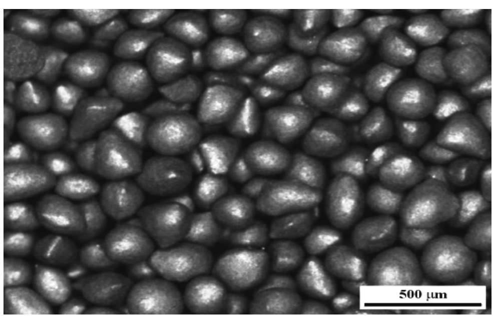


***Fig. 3.18.*** *Fine powder in as-granulated condition*

Irrespective of the processing route, organic binders, e.g. poly (butyl methacrylate), poly (alkyl methacrylate), polyvinyl butyral, paraffin wax, etc., dissolved in suitable solvents, are used to cement the powder particles together, thereby imparting desired mechanical strength to the granules. It is important that the binder has suitable thermal properties, which permit its complete removal from the material at the hot consolidation step. Otherwise, the sintered parts have higher residual porosity.

### Cold pressing

Prior to hot pressing, cold pressing may optionally be applied in situations where either the electrode has a layered structure or to increase productivity of the hot pressing process since, as exemplified in Figure 3.19, the purpose-designed graphite mould yields more sintered parts per hot pressing cycle than the conventional one filled with loose powder.

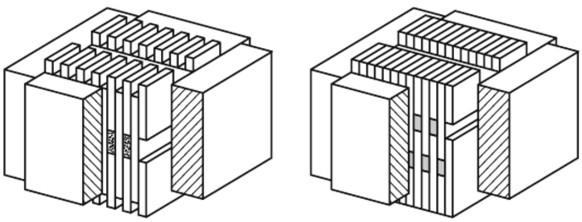

***Fig. 3.19.*** *Graphite moulds designed to accommodate either loose powder mixture (left) or green segments (right)*

Typical cold pressing operations are performed in steel dies, at low to medium pressures, utilising the double-action pressing principle. There are two types of machinery used in the powder metallurgy industry. The conventional presses are fitted with either vibratory or screw powder feeders and precision scales used to weigh out the correct amount of the powder mix to fill the die. Alternatively, the machines may incorporate feed shoes operating on the volumetric filling principle. The gravimetric presses offer higher flexibility necessary to manufacture sintered parts in smaller quantities [43] but, despite higher investment costs attributed in part to obligatory use of granulated powders, the volumetric equipment is the preferred option for mass production due to its 3-4 times greater throughput, longer life of steel dies and lower cost of other pressing consumables [44-45].

### Hot pressing

The hot pressing process consists of a simultaneous application of heat and pressure in order to obtain a product nearly free from internal porosity. Compared to the conventional cold pressing/sintering PM route, hot pressing requires merely 2-3 min hold at markedly lower temperature, but under a compressive stress, to reach higher density level.

The hot pressing of powders, or green compacts, is generally realised in high-resistance graphite moulds (Fig. 3.20) by passing electrical current directly through the mould, as schematically shown in Figure 3.21.

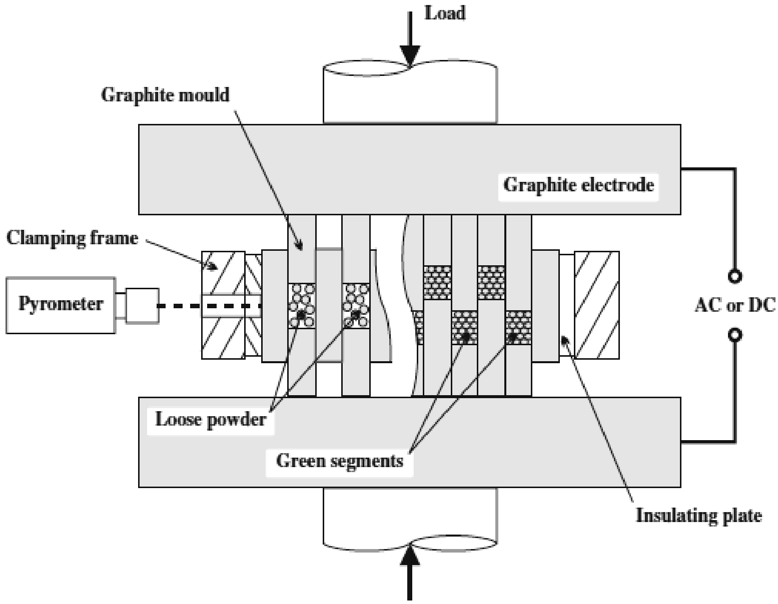


***Fig. 3.20.*** *Schematic representation of the hot pressing process*

***Fig. 3.21.*** *Hot pressing operation carried out in air*

This method offers high efficiency in production of sintered parts, at elevated temperatures, assists in protecting metallic powders against oxidation. The protection is attributed to the formation of a $CO/CO_2$ reducing atmosphere inside the graphite mould which, in the old-type equipment shown in Figure 3.21, is exposed to air.

The modern hot presses, exemplified in Figure 3.22, are fitted with protective gas chambers wherein the moulds are heated in nitrogen and therefore their service life is markedly increased.

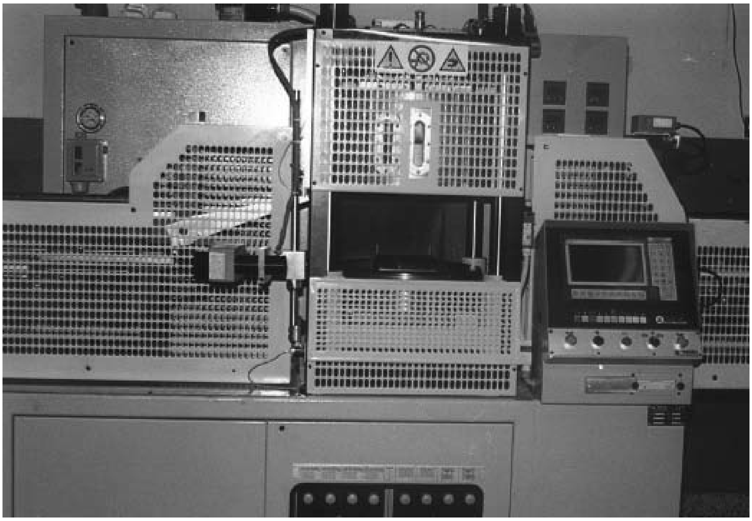

***Fig. 3.22.*** *Hot press equipped with a protective atmosphere chamber*

Deburring, quality control and finishing operations

The vast majority of sintered components require cleaning and removing edge residuals after consolidation. This is carried out during the deburring operation, which is usually performed by means of tumbling the parts extracted from the graphite mould with coarse alumina or silicon carbide grit.

The quality control of sintered electrodes may be limited their visual inspection although, hardness test and evaluation of the as-sintered density may optionally be carried out.

Grinding is usually the final operation which allows attachment of the electrode into a suitable electrode holder of the ESD apparatus.

### 3.2.4. MATERIALS AND TREATMENT PARAMETERS

In the experiment, the coatings were electro-spark deposition using a WC-Cu (50% WC and 50% Cu) electrode with a cross-section of 4 x 6 mm – the anode – onto samples made of carbon steel C45 – the cathode. The main characteristics of the powders used in this work are included in Table 3.7.

***Table 3.7.*** *Powders used to manufacture cermet electrodes*

| Powder | Particle Size, µm | Producer |
|---|---|---|
| WC | ~0.2* | OMG |
| Cu | ~0.04* | NEOMAT |

** measured using Fisher Sub-Sieve Sizer*

The equipment used for electro-spark deposited was an EIL-8A model. Basing on the results of previous research as well as instructions given by the producer, the following parameters were assumed to be optimal for ESA:

- voltage $U = 230$ V,
- capacitor volume $C = 150$ µF,
- current intensity $I = 0.7$ A.

Then, the coatings were treated with an Nd:YAG laser (impulse mode), model BLS 720. The samples with electro-spark deposited coatings were laser-modified at the following parameters:

- spot diameter d = 0.7 mm,
- power $P = 60$ W,
- laser beam velocity $v = 250$ mm/min,
- nozzle-workpiece distance $\Delta f = 6$ mm,
- pulse duration $t_i = 0.4$ ms,
- pulse repetition frequency $f = 50$ Hz,
- beam shift jump $S = 0.4$ mm,
- nitrogen gas shield $Q = 25$ l/min.

### 3.2.5. RESULTS OF INVESTIGATIONS AND DISCUSSION

#### Measurements of the surface geometric structure and roughness

Surface geometric structure (SGS) substantially influences many processes that occur in the outer layer. A lot of publications deal with measurement methods and the assessment of surface roughness and waviness [46-47].

Measurements of surface geometric structure were carried out at the Laboratory of Computer Measurements of Geometric Quantities of the Kielce University of Technology. Those were performed using Talysurf CCI optical profiler that employs a coherence correlation algorithm patented by Taylor Hobson company. The algorithm makes it possible to take measurements with the resolution in the axis *z* below 0.8 nm. The result of measurements is recorded in 1024 x 1024 measurement point matrix, which for the x10 lens yields the 1.65 mm x 1.65 mm measured area and the horizontal resolution 1.65 µm x 1.65 µm.

Three-dimensional surfaces and their analysis with TalyMap Platinum software made it possible to precisely identify the geometric structure of the surfaces under consideration. Table 3.8 provides major parameters of the surface geometric structure of the examined specimens.

*__Table 3.8.__ Parameters of the surface geometric structure*

| SGS parameters | Coating | |
|---|---|---|
| | **WC-Cu** | **WC-Cu + laser** |
| *Sa* [μm] | 4.02 | 6.95 |
| *Sq* [μm] | 5.24 | 8.48 |
| *Ssk* | 0.15 | 0.02 |
| *Sku* | 3.89 | 2.77 |
| *Sp* [μm] | 26.44 | 34.03 |
| *Sv* [μm] | 21.21 | 66.76 |
| *Sz* [μm] | 47.65 | 100.80 |

Figures 3.23-3.26 present images of surface topography, distribution of ordinates with bearing curves, isotropy diagrams and the specimen autocorrelation function before and after laser treatment.

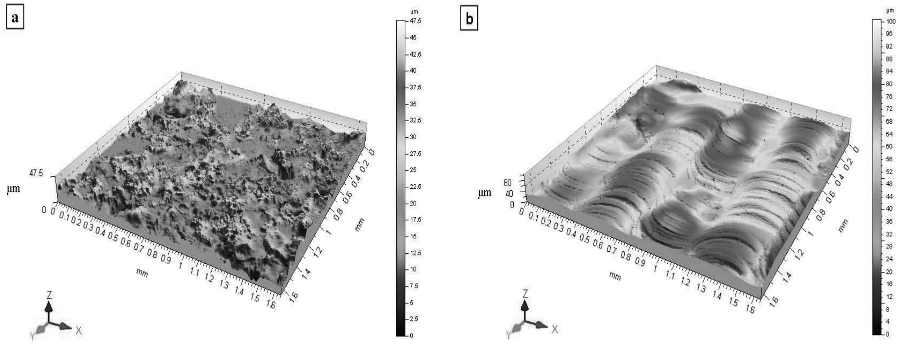


*__Fig. 3.23.__ Specimen surface topography: a) before laser treatment, b) after laser treatment*

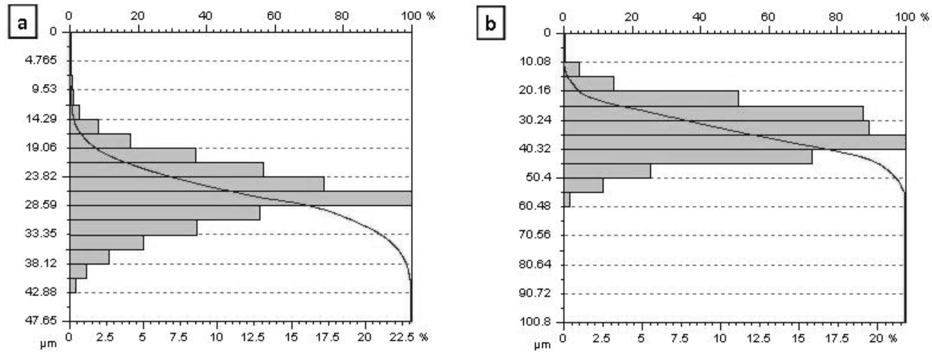


*__Fig. 3.24.__ Distribution of ordinates and specimen bearing curves: a) before laser treatment, b) after laser treatment*

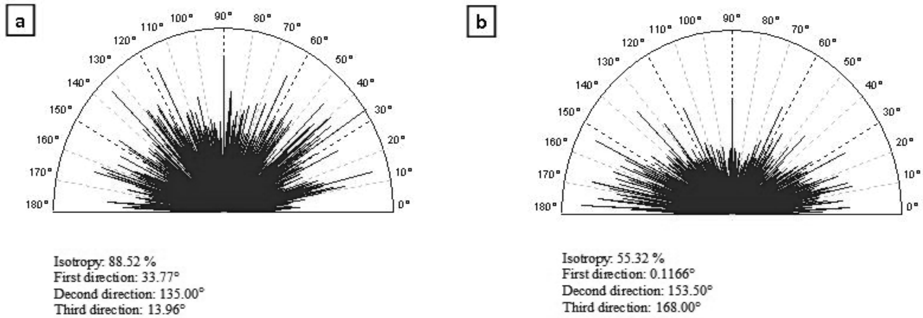


***Fig. 3.25.*** *Specimen isotropy: a) before laser treatment, b) after laser treatment*

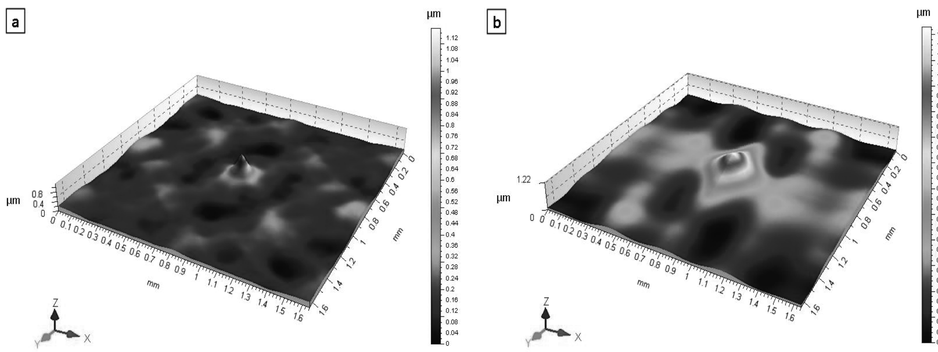


***Fig. 3.26.*** *Specimen autocorrelation function: a) before laser treatment, b) after laser treatment*

A greater value of the mean arithmetic deviation of surface roughness *Sa*, a basic amplitude parameter in the quantitative assessment of the state of the surface under analysis, was recorded for the specimen after the laser treatment, for the specimen before the laser treatment the value of this parameter was almost twice smaller. A similar tendency is observed for the root mean square deviation of surface roughness *Sq*. Complementary information on how the surface of examined elements is shaped is provided by amplitude parameters, namely the coefficient of skewness (asymmetry) *Sku* and the coefficient of concentration (kurtosis) *Ssk*. Those parameters are sensitive to occurrence of local hills or valleys, and also defects on the surface. The parameter *Ssk* has a positive value for both specimens, the value is close to zero for the specimen before treatment, which indicates the symmetrical location of the distribution of ordinates with respect to the mean plane. The values of kurtosis that were obtained are close to *Sku* = 3, which indicates that the distribution of ordinates for both specimens is close to normal distribution.

Before laser treatment, the specimen had random isotropic structure (Iz = 88.52%), whereas after the treatment, that became a periodic structure, located in the transient area between isotropic and anisotropic structures (Iz = 55.32%). That is confirmed by the shape of the autocorrelation function of both surfaces, for the surface before treatment, the shape is circular and symmetrical, whereas for the surface after treatment, it is asymmetrical and elongated.

The roughness of the WC-Cu coatings was quantitatively assessed using the Talysurf CCI optical profiler. Roughness profiles are routinely measured by dragging a stylus along the laser beam path whereas the maximum values of the arithmetic average departure from the surface plain are reported to occur in the perpendicular direction. Therefore in this study an average value of Ra was calculated for each coating from readings taken on evenly divided sampling lengths running parallel to the electrode/laser beam motion and on similar lengths at 90º. It was found that the employed surface treatments increased the average roughness value (Ra) from 0.41÷0.44 μm for the C45 steel substrate up to 2.37-3.67 μm and 3.05÷4.26 μm for the WC-Cu coatings in as-deposited and laser treated condition, respectively.

Figures 3.27 and 3.28 presents an example two-dimensional surface microgeometry measurement of the WC-Cu coatings before and after laser treatment.

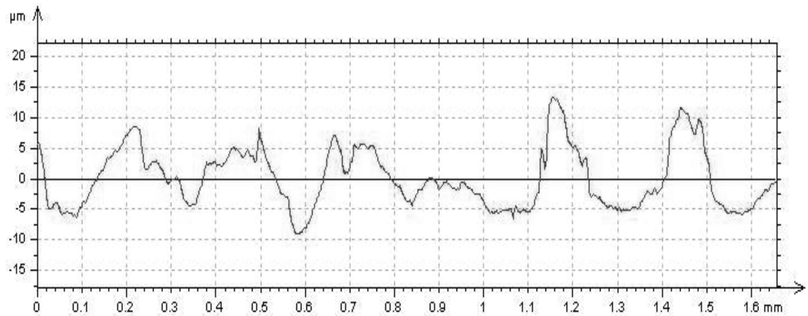


***Fig. 3.27.*** *Surface microgeometry of the WC-Cu coating deposited*

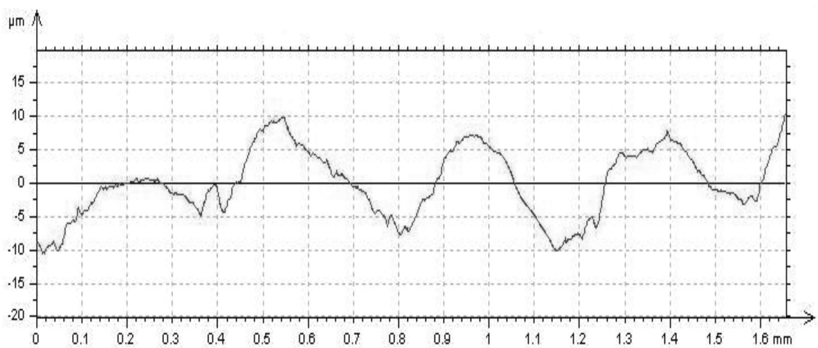


***Fig. 3.28.*** *Surface microgeometry of the WC-Cu coating deposited after laser treatment*

From the measurement results it is clear that there is an increase in the roughness of the WC-Cu coatings after laser treatment. The higher roughness resulted from the tensile forces acting on the surface, and accordingly, the motion of the liquid metal. A non-uniform distribution of temperature in a laser beam (mod $TEM_{00}$) caused the non-uniformity of the surface profile after solidification, which, to some extent, reflects the distribution of energy in the melted zone. If pulse laser treatment is applied, it is assumed that the main factor affecting the surface profile after solidification is the pressure of vapor causing the disposal of the material from the central zone and the production of characteristic flashes on the boundary between the melted and unmelted zones.

## Tribological tests

Investigations into friction resistances (technically dry friction) were performed using T-01M pin-on-disk type tribological tester. The specimens were rings of C45 carbon special steel, onto which WC-Cu coatings (before and after laser treatment) were electro-spark deposited. The counter specimen was a ball, ϕ6.3 mm in diameter, made of 100Cr6 steel.
Tribological tests were conducted for the following friction parameters:

- linear speed $v$ = 0.8 m/s,
- test duration $t$ = 3600 s,
- range of load changes $Q$ = 4.9; 9.8; 14.7 N.

An exemplary graph (Fig. 3.29) shows friction coefficient profiles as a function of time for the load of 14.7 N. The graph presented in Figure 3.22 refers to the tests on WC-Cu coating before and after modification with a laser beam.

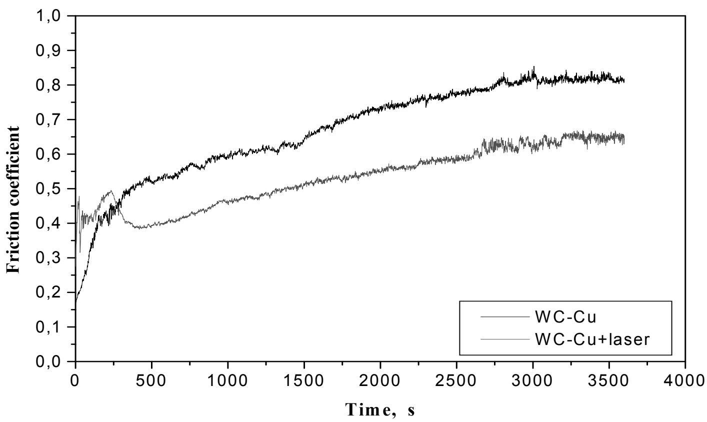


***Fig. 3.29.*** *Relationship between friction coefficient and time*

In technically dry friction, in the examined coating, the technological surface layer (TSL) was transformed into a functional surface layer (FSL). The effect was produced mainly due to sliding stresses and speed and the action of the atmosphere of the environment close to the tested surface. The stabilisation of the state of anti-wear surface layer was observed (AWSL).

In the profile (Fig. 3.29) that refers to the WC-Cu coating, it can be seen that the stabilisation of the friction coefficient takes place after approx. 3.000 seconds, the stabilisation value ranges 0.80-0.82. As regards the WC-Cu coating after laser modification, one can see that the stabilisation of the friction coefficient occurs after 3200 seconds, and the value of stabilisation is included in the range 0.61÷0.64. The average friction coefficient of the WC-Cu coating is approx. 22% higher than the friction coefficient of the WC-Cu coating after laser irradiation (at an instant of the stabilisation of the coefficients). This effect might be produced due to the elimination of surface defects (microcracks and pores) after laser treatment.

Seizure resistance tests were carried out using T-09 tribological tester, in which the friction pair consisted of a cylinder and two prisms. Prisms with deposited WC-Cu coatings and C45 steel (laser treated and untreated) acted as specimens, whereas a roller of hardened carbon steel, $\phi$6.3 mm in diameter, was a counter-specimen. In tests, three kinematic pairs were employed to investigate different material options, which made it possible to average experimental results. During the test, paraffin oil bath lubrication was used.

Figure 3.30 presents cumulative information on average values of seizure load for specimens before and after laser treatment. Those indicate that laser treatment resulted in an increase in the load that produced seizure both for electro-spark deposited coatings and for C45 steel.

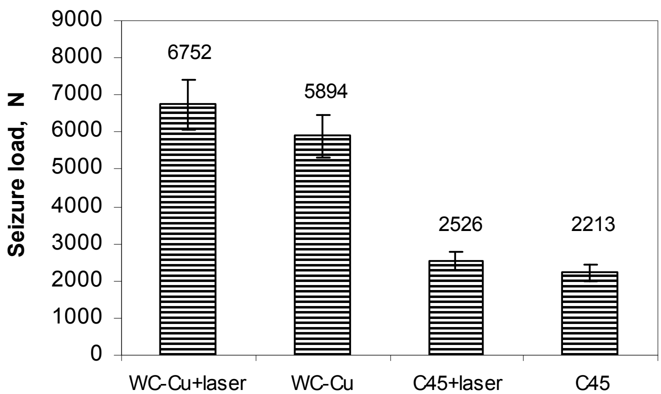


***Fig. 3.30.*** *Average values of seizure load*

Exemplary graphs (Fig. 3.31) show the dependence of load and friction values as a function of time as recorded in the tests. The patterns are typical of seizure tests conducted with T-09 instrument. An increase in the load is accompanied by a respective increase in friction force. Consequently, increasing the load applied to the sliding pair leads to such an increase in the friction force that the copper pin is broken and the test is interrupted. The maximum value of the load, at which seizure occurs and the time that elapsed from the beginning of the test, can be read from the graphs recorded.

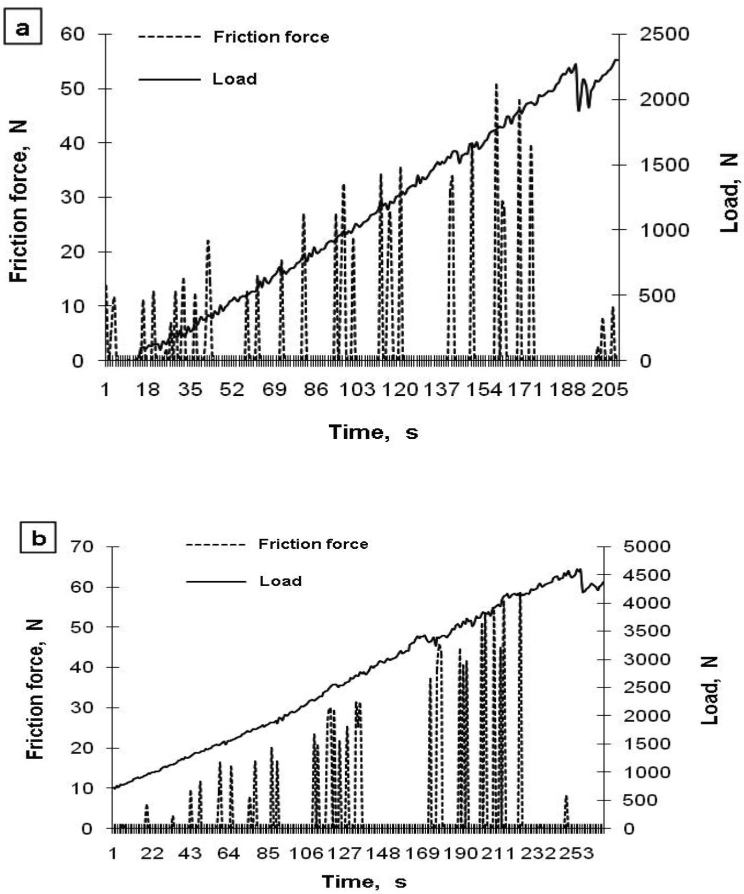


*Fig. 3.31. Dependence of friction force and load as a function of time: a) C45 steel, b) WC-Cu coating*

## Analysis of the coating microstructure

A microstructure analysis was conducted for WC-Cu coatings before and after laser treatment using a scanning electron microscope Joel JSM-5400.

In Figure 3.32 selected view of the surface microstructure of an electro-spark alloying WC-Cu coating is illustrated. It is clear that the thickness of the obtained layers was 36 to 60 μm, whereas the heat affected zone (HAZ) ranged approximately 20 to 30 μm into the substrate, one can see a Figure 3.32 also reveals a clear boundary between the coating and the substrate and pores within microcracks are observed. The electro-spark alloying WC-Cu coatings were modified by the laser treatment, which caused their composition changes. The laser treatment leads to the homogenizing of the coating chemical composition, structure refinement, and crystallization of phases supersaturated due to the occurrence of temperature gradients and high cooling rate.

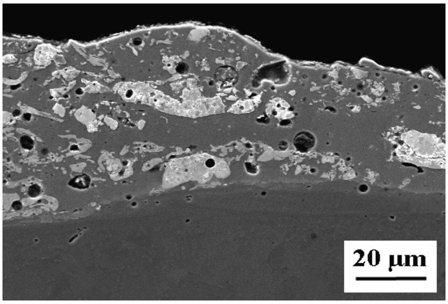


*Fig. 3.32. WC-Cu coating microstructure after electro-spark alloying*

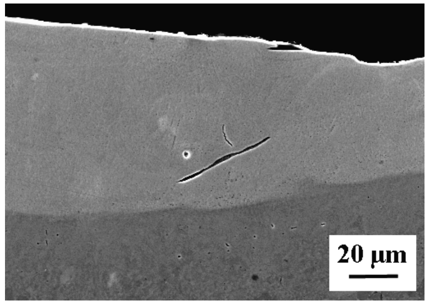


*Fig. 3.33. Microstructure in the electro-spark alloying WC-Cu coating after treatment with an Nd:YAG laser*

The laser-modified outer layer does not possess microcracks or pores (Fig. 3.33). There is no discontinuity of the coating-substrate boundary. The thickness of the laser-treated WC-Cu coatings ranges from 40 to 62 μm. Moreover, the heat affected zone (HAZ) is in the range of 25 to 35 μm, and the content of carbon in the zone is higher.

## X-ray diffraction analysis

Using the roentgen diffraction method, the analysis of the phase composition of the examined coatings was performed with Philips PW 1830 instrument. Kα filtered radiation of a lamp with Cu anode, powered at 40 kV voltage, 30 mA current intensity, was employed. Tests were carried out for the angle 20 in the range 30°-60° and the scanning velocity of 0.05°/3 seconds.

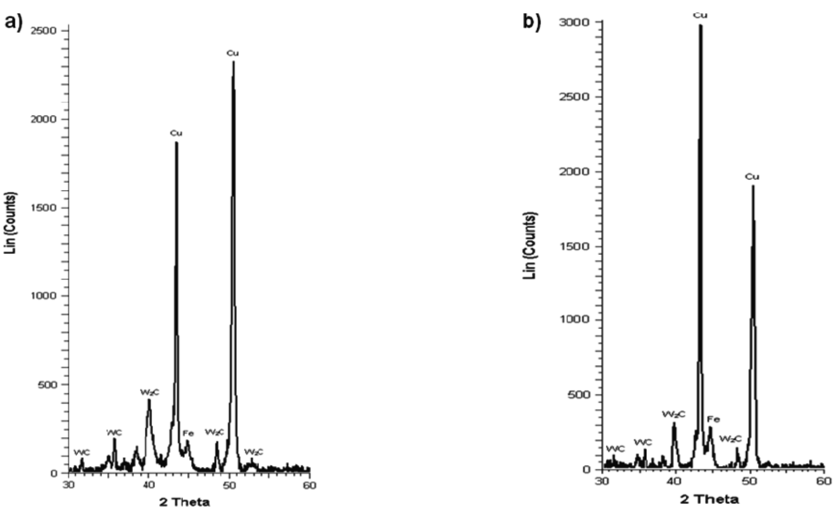


*Fig. 3.34. X-ray diffraction pattern of the WC-Cu coating: a) before laser treatment, b) after laser treatment*

The analysis of the phase composition of the WC-Cu coating (Fig. 3.34a) revealed that the surface layer of the coating consisted mainly of Cu and $W_2C$ and a small admixture of WC and Fe. Laser treatment did not cause the melting of the WC-Cu coating to penetrate into the substrate material (Fig. 34b). The surface layer of the WC-Cu coating after laser treatment has the same composition as that of the coating before the treatment. The most intense peaks originate from Cu (Fig. 3.34a and 3.34b).

### Microhardness tests

The microhardness was determined by using the Vickers method (Microtech MX3 tester). The measurements were performed under a load of 0.4 N. The indentations were made in perpendicular microsections in three zones: the white homogeneous difficult-to-etch coating, the heat affected zone (HAZ) and the substrate. The test results for the electro-spark deposited WC-Cu coating before and after laser treatment are shown in Tables 3.9 and 3.10. Electro-spark deposition caused changes in the microhardness of the material. The microhardness of the substrate after electro-spark deposition was on average 278 HV0.4; the same value was reported for the substrate before the process. There was a considerable increase in microhardness after depositing the WC-Cu coating. The microhardness of the WC-Cu coating was approx. 643 HV0.4, which gives increase of 131%. The microhardness of the WC-Cu coating in the heat affected zone (HAZ) after electro-spark treatment was 58% higher than that of the substrate material. Laser treatment had a favorable effect on the changes in the microhardness of the electro-spark deposited of the WC-Cu coating. There was an increase of 122% in the microhardness of the WC-Cu coating.

***Table 3.9.*** *Results of the microhardness tests for the WC-Cu coating before laser treatment*

| Measured zones | Microhardness HV0.4 | | | Mean value HV0.4 |
|---|---|---|---|---|
| | Measurement number | | | |
| | 1 | 2 | 3 | |
| **Coating** | 652 | 691 | 585 | 643 |
| **HAZ** | 428 | 464 | 421 | 438 |
| **Substrate** | 262 | 297 | 275 | 278 |

***Table 3.10.*** *Results of the microhardness tests for the WC-Cu coating after laser treatment*

| Measured zones | Microhardness HV0.4 | | | Mean value HV0.4 |
|---|---|---|---|---|
| | Measurement number | | | |
| | 1 | 2 | 3 | |
| **Coating** | 594 | 621 | 635 | 617 |
| **HAZ** | 391 | 397 | 432 | 407 |
| **Substrate** | 276 | 288 | 273 | 279 |

Conclusions:

1. A concentrated laser beam can be effective at modifying the state of the outer layer of electro-spark coatings and thus can modify their functional properties.
2. Laser irradiation of coatings resulted in the healing of micro-cracks and pores.
3. Parameters of surface geometric structure of electrospark coatings have lower values when compared with SGS parameters of coatings after laser treatment.
4. The surface layer of the WC-Cu coating before and after laser treatment consists mainly of Cu and $W_2C$ and a small admixture of WC and Fe.
5. The average friction coefficient obtained for WC-Cu coating in tribological tests is approx. 22% higher than the friction coefficient of the WC-Cu coating after laser modification (at the instant of their stabilisation).
6. Laser treatment caused an increase in the load at which seizure occurred for the tested materials. For laser-treated WC-Cu coatings, the value of the load is approx. 13% higher when compared with coated specimens without laser treatment.
7. Laser treatment caused a 9% decrease in the microhardness of the electro-spark alloying WC-Cu coatings.
8. Coatings of that type can be applied to sliding friction pairs and can operate as protective coatings.
9. Further research should involve measurements of internal stresses and investigations into the porosity of electrospark coatings before and after laser treatment.

## 3.3. PRODUCTION OF HETEROGENEOUS SURFACES BY ELECTRO-SPARK DEPOSITION AND LASER BEAM MACHINING

*Norbert Radek*

### 3.3.1. HETEROGENEOUS SURFACES

During tribological investigations was found that employed heterogeneous surfaces models into boundary interaction of solid surfaces make significant improvement [48]. Surfaces described as heterogeneous consist of areas, which are different one from another in geometrical, physicomechanical or physicochemical properties. The heterogeneity of surfaces is frequently due to the application of more than one technology, and can be constituted by [49-58]:

- shaped surface features such as grooves, pits or channels resulting from milling, eroding, etching, laser-beam forming, etc.;
- areas with different physicochemical and physicomechanical properties, e.g. areas with diversified hardness and mechanical strength accomplished by local surfacing or selective surface hardening (e.g. electron-beam machining, laser-beam forming or thermochemical treatment);

– areas with diversified surface microgeometry, e.g. areas eroded at the points of focus (laser treatment or electro-spark deposition), or areas with formed surface microgeometry, for instance, in terms of desired microroughness directivity or load capacity (LBM and ESD technologies).

Heterogeneous surfaces can be obtained by different methods. The laser treatment of electro-spark deposited coatings being one of them [54-56].

The first publication on surface texturing appeared in Germany in 1993 [59]. It discussed the use of an excimer laser to texture elements of a magnetic memory disk drive with the aim of reducing friction at the start. Further experiments in this area involved texturing surfaces of punches applied to plastic forming. It was found that the process caused a 169% increase in the punch service life.

The current studies focus on the influence of texturing on the performance of various friction systems in internal combustion engines, e.g. precision bearing systems. Texturing is used to improve heat removal, vaporization, wettability, biological functions, absorptivity, etc.

Reference [60] analyzes the relationships between the parameters of performance and the parameters of surface texture for a mechanical seal. In this model approach, the considerations involve solving the Reynolds equation transformed into a dimensionless form for a face seal with one textured ring. The texture is created by a number of circular pores. The radius of a pore is several times greater than the depth. The results of the theoretical investigations are presented in the form of dimensionless relations, including the ratio of the cavity depth to the cavity diameter and the ratio of the area with pores to the whole surface area (pore area coverage) as well as the dimensionless pressure and the leak tightness, Λ.

$$\Lambda = \frac{6 \cdot \mu \cdot U \cdot r_p}{p_a \cdot C^2} \tag{3.7}$$

where: $\mu$ – fluid dynamic viscosity [Pa · s], $U$ – sliding velocity [m/s], $p_a$ – ambient pressure [Pa], $C$ – clearance height [m], $r_p$ – cavity diameter [m].

The references quoted in this paper indicate that the cavity diameter and the pore area coverage have a negligible effect on the average pressure in the clearance. Of importance, however, seems to be the depth-to-diameter ratio, which can be optimized for the pre-determined parameter Λ. From the analysis it is clear that the effectiveness of micropores is dependent on the relationships between the hydrostatic and hydrodynamic effects. If the cavitation in micropores is eliminated by applying suitable parameters of performance, then the hydrostatic effects predominate and the effect of laser texturing is not significant; in consequence, the surfaces behave like non-textured ones.

An increase in the parameter Λ causes that the hydrodynamic effect of microcavities is more visible. The effect is determined basing on the value of the average pressure in the clearance. In addition, there exists an optimal value of $h_p/2r_p$, which is equal to 0.05 for $\Lambda$=1, and decreases with an increase in the parameter $\Lambda$.

Reference [61] compares results of tribological tests conducted by means of pin-on-disk devices, where the disk surfaces were polished, ground and textured (using three methods of texturing). The textured surface was covered with laser-generated pores, 4-6.5 μm in depth and 58-80 μm in diameter. Numerous tests show that texturing can be used to extend the ranges of load and sliding velocity within which hydrodynamic lubrication occurs. The hydrodynamic lubrication is observed when low- and high-viscosity lubricants are applied. Another finding is that the rough rims of cavities produced by laser beams need to be removed by lapping to ensure an optimal hydrodynamic effect. A comparative analysis was conducted to determine the friction coefficients for the polished, ground and textured surfaces. The effects of laser texturing were most visible when the values of sliding velocity were low, ranging between 0.075 and 0.3 m/s. Moreover, the high density of cavities was responsible for an increase in the friction coefficient. The results presented in the form of Stribeck curves illustrate that there was a significant reduction in friction for lubricated friction pairs operating in the boundary regime of friction.

The tests described [62] aimed at determining the effect of laser texturing on the performance of a ring being in contact with a cylinder liner. Pores with diameters of 75-78 μm and depths of 7-9 μm covered the whole or parts of the ring surface. The pore area coverage ranged between 10 and 50%. The friction observed for textured surfaces was lower than that for non-textured ones. The greatest falls in friction were reported for a pore area coverage of 30%; they were 40-45% and 23-35% for a rotational speed of 500 rev/min and 1200 rev/min, respectively. It should be noted that the decrease in friction was greater for a partly textured ring. This reduction (12-29%) was observed in the whole range of loads and rotational speeds.

Reference [63] discusses results of in-service tests conducted for face seals with textured carbide rings used in the petrochemical industry. The results were positive, because there was a decrease in the process temperature and an increase in the ring service life. Reference [64] illustrates that laser surface texturing caused an improvement in fretting fatigue life of steel tool elements.

This analysis shows that the effects of laser texturing were measured at pre-determined parameters of performance of the sliding pair; the pore depth and diameter (or their ratio) and the pore area coverage were the most significant parameters of texturing. It was found that effective reduction in friction could be obtained also for partially porous surfaces. The problems to be solved in further research include determining precisely the relationships between the texturing parameters, ring geometry, and the parameters of performance of the friction system for which the desired reduction in friction occurs. The current research focuses on establishing the effect of laser surface texturing on the mechanical properties of materials, particularly their fatigue strength.

### 3.3.2. EXPERIMENTAL

The two stages investigation was carried out. First of all Cu-Mo coatings were electro-spark deposited on C45 steel coupons and after that they were modified by Nd:YAG laser beam. The copper inside coatings is being fundamental material to created of low-friction surface layers. It is itself also internal stresses compensator. This material is characterized by good thermal conductivity, which can be very helpful in high loaded contacts – heat can be taken away into material core from friction zone. The other selected element was molybdenum as an important strengthens surface content. Mo is also helpful into creation of hard phase compounds, e.g.: MoC. In practical meanings this compound will improve durability of tools kinematics pairs. The electro-spark deposition of Cu and Mo wires with a diameter of 1 mm was performed by means of an ELFA-541, a modernized device made by a Bulgarian manufacturer. The subsequent laser treatment was performed with the aid of a BLS 720 laser system employing the Nd:YAG type laser operating in the pulse mode. The chemical composition of the steel is presented in Table 3.11.

***Table 3.11.*** *Chemical composition of C45 steel*

| Elements | C | Mn | Si | P | S |
|---|---|---|---|---|---|
| Content in weight, % | 0.42 to 0.50 | 0.50 to 0.80 | 0.10 to 0.40 | 0.04 | 0.04 |

The parameters of the electro-spark deposition established during the experiment include: current intensity $I$ = 16A (for Cu $I$ = 8A); table shift rate $v$ = 0.5 mm/s; rotational speed of the head with electrode $n$ = 4200 rev/min; number of coating passes $L$ = 2 (for Cu $L$ = 1); capacity of the condenser system $C$ = 0.47 μF; pulse duration $Ti$ = 8 μs; interpulse period $Tp$ = 32 μs; frequency $f$ = 25 kHz.

The main aim of carried out investigations was:

- observing the surface state by means of a stereoscopic microscope,
- microstructure analysis of a scanning microscope,
- analyzing the surface macrogeometry,
- measuring the microhardness with the Vickers method.

### 3.3.3. RESULTS AND DISCUSSION

The heterogeneous Cu-Mo coatings structure after electro-spark deposition on steel coupons and eroded by laser beam were investigated. The observation was done by OLYMPUS SZ-STU2 stereoscopic microscope.

The erosion was performed with the point pulsed-laser technique using the Nd:YAG type of laser under the following conditions:

– laser spot diameter, $d = 0.7$ mm,
– laser power, $P = 10$; 20; 30; 40; 50; 100 and 150 W,
– beam shift rate, $v = 1200$ mm/min,
– nozzle-sample distance, $h = 1$ mm,
– pulse duration, $Ti = 0.8$; 1.2; 1.48; 1.8; 5.5 and 8 ms,
– frequency, $f = 8$ Hz.

As can be seen from Figures 3.35 and 3.36, the effect of the laser erosion action is in the form of craters. The first one is showing lower laser power ($P = 20$ W) interaction effect on the treated surface (Fig. 3.35). The second one is illustrating phenomenon (Fig. 3.36), where 5 times laser power was increased ($P = 100$ W). The cavity depth depends mainly on the laser power density and the pulse duration. Coatings with such geometry have various tribological applications. By rubbing the surface selectively, it is possible to produce cavities inside which hydrodynamic forces can be generated during fluid film lubrication. Moreover, the hard areas around the cavities are capable of bearing normal loads.

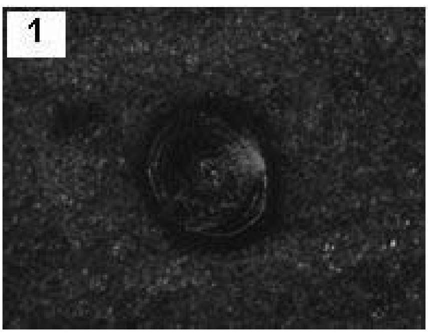


***Fig. 3.35.*** *Stereoscopic photograph of a Cu-Mo coating laser-eroded at 100 W (x57 magnification)*

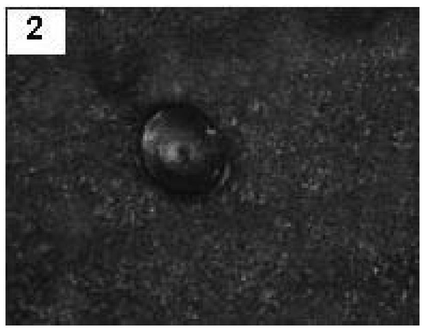


***Fig. 3.36.*** *Stereoscopic photograph of a Cu-Mo coating laser-eroded at 20 W (x57 magnification)*

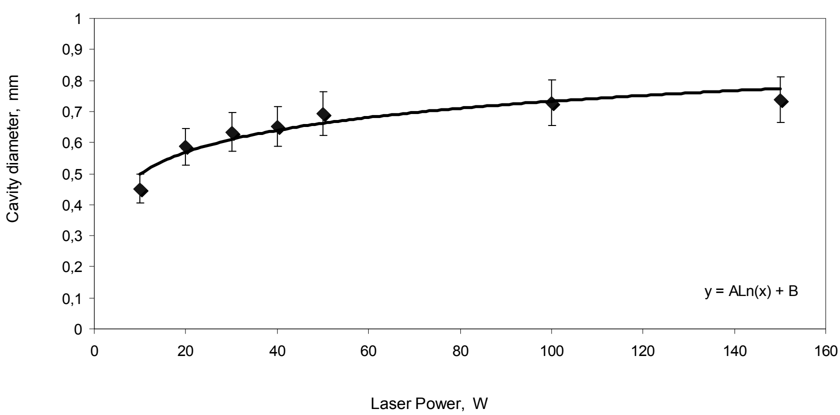


***Fig. 3.37.*** *Interdependence of cavity diameter and laser power*

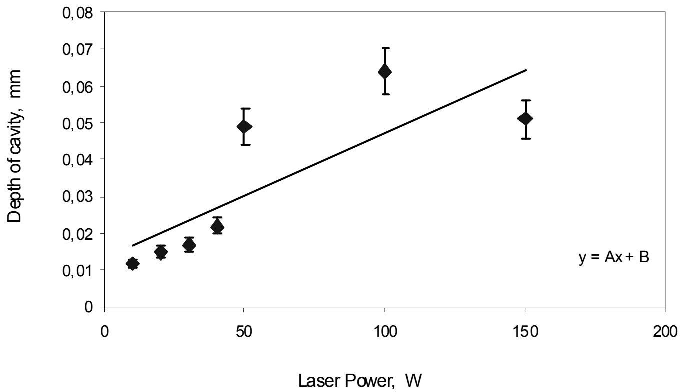


***Fig. 3.38.*** *Interdependence of cavity depth and laser power*

The investigations of the effects of the laser erosion involved measuring the diameters and depths of the cavities obtained at different laser powers. The results of the measurement performed with a PG-2/200 form surfer are presented in the form of graphs in Figures 3.37 and 3.38. It was noticed that higher laser beam power gives greater diameter and depth of the cavities. An exception is the cavity depth produced at 150 W. The value is smaller than that obtained at 100 W (Fig. 3.37). This might have been due to a considerable pulse duration ($t_i$ = 8 ms), the laser power being 150 W. However, if $P$ = 100 W, the pulse duration $t_i$ was 5.5 ms. In the case of lasers operating in the pulse mode, the power is averaged in time; thus, if the pulse durations are long, the laser beam is less effective.

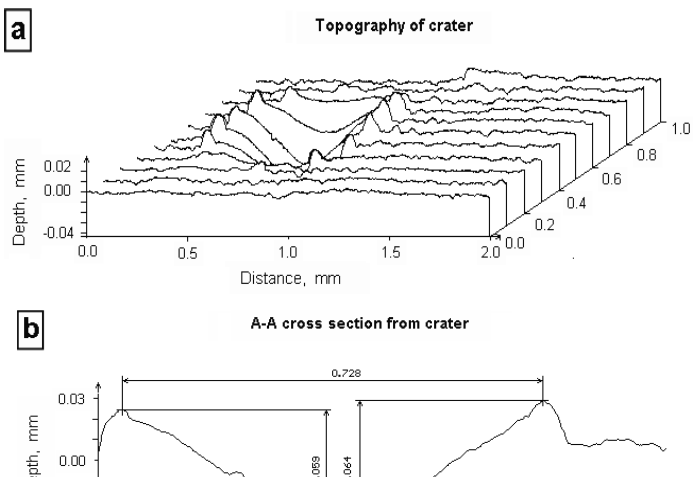


***Fig. 3.39.*** *Macrogeometry and cross section of eroded by laser crater: a) 3D crater topography; b) A-A cross section on Figure 3.35*

A 3D macrogeometry of the developed heterogeneous surface eroded by the laser craters for the used specimens with build in 2-D crater cross section A-A (Fig. 3.35) is shown on Figures 3.39a and 3.39b. As can be concluded from these built graphs crater edges are sharp and are advanced up to 0.03 mm above an average height, just treated by ESD surface, what is within a range of tolerances for designed clearance fit. The average size of the crater shown on Figure 3.35 produced by laser power 100 W has diameter about 0.7 mm and the total depth about 0.06 mm. The crater is going below so-called "ground zero level" by down to 0.030 mm. For instance, crater displayed on Figure 3.36, produced by laser power 20 W has diameter about 0.05 mm and depth of 0.015 mm. Produced crater profile (picks and valleys) and also order of craters location, depending on the required or desired surface performance, could be controlled and adjusted to acceptable level.

At the next stage, the Vickers microhardness test was conducted with a Chruszczow indenter at a load of 1 N. The measurements concerned Cu-Mo coatings laser-eroded at 20 W. The distribution of microhardness is shown in Figure 3.40.

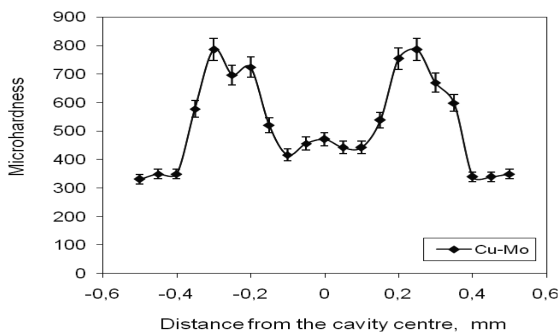


***Fig. 3.40.*** *Distribution of microhardness on the surface of a laser-treated Cu-Mo coating*

It was established that there was an increase in microhardness at the points of laser machining, the increase being strictly related to the changes in the coating structure, and therefore, to the method of laser treatment. The surface hardening at the points of laser interaction and in the heat-affected zone (HAZ) follows the phase changes occurring in the material first heated and then immediately cooled. The microhardness of the substrate (i.e. C45 steel) was, on average, 300 HV. That of the ESD coatings amounted to about 430 HV. The laser treatment of the ESD coatings caused an increase in microhardness to approximately 850-880 HV. In the heat-affected zone, the microhardness fluctuated around 580-630 HV. The laser beam surface forming resulted in changes in the microhardness of electro-spark deposited Cu-Mo coatings.

The next stage of the experiment involved analyzing the changes in the macrogeometry of Cu-Mo coatings. The laser treatment causing the formation of new surface geometry was performed with the BLS 720 Nd:YAG laser operating in the pulse mode, with the process parameters being:

– laser spot diameter, $d = 1.5$ mm,
– laser power, $P = 30$ W,
– beam shift rate, $v = 250$ mm/min,
– nozzle-sample distance, $h = 1$ mm,
– pulse duration, $ti = 0.8$ ms,
– frequency, $f = 8$ Hz.

Examples of images obtained with a stereoscopic microscope for laser-treated Cu-Mo coatings is given in Figure 3.41. In Figure 3.41 is illustrating laser treated are in micro-scale, where higher magnification was applied (x40 magnification).

***Fig. 3.41.*** *Stereoscopic photographs of the laser-treated Cu-Mo surfaces (x40 magnification)*

The investigations of the microgeometry were conducted by means of the PG-2/200 form surfer. The instrument makes it possible to measure the surface form using a contact method and to obtain a 3-D isometric image and a contour map. The isometric image presents a selected fragment of the surface measured in the form of a series of finite profiles displaced by a certain constant vector. The contour map, on the other hand, consists of lines connecting points, each one lying at the same distance from the reference surface. To measure the macrogeometry of Cu-Mo surfaces after laser treatment, it was essential to select a sector of planes with an area of 3 mm by 3 mm.

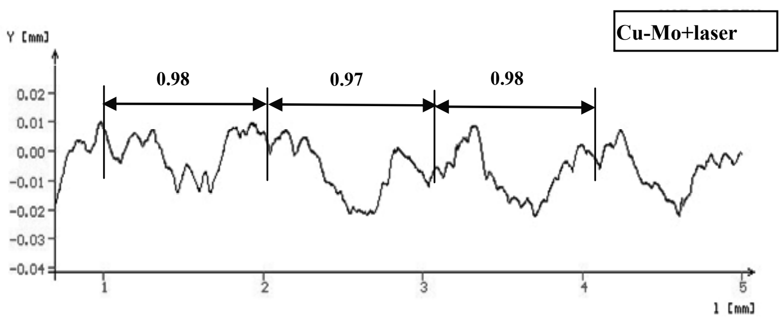


***Fig. 3.42.*** *Two dimensional surface macrogeometry of a Cu-Mo coating after laser treatment*

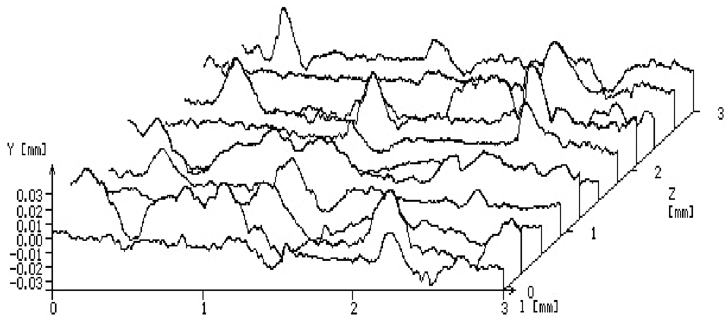


***Fig. 3.43.*** *Three dimensional surface macrogeometry of a Cu-Mo coating after laser treatment*

Figures 3.42 and 3.43 show an example profile and isometric image of a Cu-Mo coating after laser treatment. The convexities visible in Figures above are marks of laser beam passes. The regular intervals between paths constitute a specific surface structure. The first one in Figure 3.42 is showing two dimensional surface macrogeometry of a Cu-Mo coating after laser treatment.

Figure 3.43 shows that the structure is characterized by the occurrence of enclosed areas of cavities with dimensions of approximately 0.98 mm by 0.98 mm. To be used in tribological applications the coatings require additional treatment, i.e. grinding-in. As a result the concavities become flat and hard areas able to bear normal loads. The difference in surface levels before and after the operation amounts to 10 μm and is due to changes in the structure and the specific volume in the zones of laser beam heat impact. The second profile in Figure 3.43 is presenting three dimensional surface macrogeometry of a Cu-Mo coating after laser treatment.

A Joel JSM-5400 scanning microscope equipped with an Oxford Instruments ISIS-300 X-ray microanalyzer was used to test the coating microstructure. Figures 3.44a show the microstructure of electro-spark deposited two-layer Cu-Mo coating. The layer thickness is approximately 8÷10 μm, and the range of the heat affected zone (HAZ) inside the (underlying) substrate material is about 10÷15 μm. In the photograph, the boundary line between the two-layer coating and the substrate is clear. There are microcracks running across and along the coating. A linear analysis of the elements (Fig. 3.44b) of the Cu-Mo coating shows that the distribution of elements is non-uniform; there are zones with greater concentrations of Cu, Mo and Fe. Analyzing the linear distribution of elements, one can see that the adhesion of the coating to the substrate is of diffusive type. There is no clear separation of components either in the Cu-Mo coating (Fig. 3.44b). A higher content of carbon reported in the electro-spark deposited Cu-Mo coating is a result of ascending diffusion. Carbon from the C45 steel substrate travels to the electro-spark deposited technological surface layer (TSL) because of thermal interaction.

The melting and solidifying processes during laser treatment resulted in the migration of elements across the coating-substrate interface. Laser radiation caused intensive convective flow of the liquid material in the pool and, in consequence, the homogenization of the chemical composition (Fig. 3.45b). It also led to the structure refinement and highly saturated phase crystallization (Fig. 3.45a) because of considerable gradients of temperature and high cooling rates. The technological surface layers, produced by laser alloying, were free from microcracks and pores – an effect of surface sealing, and non-continuities across the coating-substrate interface. There was practically no change in the chemical composition of the substrate. The thickness of the fused two-layer Cu-Mo coating ranged 20-40 μm. In the heat affected zone (HAZ), which was 20-50 μm thick, there was an increase in the content of carbon (Fig. 3.45b).

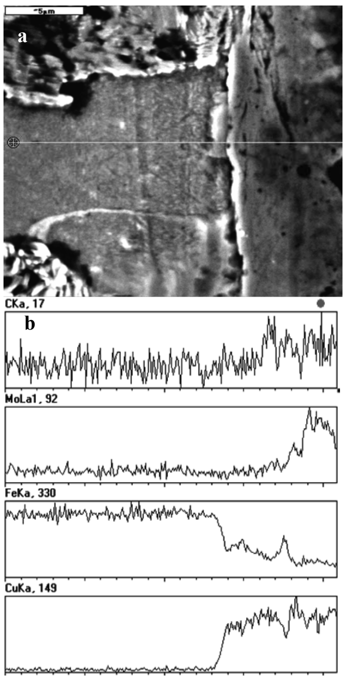


*Fig. 3.44.* *Microstructure (a) and linear distribution of elements (b) in the Cu-Mo coating*

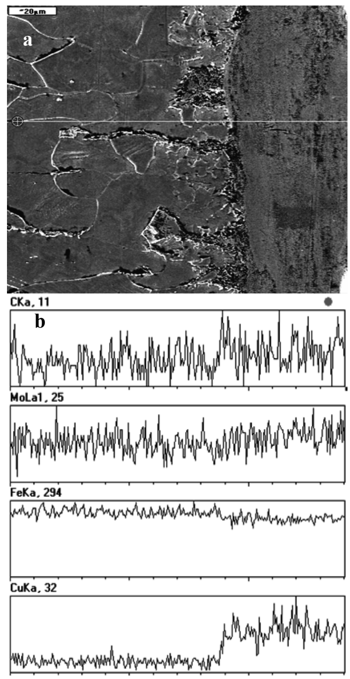


*Fig. 3.45.* *Microstructure (a) and linear distribution of elements (b) in the Cu-Mo coating after laser treatment*

The point analysis conducted for the outer surface of the technological surface layers (TSLs) (Fig. 3.46a) shows high intensity of peaks of the elements present in the coating. The Cu-Mo coating contained 66.07% at. of Cu and 10.98% at. of Mo, which may testify to the mixing of the two elements and the formation of a multi-component alloy (Fig. 3.46a).

The point analysis of the electro-spark coatings treated with a laser beam (Fig. 3.46b) shows high intensity of iron peaks in the alloyed layers. The content of iron in the laser-treated technological surface layers was between 88% at. and 97% at. After laser treatment, the intensity of peaks of Mo, Cu in the electro-spark deposited coatings was lower.

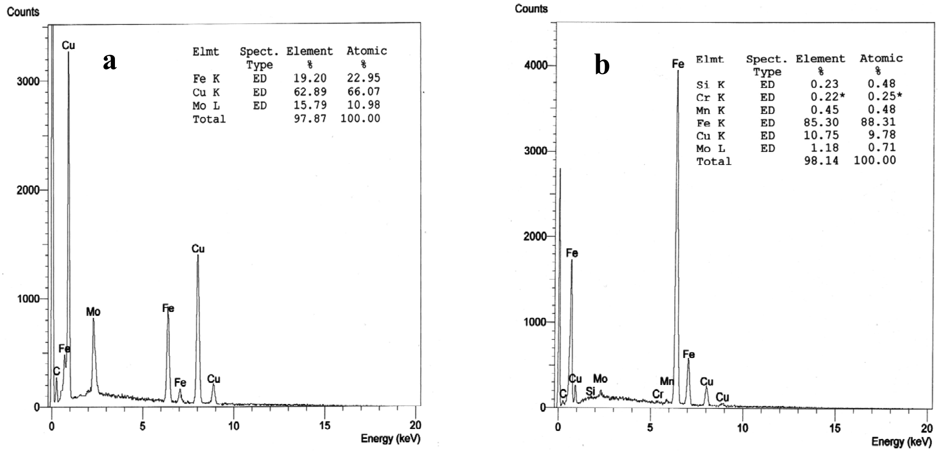


***Fig. 3.46.*** *Spectrum of an X-ray radiation for an electro-spark deposited Cu-Mo coating on a C45 steel substrate: a) before laser treatment; b) after laser treatment*

### 3.3.4. MOBILITY OF FRETTING CONTACT AFTER LASER MELTING OF SURFACE

Significant changes in the ideology of modern production and operation of mechanical systems are relates to the rapid development of computer technology. Exceptionally important role is given the structural integrity of the nominally-fixed frictional joints [65]. Today this area developed on the basis of classical mechanics of solid body (for example, the calculation of interference fits), elasticity theory [66], solid state physics fields of nonlinear contact dynamics, tribology, theory of chaotic oscillations, stochastic theory describing microgeometry surfaces, low amplitude fretting, nanotechnology and more. That focus attention on micromotion with microslip [67-69], is a logical step in approaching research facilities to places early direct damage surfaces, the origin of cracks, plastic deformation of material deterioration and, ultimately, to solve complex problems integrity of nominally-fixed joints and surface modification of parts important structures and unites.

An integral and important part of the problem of integrity of the nominally-fixed frictional joints is a factor of cyclic relative microdisplacements in contact. These phenomena are the subject of special studies of many researchers in mathematics, physics, optics, mechanics, electromechanics. At the beginning of last century tribological side of these phenomena was given in a single concept as **fretting of contact surfaces** [70-71]. Since the second half of the twentieth century is targeted research fretting, as part of increasing longevity and reliability of machine parts.

Fretting is commonly observed on the assembly interfaces of mechanical power transmission components. Typical examples include spline couplings, bearing/housing interfaces and gear/flange interfaces [72]. The fretting action can be caused by shaft misalignments as in the case of spline wear or by mechanical strain differences between mating components, as for gear/flange interfaces. In any event, the occurrence of fretting is marked by surface damage that may include crack initiation, pitting, and debris generation. The consequences often include degradation of component fatigue life, loss of critical assembly tolerance and fouling of moving components by debris [73]. Both the extent of fretting damage and the mechanisms of fretting are affected by a number of factors including slip amplitude, relative humidity, temperature, fretting frequency, normal load, and the materials comprising the fretting pair.

The method, which assess the impact of surface modification by creating a regular relief on the surfaces in long-term ability to maintain the integrity of contact under vibration loads.

Reliability and durability of equipment connect with the need to ensure adequate quality of individual units and elements of their interface that, in the case of **nominally-fixed joints (NFJ)**, often achieved by applying coatings and change the properties of the surface layer.

Among the large number of currently applied of methods for modifying surfaces remains unclear what impact the issue have of processing macrogeometry of surface for long-term ability to maintain the integrity of contact. Macrogeometrical characteristics are especially important for the initial conditions of the contact as significantly affect the elastic characteristics of contact and, consequently, tribological characteristics of the joints.

Surface profile formed in the processing of the surface layer by high-energy methods of such as laser processing, electric-sparks, has the character of regular micro and macro irregularities.

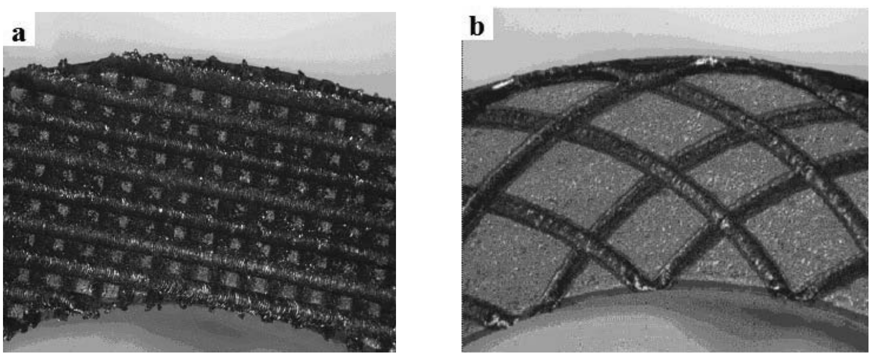


***Fig. 3.47.*** *Coating of steel C45 by the hard alloy of Cu-Mo and next reinforcing by the impulsive laser irradiation (setting of BLS-720) closeness and a) 90% and b) 10% (x10 magnification)*

Therefore, for quantitative and qualitative assessment of the working surface from a position of long-term conservation of the nominal contact of joints parts, in the design stage, it is expedient to apply the methods of mathematical analysis for the definition of the geometry of the surface. In the study of the integrity of nominally-stationary friction joints under cyclic loads were applied surface modification techniques that alter the geometry of the surface layer in a wide range of values – from changes of roughness to a regular macro geometry of surface (Fig. 3.47). It is reasonable to define the criteria that will compare the geometry of surfaces at different ways of surface modification. By uses laser treatment of electro-sparking coating of Cu-Mo is carried out on steel C45 with different character by forming of type. Creation of the reinforced surface enables to change contact stress on the spots of contact and also stiffness of surface in tangential direction. Clearly, that for the increase of the nominal fixing of contact it is necessary to decrease stiffness from one side, and from the second, to increase resistance of surface to stand the cyclic tangential loadings.

### Integrated characteristics of a contact zone

Given the proposed method of surface modification importantly determine the extent of influence of technological aspects on coatings, in particular, step and width of the modified zone. In Figure 3.48 presents the dependence of tangential stiffness of contact surfaces subjected to laser treatment and electric-sparks from the step of processing.

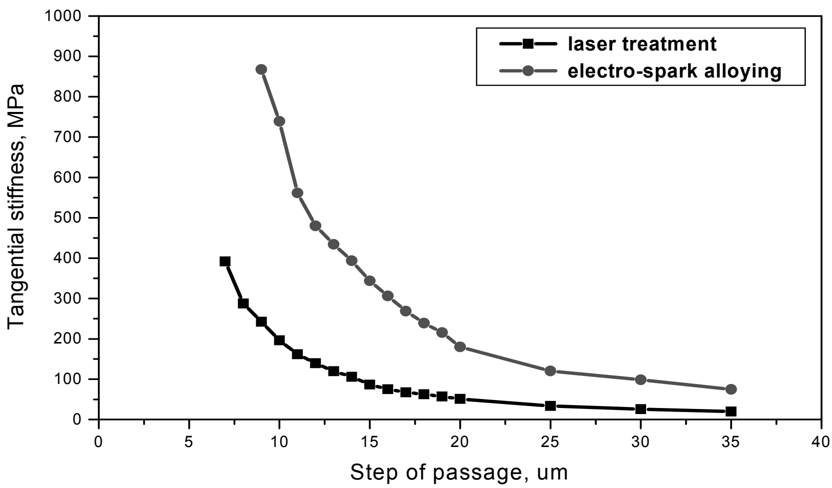


*Fig. 3.48. Dependence of tangential stiffness of contact surfaces from the step of passage of laser treatment and electro-spark alloying*

For correct modeling of behavior of contact under conditions of alternating tangentional loading, mass characteristics of the contact zone is defined as the sum of the masses of individual elements of the model, which at load involved in contacting:

$$M = \sum_{i=1}^{N} V_i \cdot \rho = \rho \sum_{i=1}^{N} \iint_D F(x,y)dxdy \tag{3.8}$$

where: $N$ – number of micro contacts, ρ – density of the material surface, $F(x, y)$ – function describing the surface mode of elliptic paraboloid, $D$ – domain of elements that is limited in height.

Results of mathematical modeling of contact by results of the offered method of the analysis of the modified surface are resulted in Table 3.12.

***Table 3.12.*** *Integrated characteristics of a contact zone for a steel C45*

| Type of processing | Specific value tangential stiffness, $\frac{N}{\mu m} \Big/ mm^2$ | | Specific value mass of modified layer, $\mu g/\mu m^2$ |
|---|---|---|---|
| | 10 MPa | 20 MPa | |
| Cu-Mo coating | 230.52 | 251.489 | 0.19 |

## Modeling of behavior of a contact zone

Given the complexity of terrain surfaces, which have been modified and given the fact that the elastic characteristics of the resulting of modification is largely different from the characteristics of the basic material, then contact of surface into a dynamic loading need consider as a separate element of dynamic system (Fig. 3.49).

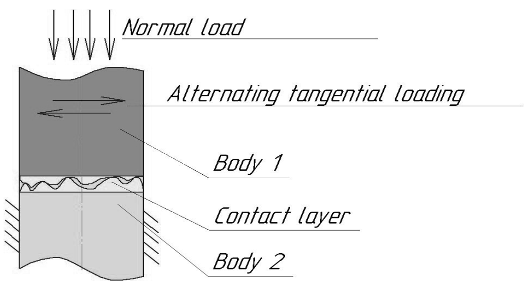


***Fig. 3.49.*** *Representation of contact as three-component dynamical system*

In this case, the mutual displacement of body 1 and body 2 $\Delta\Sigma$ can be represented as the sum of slip $\Delta K$ and deformation of the surface layer $\Delta П$ (Fig. 3.50).

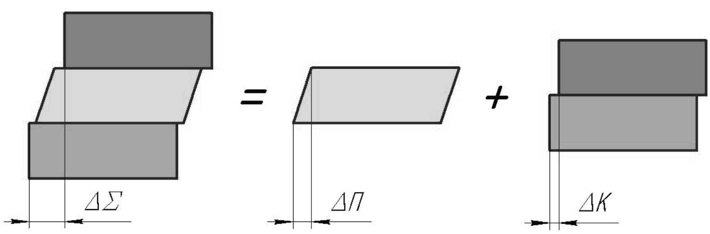


***Fig. 3.50.*** *Scheme of distribution of the relative displacement of contact parts*

The reason is that subjects in the methods of surface treatment of parts significantly alter the mechanical properties of the surface layers compared to the basic material. An important feature of the present contact zone is that area is selected layer, composition and specificity of any changes in the process of exploitation. In the initial moments at vibration of contact consist from it up microroughness of contacting bodies. With further development of fretting-wear, accumulation of wear products, area changes its structure by increasing the size of the metal layer that is drawn to the dynamic motion and replaces it with a layer of wear products that finally shows the destruction of the contact. This process is quite complex, because despite the low amplitude of reciprocal displacement, some formed by wear products derived from the contact that alters the characteristics of the layer. In general, the mass of elastically deformed layer can be represented as:

$$M = M_0 - M_{\det} \tag{3.9}$$

where: $M_0$ – initial mass of elastically-deformable surface layer that irregularities are formed by modification of surface, $M_{\det}$ – mass of material surfaces, which was removed from the surface due to wear or brought out of contact.

Assessment of fracture process of contact, based on the concept of "third body"

In condition of nominal-fixed joints, regardless of the layer products of wear, a crucial factor for ensuring the integrity of joint is share from the total area of "third body" which is indestructible machined surface irregularities. Therefore, the integrity of the contact can be evaluated in terms of structure contact zone – for contact in a state of coupling the vast majority of the masses "third body" of the mass inequalities, while in a slip of his products are wear. To estimate the effective mass of a "third body" was used method of estimation of intensity of formation of elements of a "third body" in the form of wear products:

$$M_{det} = M_{stab} + \left(M_{start} - M_{stab}\right) \cdot e^{-\left(C_S - C_W\right) \cdot \left(\frac{N}{2 \cdot \pi \cdot v}\right)} \tag{3.10}$$

where: $M_{stab}$ – weight of products of wear, $C_S, C_W$ – factors that determine the intensity of the flow of destructive processes in the contact zone and depend on the geometrical characteristics of surface and speed of relative motion, respectively, $M_{\max}$ – maximum amount of wear products in the absence of removing them from the contact, $M_{start}$ – mass of the surface layer to the flow of destructive processes, $v$ – frequency of oscillation.

In Figure 3.51 show the relationship between the mass of elastically-deformable layer from the number of loading cycles.

Modeling of work for NFJ with using the proposed method involves introducing into the model as initial values of integral characteristics of the mass and tangentional stiffness. Based on the dependence of mass elastically deformed layer on the number of loading cycles are changing the dynamic properties of the contact zone, and therefore the system's ability to resist of tangentional displacement. Simulation results for the investigated materials are shown in Figure 3.52. Charts slip coefficient depends on the number of loading cycles for surfaces subjected to laser exposure by capacity of 10 W and 15 W.

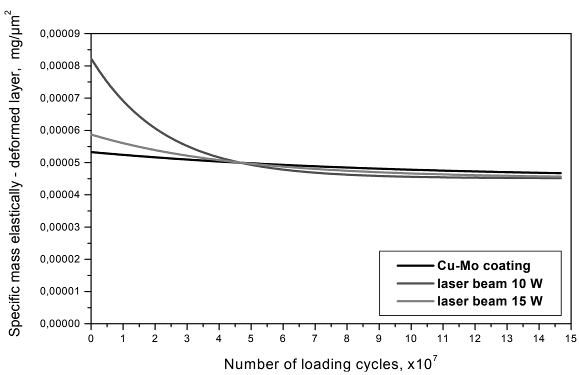


***Fig. 3.51.*** *Dependence of mass elastically-deformed layer on the number of loading cycles*

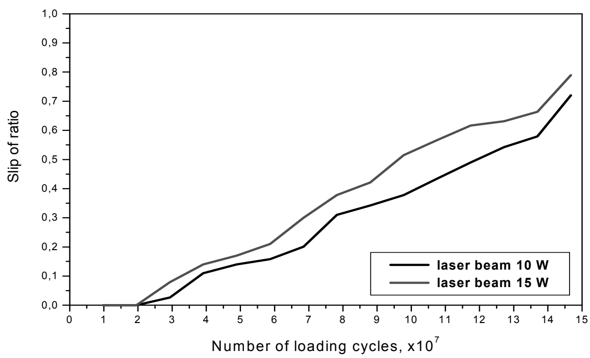


***Fig. 3.52.*** *Simulation of dependence of the coefficient of slip from number of loading cycles for surfaces subjected to laser processing by capacity of 10 W and 15 W*

## Comparison of results of numerical modeling with experimental data

Adequacy by adopted mathematical model and experimental results is shown in Figures 3.53-3.60. Contact behavior under oscillation load for steel C45 after electro-spark alloying (material electrodes – Cu and Mo wires with a diameter of 1 mm).

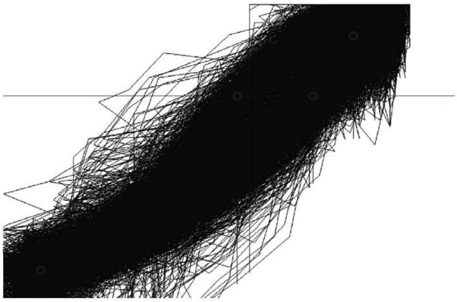

***Fig. 3.53.*** *Results of experimental studies (number of loading cycles N = 1.5·10⁷, amplitude of excitation A = 71.4 μm, normal load 45 N)*

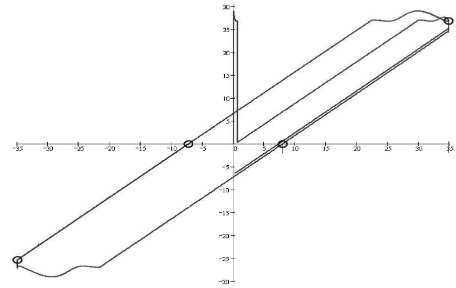

***Fig. 3.54.*** *Results of mathematical modeling (a moving mass layer m = 8.3562·10⁻⁶ g, stiffness system c = 230 N/μm, the amplitude of excitation A = 70 μm, normal load 45 N)*

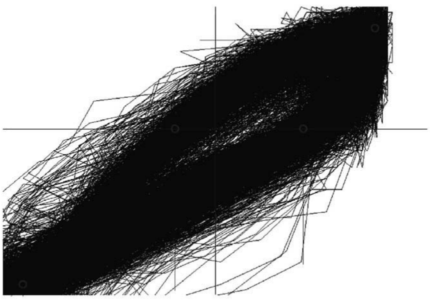

***Fig. 3.55.*** *Results of experimental studies (number of loading cycles N = 5·10⁷, amplitude of excitation A = 73.5 μm, normal load 45 N)*

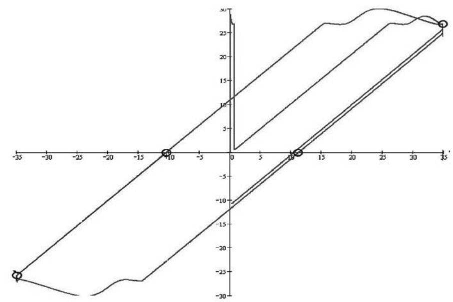

***Fig. 3.56.*** *Results of mathematical modeling (a moving mass layer m = 1.3895·10⁻⁶ g, stiffness system c = 230 N/μm, the amplitude of excitation A = 70 μm, normal load 45 N)*

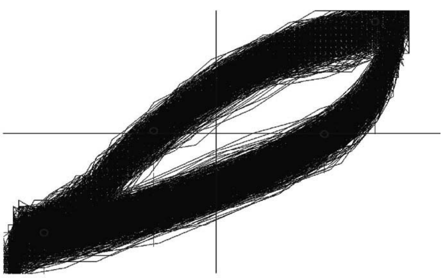

***Fig. 3.57.*** *Results of experimental studies (number of loading cycles N = 10⁸, amplitude of excitation A = 74.6 μm, normal load 45 N)*

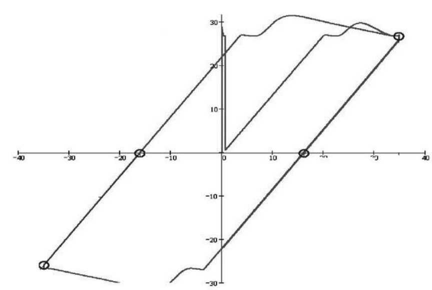

***Fig. 3.58.*** *Results of mathematical modeling (a moving mass layer m = 0.425·10⁻⁶ g, stiffness system c = 230 N/μm, the amplitude of excitation A = 75 μm, normal load 45 N)*

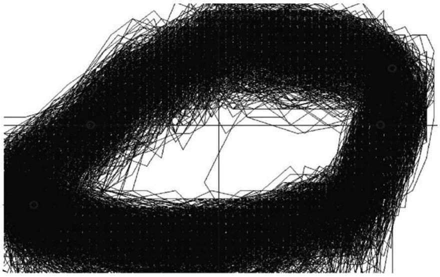

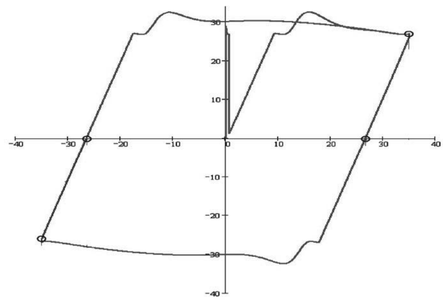

*__Fig. 3.59.__ Results of experimental studies (number of loading cycles N = 1.5·10$^8$, amplitude of excitation A = 75.21 µm, normal load 45 N)*

*__Fig. 3.60.__ Results of mathematical modeling (a moving mass layer m = 0.273·10$^{-6}$ g, stiffness system c = 230 N/µm, the amplitude of excitation A = 75 µm, normal load 45 N)*

Figure 3.61 shows the graph of slip ratio of the number of loading cycles for the experimental determination and mathematical modeling.

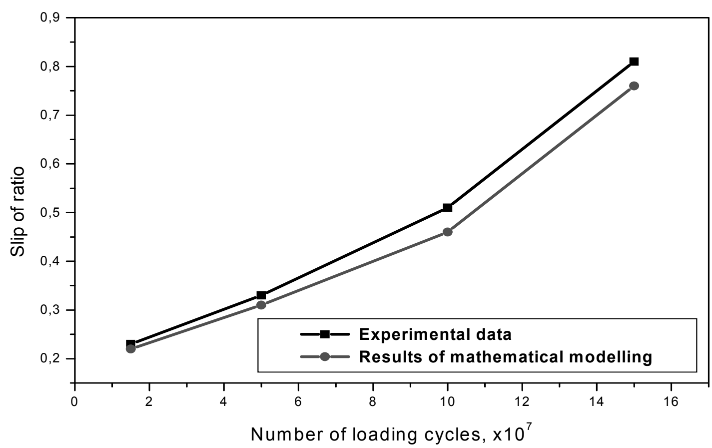


*__Fig. 3.61.__ Compare for experimental and mathematical modeling of behavior of nominally-fixed contact at treatment by electro-spark alloying*

Thus the proposed method to evaluate the influence of surface modification methods by creating a regular relief on the surfaces of nominally-fixed friction joints in long-term ability to maintain the integrity of contact under vibration loads.

The closeness of the mesh by laser treating was measured in percents, as relation of area treated by the laser irradiation to unit of area without treatment. In Figure 3.47 surfaces are shown after reinforcing by the laser irradiation of coating of Cu-Mo from 10% and 90% to the closeness of treatment.

Comparative description of vibroactivity of contact pair of harden steel C45 and steel is C45 + Cu-Mo + laser irradiation depending on the closeness of laser treatment and normal pressure is shown in Figure 3.62.

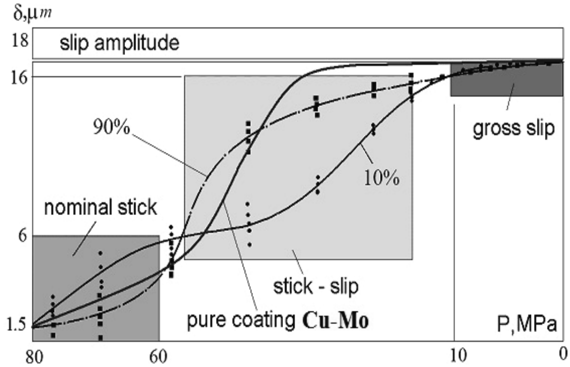


***Fig. 3.62.*** *Evolution of relative microdisplacement of contact pair in dependence from modified by the laser irradiation depending on normal pressure and 10%, 90% to the closeness of treatment. Frequency of oscillation 50 Hz, final amplitude 18…20 μm*

During the cyclic loading due to the wear normal pressure in an interface diminishes till about the zero of slip amplitude is multiplied at the same time. These two criteria determine fretting resistance of contact surfaces. We note, that duration of tests made to 200…300 o'clock of continuous oscillation.

As a result of research it is possible to draw next conclusions. More less cell which appear by the laser irradiation on coating is effective at large stress and provide the mixed contact without global slipping. The increase of sizes of cell is advantageous for stick-slip regime. The concentration of normal force on higher roughness creates effective tangential stiffness and sticking of surfaces. That at dynamic stick-slip regime duration of sticking is greater at 10% fill up surface, knife at 80% treatment of surface. For the last, we will mark that at large normal stress of force of quasi static friction sufficient in order resiliently to deform a surface layer without slip. After the laser reinforcing such type of roughness, which allows to accumulate products of fretting in hollow of separate cells and simultaneously to keep a high level adhesive and metallic joints on the spots of contact is created. It also promotes properties of sticking of surfaces. On the whole, reinforcing of electro-sparks coating by the laser irradiation depending on contact pressure lead to decrease vibration activity of contact pair to 30% in the regime of long duration of small amplitude fretting.

### 3.3.5. TEXTURE IMPACT ON CONTACT ISSUES

Frictional resistances between slide rings of the end-face seal depend on interrelations between elementary processes that occur in the gap. The processes include the following: hydrostatic and hydrodynamic action of the medium, the medium adhesion to the substrate, change in the gap geometry due to thermal and mechanical deformation, carrying away of heat, changes of phase and rheological properties of the liquid in the gap. Those interrelations, in turn, cannot be considered without referring to the physical properties of the medium, and of the surfaces that enclose the gap (e.g. viscosity, wettability), or to kinematic and dynamic relations between the above-mentioned factors. It should be understood that, depending on the factors, those elementary interrelations can produce either synergistic or antagonistic effect on the minimisation of frictional resistances in the seal gap. Bearing that in mind, the role of macro- and micro-geometry of the surfaces that constitute the gap needs to be taken into account. Departure from smooth and flat surface, if regular in character and properly designed, can bring about synergistic effect on the desirable properties of a sliding pair, such as bearing, durability and reliability. In view of all the arguments above, an important role for surface engineering technologies in producing sliding friction pairs should be emphasised. Those technologies, which once contributed to the manufacturing of flat and smooth surfaces, are currently employed to make heterogeneous and textured surfaces [74-77].

Figures 3.63 and 3.64 show examples of heterogeneous surfaces.

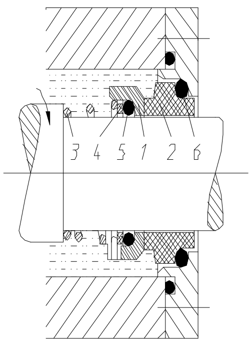


***Fig. 3.63***. *Schematic diagram of the face seal: 1 – axially shifted sliding ring, 2 – anti-ring, 3 – spring, 4 – clamping ring, 5, 6 – secondary seals [74]*

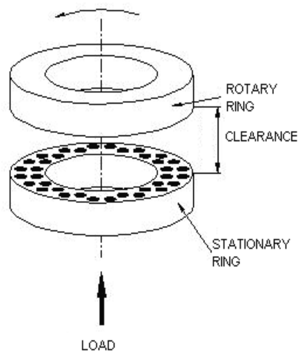


***Fig. 3.64.*** *Model sliding pair with textured surface [74]*

Generally, the real contact surface is smaller than the nominal one and contact load onto real contact surfaces are higher than the corresponding nominal values. In particular, while analysing the real geometries of contact of geometrically textured surfaces, it is necessary to have data on the real contact surface.

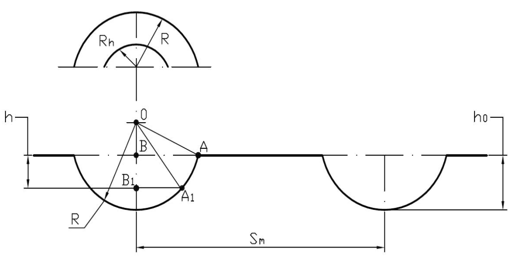


***Fig. 3.65.*** *Diagram of a geometric texture with spherical dimples*

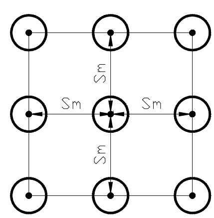


***Fig. 3.66.*** *Dimple spacing in the surface with uniform texture*

Depending on load, and also due to wear, the surface bearing profile undergoes changes. The analysis of changes in the bearing surface for the shape profile with spherical dimples is presented below (Fig. 3.65 and 3.66). As a result of deformations caused by load or wear, the depth of dimples of $h$ values is reduced in service, which also produces a reduction in the dimple radius to the value of $R_h$.

$$R_h = A_1B_1 = \sqrt{R^2 - (R - h_0 + h} = \sqrt{(h_0 - h)(2R - h_0 + h)} \tag{3.11}$$

For $2R >> h$

$$R_h = A_1B_2 = (R - h_0)^{\frac{1}{2}} (h_0 - h)^{\frac{1}{2}} \tag{3.12}$$

Because of exploitation, the bearing surface α (the ratio of the surface without dimples to the nominal surface) will be changed to the value of $\alpha_h$

$$\alpha = \frac{A_n}{A_0}, \quad \alpha_h = \frac{A_h}{A_0} \tag{3.13}$$

where: $A_n = A_0 - k\pi R^2$, $A_h = A_0 - k\pi R_h^2$ ($k$ – number of dimples on the surface $A_0$).

If loading with $F$ force is assumed, the following dependence for the value of pressure on the surface is received:

$$\sigma_h = \frac{F}{A_h} \tag{3.14}$$

After substituting dependences (3.12) and (3.13), the following is obtained:

$$\sigma_h = \left( \frac{1}{A_0 - k\pi (R - h_0)(h_0 - h)} \right) \sigma_0 \tag{3.15}$$

The amount of lubricant, its distribution and properties create various situations in the sliding pair. Those generate processes in the contact zone, which are different qualitatively and quantitatively. If only the amount and wetting properties of the lubricant are taken into account, four cases should be differentiated (Fig. 3.67).

Texture is described by geometric relations for a single texture element, and also by relations that refer to their spacing on the friction surface. As regards a texture composed of uniformly distributed dimples having the form of spherical bowls, it is possible to state relations between a degree of blackening, diameter and depth of dimples and their volume.

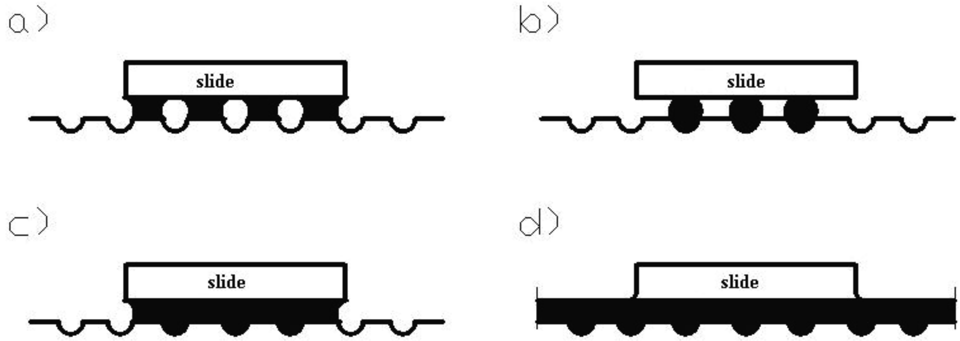


*Fig. 3.67. The interaction of the lubricant and the textured surface in the sliding pair: a) lean lubrication with a weak wetting agent, b) lean lubrication with a good wetting agent, c) sufficient lubrication of the slide with a good wetting agent, d) abundant and continuous lubrication of the textured surface*

## Texturing methodology and wear tests

Laser surface texturing is one of the most common and promising methods of surface roughening. Categorized as a metal removal process, laser texturing is usually performed at a power density of $10^6 \div 10^9$ W/cm$^2$. At present, it accounts for about 2% of all laser-based material processing processes used in the world. In laser surface texturing, a pulsed laser beam is focused on a material to melt a hole. The hole depth is dependent mainly on the power density and the pulse duration. The drilling debris is removed from a hole being drilled using compressed air or another inert gas.

The tests were conducted for Cu-Mo coatings produced by electro-spark deposition onto rings made of carbon steel C45.

The texturing was performed using an Nd:YAG laser (impulse mode), model BLS 720, and operating in the pulse mode under the following conditions:

- laser spot diameter, $d = 0.7$ mm,
- laser power, $P = 20$ W,
- beam shift rate, $v = 1200$ mm/min,
- nozzle-sample distance, $h = 1$ mm,
- pulse duration, $t_i = 1.2$ ms,
- frequency, $f = 8$ Hz.

A Joel JSM-5400 scanning electron microscope was used to study the effects of laser surface texturing. Selected SEM images are presented in Figures 3.68 and 3.69. As can be seen, the surface structure after laser surface texturing is regular. The surface is covered by bumps and dimples resulting from phase and structural modifications and the accompanying specific volume changes in the laser affected zones. Lapping and super finish are used to obtain hard flat areas transferring normal loads and areas of pores where the hydrodynamic forces are generated during fluid lubrication. Surfaces with such a texture can be applied, for instance, to sliding friction systems. The microscopic analysis showed that the removal of the drilling debris was not complete when the laser beam was focused locally. This was probably due to insufficient power density. The action of the thermocapillary forces and the convective motion resulted in the formation of rims, whose structure consisted of molten and then crystallized Cu-Mo.

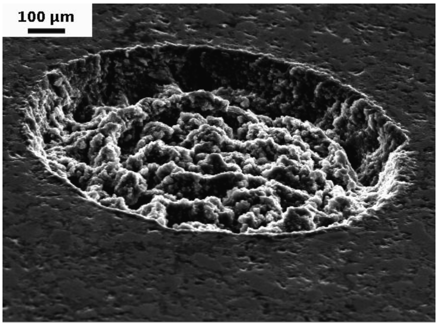


*Fig. 3.68*. A view a single microcavity on the ring

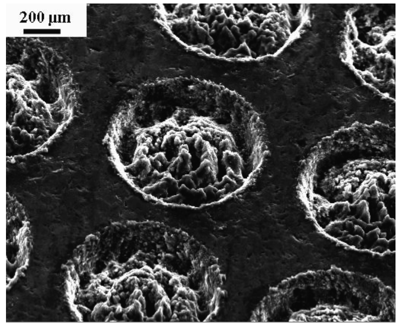


*Fig. 3.69.* A view of a system of microcavities on the ring

The wear tests of the Cu-Mo electro-spark deposited coatings before and after laser surface texturing were carried out using a pin-on-disc tester, T-01M.

The tester makes it possible to measure the friction force for a predetermined load. The pin ϕ 4 x 20 mm was made of tool steel. The samples and anti-samples were prepared in accordance with the instruction. The tests were conducted at the following parameters of friction:

– linear velocity $v = 0.8$ m/s,
– test duration $t = 3600$ s,
– sliding distance $S = 2880$ m.
– range of load changes: 5, 10, 15 N.

A drop of lubricant – paraffin oil was applied on the ring raceway only once. It was necessary to measure the time after which the value of the friction coefficient increased.

The wear test results for the electro-spark deposited Cu-Mo coating before and after laser surface texturing are shown in Tables 3.13 and 3.14.

***Table 3.13.*** *Results of the wear test for the Cu-Mo coating after laser surface texturing*

| **Load, N** | **Weight loss, mg** | | | |
|---|---|---|---|---|
| | not lubricated | | lubricated oil | |
| | pin | disc | pin | disc |
| **5** | 5.44 | 6.88 | 3.35 | 4.26 |
| **10** | 10.24 | 12.16 | 7.11 | 8.63 |
| **15** | 14.88 | 20.16 | 10.29 | 15.72 |

***Table 3.14.*** *Results of the wear test for the Cu-Mo coating before laser surface texturing*

| **Load, N** | **Weight loss, mg** | | | |
|---|---|---|---|---|
| | not lubricated | | lubricated oil | |
| | pin | disc | pin | disc |
| **5** | 6.16 | 9.64 | 4.89 | 6.33 |
| **10** | 13.05 | 16.84 | 9.06 | 11.54 |
| **15** | 19.41 | 23.28 | 13.14 | 18.67 |

Table 3.15 shows the values of the friction coefficient for the Cu-Mo coating before and after laser surface texturing.

***Table 3.15.*** *Results of the friction coefficient for the Cu-Mo coating before and after laser surface texturing*

| **Load, N** | **Friction coefficient** | | | |
|---|---|---|---|---|
| | not lubricated | | lubricated oil | |
| | Cu-Mo | CuMo+laser | Cu-Mo | Cu-Mo+laser |
| **5** | 0.39 | 0.40 | 0.21 | 0.14 |
| **10** | 0.54 | 0.46 | 0.35 | 0.23 |
| **15** | 0.67 | 0.48 | 0.43 | 0.32 |

## REFERENCES


[1] Ho K.H., Newman S.T.: *State of the art electrical discharge machining*. International Journal of Machine Tools & Manufacture, 43 (2003), pp. 1287-1300.

[2] Miernikiewicz A.: *The bases of experimental and theoretical in electro discharge machining (EDM).* Technical University of Cracow, 274 (1999).

[3] DiBitonto D.D., Eubank P.T., Patel M.R., Barrufet M.A.: *Theoretical models of the electrical discharge machining process. I-A simple cathode erosion model*. Journal of Applied Physics 66, 9 (1989), pp. 123-131.

[4] Spadło S. et al.: *Investigation of electro-discharge mechanical dressing (EDMD) of diamond abrasive wheels with conductive bonds using brush electrodes*. Journal Engineering Manufacture, Vol. 219, part B, (2005), pp. 1-8.

[5] Ribalko A.V., Sahin O.: *The use of bipolar current pulses in electro-spark alloying of metal surfaces.* Surface & Coatings Technology, 168 (2003), pp. 129-135.

[6] Galinov I.V., Luban R.B.: *Mass transfer trends during electrospark alloying*. Surface & Coatings Technology, 79 (1996), pp. 9-18.

[7] Spadło S., et al.: *The superficial layer of parts machined by brush electro discharge mechanical machining (BEDMM)*. Journal Engineering Manufacture, Vol. 218, part B (2004), pp. 9-15.

[8] Radek N., Wrzałka Z., Szalapko J.: *Measurement of electric impulses and properties of carbides electro-spark coatings*. [in:] *Scientific basis of modern technologies: experience and prospects*. ed. by J.I. Shalapko and L.A. Dobrzański, Jaremche 201, Ukraine, pp. 223-235.

[9] Radek N., Wrzałka Z., Szalapko J., Bronček J.: *Struktura geometryczna powierzchni i własności tribologiczne przeciwzużyciowych powłok elektroiskrowych* [w:] *Inżynieria Powierzchni wybrane zagadnienia*. Red. Bogdan Antoszewski, Wydawnictwo Politechniki Świętokrzyskiej, Kielce 2011, s. 132-139.

[10] U.S. Patent No. 5071059 Method for joining single crystal turbine blade halves – 1991.

[11] http:// www.stt-inc.com

[12] G.B. Patent No. 637793 A metod of working Metals – 1946.

[13] DiBitonto D.D., Eubank P.T., Patel M.R., Barrufet M.A.: *Theoretical models of the electrical discharge machining process. I-A simple cathode erosion model.* Journal of Applied Physics, 66/9 (1989), pp. 123-131.

[14] Zolotych B.N.: *Osnovnyje voprosy kaciestviennoj teorii elektroiskrovoj obrabotki v zidkoj dielektricieskoj srede. Problemy elektrićeskoj obrabotki metallov*. Moskwa 1962.

[15] Petrow J. (red.): *Elektroiskrowoje legirowanie metallićieskich powierchnostoj*. Kisziniew 1985.

[16] Abu Zeid O.A.: *On the effect of electrodischarge machining parameters on the fatigue life of AISI D6 tool steel.* Journal of Materials Processing Technology, 68, 1 (1997), pp. 27-32.

[17] Lazarenko B.R., Lazarenko N.I.: *Elektroiskrovaja obrabotka tokoprovodiaszćih materiałow.* Akademia Nauk CCCP, Moskwa 1958.

[18] Galinov I.V., Luban R.B.: *Mass transfer trends during electrospark alloying*. Surface and Coatings Technology, 79 (1996), pp. 9-18.

[19] Samsonow G., Wierhotyrow A., Bowkun G., Sycziew B.: *Elektroiskrowoje legirowanie metalliczeskich powierchnostoj.* Wydawnictwo Naukowa Dumka, Kijev 1976.

[20] Pierzynowski R.: *Badania elektroiskrowego stopowania powierzchni elektrodami szczotkowymi*. Rozprawa doktorska, PW, Warszawa 2001.

[21] Wierhotyrow A.D., Mulin J.I., Astapowa E.S., Agapiatow W.A., Cietinin M.I., Kozyr A.W., Sołowiew W.W.: *Wlijanie riezimow eliektroiskrowogo liegirowanija i eliektrodnych materiałow na struktury i iznosostoikost pokrytij*. Elektronnaja Obrabotka Materiałow, 3 (2004), s. 21-25.

[22] Konstanty J.: *Powder metallurgy diamond tools*. Elsevier, Oxford 2005, pp. 74-76.

[23] Hebda M., Wachal A.: *Trybologia.* Wydawnictwo Naukowo-Techniczne, Warszawa 1980.

[24] Kupczyk M.: *Jakość technologiczna i użytkowa ostrzy skrawających z powłokami przeciwzużyciowymi*. Politechnika Poznańska – Rozprawy, 320, Poznań 1997.

[25] Dobrzański L.A.: *Podstawy nauki o materiałach i metaloznawstwo*. Wydawnictwo Naukowo-Techniczne, Warszawa 2002.

[26] Wrzałka Z., Radek N.: *Pomiary i analiza impulsów elektrycznych podczas obróbki elektroiskrowej.* Zeszyty Naukowe Politechniki Świętokrzyskiej – Terotechnologia 2008, Budowa i Eksploatacja Maszyn, 11 (2008), s. 329-336.

[27] Radek N.: *Determining the operational properties of steel beaters after electrospark deposition*. "Eksploatacja i Niezawodność – Maintenance and Reliability", 4 (2009), pp. 10-16.

[28] Radek N., Broncek J.: *Tribological properties of anti-wear carbides coatings*. Technolog, 6 (2009), pp. 56-59.

[29] Chang-bin T., Dao-xin L., Zhan W., Yang G.: *Electro-spark alloying using graphite electrode on titanium alloy surface for biomedical applications.* Applied Surface Science, 257 (2011), pp. 6364-6371.

[30] Radek N., Bartkowiak K.: *Performance properties of electro-spark deposited carbide-ceramic coatings modified by laser beam*. Physics Procedia, 5 (2010), pp. 417-423.

[31] Radek N., Bartkowiak K.: *Laser treatment of Cu-Mo electro-spark deposited coatings*. Physics Procedia, 12 (2011), pp. 499-505.

[32] Radek N., Wajs W., Luchka M.: *The WC-Co electrospark alloying coatings modified by laser treatment.* "Powder Metallurgy and Metal Ceramics", 3-4 (2008), pp. 197-201.

[33] Radek N., Antoszewski B.: *Influence of laser treatment on the properties of electro-spark deposited coatings*. Kovove Materialy-Metallic Materials, 1 (2009), pp. 31-38.

[34] Burakowski T., Wierzchoń T.: *Inżynieria powierzchni metali*. Wydawnictwo Naukowo-Techniczne, Warszawa 1995.

[35] Domański R.: *Promieniowanie laserowe – oddziaływanie na ciała stałe*. Wydawnictwo Naukowo-Techniczne, Warszawa 1990.

[36] Kusiński J.: *Lasery i ich zastosowanie w inżynierii materiałowej*. Wydawnictwo Naukowe Akapit, Kraków 2000.

[37] Konstanty J.: *Powder metallurgy diamond tools*. Elsevier, Oxford 2005, pp. 74-76.

[38] Moriya N.: Granulating apparatus. US Patent 4,655,701 (April 7, 1987).

[39] Weber G.: *Granulating: a new process for diamond tool producers.* In Proceedings of International Workshop on Diamond Tool Production, Turin, Italy, November 8-10, 1999, pp. 73-82.

[40] Baert M.: *Coating of diamonds and granulation of metal powders.* In Proceedings of Seminar on PM Diamond Tools, Lausanne, Switzerland, November 2-3, 1995, pp. 24-40.

[41] Van Doorslaer T.: *Coating of abrasive grains and the granulation of metal powders.* In Proceedings of International Workshop on Diamond Tool Production, Turin, Italy, November 8-10, 1999, pp. 83-88.

[42] Burckhardt S.: *New technique for granulating diamond and metal powders.* Industrial Diamond Review 57, 4 (1997), pp. 121-122.

[43] Weber K.: *Modern diamond segment production on cold presses and hot presses.* In Proceedings of Seminar on PM Diamond Tools, Lausanne, Switzerland, November 2-3, 1995, pp. 48-50.

[44] Weber G., Burckhardt S.: *Economic production of diamond segments.* Industrial Diamond Review 58, 4 (1998), pp. 111-112.

[45] Anon.: *New high-performance cold press from Dr Fritsch*. Industrial Diamond Review 63, 4 (2003), p. 25.

[46] Adamczak S.: *Pomiary geometryczne powierzchni. Zarysy kształtu, falistości i chropowatości*. Wydawnictwo Naukowo-Techniczne, Warszawa 2008.

[47] Adamczak S.: *Normalizacja pomiarów struktury geometrycznej powierzchni*. Cz. 7, *Ocena chropowatości i falistości powierzchni*. „Mechanik", 5-6 (2005), s. 526-529.

[48] Antoszewski B.: *Influence of laser and plasma modification on surface properties of sliding and rubbing components*. Technical University of Kielce, 17, Kielce 1999, pp. 39-52.

[49] Gyk G., Etsion I.: *Testing piston rings with partial laser surface texturing for friction reduction*. Wear 216 (2006), pp. 792-796.

[50] Wan Yi, Xiong Dang-Sheng: *The effect of laser surface texturing on frictional performance of face seal*. Journal of Materials Processing Technology, 197 (2008), pp. 96-100.

[51] Antoszewski B., Radek N.: *Tribologiczne i technologiczne aspekty teksturowania par ślizgowych o powierzchniach płaskich.* „Tribologia, teoria i praktyka", 2 (2008), s. 25-33.

[52] Antoszewski B., Radek N., Tarelnik W.: *Mikroteksturowanie powierzchni ślizgowych par tarcia obróbką elektroerozyjną*. Zeszyty Naukowe Politechniki Świętokrzyskiej – „HERVICON 2008", Budowa i Eksploatacja Maszyn, 10 (2008), s. 231-238.

[53] Antoszewski B., Radek N.: *Technologia oraz cechy powierzchni teksturowanych metodą laserową i elektroerozyjną*. „Inżynieria Maszyn", R. 12, 4 (2009), s. 5-12.

[54] Antoszewski B., Radek N., Tarelnik W., Wajs E.: *Electro discharge and laser texturing of sliding face of mechanical seals*. IX International Conference HERVICON – Sumy, Ukraina, T. 3, 2005, 1, pp. 15-123.

[55] Radek N., Antoszewski B.: *Mikroteksturowanie powierzchni ślizgowych par tarcia technologią laserową i elektroerozyjną.* „Logistyka", 2 (2010), pp. 2149-2156.

[56] Radek N.: *Laserowe i elektroerozyjne teksturowanie par ślizgowych o powierzchniach płaskich.* „Mechanik", 11 (2010), s. 822-825.

[57] Kunda J., Broncek J., Hadzima B.: *Experimental access to invvestigation of tribocorrsive properties of mechanical parts surfaces.* Scientific basic of moder Technologies: Experience and Prospects, Ukraina, (2011), pp. 299-310.

[58] Broncek J., Vidiečan J., Dzimko M.: *Comparison of roughness measurement methods*. Zeszyty Naukowe Politechniki Świętokrzyskiej – IV Letnia Szkoła Inżynierii Powierzchni (2010), pp. 19-26.

[59] Arnold J., Muller G., Schneider H., Muller H.K., Hugel H.: *Production of micro structures in SiC slide rings with an excimer laser*. "Laser und Optoelektronik", 25 (1993), pp. 12-16.

[60] Etsion I.: *A laser surface textured hydrostatic mechanical seal sealing technology*. Sealing Technology, 3 (2003), pp. 6-10.

[61] Yu X.Q., He S.: *Frictional characteristics of mechanical seals with a laser textured seal face*. Journal of Materials Processing Technology, 129 (2002), pp. 463-466.

[62] Kovalchenko A., Ajayi A., Erdemir A., Fenske G., Etison I.: *The effect of laser surface texturing on transitions in lubrication regimes during unidirectional sliding contact.* Tribology International, 38 (2005), pp. 219-225.

[63] Erdemir A.: *Review of engineered tribological interfaces for improved boundary lubrication*. Tribology International, 38 (2005), pp. 249-256.

[64] Volchok A., Halperin G., Etsion I.: *The effect of surface regular microtopography on fretting fatigue life*. Wear 235 (2002), pp. 509-515.

[65] Miller K.J.: *Structural integrity – whose responsibility?,* 36$^{th}$ John Player Lecture, IMechE, Sheffield 2001, p. 24.

[66] Mindlin R.D., Deresiewicz H.: *Elastic spheres in contact under varying oblique forces.* ASME J. Appl. Mech., 75 (1953), pp. 327-344.

[67] Ciavarella M.: *The generalized Cattaneo partial slip plane contact problem*. I-Theory. Int. J. Solids Struct 35, 18 (1998), pp. 2349-2362.

[68] Menq C.H., Bielak J., Griffin J.H.: *The influence of microslip on vibratory response. A new microslip model.* Part I. Journal of Sound and Vibration 107, 2 (1986), pp. 279-293.

[69] Menq C.H., Bielak J., Griffin J.H.: *The infuence of microslip on vibratory response a new microslip model.* Part II, Journal of Sound and Vibration 107, 2 (1986), pp. 295-307.

[70] Tomlinson G.A.: *The rusting of steel surfaces in contact*. Proc. Roy. Soc. Lond. A 115, 1927, pp. 472-483.

[71] Tomlinson G.A., Thorpe P.L., Gough H.J.: *An Investigation of the Fretting Corrosion of Clossely Fitting Surfaces*. Proc. Inst. Mech. Eng., 141 (1939), pp. 223-249.

[72] Ruiz C., Chen K.C.: *An investigation of fatigue and fretting in a dovetail joint*. Experimental Mechanics, 24 (1984), pp. 208-217.

[73] Tritschler B., Forest B., Rieu J.: *Fretting corrosion of materials for orthopaedic implants: a study of a metal/polymer contact in an artificial physiological medium.* Tribol. Int., 32 (1999), pp. 587-596.

[74] Antoszewski B.: *Warstwy powierzchniowe z teksturą – kształtowanie wybranymi technologiami wiązkowymi oraz właściwości tribologiczne.* Wydawnictwo Politechniki Świętokrzyskiej, Kielce 2010.

[75] Antoszewski B.: *Problems of maintenance of sustainable technological systems.* [w:] *Improvement of the conditions of lubrication friction ties by laser textured lubrication*. Wydawnictwo PNTTE 2010, Tom 1, pp. 62-75.

[76] Antoszewski B.: *The formation of antiwear surface layers on elements of machine parts.* Zagadnienia Eksploatacji Maszyn, Vol. 44, 2 (2009), pp. 7-19.

[77] Antoszewski B.: *Production, properties and application of laser textured components*. "Logistyka" 6 (2009), pp. 88-100.

The paper was performed within N N503 150736 project financed by the Ministry of Science and High Education